Acoustofluidics

2022

Table of Contents

Copyright Page

Welcome Letter

It is with great pleasure that we welcome you all to the annual Acoustofluidics conference 2022. Although the on-line conferences of the last two years were a big success and well received by all participants, we are very happy to be able to return to in-person conferences. After the two years of challenges caused by the COVID-19 pandemic, we whole-heartedly welcome everyone to the return of this in-person conference in Glasgow.

This year we received an unprecedented number of abstract submissions at 97 from 20 countries, 6 from the Americas, 35 from the Asia / Pacific Rim region and 56 from Europe and Africa. All the abstracts were of very high standard, and this made the review and selection process particularly difficult. We have tried to fit in as many talks, flash talks and poster presentations as possible. We also decided to have the abstracts recognised as publications by getting ISBN registered. We hope this will add to the visibility of the conference and the Acoustofluidics Society, and, in particular, to the young research authors who contributed an abstract.

We are very fortunate to have a series of excellent keynote and invited speakers for you, who will give fascinating insights in their chosen topics. We thank them for agreeing to present at this conference and give us the benefit of their expertise. This year we introduced a novel category for choosing an invited speaker. This year we asked the winner of the previous year's poster prize to attend the conference as an invited speaker. In addition to our prestigious W. Terence Coakley Award, a new award has been introduced, the "Best Acoustofluidic Research Image". This new award is sponsored by the Royal Society of Chemistry, Lab-on-a-Chip, and the winning image is published in Lab-on-a-Chip. There will also be Flash Talks and an Olympiad with hand-on demonstrations where they will be competing for a medal.

We would like to thank all the support and feedback we have received from the members of the Acoustofluidics Society and community that has enabled us to put on this event. We greatly appreciate the help of the Scientific Committee with the evaluation and rapid turnaround of the abstracts submitted for the conference. This event would not have been possible without the excellent support received from PMMI Global. Finally, we appreciate the support from our long-standing sponsors the Acoustofluidics Society and CBMS.

We are fortunate in being able to host this conference in the newly opened Mazumdar-Shaw Advanced Research Centre (ARC) with its state-of-the-art conference and research facilities. It will be great to see you again in person and have a truly exciting, stimulating and productive conference on the 19th – 21st October 2022.

Thomas Franke
Glasgow University, UK
Chair Acoustofluidics 2022

Richard Fu
Northumbria University, UK
Chair Acoustofluidics 2022

General Information

Wireless Internet Service
Wireless Internet will be available in the meeting space. A password is not needed.

• Staff or Students of the University of Glasgow may use: **Eduroam**
• All others should select: **UoGvisitor Wi-Fi**

Chimes
The chimes will ring five minutes before the end of each scheduled break. The sessions will begin on time, so please return to the sessions when you hear the chimes.

Cellular Phones and Alarms
As a courtesy to our speakers and other attendees, please turn off any cellular phones and alarms during sessions.

Video Recording
Video recordings are strictly prohibited in the sessions and poster presentations.

Banquet
Thursday, 20 October
19:30 - 21:30
Glasgow Union Dining Hall
32 University Avenue, Ground Floor

No conference is complete without a banquet. Join us on Thursday evening at the Glasgow Union Dining Hall where you will a delicious meal and a chance to network with colleagues. Please note that transportation will not be provided by the conference. Check with your hotel front desk for directions. Two glasses of wine will be provided during dinner and a cash bar will be available for additional drinks.

Flash Presentations
Some of the flash presentations will also present a poster on the same day as their presentation. Friday flash posters will present on Thursday.   Participating posters are marked with ◇ in the schedule.

Conference Officials

Conference Chairs

Thomas Franke .... University of Glasgow, SCOTLAND
Richard Fu .... Northumbria University, UK

Local/Hybrid Organizing Committee

Raymond Sparrow .... University of Glasgow, SCOTLAND
Esther Richter .... University of Glasgow, SCOTLAND
Andreas Link .... University of Glasgow, SCOTLAND
Mathew Woods .... University of Glasgow, SCOTLAND
Mustafa Zaimagaoglu .... University of Glasgow, SCOTLAND
Per Augustsson .... Lund University, SWEDEN

Advisory Committee

Per Augustsson .... Lund University, SWEDEN
Rune Barnkob .... Independent Consultant, ITALY
Xuexin Duan .... Tianjin University, CHINA
Thomas Franke .... University of Glasgow, SCOTLAND
James Friend .... University of California, San Diego, USA
Richard Fu .... Northumbria University, UK
Peter Glynne-Jones .... University of Southampton, UK
Mark Meacham .... Washington University, St. Louis, USA
Ashis Kumar Sen .... Indian Institute of Technology, Madras, INDIA
Tim Segers .... University of Twente, NETHERLANDS
Glauber T. Silva .... Universidade Federal de Alagoas, BRAZIL
Maria Tenje .... Uppsala University, SWEDEN

Scientific Committee

Henrik Bruus (Chair) .... Technical University of Denmark, DENMARK
Michaël Baudoin .... Université de Lille, France
Anne Bernassau .... Heriot Watt University, UK
Philippe Brunet .... Université Paris Diderot, FRANCE
Feiyan Cai .... Shenzhen Institute of Advanced Technology, CHINA
Bruce Drinkwater .... University of Bristol, UK
Jürg Dual .... ETH Zürich, SWITZERLAND
Mohamed El Malki .... Mohammed First University, MOROCCO
Itziar González Gómez .... CSIC, SPAIN
Xiasheng Guo .... Nanjing University, CHINA
Martyn Hill .... University of Southampton, UK

Scientific Committee

Tony Jun Huang .... Duke University, USA
Thomas Laurell .... Lund University, SWEDEN
Andreas Lenshof .... Lund University, SWEDEN
Kian-Meng Lim .... National University of Singapore, SINGAPORE
Jikui "Jack" Luo .... Zhejiang University, CHINA
Philippe Marmottant .... Université Grenoble Alps, FRANCE
Adrian Neild .... Monash University, AUSTRALIA
Stefan Radel .... TU Wien, AUSTRIA
Hagen Schmidt .... IFW Dresden, GERMANY
Karthick Subramani .... Indian Institute of Information Technology, Design and
Manufacturing Kancheepuram, INDIA
Hyung Jin Sung .... Korea Advanced Institute of Science & Technology, KOREA
Michel Versluis .... University of Twente, NETHERLANDS
Martin Wiklund .... KTH Stockholm, SWEDEN

Acoustofluidics Society

The Acoustofluidics Society is an international body that represents and facilitates the interests of researchers and industries in the fields of acoustic particle manipulation, acoustic fluid control, and associated technologies, with particular applications in the Life sciences.
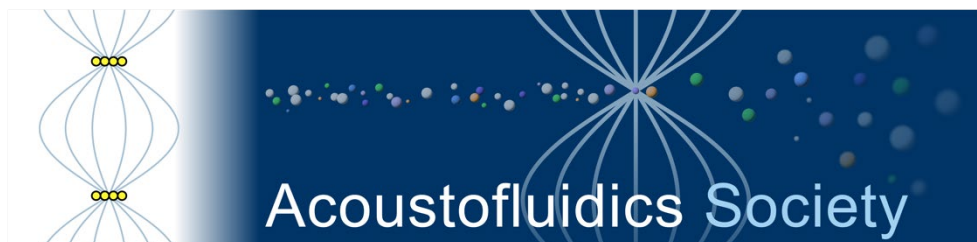
Executive Committee

Peter Glynne-Jones .... President
Per Augustsson .... Vice-President
Thomas Franke .... Secretary
James Friend .... Treasurer

Board Members

Mark Meacham	Ashis Kumar
Glauber T. Silva	Maria Tenje
Richard Fu	Rune Barnkob
Xuexin Duan	Tim Segers

Benefactors

Conference Sponsor

**Chemical and Biological Microsystems
Society (CBMS)**
www.cbmsociety.org

Gold Benefactors

BelektroniG GmbH
Hauptstrasse 38
Freital, 01705 GERMANY
r.bruenig@belektronig.de
www.belektronig.de

usePAT GmbH
Schoenbrunnerstrasse 231
Vienna, 1120 AUSTRIA
phone: +43-67-0606-6582
info@usepat.com
www.usePAT.com

Silver Benefactor

Nanotechnology and Precision Engineering
c/o AIP Publishing
1305 Whitman Road, Suite 110
Melville, NY 11747 USA
phone: 1-516-576-2200
journals@aip.org
npe.aip.org

Best Acoustofluidics Research Image Award Sponsor

Royal Society of Chemistry
Thomas Graham House (290)
Science Park, Milton Road
Cambridge, CB4 0WF UK
phone: +44-1223-420-066
www.rsc.org

Floorplan
Mazumdar-Shaw Advanced Research Centre (ARC)

Olympiad
OSAFT
Studio 2

Restrooms

General Session
Seminar Room

Posters and Exhibits

Registration

ARC Entrance

Restrooms

University of Glasgow — Estates | Directorate
University Ave
Glasgow
G12 8QQ
0141 330 2000/330 6000
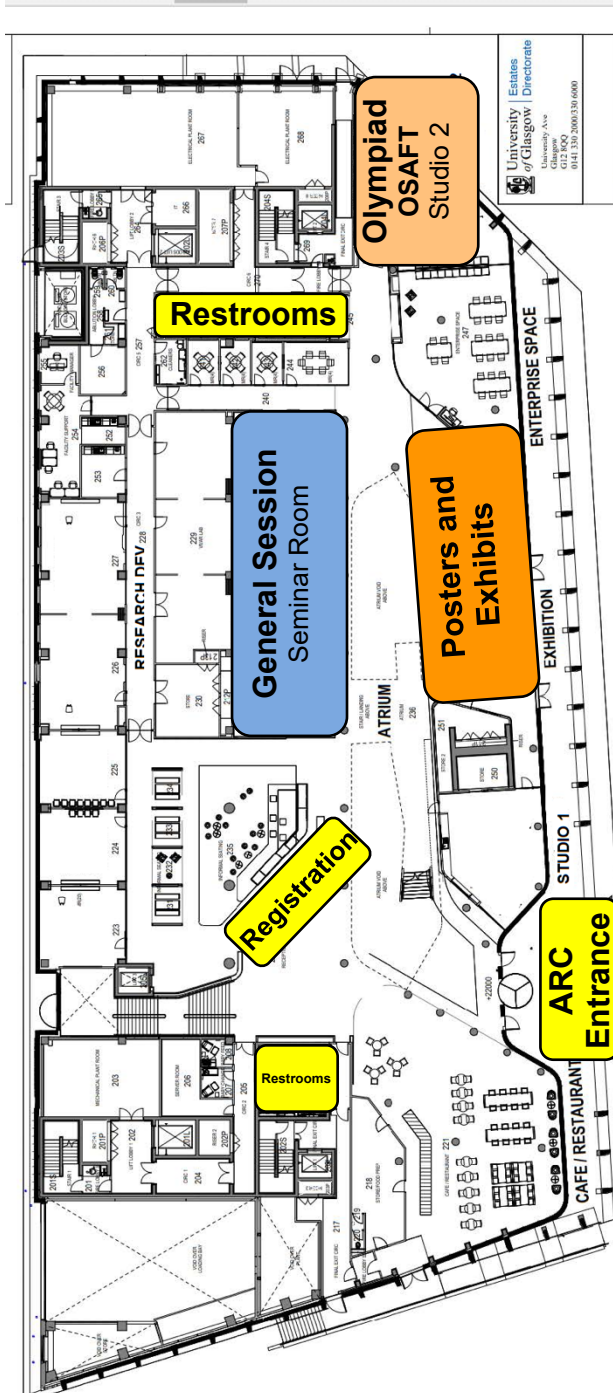
Keynote Speakers

ACOUSTIC LEVITATION: FASTER, HIGHER, STRONGER
Bruce Drinkwater
University of Bristol, UK

MECHANICS AND EXPERIMENTAL DYNAMICS: FROM ACOUSTOFLUIDICS TO GRAVITATIONAL INTERACTION
Jürg Dual
ETH Zürich, SWITZERLAND

HEARING IS BELIEVING: CORRELATING OPTICAL AND ACOUSTIC IMAGING OF BUBBLE DYNAMICS IN A MICROFLUIDIC SYSTEM
Eleanor Stride
University of Oxford, UK

ACOUSTIC CONTROL OF SORTING AND FLUID INJECTION IN MICROFLUIDIC DEVICES
David Weitz
Harvard University, USA

Invited Speakers

EXPLOITING ACOUSTIC FIELD-MICROSWIMMER INTERACTIONS TO ACCELERATE ACOUSTOFLUIDIC DEVICE DEVELOPMENT
Mark Meacham
Washington University in St. Louis, USA

STANDING WAVE ACOUSTOPHORESIS OF LEGIONELLA SPECIES AND THE INFLUENCE OF MULTIBODY EFFECTS
Alen Pavlič
ETH Zürich, SWITZERLAND

MOMENTUM CONSERVATION AND THE 2ND LAW IN BIOLOGICAL COMMUNICATION
Matthias Schneider
Technische Universität Dortmund, GERMANY

LEVERAGING TIME AND FREQUENCY MULTIPLEXING FOR DYNAMIC ACOUSTIC TWEEZERS
Zhenhua Tian
Virginia Tech, USA

Acoustofluidics Olympiad

The demonstrations room has acoustofluidic systems under development. You will see how well these systems perform in the real world. The Acoustofluidic Olympics will take place during the demonstration session where all systems will be open to your full scrutiny. There will be categories such as speed of particle and liquid movement, heaviest particle, cornering speed and smallest electronic circuit. "

OSAFT (Open-Source Acoustofluidic Theory) Demo

Thursday, 20 October
16:05 – 18:05
Christoph Goering and Jonas Fankhauser
ETH Zürich, SWITZERLAND

The OSAFT (open-source acoustofluidic theory) library is written in python and the documentation to the most recent released version can be found here (https://osaft.readthedocs.io/en/stable/). OSAFT was designed to achieve two main objectives:

1. An unified API for different theories for calculating the acoustic radiation force (ARF); 8 different models up to now.
2. Easy usage

During this demo we will show you how make use of them. Both founders of OSAFT (Jonas Fankhauser and Christoph Goering) are present during the demo to help answer any questions and help with possible difficulties. This demo is roughly divided into 3 parts but it is highly flexible to the questions/demands of the audience.

1. Available resources (Documentation & Gitlab)
2. Installation & 2 Examples (ARF calculation & Education)
3. Q&A

We encourage everybody to have a look at the software and its available examples beforehand. Feel free to contact any of us two in advance if you have any questions.

Program Schedule

Wednesday 19 October

All Times are British Summer Time

09:00   **Welcome and Opening Remarks**
Thomas Franke, *University of Glasgow, UK*
Richard Fu, *Northumbria University, UK*

Session 1
Session Chair: Thomas Franke, *University of Glasgow, UK*

Keynote Speaker 1

09:15   **ACOUSTIC LEVITATION: FASTER, HIGHER, STRONGER**
Bruce Drinkwater
University of Bristol, UK

Contributed Talks

10:00   **TOWARDS HIGH-THROUGHPUT MICROFLUIDIC COMPRESSIBILITY
CYTOMETRY USING GRADIENT ACOUSTIC FOCUSING INTEGRATED
WITH DENSITY CENTRIFUGATION** 30
Mahdi Rezayati Charan, Oskar Andersson, Ola Jakobsson, and Per Augustsson
Lund University, SWEDEN

10:10   **USING OPEN-CHANNEL ACOUSTOFLUIDICS
FOR FABRICATION OF SKIN EQUIVALENCE** 32
Dhananjay V. Deshmukh, Jessica Polak, Christine Fux,
Mirko Meboldt, Mark Tibbitt, and Jürg Dual
ETH Zürich, SWITZERLAND

10:20   **BULK ACOUSTIC WAVES-BASED SYSTEM FOR
A RAPID AND HIGH THROUGHPUT CELL WASHING** 34
Hugo R. Sugier[1,2], Ludovic Bellebon[3], Jean-Luc Aider[3],
Jérôme Larghero[4], Juliette Peltzer[5], and Christophe Martinaud[6]
*[1]Aenitis Technologies, FRANCE, [2]Institut André Lwoff, FRANCE,
[3]Sorbonne Université, FRANCE, [4]Université de Paris, FRANCE,
[5]Institut de Recherche Biomédicale des Armées, FRANCE, and
[6]Centre de Transfusion Sanguine des Armées, FRANCE*

Flash Presentations

10:30   **NOVEL ACOUSTOFLUIDIC APPROACH USING A BULK ACOUSTIC
WAVE RESONATOR TO CONTROL THE TOPOLOGY AND CULTURE
CONDITIONS OF BRAIN DERIVED SPHEROIDS** 36
Chloé Dupuis[1,2], Xavier Mousset[1,2], Guillaume Viraye[2], Pierre-Ewen Lecoq[1,2],
Mauricio Hoyos[1], Jean-Michel Peyrin[2], and Jean-Luc Aider[1]
*[1]Ecole Supérieure de Physique et de Chimie Industrielles (ESPCI), FRANCE and
[2]Sorbonne Université, FRANCE*

10:35 **ACOUSTIC WAVE ACTIVATION OF THE GROWTH OF DIELECTRIC AND METAL THIN FILMS BY PLASMA DEPOSITION TECHNIQUES**

Manuel Oliva-Ramirez[1], Helene Reichel[1], Aurelio Garcia-Valenzuela[1], Víctor Rico[1], Juan P. Espino[1], Teresa C. Rojas[1], Guillermo Regodon-Harkness[1], Jorge Gil-Rostra[1], Armaghan Fakhfouri[2], Ana Gómez-Ramírez[1], Rafael Alvarez[1], Ana Borras[1], Alberto Palmero[1], Andreas Winkler[2], and Agustin R. González-Elipe[1]
[1]Instituto de Ciencia de Materiales de Sevilla (ICMS), SPAIN and [2]IFW-Dresden, GERMANY

10:40 **Coffee Break**

Session 2
Session Chair: Matthias Schneider, *Technische Universitat Dortmund, GERMANY*

INVITED SPEAKER 1

11:10 **STANDING WAVE ACOUSTOPHORESIS OF LEGIONELLA SPECIES AND THE INFLUENCE OF MULTIBODY EFFECTS**

Alen Pavlič
ETH Zürich, SWITZERLAND

Contributed Talks

11:30 **CULTURE OF HEPATIC AND STEM CELL SPHEROIDS IN ACOUSTIC LEVITATION INDUCES DIFFERENT SELF-ORGANISATION DYNAMICS**

Lucile Rabiet[1,2], Lousineh Arakelian[2], Duván Rojas García[1], Nathan Jeger-Madiot[1], Mauricio Hoyos[1], Jérôme Larghero[2], and Jean-Luc Aider[1]
[1]Ecole Supérieure de Physique et de Chimie Industrielles (ESPCI), FRANCE and [2]Inserm U976 HIPI - Hôpital Saint-Louis, FRANCE

11:40 **MULTI LINE PATTERNING OF HUMAN UMBILICAL VEIN ENDOTHELIAL CELLS FOR 3D MICROVASCULAR NETWORK FORMATION**

Le Thi Huong[1], Andreas Lenshof[2], Huu Lam Phan[1], Van Thuy Duong[1], Thomas Laurell[2], and Kyo-in Koo[1]
[1]University of Ulsan, KOREA and [2]Lund University, SWEDEN

11:50 **DISCOVERY OF THE MECHANISM RESPONSIBLE FOR ULTRASOUND'S EXCITATION OF ION CHANNELS IN CELLS**

Aditya Vasan[1], Jeremy Orosco[1], Uri Magaram[2], Marc Duque[2], Connor Weiss[2], Yusuf Tufail[2], Sreekanth H. Chalasani[2], and James Friend[1]
[1]University of California, San Diego, USA and [2]Salk Institute for Biological Studies, USA

Flash Presentations

12:00 **ACOUSTIC ACTIVATED ABSORBANCE DROPLET SORTING AT kHz DROPLET RATES**

Esther S. Richter[1], Andreas Link[1], Raymond W. Sparrow[1], John S. McGrath[1], Florian Hollfelder[2], and Thomas Franke[1]
[1]University of Glasgow, UK and [2]University of Cambridge, UK

12:05 ACOUSTIC BUBBLE FOR SPHEROID TRAPPING, ROTATION, AND CULTURE: A TUMOR-ON-A-CHIP PLATFORM (ABSTRACT PLATFORM) 48

Yuan Gao[1,2], Mengren Wu[1], Qiyue Luan[1], Ian Papautsky[1], and Jie Xu[1]
[1]University of Illinois, Chicago, USA and [2]University of Memphis, USA

12:10 Lunch

Session 3
Session Chair: Bruce W. Drinkwater, University of Bristol, UK

Keynote Speaker 2

13:10 HEARING IS BELIEVING: CORRELATING OPTICAL AND ACOUSTIC IMAGING OF BUBBLE DYNAMICS IN A MICROFLUIDIC SYSTEM
Eleanor Stride
University of Oxford, UK

Contributed Talks

13:55 PARTICLE TRAPPING USING AXIAL PRIMARY RADIATION FORCE 50
Lokesh Malik[1], Amal Nath[1], Subhas Nandy[1],
Thomas Laurell[2], and Ashis Kumar Sen[1]
[1]Indian Institute of Technology, Madras, INDIA and [2]Lund University, SWEDEN

14:05 SHORT ULTRASONIC PULSES FOR ACOUSTIC TWEEZERS 52
Qing Wang[1], Zhixiong Gong[2], Shuhan Chen[1], Jia Zhou[1],
Michael Baudoin[2,3], and Antoine Riaud[1]
[1]Fudan University, CHINA, [2]University of Lille, FRANCE, and
[3]Institut Universitaire de France, FRANCE

14:15 DYNAMIC PATTERNING OF MICROPARTICLES WITH ACOUSTIC IMPULSE CONTROL 54
Luke Cox, Anthony Croxford, and Bruce W. Drinkwater
University of Bristol, UK

Flash Presentations

14:25 HIGH-PERFORMANCE BULK-WAVE-ACOUSTOPHORESIS DEVICES DRIVEN BY LEAD-FREE PIEZOELECTRIC MATERIALS 56
Wei Qiu
Lund University, SWEDEN

14:30 SHEATHLESS MICROFLOW CYTOMETRY USING GIGAHERTZ ACOUSTIC STREAMING 58
Yaping Wang, Wei Wei, Yang Yang, Wei Pang, and Xuexin Duan
University of Tianjin, CHINA

14:35 Coffee Break

Invited Speaker 2

15:05 **MOMENTUM CONSERVATION AND THE 2ND LAW IN BIOLOGICAL COMMUNICATION**
<u>Matthias Schneider</u>
Technische Universitat Dortmund, GERMANY

Contributed Talks

15:25 **FLUIDO-ACOUSTICS: DYNAMIC MULTI-SLIT METAMATERIAL TUNED USING LIQUID DROPLETS** 60
<u>Shubhi Bansal</u>, Ryuji Hirayama, and Sriram Subramanian
University College London, UK

15:35 **ON-CHIP LOCALIZED MICROFLUIDIC PUMPING POWERED BY GUIDED FLEXURAL WAVES OVER SILICON-ON-NOTHING MEMBRANE WAVEGUIDES** 62
<u>Philippe Vachon</u>[1,2], Srinivas Merugu[1], Jaibir Sharma[1], Amit Lal[1,3], Eldwin J. Ng[1], Yul Koh[1], Joshua E.-Y. Lee[1], and Chengkuo Lee[2]
[1]Institute of Microelectronics, A*STAR, SINGAPORE,
[2]National University of Singapore, SINGAPORE, and [3]Cornell University, USA

15:45 **COMPLEX MICROSCALE PATTERNING WITH SUB-WAVELENGTH ACOUSTIC MICROFEATURES** 64
<u>Kirill Kolesnik</u>, Philipp Segeritz, Daniel J. Scott, Vijay Rajagopal, and David J. Collins
University of Melbourne, AUSTRALIA

Flash Presentations

15:55 **HIGH SENSITIVITY MEASUREMENTS OF THE ACOUSTIC CONTRAST FACTOR OF STIFFNESS ALTERED BIOLOGICAL CELLS** 66
<u>Cooper Lars Harshbarger</u>[1,2,3], Alen Pavlic[1], Davide Bernardoni[2,3], Amelie Viol[1], Jess Gerrit Snedeker[2,3], and Jürg Dual[1]
[1]ETH Zürich, SWITZERLAND, [2]University of Zurich, SWITZERLAND, and [3]Swiss Federal Institute of Technology Zurich, SWITZERLAND

16:00 **ACOUSTOPHORESIS-BASED CELL MANIPULATION DEVICE FOR ADVANCED THERAPY MEDICINAL PRODUCTS MANUFACTURING AUTOMATION** 68
<u>Florian Jouy</u>[1], Fabien Rémy-Martin[1], Franck Lardet-Vieudrin[1], Alain Rouleau[1],Pauline Bourgeois[1], Rabah Zeggari[1,2], Annie Frelet-Barrand[1], and Jean-Francois Manceau[1]
[1]Université Bourgogne Franche-Comté, FRANCE and
[2]FEMTO Engineering, FRANCE

Olympiad

16:10 - 18:10   Studio 2

A FOCUSED LINE OF CELLS FLOWING IN A CAPILLARY BRIDGE CHANNEL
Jeremy Hawkes
Acoustic Machines Ltd., UK

BENDING AND DEFORMATION OF SAW DEVICES FOR WEARABLE ACOUSTOFLUIDICS APPLICATIONS
Jikai Zhang, Luke Haworth, and Huiling Ong
Northumbria University, UK

BRISTOL ACOUSTIC MANIPULATOR
Mario Ortega Sandoval
University of Bristol, UK

COMPACT MICRO-ACOUSTIC LIQUID ATOMIZERS
Mehrzad Roudini and Andreas Winkler
Leibniz Institute for Solid State and Materials Research (IFW), GERMANY

DICED MICROCHANNELS AND GLASS CAPILLARIES: CHEAP NM-PARTICLE HANDLING
Michael Gerlt
ETH Zürich, SWITZERLAND

HIGH SPEED ACOUSTOFLUIDIC PARTICLE FOCUSING AND HIGHER HARMONICS USING LATERAL MODES OF A PLATE TRANSDUCER
Andreas Fuchsluger
Johannes Kepler University Linz, AUSTRIA

NEXT GENERATION CENTRIFUGE - PARTICLE AND CELL SEPARATION WITH FULLY MICROFABRICATED ACOUSTOFLUIDIC CHIPS
Stefanie Hartmann, Melanie Colditz, and Andreas Winkler
Leibniz Institute for Solid State and Materials Research (IFW),
µAcoustiX Startup Project, GERMANY

ON-CHIP LOCALIZED MICROFLUIDIC PUMPING AND PARTICLES TRANSPORT POWERED BY GUIDED FLEXURAL WAVES OVER SILICON-ON-NOTHING MEMBRANE WAVEGUIDES
Philippe Vachon
National University of Singapore, SINGAPORE

TINYLEV
Luke Cox
University of Bristol, UK

Poster Session I, Exhibit Inspection, & Drinks Reception

16:10 - 18:10 **Poster presentations are listed by topic category with their assigned number starting on page 23.**

Virtual Exhibit 1

16:10 – 16:40 BelektroniG GmbH representative will be in the Zoom Room.

BelektroniG focusses on frequency generators and temperature controllers. We present our revised product SAW Generator-G20 to drive acoustofluidic setups.

Virtual Exhibit 2

16:40 – 17:10 usePAT GmbH representative will be in the Zoom Room.

usePAT offers ultrasonic systems for enhancing in-line, real-time measurements in industrial liquids and R&D and thereby supports its customers in optimizing process management.

Virtual Exhibit 3

17:10 - 17:40 Royal Society of Chemistry representative will be in the Zoom Room.

Lab on a Chip Development Editor, David Lake, will be delighted to speak to you about your work, the journal, and all things acoustofluidics!

18:10 **Adjourn for the Day**

Thursday, 20 October

All Times are British Summer Time

09:00   Announcements

Session 5
Session Chair: Michael Baudoin, *IEMN, FRANCE*

Keynote Speaker 3

09:15   MECHANICS AND EXPERIMENTAL DYNAMICS:
**   FROM ACOUSTOFLUIDICS TO GRAVITATIONAL INTERACTION**
            Jürg Dual
            ETH Zürich, SWITZERLAND

Contributed Talks

10:00   DYNAMIC PATTERNING OF DIELECTRIC
**   PARTICLES ON A PMUT ARRAY** **72**
            Bart P. Weekers[1,2], Liesbet Lagae[1,2], Xavier Rottenberg[2],
            and Veronique Rochus[2]
            [1]KU Leuven, BELGIUM and [2]imec, BELGIUM

10:10   IN-SITU INVESTIGATION OF THREE-DIMENSIONAL
**   ACOUSTOPHORETIC AND ACOUSTOTHERMAL**
**   EFFECTS IN SAW-BASED ACOUSTIC TWEEZERS** **74**
            Vijay V. Kondalkar[1], Zhichao Deng[2], Alexandre N. Darinskii[3], Robert Weser[1],
            Christian Cierpka[2], Jörg König[2], and Hagen Schmidt[1]
            [1]Leibniz Institute for Solid State and Materials Research Dresden, GERMANY,
            [2]Technische Universität Ilmenau, GERMANY, and
            [3]Institute of Crystallography FSRC, RUSSIA

10:20   ACOUSTIC MICROPARTICLE PATTERNING OF
**   ARBITRARY-DEFINED SHAPES BY 3D WAVEGUIDES** **76**
            William S. Harley, Kirill Kolesnik, Daniel E. Heath, and David J. Collins
            University of Melbourne, AUSTRALIA

Flash Presentations

10:30   ON-CHIP PARTICLE CENTRIFUGE USING SPIRAL SURFACE
**   ACOUSTIC WAVES ON ZnO/GLASS SUBSTRATE** **78**
            Zhihao Zhu and Xiasheng Guo
            Nanjing University, CHINA

10:35   CHARACTERIZATION AND CONTROL OF A BROADBAND ACOUSTIC
**   CAVITY: APPLICATION TO CELLS SPHEROIDS MANIPULATION** **80**
            Nathan Jeger-Madiot[1], Xavier Mousset[1,2], Chloé Dupuis[1,2], Lucile Rabiet[1,3],
            Mauricio Hoyos[1], Jean-Michel Peyrin[2], and Jean-Luc Aider[1]
            [1]Ecole Supérieure de Physique et de Chimie Industrielles (ESPCI), FRANCE,
            [2]Sorbonne Universités, FRANCE, and [3]APHP Hôpital Saint-Louis, FRANCE

10:40   Coffee Break

Session 6
Session Chair: Mark Meacham, *Washington University, St. Louis, USA*

Invited Speaker 3

11:10 **LEVERAGING TIME AND FREQUENCY MULTIPLEXING FOR DYNAMIC ACOUSTIC TWEEZERS**
Zhenhua Tian
Virginia Tech, USA

Contributed Talks

11:30 **TRANSVERSE MODE OF BULK ACOUSTIC WAVE FOR SUB-100 NM NANOPARTICLES MANIPULATIONS** 82
Wei Wei, Zhaoxun Wang, and Xuexin Duan
University of Tianjin, CHINA

11:40 **3D CELL ROTATION BASED ON A VIBRATION-INDUCED FLOW** 84
Hiroyasu Kobayashi, Yuha Koike, and Takeshi Hayakawa
Chuo University, JAPAN

11:50 **HIGH PERFORMANCE ACOUSTOFLUIDIC PARTICLE FOCUSING IN SILICON-BASED AND POLYMER-BASED DEVICES USING LATERAL MODES OF PLATE TRANSDUCERS** 86
Andreas Fuchsluger[1], Annalisa De Pastina[2], Norbert Cselyuszka[2], Nikolai Andrianov[2], Ali Roshanghias[2], Rafael Ecker[1], Tina Mitteramskogler[1], Thomas Voglhuber-Brunnmaier[1], Mohssen Moridi[2], and Bernhard Jakoby[1]
[1]Johannes Kepler University Linz, AUSTRIA and [2]Silicon Austria Labs, AUSTRIA

Flash Presentations

12:00 **IN-FLOW MEASUREMENT OF ACOUSTIC MOBILITY** 88
Thierry Baasch, Linda Péroux, Andreas Lenshof, and Thomas Laurell
Lund University, SWEDEN

12:05 **CONSTANT VOLTAGE VERSUS CONSTANT POWER IN ACOUSTOFLUIDIC APPLICATIONS** 90
Fabian Lickert, Henrik Bruus, and Massimiliano Rossi
Technical University of Denmark, DENMARK

12:10 **Lunch**

Session 7
Session Chair: Jürg Dual, ETH Zürich, SWITZERLAND

Invited Speaker 4

13:10 **EXPLOITING ACOUSTIC FIELD-MICROSWIMMER INTERACTIONS TO ACCELERATE ACOUSTOFLUIDIC DEVICE DEVELOPMENT**
<u>Mark Meacham</u>
Washington University, St. Louis, USA

Contributed Talks

<u>Claude Inserra</u>[1], Maxime Fauconnier[1], Jean-Christophe Béra[1], Cyril Mauger[2], Alexander Doinikov[2], and Philippe Blanc-Benon[2]
[1]Université Claude Bernard Lyon, FRANCE and [2]Ecole Centrale de Lyon, FRANCE

Shuren Song, Jia Zhou, and <u>Antoine Riaud</u>
Fudan University, CHINA

<u>Md Ehtashamul Haque</u>[1], Alvaro Conde[2], Harikumar Kuzhikkattu Chandrasekharan[1], William N. MacPherson[1], Stephen Knight[3], Richard Carter[1], and Maïwenn Kersaudy-Kerhoas[1]
[1]Heriot-Watt University, UK, [2]Micronit B.V., NETHERLANDS, and [3]University of Edinburgh, UK

<u>Michael Gerlt</u>, Nicola Hagger, and Jürg Dual
ETH Zürich, SWITZERLAND

Flash Presentations

◇ <u>Thierry Baasch</u>, Alexander Edthofer, Andreas Lenshof, and Thomas Laurell
Lund University, SWEDEN

◇ <u>Qiaoyun Wang</u>[1,2], Jikai Zhang[2], Hui Ling Ong[2], and Yong-Qing (Richard) Fu[2]
[1]Northeastern University, CHINA and [2]Northumbria University, UK

14:20 **Coffee Break**

Session 8
Session Chair: Zhenhua Tian, Virginia Tech, USA

Contributed Talks

14:50   **SINGLE FOCUSED-BEAM ACOUSTICAL TWEEZERS** **104**
Zhixiong Gong[1] and Michael Baudoin[1,2]
[1]IEMN, FRANCE and [2]Institut Universitaire de France, FRANCE

15:00   **AMPLIFICATION OF SECONDARY BJERKNES FORCES USING MICROBUBBLE ARRAYS FOR PRECISE ACOUSTOFLUIDIC MANIPULATION** **106**
Rahul Goyal[1], Athanasios G. Athanassiadis[1,2], Zhichao Ma[3], and Peer Fischer[1,2]
[1]Max Planck Institute for Medical Research, GERMANY,
[2]Heidelberg University, GERMANY, and [3]Shanghai Jiao Tong University, CHINA

15:10   **OSAFT: A PYTHON LIBRARY FOR ACOUSTOFLUDICS** **108**
Jonas Fankhauser, Christoph Goering, Merrill Gutzwiller, and Jürg Dual
ETH Zürich, SWITZERLAND

Keynote Speaker 4

15:20   **ACOUSTIC CONTROL OF SORTING AND FLUID INJECTION IN MICROFLUIDIC DEVICES**
David Weitz
Harvard University, USA

OSAFT (Open-Source Acoustofludic Theory) Demo

16:05   **Studio 2**
Christoph Goering and Jonas Fankhauser
ETH Zürich, SWITZERLAND

Poster Session II, Exhibit Inspection, & Drinks Reception

16:05   **Poster presentations are listed by topic category with their assigned number starting on page 23.**

18:05   **Adjourn for the Day**

Conference Banquet

19:30 – 21:30   **Glasgow Union Dinning Hall**

Friday, 21 October

All Times are British Summer Time

09:00   Announcements

Session 9
Session Chair: Alen Pavlic, *ETH Zürich, SWITZERLAND*

Contributed Talks

**09:15   ELECTRICAL IMPEDANCE SPECTROSCOPY
FOR ACOUSTOFLUIDIC APPLICATIONS** 110
William N. Bodé[1], Fabian Lickert[1], Per Augustsson[2], and Henrik Bruus[1]
[1]Technical University of Denmark, DENMARK and [2]Lund University, SWEDEN

**09:25   THERMOVISCOUS CORRECTIONS TO THE ACOUSTIC
RADIATION FORCE ON A SPHERICAL PARTICLE
INCLUDING SCATTERING AND MICROSTREAMING** 112
Bjørn G. Winckelmann and Henrik Bruus
Technical University of Denmark, DENMARK

**09:35   INTERFACIAL EVOLUTIONS AND PHASE CHANGES OF
RIME ICE ACTIVATED BY THIN-FILM SURFACE ACOUSTIC WAVES** 114
Deyu Yang[1], Luke Haworth[2], Xianghui Hou[1], and Yong-Qing (Richard) Fu[2]
[1]University of Nottingham, UK and [2]Northumbria University, UK

**09:45   ANALYSIS OF ACOUSTIC RELOCATION OF
IMMISCIBLE FLUIDS IN A MICROCHANNEL** 116
Varun Kumar Rajendran, Aravind Ram S P, and Karthick Subramani
*Indian Institute of Information Technology, Design and Manufacturing,
Kancheepuram, INDIA*

Flash Presentations

**09:55   MEASUREMENT OF THE ACOUSTICALLY INDUCED FLUID
FLOW IN A 2DsSAW TWEEZER AND ITS INFLUENCE ON
SINGLE CELL PATTERNING** 118
Zhichao Deng[1], Hagen Schmidt[2], Christian Cierpka[1], and Jörg König[1]
[1]Technische Universität Ilmenau, GERMANY and [2]SAWLab Saxony, GERMANY

**10:00   FORMATION OF MICRON SIZED DROPS FROM LOW VISCOSITY LIQUID FILMS
UNDER THE ACTION OF SURFACE ACOUSTIC WAVES** 120
Niladri Sekhar Satpathi and Ashis Kumar Sen
Indian Institute of Technology, Madras, INDIA

10:05   Coffee Break

Session 10

Session Chair: Richard Fu, *Northumbria University, UK*

Contributed Talks

10:35   **SELF-INDUCED RADIATION FORCE ON
A MOVING MONOPOLAR SOURCE** **122**
Michael Baudoin, Aymeric Roux, and Jean-Paul Martishang
University of Lille, FRANCE

10:45   **EFFECTS OF WETTABILITY IN RELOCATION OF COFLOWING
IMMISCIBLE LIQUIDS EXPOSED TO BULK ACOUSTIC WAVE** **124**
Sazid Z. Hoque and Ashis K. Sen
Indian Institute of Technology, Madras, INDIA

10:55   **LIQUID LAYER EVOLUTION CHARACTERIZATION USING
GHz ULTRASONIC PULSES: LINEAR AND NONLINEAR EFFECTS** **126**
Rohan Sanghvi, Justin Kuo, and Amit Lal
Cornell University, USA

11:05   **THERMOACOUSTIC STREAMING INDUCED
BY ASYMMETRIC LASER HEATING** **128**
Franziska Martens, Wei Qiu, and Per Augustsson
Lund University, SWEDEN

11:15   **ACOUSTIC NEAR-RESONANCE MODES IN A
CYLINDRICAL HALF-WAVELENGTH MICROCAVITY** **130**
Glauber T. Silva
Federal University of Alagoas, BRAZIL

11:25   **STABLE, OBSTRUCTION-FREE, AUDIBLE-FREQUENCY ACOUSTIC
MICROSTREAMING BY A PINNED OSCILLATING MEMBRANE** **132**
Anthony Mercader and Sung Kwon Cho
University of Pittsburgh, USA

11:35   **Award Announcements**

11:55   **Announcement of Acoustofluidics 2023**

12:00   **Conference Adjourns**

Poster Presentations

W – Wednesday, 19 October (16:10 - 18:10)
Th – Thursday, 20 October (16:05 - 18:05)
All Times are British Summer Time

Manipulation, Transport and Control - Acoustic Manipulation

WP-06 **APPLICATION OF LIVING PROBES TO ASSESS SAW-BASED ACOUSTOFLUIDIC DEVICE PERFORMANCE** 146

Advaith Narayan[1], Mingyang Cui[1,2], and J. Mark Meacham[1]
[1]Washington University, Saint Louis, USA and
[2]Massachusetts Institute of Technology, USA

WP-07 **DEFORMATION OF THALASSAEMIA MINOR AND MAJOR RED BLOOD CELLS INDUCED BY SURFACE ACOUSTIC WAVES** 148

Mustafa Zaimagaoglu, Andreas Link, and Thomas Franke
University of Glasgow, UK

WP-08 **GENERATION OF VARIOUS CELL PATTERNS WITH MILLIMETER SCALE WITH STANDING WAVES ON A LIQUID SURFACE** 150

Kohei Morita and Takeshi Hayakawa
Chuo University, JAPAN

WP-09 **SIZE-SELECTIVE SEPARATION AND ENRICHMENT OF NANO/MICROPARTICLES USING GHz ACOUSTIC STREAMING** 152

Shen Sihong, Shen Xiaotian, and Duan Xuexin
Tianjin University, CHINA

Manipulation, Transport and Control - Droplets

WP-10 **ACOUSTIC STREAMING FLOW INDUCED IN-DROPLET CHEMICAL CONCENTRATION CONTROL OF PICOLITER SCALE DROPLET** 154

Woohyuk Kim and Jinsoo Park
Chonnam National University, KOREA

WP-11 **RAPID DROPLET MIXING USING STEREO ACOUSTOFLUIDIC VORTICES** 156

Xiaotian Shen, Tiechuan Li, and Xuexin Duan
Tianjin University, CHINA

Manipulation, Transport and Control - Theory and/or Simulation

WP-12 **THE ANALYTICAL STUDY OF CELL COUNTING DEVICE BASED OF FOCUSED SURFACE ACOUSTIC WAVE** 158

Yingqi Jiang and Weipeng Xuan
Hangzhou Dianzi University, CHINA

Physics - Acoustic Thermal Effects and Energy

WP-13 **STUDY OF THE ACOUSTOTHERMAL HEATING INSIDE A LIQUID DROPLET USING IR THERMOGRAPHY** 160

Etien Martinez Roman, Diego Sánchez Saldaña,
Maria Fernandino, and Carlos A. Dorao
Norwegian University of Science and Technology (NTNU), NORWAY

Physics - Theory and/or Simulation

WP-14 **NONLINEAR LARGE DEFORMATION OF A SPHERICAL RED BLOOD CELL INDUCED BY ULTRASONIC STANDING WAVE** 162
Fengxian Xin and Yifan Liu
Xi'an Jiaotong University, CHINA

Applications - Biology

ThP-15 **MICROMIXER BASED ON GHz BULK ACOUSTIC WAVE FOR CONTROLLABLE LIPOSOME SYNTHESIS** 166
Huihui Xu, Chen Wu, Zhaoxun Wang, and Xuexin Duan
Tianjin University, CHINA

Devices - Integrated System

ThP-16 **A MANIPULATION SYSTEM FOR PHASE-CONTROLLABLE ACOUSTOFLUIDIC MANIPULATIONS OF MICROPARTICLES** 168
Hayato Yamaki, Natsumi Hirata, and Takeshi Hayakawa
Chuo University, JAPAN

Devices - Theory and/or Simulation

ThP-17 **PIEZOELECTRIC MICROMACHINED ULTRASOUND TRANSDUCERS (PMUTs) FOR ACOUSTIC POSITIONING OF SUSPENDED MICROTISSUES** 170
Emilie Vuille-dit-Bille[1,2], Dara Zaman Bayat[1], Marc-Alexandre Dubois[1], Thomas Overstolz[1], Sarah Heub[1], Michel Despont[1], Mahmut Selman Sakar[2], and Gilles Weder[1]
[1]CSEM SA, SWITZERLAND and
[2]École Polytechnique Fédérale de Lausanne (EPFL), SWITZERLAND

Devices - Transducer Fabrication

ThP-18 **ADDED MASS CONTROLS: THE SEPARATION, ALIGNMENT AND INTENSITY OF NODES IN ACOUSTOFLUIDIC CAPILLARY BRIDGES** 172
Jeremy J. Hawkes[1], Sadaf Maramizonouz[2,3], Mohammad Rahmati[2], Yong-Qing Fu[2], and Stephen J. Wilkinson[4]
[1]Acoustic machines Ltd., UK, [2]Northumbria University, UK,
[3]Newcastle University, UK, and [4]University of Chester, UK

Manipulation, Transport and Control - Acoustic Manipulation

ThP-19 **AN ACOUSTOFLUIDIC MICROMANIPULATION SYSTEM WITH AN OPEN MICROFLUIDIC CHIP** 174
Natsumi Hirata and Takeshi Hayakawa
Chuo University, JAPAN

ThP-20 **COUPLING ACOUSTOPHORESIS AND THERMOPHORESIS FOR ENRICHING NANOPARTICLES** 176
Jing Dong[1], Dongfang Liang[1], and Xin Yang[2]
[1]University of Cambridge, UK and [2]Cardiff University, UK

Manipulation, Transport and Control - Droplets

Manipulation, Transport and Control - Theory and/or Simulation

Physics - Acoustic Fields and Streaming

Physics - Acoustic Thermal Effects and Energy

Physics - Theory and/or Simulation

D. Spencerh Bidouba Sanvany, Francic Kosior, Denis Beyssen,
Aude Gigodot, Elisabeth Gaudion, and Frederic Sarry
Université de Lorraine, France

Open Poster

Martin Wiklund[1], Niklas Sandström[1], Valentina Carannante[2], Karl Olofsson[1],
Patrick A. Sandoz[1], Hanna Van Ooijen[1], Quentin Verron[1], Thomas Frisk[1],
and Björn Önfelt[1,2]
*[1]KTH Royal Institute of Technology, SWEDEN and
[2]Karolinska Institutet, SWEDEN*

Abstract Only Presentations

Povilas Dumčius[1], Roman Mikhaylov[1], Xiaoyan Zhang[1],
Mercedes Stringer Martin[1], Aled Clayton[1], Chao Sun[2], and Xin Yang[1]
[1]Cardiff University, UK and [2]Northwestern Polytechnical University, CHINA

Liying Zhang, Panpan Chen, and Shuhu Du
Nanjing Medical University, CHINA

Xiaolong Lu[1,2], Jens Twiefel[3], Zhichao Ma[2], and Peer Fischer[2]
[1]Nanjing University of Aeronautics and Astronautics, CHINA, [2]Max Planck Institute for Intelligent Systems, GERMANY, and [3]Leibniz Universität Hannover, GERMANY

Hui Ling Ong, Jikai Zhang, Prashant Agrawal, Hamdi Torun,
Kunyapat Thummavichai, Qiang Wu, and Yong-Qing (Richard) Fu
Northumbria University, UK

Nino F. Läubli[1,2], Jan T. Burri[1], Gabriele S. Kaminski Schierle[2],
Daniel Ahmed[1], and Bradley J. Nelson[1]
[1]ETH Zürich, SWITZERLAND and [2]University of Cambridge, UK

Abstracts - Oral Presentations

Towards high-throughput microfluidic compressibility cytometry using gradient acoustic focusing integrated with density centrifugation

Mahdi Rezayati Charan, Oskar Andersson, Ola Jakobsson and Per Augustsson

Department of Biomedical Engineering, Lund University, Lund, Sweden
E-mail: per.augustsson@bme.lth.se, URL: http://bme.lth.se/staff/augustsson-per/research/

Introduction

Single-cell information about a cell's density, compressibility, and size enables the determination of its motion in any medium and acoustic field. This is useful both for optimizing cell separations and for cytometry based on acoustic properties. Iso-acoustic focusing (IAF) scans the equilibrium position of single cells in a continuous gradient of acoustic impedance and reports their effective acoustic impedance [1], which is the square root of the ratio of the density and compressibility. But to fully characterize the motion of individual cells in any media and acoustic field, the size, density, and compressibility must be known, and the compressibility must therefore be decoupled by an independent measurement of the density for each cell. In the present study, we fractionate K562 cells off chip in a density gradient of iodixanol and feed three fractions of known density as an input into an IAF device. Our measurements show that the distribution of compressibility is almost similar for K562 cells of different densities ($3.78+/-0.058 \times 10^{-10}$ Pa^{-1}) and agree well with previous measurements of cancer cells [2,3].

Materials and methods

An acoustofluidic glass-silicon-glass chip illustrated in Fig. 1(a) of length 70 mm and width 4 mm was fabricated to operate two resonant channels. The first channel of cross section 300×150 μm was dedicated to pre-focus the cells before they enter the IAF channel. The IAF channel of cross section 375×150 μm to support a single node standing wave hosts the central stream of a high impedance medium containing 35% iodixanol and low impedance media (10 – 12% iodixanol) containing the cells from both sides. To map the development of the diffusing acoustic impedance gradient, we added fluorescent tracer molecules to the central fluid. Two piezo-ceramic transducers resonant at 5 and 2 MHz were bonded underneath and to the side of the chip using cyanoacrylate glue, respectively. A confocal microscope with a 20x, 0.45 NA objective equipped with a CMOS camera was used for sequence illumination at the end of the IAF channel.

K562 cells were used in this study. Cells were stained with cell-permeant fluorescence dye for microscopy imaging, washed, and resuspended in 1 mL of phosphate-buffered saline (PBS) before adding to a tube containing 10 mL of the continuous iodixanol density gradient. Iodixanol density gradient was generated by mixing Optiprep™ (containing 60% iodixanol) and PBS in a microfluidic mixer. Based on the density of K562 cells in the literature (1060 - 1070 kg/m^3) [4], tubes containing a linear gradient of 10-12% iodixanol were prepared, Fig. 1(b). After centrifugation at 700xg without brake for 30 minutes, we injected heavy oil (HFE 7500) with the flow rate of 1 ml/min to the bottom of the tube to recover the cells with different densities. Ten samples were recovered and fed to a refractometer for measuring the refractive indices to retrieve the density of each fraction. We selected three fractions of K562 cells with different densities and supplied them to the IAF device for final measurements.

Results and discussion

We first run the whole population of K562 cells through the chip to evaluate the measurement of effective acoustic impedance. The side streams with pre-aligned cells, Fig. 1(c), contain 10% iodixanol, and the central stream was filled with 35% iodixanol. The flow rate in the central stream was fixed to 5 μL/min, and the total flow rate was varied to tune the gradient profile, Fig. 1(d). For three different settings, Fig. 1(f) shows a

consistent measurement for the effective acoustic impedance of K562 cells indicating that sufficient acoustic energy density was applied to translate cells to their iso-acoustic point (IAP). We continued the experiment for three different fractions of K562 cells recovered at different heights of the density gradient centrifugation tube, Fig. 2(a). For each sample, the distribution of the measured compressibility is shown in Fig. 2(c) based on the density of each fraction and the measured effective acoustic impedance.
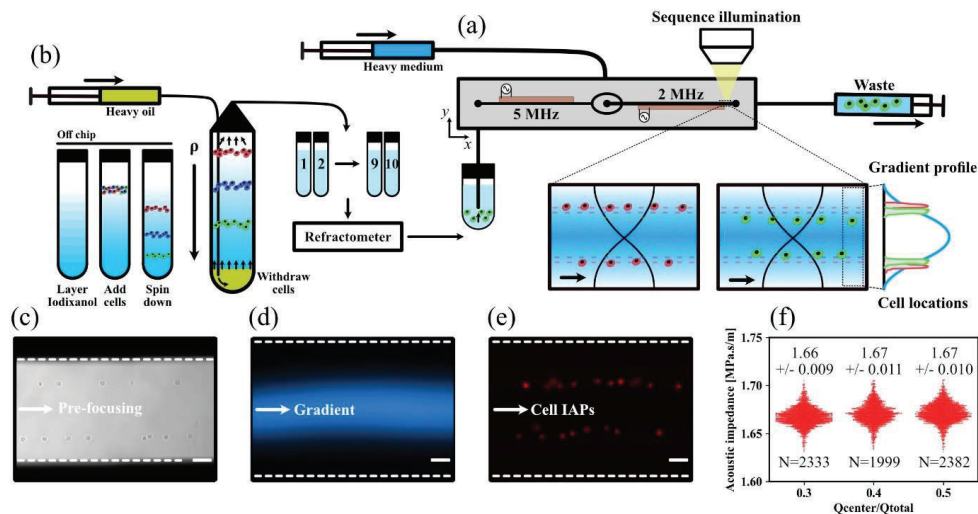
Figure 1: (a) Schematic illustration of the experimental set-up for integration of the density gradient centrifugation and the IAF. (b) To fractionate cells off the chip, cells were added to the top of the iodixanol layers and spun down. Heavy oil was supplied to the bottom of the centrifugation tube to lift the cell layers. The buoyant density of each fraction (1 to 10) was recorded by measuring the refractive indices. (c) Bright-field image of pre-focused cells before entering the IAF channel. (d) Fluorescence image of the gradient and the corresponding (e) cell IAPs. (f) The measured effective acoustic impedance of K562 cells for Qcenter = 5 μL/min. The scale bar is 50 μm.
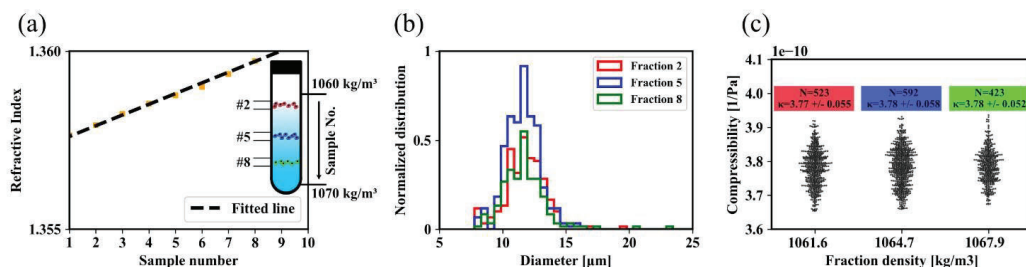

Figure 2: (a) Measured refractive indices of ten samples extracted from the centrifugation tube. (b) Size distribution of the K562 cells in three different fractions measured by Coulter Counter. (c) Distribution of the compressibility for three fractions of different densities. Fractions are color coded.

Conclusion

We combined density gradient centrifugation with IAF to decouple the density and compressibility for K562 cells. Our main finding was that for K562 cells, we observed no clear correlation between density and compressibility or size. Our continued work will focus on further resolving the link between these cell properties, and we think that the approach can be further developed for multiparametric measurement of single-cell properties.

References:
[1] Augustsson, P., *et al.*, *Nat Commun* **7**, 11556 (2016).
[2] Yanqi, W., *et al.*, *Lab Chip*, 2021, **21**, 2812-2824.
[3] Hartono, D., *et al.*, *Lab Chip*, 2011, **11**(23): p. 4072.
[4] Riaud, A., *et al.*, *Physical Review Applied*, 2020, **13**(3): p.12.

Using open-channel acoustofluidics for fabrication of skin equivalence

Dhananjay Deshmukh[1,2], Jessica Polak[3], Christine Fux[1], Mirko Meboldt[3], Mark Tibbitt[2], and Jürg Dual[1]

[1] Institute for Mechanical Systems, Department of Mechanical and Process Engineering, ETH Zürich, 8092 Zürich, Switzerland
E-mail: deshmukd@ethz.ch
[2] Macromolecular Engineering Laboratory, Department of Mechanical and Process Engineering, ETH Zürich, 8092 Zürich, Switzerland
[3] Product Development Group Zurich, Department of Mechanical and Process Engineering, ETH Zürich, 8092 Zürich, Switzerland

Introduction

Skin is one of the largest organs in our body and has diverse functions. The ability to engineer skin tissue is promising for skin grafts and for drug testing. A common approach for skin fabrication ex vivo involves layer-by-layer deposition of dermal fibroblasts and keratinocytes in a biomaterial scaffold. [1] This is usually done in an insert well membrane. However, skin is a diverse tissue consisting of many different cell types apart from keratinocytes and fibroblasts. For example, vascular network formation is essential for effective wound healing for skin burns. [2] Hair follicles on the other hand are important for thermoregulation in skin. [3] In both these cases higher localized concentration of cells can lead to formation of functional tissues. Acoustofluidics has been previously used to pattern cells to mimic various tissues. [4]

In our work, we designed a metal device for patterning cells into lines or clumps. By using an open channel device, we can pattern cells in different layers of the skin equivalence models. Since acoustofluidics is a label-free technique, it is possible to pattern various types of cells using our method. Since skin equivalent is generally fabricated in well plate inserts, we designed our device such that the inserts could be transferred to the acoustofluidic device where cells can be patterned on existing layers of the skin equivalents.
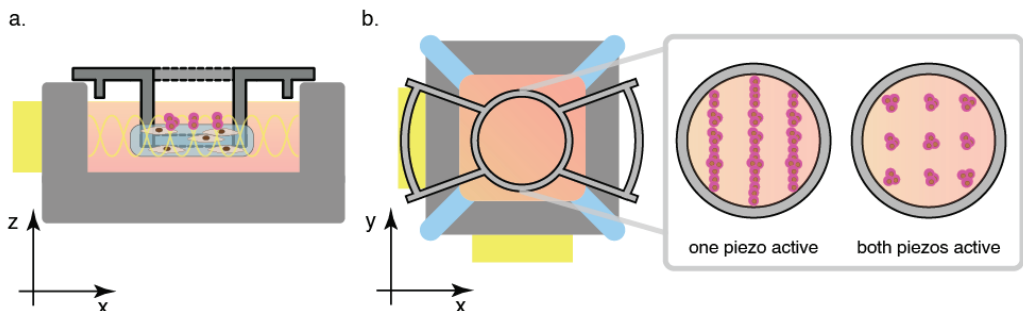

Figure 1: Design of skin patterning device. a) (side view) An insert with a skin equivalent can be transferred to an open metallic acoustofluidic device. A piezoelectric transducer (yellow) is attached to the side of the device. Cells can be patterned on top of the samples using a standing acoustic wave in the cavity. **b)** (top view) two piezoelectric transducers were used to pattern in both directions. To avoid crosstalk between the two transducers, the diagonal edges were filled with PDMS (blue) to decouple the patterning in the two directions.

Patterning was possible on top of inserts

We designed a metal device with a square cavity in the center. Two piezoelectric transducers were attached for patterning cells in both x and y directions independently (Figure 1). To decouple the crosstalk between the two piezoelectric transducers, we introduced a groove on the diagonal edges and filled it with PDMS. The
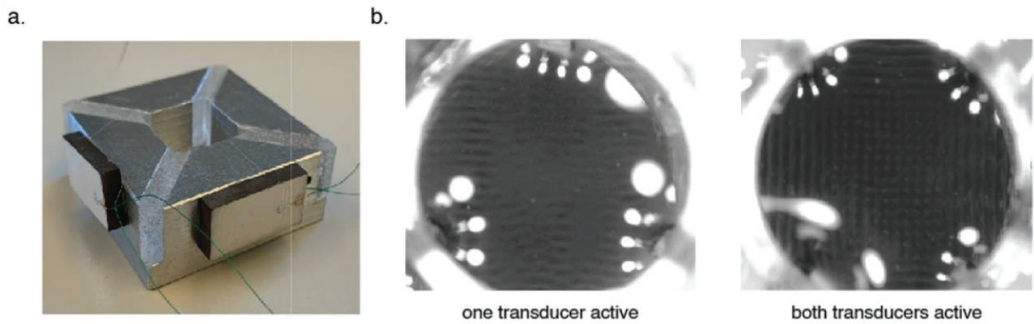
Figure 2: Patterning experiments with the device. a) Metal device with two piezoelectric transducers and PDMS filled in the diagonals. b) Polystyrene beads were patterned on top of the 3D printed inserts. A sinusoidal signal of 1.9 MHz, 20 Vp-p was applied to the transducer. With one transducer active lines of beads were formed, while clumps were formed when both transducers were active.

device was tested with tracking particles (polystyrene beads, Ø = 15 μm). The devices were tested without any inserts to determine the operating frequencies. To mimic the skin equivalents, we 3D printed an insert with a flat bottom where the skin equivalents will be. We observed both clumps and lines forming on top of the inserts (Figure 2). Through decoupling the x and y patterning, we could control the patterning in both directions independent of each other.

Initial proof-of-concept experiments were performed by patterning GFP-fibroblasts on the dermal fibroblast layer. Dermal fibroblasts mixed in collagen were placed in the transwell inserts. The samples were allowed to adhere to the inserts for 10 days after which the insert was transferred to the acoustic patterning device and GFP-fibroblasts were patterned in clumps with both piezoelectric transducers active (Figure 3).
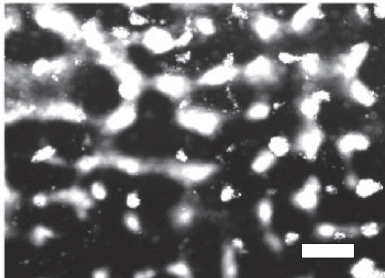

Figure 3: GFP fibroblasts were patterned on top of the dermal layer of the skin equivalent. Clumps of cells were observed under a fluorescent microscope while performing the patterning experiments. Scale bar, 200 μm

Conclusion

We developed an open-channel, easy-to-use acoustofluidic device which can be used to pattern cells in skin equivalent or other models. The device can pattern cells either in clumps or lines with patterning in each direction decoupled with each other. Initial cell patterning experiments have shown very encouraging results. This device can potentially be used not just for skin tissue engineering but also to study cell patterning in other tissue types.

References

[1]   F. Meier, M. Nesbit, M.-Y. Hsu, B. Martin, P. Van Belle, D. E. Elder, G. Schaumburg-Lever, C. Garbe, T. M. Walz, P. Donatien, T. M. Crombleholme, M. Herlyn, *Am. J. Pathol.* **2000**, *156*, 193.
[2]   H. Shahin, M. Elmasry, I. Steinvall, F. Söberg, A. El-Serafi, *Burn. Trauma* **2020**, *8*, 22.
[3]   M. R. Schneider, R. Schmidt-Ullrich, R. Paus, *The Hair Follicle as a Dynamic Miniorgan*, Vol. 19, Cell Press, **2009**, pp. R132–R142.
[4]   L. Ouyang, J. P. K. Armstrong, M. Salmeron-Sanchez, M. M. Stevens, *Adv. Funct. Mater.* **2020**, *30*, 1909009.

Bulk acoustic waves-based system for a rapid and high throughput cell washing

Hugo R. Sugier[1,2], Ludovic Bellebon[3], Jean-Luc Aider[3], Jérôme Larghero[4], Juliette Peltzer[5] and, Christophe Martinaud[6].

[1]Aenitis technologies, Paris, France
E-mail: hugo.sugier@aenitis.fr, URL: http://www.aenitis.fr
[2]Institut André Lwoff, INSERM UMR-MD 1197, Villejuif, France
[3]Laboratoire PMMH, UMR7636 CNRS, ESPCI Paris - PSL, Paris Sciences Lettres, Sorbonne Université, Paris, France
[4]Université de Paris, Assistance Publique-Hôpitaux de Paris, Hôpital Saint-Louis, Paris, France; Unité de Thérapie Cellulaire, INSERM U976, Centre d'investigation clinique de Biothérapies CBT501, Paris, France
[5]Institut de Recherche Biomédicale des Armées, Clamart, France
[6]Centre de Transfusion Sanguine des Armées, Clamart, France

Introduction

These last decades have seen the emergence and development of cell-based therapies, notably those based on mesenchymal stromal cells (MSCs), human induced pluripotent stem cells (iPSCs) and, CAR-T cells. The advancement of these promising therapies necessitates scaling up the throughput of cell processed for industrialization and lowering the production costs. Among the different cell processes, the cell transfer from one medium to another (e.g., change of cell culture medium, removal of enzymes and viruses, removal of cell debris) is particularly common for the cell manufacturing (1). The classical and most widely used method to remove a medium, and its components, is the conventional centrifugation. However, in addition to inducing high physical stress on the cells, the centrifugation is time consuming and requires operator intervention making this step complicated to integrate into an automated process.

To overcome those drawbacks, the use of acoustic force to manipulate cells (acoustophoresis) has emerged as a promising solution (2). Indeed, acoustophoresis offers the advantages of being a non-contact method, inducing low mechanical stress and, being easily integrated in a controlled and closed fluidic system. All of these qualities allow acoustophoresis to be a good manufacturing practices (GMP) compliant technology and a game-changer in cell manufacturing.

In this work, we developed a system based on bulk acoustic waves allowing the transfer of cells from one medium to another while limiting the transfer of proteins. Moreover, we optimized the flow rate in order to make the throughput of processed cells consistent with the needs of cell manufacturing.

Methods

The experimental device is composed of a piezoelectric ceramic (optimized for a frequency f = 2.5 MHz), a liquid-cooling system (regulating the temperature of the system at 20°C) and, a stainless-steel channel (Fig 1). The inner thickness of the channel is 250 μm. The flow rates of the 3 inlets and both side outlets are controlled independently with peristaltic pumps. Red blood cell (RBC) concentrates were obtained by centrifugation of whole blood collected from volunteer informed donors. RBC and albumin were suspended in physiological serum and injected in both side inlets. Physiological serum was injected in the central inlet. The albumin concentration was measured with an albumin assay kit. The RBC recovery was assessed by flow cytometry.

Results

The experimental process is shown in Fig 1. We investigated different flow rate configurations in order to maximize the efficiency of the separation: side flow rate Q_S > central flow rate Q_C, $Q_S = Q_C$ and, $Q_S < Q_C$. The separation efficiency of albumin and RBC was higher for $Q_S < Q_C$ and lower for $Q_S > Q_C$ (mean = 1.410 ± 0.092 vs mean = 1.114 ±0.063 respectively, p=0.007, n=4). Then, we applied a flow rate configuration Q_S = 0.75 mL/mn and increased Q_C up to 12 mL/mn. The separation efficiency was positively correlated to Q_C (Fig 2A). The mean of albumin removal increased with Q_C to reach a mean = 89.1 % (±0.6, n=4) with Q_C = 12 mL/mn. Despite the lack of significant difference, the RBC recovery tends to be more efficient at Q_C = 6 mL/mn with a mean of RBC = 87.7% ±2.9. Finally, we applied a central flow rate Q_C = 9 mL/mn and increased the throughput with Q_S up to 6 mL/mn. The separation efficiency was negatively correlated to Q_S and was maximal for Q_S = 0.75 mL/mn.
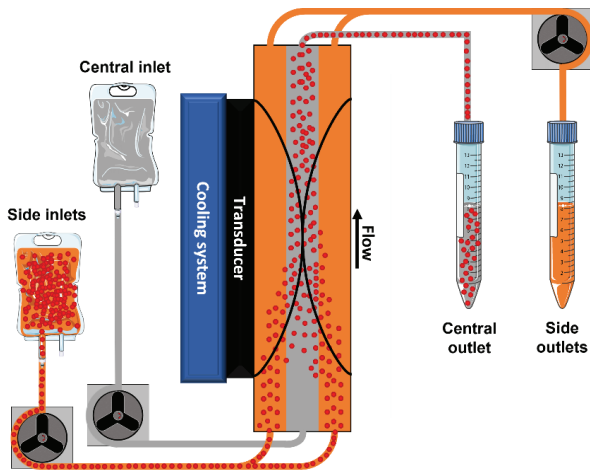
Figure 1: Schematic representation of the bulk acoustic waves-based cell washing setup. RBC and albumin solution are injected in the side inlets. While acoustic is turned on, most of the cells are recovered in the central outlet while the majority of the albumin remains in the side outlets.
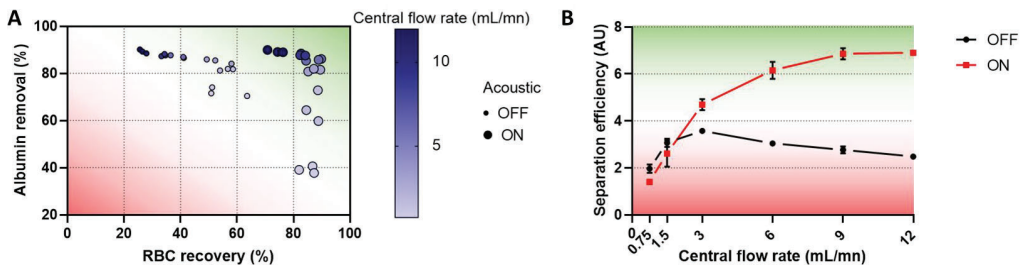

Figure 2: Cell washing efficiency depending on the central flow rate. **A** RBC recovery and albumin removal depending on the central flow rate. Side flow rate was 0.75 mL/mn, central flow rate was 0.75 to 12 mL/mn, input power was 8 W, n=3. **B** Separation efficiency of RBC and albumin depending on the central flow rate. The separation efficiency (Arbitrary Unit) was calculated as a ratio of RBC recovery and albumin concentration in the central outlet. The black and red lines represent the separation while the acoustic is turned off and on, respectively.

Perspectives

Next steps will be to investigate the impact of higher cell and protein concentrations on the separation's efficiency. We plan to use a loop system to expose cells to acoustics twice in order to increase our separation efficiency and to reiterate those results with other cell types. Finally, we will study the impact of the process on both the cells' morphology and viability.

Conclusion

In this study, we developed an acoustic device for cell washing allowing the transfer of cells from one medium to another and the removal of proteins.

We optimized the flow rates in order to remove nearly 90% of the proteins and recover 83% of the cells in a single passage through our system with an input flow rate of 0.75 mL/mn. These results highly suggest that cell washing based on acoustophoresis is a relevant and promising solution for numerous applications in cell manufacturing.

References

1. Li A, Kusuma GD, Driscoll D, Smith N, Wall DM, Levine BL, et al. Advances in automated cell washing and concentration. Cytotherapy. sept 2021;23(9):774-86.

2. Mohanty S, Khalil ISM, Misra S. Contactless acoustic micro/nano manipulation: a paradigm for next generation applications in life sciences. Proc Math Phys Eng Sci. nov 2020;476(2243):20200621.

Novel acoustofluidic approach using a Bulk Acoustic Wave resonator to control the topology and culture conditions of brain derived spheroids

Chloé Dupuis[1,2], Xavier Mousset[1,2], Guillaume Viraye[2], Pierre-Ewen Lecoq[1,2], Mauricio Hoyos[1], Jean-Michel Peyrin[2], Jean-Luc Aider[1]

E-mail: chloe.dupuis@espci.fr, jean-luc.aider@espci.fr, jean-michel.peyrin@sorbonne-universite.fr
[1]Laboratoire Physique et Mécanique des Milieux Hétérogènes (PMMH), ESPCI Paris, France
[2]Neurosciences Paris Seine (NPS), Institut de Biologie Paris Seine (IBPS), Sorbonne Université, Paris, France

Introduction

For the last decade, organoids have proven to be a good candidate to study developmental stages as they self assemble, recapitulating some of the tissue properties. Recent studies showed that guiding their self assembly by tuning both mechanical and signaling properties of their environment improves differentiation and repeatability [1]. Alternatively, many techniques from bio-printing to microfluidic organ-on-a-chip are emerging with increased repeatability and control over both the topology and chemical environment of the engineered tissue. To unify this two parallel visions, a new scaffold-free approach, the acoustic levitation, arises as a way to both structure organoids and let them self-organize. We previously showed that human mesenchymal stem cells (hMSC) self-organized into spheroids in just 24 hours of acoustic levitation and exhibited accelerated differentiation compared to classical 2D culture conditions [2]. We also demonstrated that varying the acoustic frequency in a multi-node configuration allows for the spatial manipulation of cell spheroids giving the possibility to merge them, leading to the formation of "assembloids" composed of contiguous spheroids [3]. Here, we first demonstrate the possibility of growing brain derived spheroids made of mouse primary neurons or patient derived glioblastoma cells for a week in constant acoustic levitation. Furthermore, we introduce an innovating method combining the fine tuning and shaping of acoustic radiation force fields with controlled microfluidic flows to structure concentric assembloids of different types of cells, recapitulating more faithfully the topology that can be found in vivo.

Theoretical background & experimental setup

In Bulk Acoustic Wave (BAW) resonators filled with water or liquid medium, spherical objects such as particles or cells can be attracted towards precise positions in the middle of the fluid (Figure 1.a). At these positions, the gravity is counterbalanced by the Acoustic Radiation Force (ARF) created when the resonance condition is respected ($h = \frac{1}{2}\lambda_{ac}$, with h the height of the cavity and λ_{ac} the acoustic wavelength). Thanks to this phenomenon, acoustic levitation can be used to create large aggregates of cells in a contact-less and label-free manner and with enhanced cell-cell adhesion. In this work, we designed two different BAW resonators - millifluidic chips of PDMS bonded on a glass slide - for specific experimental needs: a higher one to cultivate multiple spheroids with a lateral optical access based on previous studies [2]; a smaller one with a particular geometry which allows us to control fluid flows around a single aggregate and structure assembloids in a concentric manner.

Results

With the specific setup allowing for monitoring of multiple cell spheroids growth in acoustic levitation, we were able to observe their self-organization from sheet to sphere in 24 hours as previously shown [2] for all types of brain derived cells (Figure 1.b). The spheroids were recovered after few days of culture and analyzed to evaluate their survival. On Figure 1.c, a cryosection of a cortical spheroid cultivated by acoustic levitation is shown, with specific staining to identify particular compartments of neuronal cells like dendrites and somas (MAP2). Different techniques were used to assess the health of the spheroids and the survival rates are plotted on figure 1.d. We observed that for all types of cells, the spheroids cultivated in acoustic levitation had similar survival rates than control spheroids. For the structuration of assembloids, a feasibility assessment was conducted with the injection of fluorescent liquid in the BAW resonator already containing a neuronal spheroids. We observed that laminar flows were moving forward into the chamber without mixing with culture medium and wrapping up the spheroid by hydrodynamic effect (Figure 1.e). The enfolding effect due to hydrodynamic flows was then even enhanced by the axial component of the ARF. As a proof of concept of the structuration of concentric
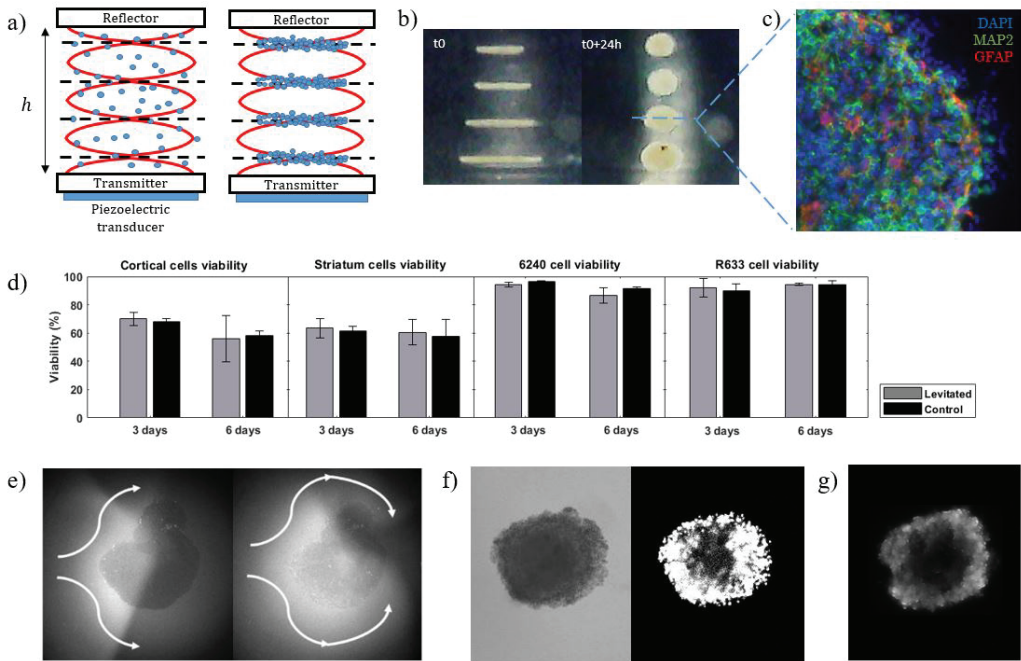
Figure 1: (a) Schematic of the multi-node acoustic wave resonator (b) Time lapse snapshots showing the self-organization of cortical primary neurons after 24 hours of culture (c) Cryosection of a spheroid of cortical primary neurons cultivated for 6 days in levitation, stained with DAPI (nucleus), MAP2 (dendrites and cell body) and GFAP (astrocytes) (d) Viability results of spheroids after 3 and 6 days of culture in levitation with different cell types. From left to right, cortical and striatal mouse primary neurons (E14), 6240 and R633 patient derived cancer cells. For mouse primary neurons, a quantification algorithm of healthy DAPI staining was used to assess the survival of the spheroids. For patient derived cancer cells, viability was assessed with trypan blue exclusion test. (e) Demonstration of acoustofluidic enfolding of a cell agregate with fluorescent solution. (f) Striatal neurons core surrounded with cortical neurons stained with CM-DIL after 24 hours of culture in acoustic levitation. (g) Cryosection of the cortico-striatal assembloid, fixed after 24 hours of culture.

assembloids with the combination of those two phenomena, a first aggregate of striatal neurons was formed at the center of the BAW resonator chamber. Then, cortical neurons, stained with a fluorescent marker, were injected in the chamber and surrounded the first aggregate as expected from previous experiments. The resulting concentric assembloid was cultivated for 24 hours under a microscope and the same self-organization than monocellular spheroids was observed (Figure 1.f). Finally, the assembloid was recovered and analyzed with the same cryosectioning and staining protocol, showing that the concentric topology was conserved (Figure 1.g). Cortico-striatal assembloids cultivated for 6 days showed high viability and on-going analysis aim to verify the stability of the topology and establish connection patterns between the different neuronal types.

Conclusion

In this study, we succeeded in growing brain derived spheroids from mouse primary neurons and patient glioblastoma cells for a week in constant acoustic levitation with similar viability than control spheroids. Moreover, we demonstrated a new method to structure concentric assembloids thanks to the combination of hydrodynamic and acoustic forces. This proof of concept is a step towards complex organoid architecture with controlled topology, offering the possibility to build ordered neuronal networks like the cortico-striatal neuroanatomic pathway or co-culture of neurospheres and tumoroids.

References

[1] Karzbrun, E., Kshirsagar, A., Cohen, S.R. et al. Human brain organoids on a chip reveal the physics of folding. Nature Phys **14**, 515â522 (2018).

[2] Jeger-Madiot N., Arakelian L., Setterblad N., et al. Self-organization and culture of Mesenchymal Stromal Cell spheroids in acoustic levitation. Sci Rep **11**, 8355 (2021).

[3] Jeger-Madiot N., Mousset X., Dupuis C., et al. Controlling the force and the position of acoustic traps with a tunable acoustofluidic chip: Application to spheroid manipulations. J. Acoust. Soc. Am. **151**, 6 (2022).

Acoustic wave activation of the growth of dielectric and metal thin films by plasma deposition techniques

M. Oliva-Ramírez[1], H. Reichel,[1] A. García-Valenzuela,[1] V. Rico,[1] J.P. Espino,[1] TC Rojas,[1] G. Regodon-Harkness,[1] J. Gil-Rostra,[1] A. Fakhouri,[2] A. Gómez-Ramírez,[1] R. Alvarez,[1] A. Borras,[1] A. Palmero,[1] A. Winkler,[2] A.R. González-Elipe[1]

[1] Instituto de Ciencia de Materiales de Sevilla (CSIC-Univ. Sevilla). Avda. Américo Vespucio 49. 41092 Sevilla (Spain).
E-mail: M.Oliva@icmse.csic.es; URL: https://sincaf.icms.us-csic.es
[2] IFW Dresden, SAWLab Saxony, Helmholtzstr. 20, 01069 Dresden (Germany)

Introduction

Time and spatial dependent mechanical deformation and surface electric polarization are known to occur when a piezoelectric substrate is subjected to a RF signal excitation generating a propagating acoustic wave (AW). However, the interaction of AWs with a nearby gas plasma has been almost unnoticed, despite its obvious interest due the new physics it may entail and the potential applications in a large variety of fields. In this communication we report the unexpected patterning phenomena that appear when a dielectric or a metal thin film are deposited by magnetron sputtering, i.e., in the presence of a plasma, on a RF excited piezolelectric substrate. Quite large differences in nucleation have been found during the earlier stages of MS deposition of silver, while a substantial domain patterning in a size scale in the order of the wavelength of the AWs occurs during the deposition of the TiO$_2$ thin film (1). Although a modeling of the deposition process is still required, we attribute the unexpected effects on the thin film growth mechanisms to the interaction of the alternant polarization field developed onto the substrate and the plasma in contact with it.

Experiment description

A LiNbO$_3$ plate provided by two metal electrodes was excited with a RF signal tuned to the natural resonance frequency of the piezoelectric plate (between 3.4 and 3.5 MHz) and utilized as a substrate to deposit a submonolayer of silver particles or a TiO$_2$ thin film by MS. The experimental configuration was such that the substrate was embedded within the plasma inducing the sputtering of the target atoms for their deposition onto the substrate. Experiments were also carried out at overtone frequencies and changing the deposition geometry and configuration. Special attention was paid to the different experimental conditions required for the deposition of a metal or a dielectric onto the AW excited piezoelectric substrate.

AW induced 2D patterning of plasma deposited films.

A common observation by the deposition of either a submonolayer of the silver metal or the TiO$_2$ thin film is a 2D pattering of its morphology. Domain sizes in the order of the wavelength of the standing AWs (i.e., around 1 mm) were obtained according to a pattern that mimics their simulated propagation of AWs over the substrate surface. Figures 1 and 2 show, respectively, a photograph of the silver submonolayer film and the TiO$_2$ thin film both accompanied by an electron microscopy analysis of the deposit microstructure. Differences in the silver nanoparticle size distribution and agglomeration state are apparent in comparison with a similar submonolayer film prepared without AW activation (Figure 1). Topography and differences in the film nanostructure of the TiO$_2$ (Figure 2), as well as other features affecting the thin film crystallographic structure and the agglomeration degree are also apparent in the TiO$_2$ thin film. These singular differences in topography and microstructure depending on domain have been qualitatively interpreted in terms of the bombardment of the substrate and growing film with plasma ions, which would be accelerated and focused under the action of the electrical polarization field developed at the piezoelectric substrate. In accordance with this electrical field modulation of the deposition process, full coverage of the substrate surface with the silver layer completely smears out the patterning process, while patterning persisted up to several hundreds of nanometer in the case of the dielectric films.

These preliminary results in the still unexplored field of the interaction of piezoelectric AWs with plasmas provide a scenario rich in possibilities for the deposition and patterning of thin films, the modification of plasmas and plasma reaction process or the controlled management of focalized plasma devices. A critical discussion is carried out regarding the variables requiring full control of this kind of experiemnts and the

possibilities and limitations of plate and surface AW devices (these latter activated with interdigitated electrodes) for the management of such processes.
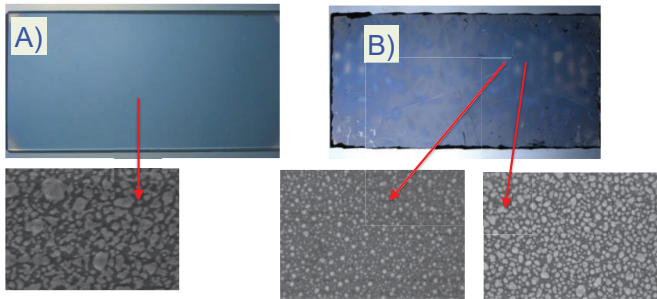

Figure 1: Photograph of submonolayer silver particles formed onto flat substrates upon MS deposition without (A)) and with (B) AW excitation. The arrows relate the homogenous aspect of the silver deposit in (A) and the two kind of silver domains in (B) with SEM images showing the different characteristics of the silver nanoparticles formed in each case.
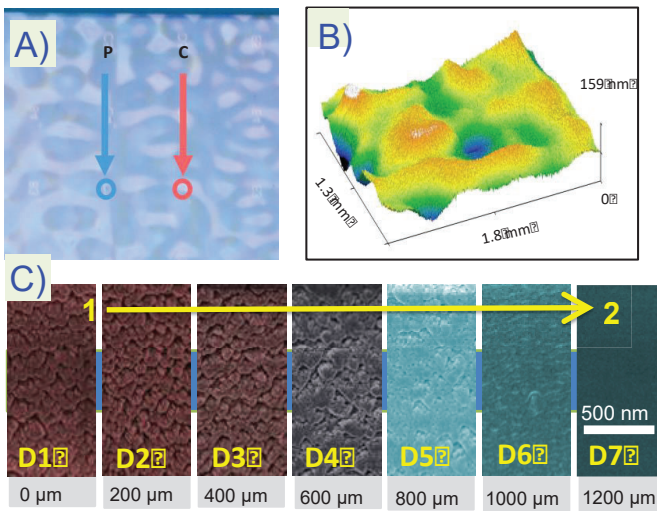
Figure 2: A) Photograph of a TiO_2 thin film MS deposited under AW excitation in an oblique angle configuration under AW excitation. B) Confocal microscopy analysis of surface topography of the TiO_2 thin film. They are apparent the changes in surface topography and the formation of distinct domains. C) SEM micrographs taken along a line connecting domains of different aspect. The separation between each micrograph is 200 microns as indicated.

Conclusions. The deposition of plasma thin films onto piezoelectric substrates under AW activation produces patterning phenomena and local differences in microstructure that are tentatively associated to focalized ion bombardment effects induced by the interaction of the electric polarization of the substrate with the ions in the plasma sheath formed over the substrate. This amazing physical interaction can be used to tailor the microstructure of dielectric thin films, induce their patterning and to induce other still unknown plasma phenomena. In the case of metal submonolayers differences in nucleation and agglomeration take place as resulting from these interactions.

References
[1] A. García-Valenzuela, A. Fakhfouri, M. Oliva-Ramírez, V. Rico-Gavira, T. C. Rojas, R. Alvarez, S. B. Menzel, A. Palmero, A. Winkler, A. R. González-Elipe. Patterning and control of the nanostructure in plasma thin films with acoustic waves: mechanical vs. electrical polarization effects. Mater. Horizons 8, 515 (2021).

Culture of hepatic and stem cell spheroids in acoustic levitation induces different self-organisation dynamics

Lucile Rabiet[1,2], Lousineh Arakelian[2], Duván Rojas García[1], Nathan Jeger-Madiot[1], Mauricio Hoyos[1], Jérôme Larghero[2] and Jean-Luc Aider[1]

[1]Laboratoire Physique et Mécanique des Milieux Hétérogènes (PMMH), UMR 7636 CNRS, ESPCI Paris - PSL, Sorbonne University, Campus Jussieu, 7-9 quai Saint-Bernard, 75005, Paris, France
[2]Unité Human Immunology Pathophysiology Immunotherapy (HIPI), Inserm U976, Hôpital Saint-Louis, Paris, France
E-mail: lucile.rabiet@espci.fr

Introduction

More than half of acute liver failures can be attributed to drug-induced liver injuries (DILI), causing major challenges for public health and drug development [1]. Currently, pharmaceutical tests of upcoming drugs mainly rely on animal models and two-dimensional (2D) human cell culture. However, both models suffer from serious limitations: variations between human and animal liver pathways cause some DILI to remain undetected in animal models, and the lack of long-term functionality of 2D cultures impairs reliability, costs, and convenience of *in vitro* tests [1].

A need for a shift in paradigm has emerged in recent years, calling for increasing functionality of human-based toxicity tests, for instance through the development of three-dimensional (3D) cultures [2]. With the development of organoids, organs-on-chip and microphysiological systems, the desired shift could be reached within years. These prementioned techniques can benefit from the field of acoustofluidics: acoustic manipulation of single cells can be used to form multicellular spheroids and organoids.

We have shown that in our microfluidics chip, viable and functional spheroids of cells can be cultured for long periods of time and submitted to different treatments via a continuous flux of medium [3]. Our robust technique allows self-organisation of the cells, which form standardized spheroids inside the microchip.

Theory and Experimental procedure

Acoustofluidics manipulation [4,5] allows the aggregation of a suspension of cells into monolayers, due to the acoustic radiation force (ARF) created by an ultrasonic standing wave of a few megahertz. Using this technology, we can create 30 to 50 large cell sheets (hundreds of micrometres long) in one PDMS (Polydimethylsiloxane) chip. A transparent side-wall allows optical microscopy. The ARF maintains the aggregates in acoustic levitation in the cell culture medium (no need of hydrogel or extracellular matrix) without any contact with the walls of the microfluidic chip.

Results and Discussion

We have shown previously that after a few hours, monolayers of mesenchymal stromal cells (MSC) spontaneously self-organize into spheroids [3]. We now successfully apply this method to other cell types, including the hepatic cell line HepaRG, cryopreserved primary hepatocytes and human umbilical vein endothelial cells (HUVEC). Except if stated otherwise, voltage is 3,5V and frequency is 2,2MHz, both stay constant during culture. In all cases, the self-organisation of cell sheets into spheroids is observed, see Fig. 1.
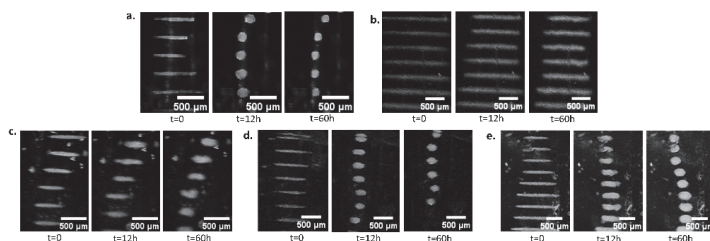

Figure 1: Optical imaging of the side-view of the chip during 60 hours of levitation of mesenchymal stromal cells (a), cryopreserved primary hepatocytes (b), HepaRG hepatic cell line (c), human umbilical vein endothelial cells HUVEC (d) and a coculture of HepaRG and HUVEC cells (e). (voltage: 3,5V / frequency: 2,2MHz)
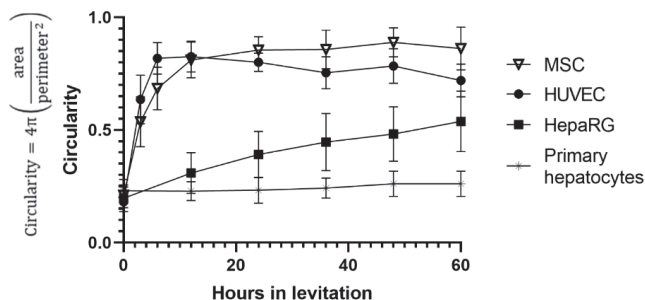
$$\text{Circularity} = 4\pi\left(\frac{\text{area}}{\text{perimeter}^2}\right)$$

Figure 2: Circularity dynamic of different cell types levitated during 60 hours: human umbilical vein endothelial cells (HUVEC), mesenchymal stromal cells (MSC), HepaRG hepatic cell line and cryopreserved primary hepatocytes. (voltage: 3,5V / frequency: 2,2MHz)

The spheroids were levitated during several days without damaging cell viability, and kept at fixed positions while perfused with a flux of medium. Differences in shape of the spheroids and variation in the self-organisation dynamic depend on the cell type, and stay consistent between spheroids of the same cell type (see Fig. 2). The dynamic was not impacted by variations in the acoustic radiation force, thus suggesting a prominent role played by cell-cell interactions, see Fig. 3.
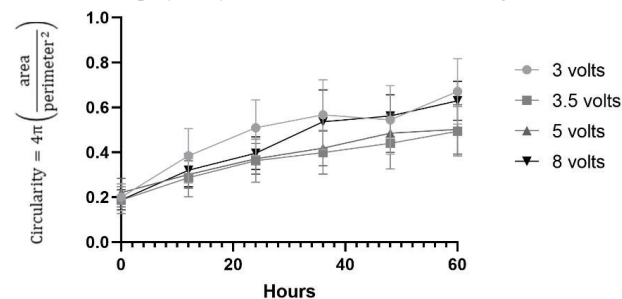

$$\text{Circularity} = 4\pi\left(\frac{\text{area}}{\text{perimeter}^2}\right)$$

Figure 3: Circularity dynamic of HepaRG spheroids submitted to different voltages. (voltage: 3 to 8V / frequency: 2,2MHz)

Furthermore, dynamic was impacted by disruption of actin-mediated or E-cadherin-mediated self-organisation mechanisms, via treatment with ROCK inhibitor Y27632 or calcium chelator EDTA Ethylenediaminetetraacetic acid, see Fig. 4.
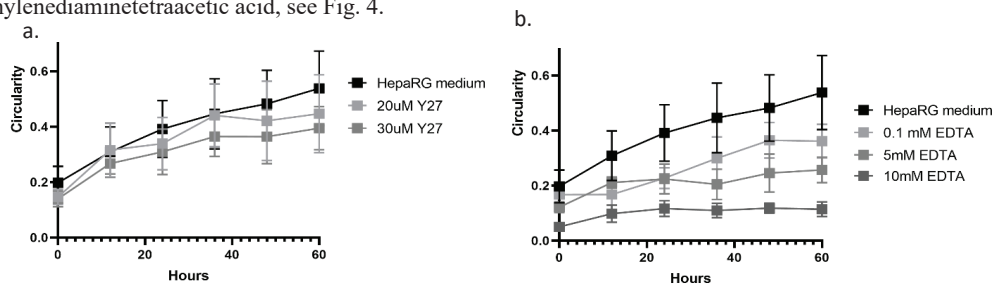

Figure 4: Circularity dynamic of HepaRG spheroids treated during 60 hours with ROCK inhibitor Y27632 (a) or calcium chelator EDTA Ethylenediaminetetraacetic acid (b). (voltage: 3,5V / frequency: 2,2MHz)

Conclusion

We can reproducibly create viable 3D spheroids, with a specific self-organisation dynamic for each cell type, and then culture them during several days. Self-organisation dynamic is not impacted by variations in the acoustic radiation force, but can be modified by altering cell-cell adhesion or actin-myosin interactions. This shows the prominent role played by cell-mediated forces compared to acoustic forces during this organisation.

References

[1] R.J., Weaver, E.A., Blomme, A.E., Chadwick, *et al.* Managing the challenge of drug-induced liver injury: a roadmap for the development and deployment of preclinical predictive models. Nat Rev Drug Discov **19**, 131–148 (2020).
[2] H. Clevers, M. Lancaster, T. Takebe, Advances in Organoid Technology: Hans Clevers, Madeline Lancaster, and Takanori Takebe. Cell Stem Cell 20, 759–762 (2017).
[3] N. Jeger-Madiot, L. Arakelian, N. Setterblad, P. Bruneval, M. Hoyos, J. Larghero and J-L. Aider, Self-organization and culture of Mesenchymal Stem Cell spheroids in acoustic levitation Sci. Rep. **11** 8355 (2021)
[4] H. Bruus, Acoustofluidics 1: Governing equations in microfluidics, Lab Chip **11** 3742-3751 (2011)
[5] M. Wiklund, Acoustofluidics 12: Biocompatibility and cell viability in microfluidic acoustic resonators Lab. Chip 12 2018–28 (2012)

Multi Line Patterning of Human Umbilical Vein Endothelial Cells for 3D Microvascular Network Formation

Le Thi Huong[1], Andreas Lenshof[2], Huu Lam Phan[1], Van Thuy Duong[1], Thomas Laurell[2, *], and Kyo-in Koo[1, *]

[1] Department of Electrical, Electronic and Computer Engineering, University of Ulsan, Ulsan, Rep. of Korea
E-mail: lehuong94alhp@gmail.com, URL: http://mdl.ulsan.ac.kr
[2] Department of Biomedical Engineering, Lund University, Lund, Sweden

* These authors equally contribute as corresponding authors.

Introduction

Three-dimensional network-structured tissue has been a long-term goal in the field of engineered organs [1, 2]. To avoid a necrotic core creation, cells inside engineered tissue should be within 100 - 200 µm to evenly distributed blood capillaries [3, 4] . Hence, one of the biggest challenges in tissue engineering is creating dense vascularized networks. Endothelial cells (ECs) enables to form new vessel networks and maintain the integrity of vascular walls [5]. In the past, we reported a fibroblast cell network utilizing acoustic focusing of cells [6]. In this study, ECs were acoustofluidically patterned in the mixture of decellularized extracellular matrix (dECM) and sodium alginate for the formation of a functional microvascular network.

Materials and Methods

One 400 µm and one 800 µm square-shaped glass capillaries (VitroCom, NJ, USA) were glued to 1 mm thick ultrasound transducers (MEGITT A/S, Kvistgaard, Denmark) (Fig. 1a). The device has three inlets. The mixture of sodium alginate (MERCK, Madison, USA) (0.5% w/v) and dECM (20 mg/mL) at ratio 1:9 in 1 mL of the total volume mixed with 60 µL of 10-micrometer (diameter) polystyrene microparticles (MERCK, Madison, USA). This mixture was pumped into inlet 1. The same ratio of dECM and alginate was supplied into the inlet 2. Sodium alginate (1% w/v) was injected in inlet 3 with. For the cell experiment, instead of the microparticles, 100 µL of 8×10^6 cells/mL RFP-HUVECs (Angio-Proteomie, Boston, USA) was utilized. The outlet of the acoustic cell alignment system was injected into a beaker of 300 mM $CaCl_2$ (MERCK, Madison, USA) for cross-linking. The fabricated cell scaffolds were pre-cultured at 37 °C, 5% CO_2 for one day. After that, alginate lyase enzyme (MERCK, Madison, USA) was added to the culture media of the cell scaffold at 10 units/mL in final concentration to release the formed cell scaffold from the sodium alginate support. The formation of a closed cylindrical cell scaffold was tested by perfusing the vascular network with FITC-Dextran (Thermo Fisher, Massachusetts, USA).
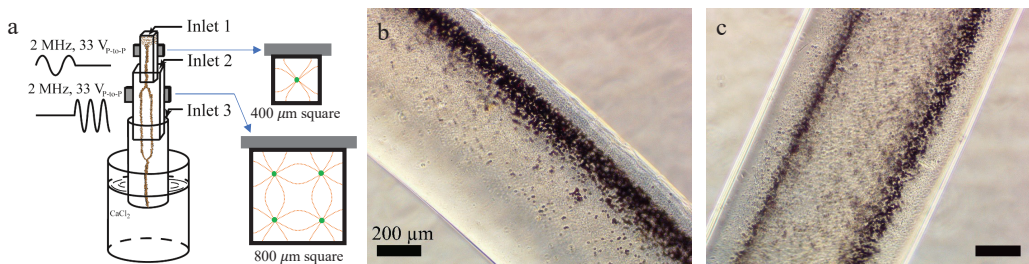

Figure 1. (a)The conceptual sketch of the developed device. The green dots are the pressure nodes. (b and c) The micropartilces were aligned as one line (b) and four lines (c) along the pressure nodes. (c) In this 2D photo, some parts of the patterned 4 lines were observed.

Acoustic microparticles patterning in the dECM and sodium alginate mixture hydrogel

When applying 2 MHz ultrasound in the 400 µm square-shaped glass capillary, the acoustic radiation force focused the microparticles into one stream at the center of the capillary (Fig. 1b). At the 800 µm square-shaped glass capillary, 2 MHz ultrasound patterned four parallel lines of microparticles (Fig. 1c). Alternating the on-and-off of 2 MHZ enabled the microparticles continually and repeatedly to split into four streams and to merge into one stream. This structure was surrounded by a sodium alginate shell by the Inlet 3 as a supporting structure during the pre-culturing step that facilitated the handling of the internal cell structure.

Acoustic RFP-HUVEC cells pattering in the dECM and sodium alginate mixture hydrogel

The RFP-HUVECs were patterned as one line at the 400 μm region and as four lines at the 800 μm (Fig. 2 a and b) as well. After 3 days of culturing, the RFP-HUVECs had proliferated to form a tube and start to sprout at the one line area (Fig. 2c). In the four lines area, the cells well interconnected to form the micro-vascular network (Fig. 2d). Due to the alginate lyase, the alginate inside the scaffold was removed and the dECM remained only. This was supposed to enhance proliferation, migration, and angiogenesis of the RFP-HUVECs.
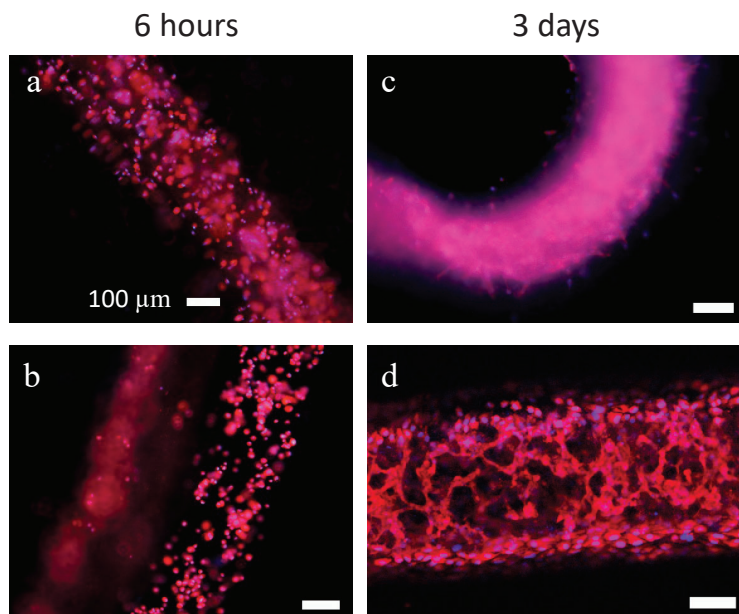
6 hours   3 days

Figure 2. (a and b) The fluorescent images after 6 hours of the scaffold fabrication with cells focused in one line (a) and in four lines (b), respectively. (c and d) The fluorescent images after 3 days of culturing with aligning as one line (c) and four lines (d), respectively. (b and d) In these photos, some parts of the patterned four lines were observed.

For perfusability test of the micro-vascular network, FITC-Dextran was pumped through a lab-made connector into the cell scaffold. Figure 3a showed the pumped FITC-Dextran solution flowed out through another open end of the cell scaffold. Figure 3b exhibited the remained FITC-Dextran (green) marked with white triangles inside the micro-vascular network after the pumping. Considering these results, the RFP-HUVECs patterned in the hydrogel looks well formulated into the vascular network.
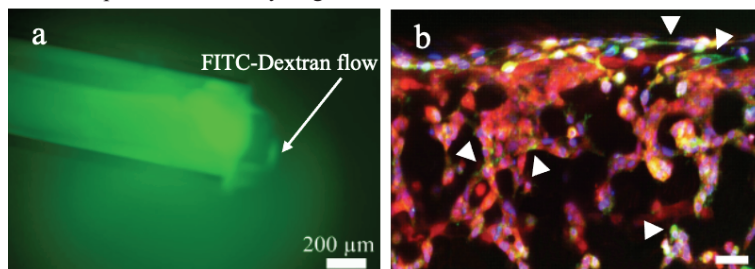

Figure 3. (a) The FITC-Dextran flows out after pumping. (b) The FITC-Dextran 70 kDa (green) marked with the white triangles remained inside the micro-vascular network after pumping. (red: RFP-HUVEC; blue: DAPI; green: FITC-Dextran) The scale bar is 50 μm.

Conclusion

Using 1 mm thick transducers glued to square glass capillaries (400 and 800 um) enabled endothelial cell branch formation. Alginate lyase enzyme facilitated the formation and maturation of vascular networks efficiently. The obtained functional vascular network was demonstrated by perfusion with FITC-dextran.

References

[1] M. Nomi, A. Atala, P.D. Coppi, S. Soker, Molecular Aspects of Medicine 23(6) (2002) 463-483.
[2] V.T. Duong, T.T. Dang, J.P. Kim, K. Kim, H. Ko, C.H. Hwang, K.I. Koo, Eur Cell Mater 38 (2019) 1-13.
[3] V.T. Duong, T.T. Dang, C.H. Hwang, S.H. Back, K.-i. Koo, Biofabrication 12(4) (2020) 045033.
[4] M.D. Sarker, S. Naghieh, N.K. Sharma, X. Chen, Journal of Pharmaceutical Analysis 8(5) (2018) 277-296.
[5] C.T. Nguyen, V.T. Duong, C.H. Hwang, K.-i. Koo, International Journal of Bioprinting; Vol 8, No 3 (2022).
[6] K.-i. Koo, A. Lenshof, L.T. Huong, T. Laurell, Micromachines 12 (2021) 1-12.

Discovery of the mechanism responsible for ultrasound's excitation of ion channels in cells

Aditya Vasan,[1] Jeremy Orosco,[1] Uri Magaram,[2] Marc Duque,[2] Connor Weiss,[2] Yusuf Tufail,[2] Sreekanth H Chalasani,[2] James Friend[1]

[1]Medically Advanced Devices Laboratory, Department of Mechanical and Aerospace Engineering, Jacobs School of Engineering and Department of Surgery, School of Medicine, University of California San Diego, La Jolla CA 92093 USA
E-mail: jfriend@ucsd.edu, URL: http://friend.ucsd.edu
[2]Molecular Neurobiology Laboratory, The Salk Institute for Biological Studies, La Jolla, CA 92037

Introduction

We combine theory, computation, and experiment to elucidate the mechanism responsible for ultrasound's effect on ion channel activation in the membranes of cells. Once thought to be driven by cavitation [1], indirect auditory signalling *in vivo* [2], or lipid clustering producing a change in the membrane tension [3], we conclusively determine that it is in fact the stretch of the cellular membrane from exposure to ultrasound that causes a change in the capacitance across the membrane, in turn leading to a transmembrane current in the presence of an ever-present chemical potential gradient.

Method and Brief Results

Here we use high-speed digital holographic microscopy (to 100-kHz order; Lyncee-tec) to visualize the cellular membrane dynamics. We show that neuronal and fibroblast membranes deflect about 150 nm upon ultrasound stimulation, with results shown in Fig. 1 for a typical cell mounted upon a substrate.

Next, we develop a biomechanical model that predicts changes in membrane voltage after ultrasound exposure. Summarizing, the damped wave equation describing the deflection, u, of the membrane in response to ultrasonic pressure, P_{US}, while immersed in a fluid medium is written as

$$\rho \, \partial_t^2 u = 2\,\eta\,\frac{\partial^3 u}{\partial x^2 \partial t} + \left(2\,\gamma\,\partial_x^2 u + P_{US}\right)\left(\frac{\pi}{d}\right), \tag{1}$$

where ρ and η are the dynamic viscosity and density of the surrounding fluid, both assumed to be the same as water as used in prior studies [4, 5]); γ is the surface tension between the membrane and media;
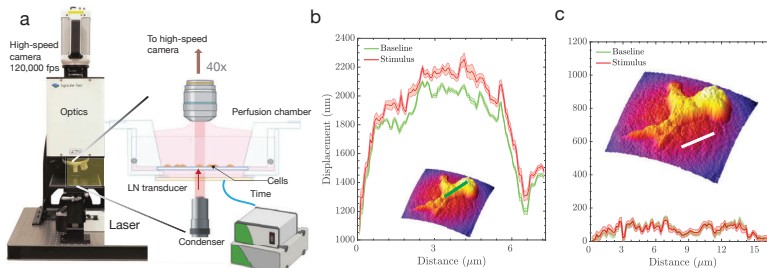

Figure 1: (a) A transmission digital holographic microscope combined with a high-speed (1Mfps) camera can produce imagery at 120,000 fps to describe the deformation of a cell membrane within the field of view to 100 nm displacement resolution. The DHM setup consists of a lithium niobate transducer operating in a simple thickness mode at 6.72 MHz driven by a signal generator and an amplifier. The cells are mounted on a coverslip and placed in a custom perfusion chamber maintained at 37° C. The b) holograms directly describing the (b) cell membrane height above a substrate without (baseline) and with 6.72 MHz, 0.25 MPa US stimulus recorded for 25 ms. Note that this pressure is well below the threshold required to induce any cavitation in cells (mechanical index = 0.37 ≪ 1.9). The median change in this HEK293 cell membrane height was about 214 nm ±20 nm due to thermal excitation; the median change in individual and clusters of neurons was similar at about 160 nm ±20 nm. The substrate itself (c) exhibits negligible motion upon the application of US: the baseline and stimulus measurements are indistinguishable.

and d is the characteristic length of the membrane between anchor points. The deflection predicted by the model for dimensions relevant to the size of a cell are between 100 nm to 400 nm, irrespective of the value of surface tension and similar to the DHM results. The character of the membrane "slow time" response—that is, its ability (or lack thereof) to sustain oscillations—is governed by the value of the Ohnesorge number, Oh; typical Oh values for neurons range from ∼0.06 to ∼0.45. This implies that inertial and surface tension forces dominate over viscous forces: the slow time membrane response is characteristically oscillatory.

Modeling the electrical output of a neuron under the influence of ultrasound involves defining a modified version of the original Hodgkin-Huxley equations [6],

$$\frac{dV_m}{dt} = -\frac{1}{C_m}\left[I_{\text{app}} + I_{\text{Na}} + I_{\text{Kd}} + I_{\text{M}} + I_{\text{leak}}\right]. \tag{2}$$

In this equation, the membrane potential of the neuron, V_m, changes over time with respect to the membrane capacitance, C_m, and the underlying currents, I_{app}, I_{Na}, I_{Kd}, I_{M}, and I_{leak}. At rest, $V_m = -71.9$ mV is the well-known membrane potential of the cell and, notably, the action potential generation is controlled by the presence of an applied current, I_{app}, while the other currents are based on the membrane morphology and chemistry. The capacitance, C_m, may also fluctuate due to a morphological change in the membrane, not in the original model, such that $I_{\text{app}} \equiv V_m \frac{dC_m}{dt}$. Solving this produces Fig. 2, indicating the change in capacitance due to 6.72 MHz ultrasound at 0.5 MPa (Fig. 2a) and 1 MPa (Fig. 2b) with the corresponding area fluctuations that bring about the change in capacitance represented in Fig. 2c. A slow time capacitive is produced, bearing order of magnitude equivalence to the ion channel relaxation times in the modified Hodgkin-Huxley model [7].
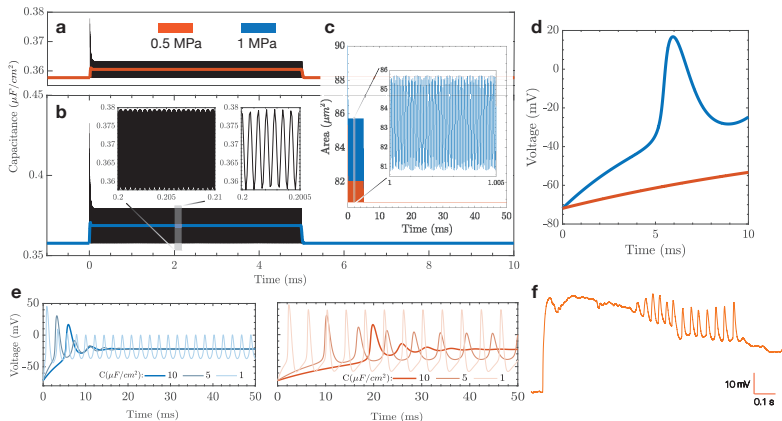

Figure 2: The mechanism of (a,b) ultrasound driving capacitance changes over 5 ms stimulus for 0.5 and 1.0 MPa. The capacitance changes occur from changes in the (c) area of the membrane due to its deflection from ultrasound, which gives rise to depolarization of the membrane in (d) the 1.0 MPa case, but not the 0.5 MPa case, indicating there is a threshold ultrasound amplitude required to drive the depolarization. A longer stimulus of (e) 50 ms duration shows how the action potential across the membrane evolves, with remarkable similarity to (f) in vitro current clamp electrophysiology results.

Conclusions

For the first time, we describe how ultrasound results in membrane deflection and eventually leads to transmembrane voltage changes and ion channel activation. Moreover, we demonstrate real-time membrane deflection due to ultrasound using high-speed DHM imaging. At the presentation, we will present how this fits into the context of neuronal excitation and potential medical benefits in humans, from the treatment of diabetes to pacing the heart.

References

1. Plaksin, M. et al. *Physical Review X* **4,** 011004 (2014). 2. Guo, H. et al. *Neuron* **98,** 1020–1030 (2018). 3. Di Giacinto, F. et al. *Ultrasound in Medicine & Biology* **45,** 1143–1150 (2019). 4. Israelowitz, M. et al. *Journal of Healthcare Engineering* **3,** 455–476 (2012). 5. Guyot, Y. et al. *Biotechnology and Bioengineering* **112,** 2591–2600 (2015). 6. Hodgkin, A. L. et al. *The Journal of Physiology* **117,** 500–544 (1952). 7. Abbott, L. et al. in *Statistical mechanics of neural networks* 5–18 (Springer, 1990).

Acoustic activated absorbance droplet sorting at kHz droplet rates

Esther S. Richter[1], Andreas Link[1], Raymond W. Sparrow[1], John S. McGrath[1], Florian Hollfelder[2] and Thomas Franke[1]

[1]Division of Biomedical Engineering, School of Engineering, University of Glasgow, Glasgow, UK
[2]Department of Biochemistry, University of Cambridge, Cambridge, CB2 1GA, United Kingdom
E-mail: thomas.franke@glasgow.ac.uk

Introduction

Microfluidic droplet sorting is an established technique in biotechnology for chemical, biochemical and molecular biology applications such as directed evolution, drug screening, single cell analysis and protein engineering [1,2,3,4,5]. The most common detection method is fluorescence which requires the addition of a fluorophore, which is an artifact, to the sample to generate the fluorescence signal [4]. There is a demand for label free droplet sorting techniques to screen systems [6,7]. Using the natural absorption properties of molecules within samples overcomes this issue and is more readily quantifiable than fluorescence [4]. Absorbance and the quantitative data that can be taken enables a greater range of systems to be detected.

Droplet microfluidics allows for rapid screening and high-throughput sorting of droplets from a large population. This, with low sample volumes is ideal for directed evolution and many other systems.

Using travelling surface acoustic waves (TSAW) generated by an interdigitated transducer (IDT) to sort sub-populations of droplets using the acoustic streaming effect removes the need for responsive particles, magnetic or dielectric labelling [2,3]. As proven in previous work [2,3,5], acoustics are less invasive or harmful to cells, thus leading to increased cell viability. Integrated optic fibres in microfluidics for detecting fluorescence, scattered light and absorbance is well documented [4,5,6,7]. So far, absorbance droplet sorting rates using dielectrophoresis are low at 150 – 300Hz [6]. We present an acoustic activated absorbance droplet sorter (AcAADS) enabling label free sorting at kHz droplet rates.

Methods

Droplets are produced in a flow focusing production chip and injected into the AcAADS-chip for sorting. There the droplets are spaced and focused using oil. We integrated an absorbance detection unit for label free characterization of droplet content concentrations. In the deflection region the acoustic streaming deflects drops when activated and sorted drops flow out the sorting outlet while the others follow the preferential flow to the waste outlet, (see Figure 1).
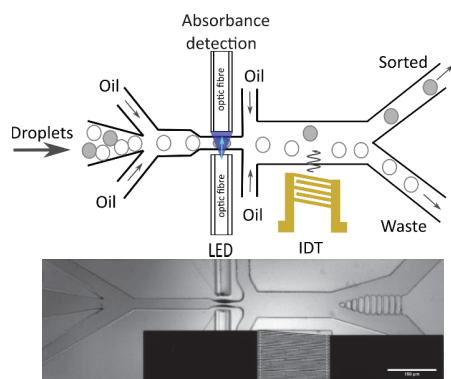

Figure 1: Schematic of the AcAADS and microscope image of the device. The AcAADS can be separated in the five regions: spacing of the droplet, absorbance detection, focusing of the droplet to the preferential flow, deflection of the droplet by TSAW and sorting into the two outlet channels. The arrows indicate flow directions, and the colour of the droplets represent different absorbance values of the droplet content.

The device consists of a tapered IDT (TIDT) on piezoelectric LiNbO3 substrate, PDMS micro-channels and optic fibres. The TIDT generates traveling surface acoustic waves with a resonance frequency of 161-171MHz. Our chip holder enables the IDT and fibres to be reusable due to mechanical sealing of the PDMS onto the IDT and the fibres held in place by the holder's design. No bonding of the PDMS is needed and fibres are aligned easily.

One optic fibre is connected to an LED (455nm) illuminates the droplets continuously and a second one attached to a photodetector detects a voltage signal. The detected voltage can be used to calculate the

absorbance via the Beer-Lamberts law. If a droplet signal crosses a pre-set threshold the TSAW is triggered and creates acoustic streaming in the microchannel deflecting the target droplet. We used an operating frequency of 162MHz and 24dBm power to sort droplets with kHz rates. Simultaneous saving of the video and is triggered and sorting efficiency is verified by overlaying the signal and the video.

Results and discussions

Overlaying the corresponding signal with a reslice of the video allows us to characterize the droplet signal shape. The signal is composed of two downwards peaks below the oil baseline and a middle peak. For low concentrations the middle peak is above the oil baseline. This characteristic shape of the signal has also been reported by other groups [4,6]. They proposed that the mismatch of refractive index of the oil (1.287) and water-phase (1.33) causes these artefacts. Using our overlay, we can confirm that the peaks below the baseline are generated when the droplet edges pass the detector. Yellow food dye (tartrazine) was used to calibrate the absorbance detection, by collecting signals of droplets with defined concentrations (between 0 and 1mM). Our sorting algorithm enables us to sort droplets with concentrations below 100μM. We conducted sorting experiments with varying droplet rates, acoustic pulse duration and powers to determine the parameter range for kHz sorting. For higher drop rates, higher powers and longer minimum pulse length are necessary to achieve 100% sorting efficiency. To sort kHz droplet rates successfully an applied power of 24dB is required. We can sort 2.5 kHz rates with pulse duration of 0.3ms and delay time below 2ms. In Figure 2 a reslice of the outlet channels and signal of a sorting experiments are shown.
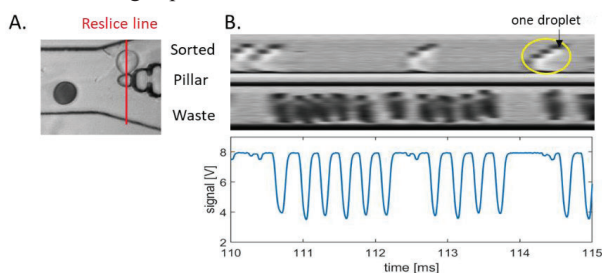

Figure 2: Sorting of 100μM tartrazine droplets (white) and 10mM bromophenol blue drops (dark) at 2.8 kHz sorting rates. Signals and microscope videos are saved simultaneous (for 1s) enabling us to assign each drop to its corresponding signal. **A.** shows the location of reslice in ImageJ at the chip outlets. **B.** shows the time frame of a sorting experiment signal with the corresponding reslice of the outlets showing that only the tartrazine droplets enter the sorted outlet channel, and the water drops flow down the waste outlet. Due to the frame rate of 8000fps and high droplet speed the edges of the droplets in the reslice have a lower resolution and appear blurred, as indicated by the yellow circle which actually shows a single droplet. Here we show the signal and video reslice between 110 and 115ms of the 1s signal and video saved simultaneously.

Conclusion

Here we present an acoustic activated absorbance droplet sorter with integrated optic fibres and tapered IDT. Using the AcAADS device we can sort label free droplets and at kHz sorting rates (reaching 2.5 kHz). For higher drop-rates higher powers might need to be applied for successful sorting as a longer acoustic pulse length can influence neighbouring droplets. Our chip assembly and holder make the optic fibres as well as the IDT reusable since the PDMS micro-channels are mechanically sealed onto the substrate and not bonded. Optofluidic components can be integrated to increase the absorbance detection sensitivity as shown in Hengoju *et al.* [4].

Acknowledgment

References

[1] J.C. Baret, O.J. Miller, V. Taly, M. Ryckelynck, A. El-Harrak, L. Frenz, C. Rick, M.L. Samuels, J.B. Hutchison, J. J. Agresti, D.R. Link, D.A. Weitz and A.D. Griffiths. Lab on a Chip **9**, 1850-1858 (2009).
[2] L. Schmid, D.A.Weitz and T. Franke. Lab on a Chip **19**, 3710-3718 (2014).
[3] T. Franke, S. Braunmüller, L. Schmid, A. Wixforth and D. A. Weitz. Lab on a Chip **10**, 789-794 (2010).
[4] S. Hengoju, S. Wohlfeil, A. S. Munser, S. Boehme, E. Beckert, O. Shvydkiv, M. Tovar, M. Roth and M. A. Rosenbaum. Biomicrofluidics **14**, 2 024109 (2020).
[5] R. Zhong, S. Yang, G. S. Ugolini, T. Naquin, J. Zhang, K. Yang, J. Xia, T. Konry, T.J. Huang. Small ,**17** (46), 2103848 (2021).
[6] F. Gielen, R. Hours, S. Emond, M. Fischlechner, U. Schell and F. Hollfelder. PNAS **113** (2016).
[7] T.A. Duncombe, A. Ponti, F.P. Seebeck, and P.S. Dittrich. Anal. Chem. **93**, 38, 13008–13013 (2021).

Acoustic bubble for spheroid trapping, rotation, and culture: a tumor-on-a-chip platform (ABSTRACT platform)

Yuan Gao[1,2], Mengren Wu[1], Qiyue Luan[3], Ian Papautsky[3] and Jie Xu[1]

[1]Department of Mechanical and Industrial Engineering, University of Illinois Chicago, Chicago, USA
E-mail: ygao51@uic.edu, URL: https://xu.uic.edu/
[2]Department of Mechanical Engineering, University of Memphis, Memphis, USA
[3]Department of Biomedical Engineering, University of Illinois Chicago, Chicago, USA

Introduction

In recent years, microfluidics has attracted great interest in isolation and downstream analysis of CTCs on the microscale because of their low sample volume requirements, high controllability and biocompatibility. An effective "all-in-one" approach to trapping, release and culture CTCs is highly sought after, which would greatly facilitate analysis like mutation profiling and drug screening and provide critical information for personalized medicine for cancer treatment [1]. In this work, we present a CTC-processing system: acoustic bubble for spheroid trapping, rotation, and culture: a tumor-on-a-chip platform (ABSTRACT). The platform consists of a main channel, several parallel sub-microchannels with microcavities and culture chambers. The microcavity is designed to trap a bubble with desired shape at the entrance of the sub-microchannel. Under the acoustic actuation, the trapped bubble oscillates and creates a secondary radiation force to trap and rotate CTCs at a desired location. By controlling the acoustic bubble, CTCs can be continuously trapped from the blood flow, rotated to form a spheroid, and released to the microchamber for culture. We systematically investigated the effects of device geometry, flow parameters, and input voltage on trapping of CTCs to optimize the performance. Additionally, the successful on-chip spheroid culture demonstrates the biocompatibility and the simplicity of this platform. Besides simplifying conventional complex CTC processing procedures, this ABSTRACT platform also shows great potential for downstream analysis of tumor cells, such as monitoring the progression of metastasis and personalized drug testing.

Working mechanism of the ABSTRACT platform

A schematic illustration and an experimental demonstration of the acoustic bubble-based tumor-on-a-chip platform for trapping, rotation and culture of CTC spheroids are shown in Fig 1 and Fig 2. This ABSTRACT platform consists of a predesigned microchannel with a cavity structure and a piezoelectric transducer bonded to a glass substrate. The microchannel is filled with air before the liquid injection. When the liquid flows through the microchannel, the bubble is passively formed in the pre-designed sidewall cavity structure due to the surface tension and contact line pinning at the edge of the cavity. The piezoelectric transducer can induce an acoustic field to actuate the bubble when an input voltage is applied. In a low-frequency acoustic field (23–28 kHz), the trapped air bubbles are actuated and induce two important phenomena – microstreaming flow induced drag force and secondary radiation force (SRF). Under the action of these two forces, CTCs are trapped on the bubble surface and separated from blood flow due to the difference in size and density. Besides trapping CTCs, the acoustic bubble also generates rotational motion for CTCs on its surface. With the help of the rotational motion, the CTCs aggregate and form a CTC spheroid. The size of the spheroid then increases with an increasing number of trapped CTCs. When the spheroid reaches the desired size, it is released to the culture chamber for on-chip spheroid culture by turning off the acoustic field. During the culture process, the nutrient is delivered from the main channel to the chamber by diffusion.
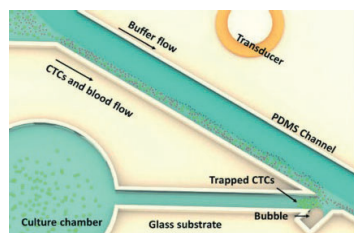

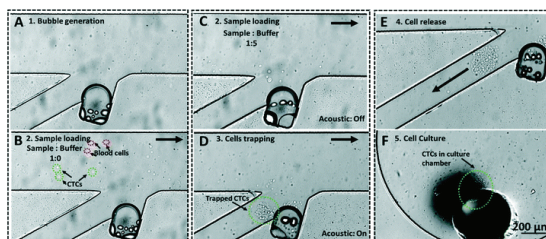**Figure 1.** Schematic illustration of the ABSTRACT platform

Figure 2. Experimental demonstration of CTC-processing in the ABSTRACT platform

Result and discussion

To improve the CTCs trapping performance in the ABSTRACT platform, we optimized the platform design by systematically comparing several parameters with a set of experiments, including the geometry of the cavity structure, sample distance from the wall, flow rate of the spiked blood sample as well as input voltage on the piezoelectric transducer. These parameters are expected to impact the trapping efficiency.

Theoretically, the magnitude of the secondary radiation force is strongly related to the distance between the bubble and the cell. Specifically, the largest secondary radiation force experienced by cells is estimated to be located at a fixed distance ($d \sim r_b + r$) away from the bubble surface [2]. This theoretical estimation is supportive of our experimental findings, which show that more CTCs are likely to be trapped when they close to the side of the wall where the bubble is located (lower wall). Therefore, we divided the channel (x-y plane) into six equal parts (w1-w6) along the y-axis for measuring the trapping efficiency (Fig. 2A). The measured result shows that the trapping efficiency of CTCs decreases when the distance increases. Since the trapping location of CTCs depends on the shape of the bubble, the cavity geometry is a critical parameter to determine the trapping efficiency of CTCs. To identify the optimal trapping efficiency, we designed and tested five devices with different angled cavity structures (D1-D5, θ = 90°, 120°, 45°, 30°, 135°). After measuring and comparing the average trapping efficiency, we found D4 has the highest trapping efficiency among five devices, which is probably due to the fact that the trapping location is somewhat inside the sub-channel and CTCs are easier to be trapped because of the lower flow speed. To enhance the trapping efficiency, we also investigated the effect of different sheath flow ratios at the same total flow rate (2 μl min⁻¹). Fig. 2B shows the result of trapping efficiency with respect to the sheath flow ratio. At the flow ratio of 1:5, the trapping efficiency reaches 92%, while the trapping efficiency is 43% and 25% at the 1:1 and 1:0 flow ratio, respectively. Therefore, we conclude that the trapping efficiency increases by increasing the sheath flow ratio. Fig. 2C shows that increasing the input voltage significantly improves the trapping efficiency from 1 to 5 Vpp, when the voltage increases from 5 Vpp to 6 Vpp, the trapping efficiency plateaued, and reaches the optimum value (~91%) in this device and to the threshold.
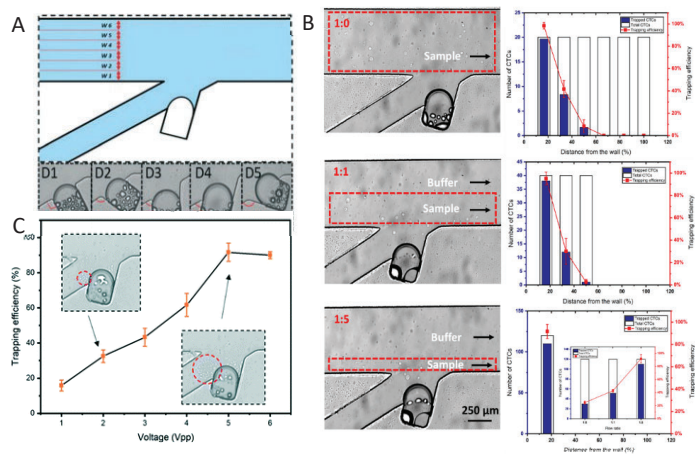

Figure 3. A. Six regions are equally divided for measuring the sample distance from the wall. B. Images of spiked blood samples with different sheath flow ratios and plot of CTCs trapping efficiency at different sheath flow ratios (1:0, 1:1, 1:5). C. CTCs trapping efficiency *versus* input voltage.

During the experiment, when the acoustic field was applied to generate microstreaming, the CTCs aggregated around the bubble surface and the spheroids were then collected to the culture chambers *via* the sub-channels by opening the culture chambers. To demonstrate the cell viability during the acoustic trapping and culture process, the live/dead cell assay was performed at the endpoint of spheroid culture. The result shows that the high cell viability was maintained after 3 days of culture. Based on the experimental results, our acoustic bubble-based tumor-on-a-chip platform demonstrates to be capable of forming and culturing viable CTC spheroids.

Conclusion

In summary, this ABSTRACT platform has been shown to successfully trap and rotate CTCs, as well as form and culture CTC spheroids on a single chip without bulky lab equipment and complex operating procedures. By controlling the acoustic bubble, we demonstrate the ability of this platform to selectively capture CTCs from the continuous blood flow based on their physical properties. We also explore the effect of geometry parameters, fluid parameters and input voltages on trapping CTCs to optimize the trapping efficiency of this platform. Moreover, we successfully show that the trapped CTCs can rapidly aggregate under acoustic actuation, as well as can release to the culture chamber to form the CTC spheroid through the sidewall sub-microchannel. More importantly, this platform has the capability to deliver culture medium to the CTC spheroids through the main channel by fluid diffusion for on-chip culture, which may be applied to test the drug effect on the CTC spheroids and contribute to developing personalized drug treatment in future.

References

[1] S. Sharma, R. Zhuang, M. Long, M. Pavlovic, Y. Kang, A. Ilyas and W. Asghar, Biotechnol. Adv **36**, 1063–1078 (2018).

[2] P. Rogers and A. Neild, Lab Chip **11**, 3710–3715 (2011).

Particle trapping using axial primary radiation force

Lokesh Malik[1], Amal Nath[1], Subhas Nandy[1], Thomas Laurell[2] and Ashis Kumar Sen[1]

[1]Department of Mechanical Engineering, Indian Institute of Technology Madras, Chennai, India
E-mail: lokeshiitmadras@gmail.com
[2]Department of Biomedical Engineering, Lund University, Lund, Sweden

Introduction

Development in bio-particle handling microfluidic systems is subject to advancements in efficient techniques of trapping them. Contactless and gentle trapping [1] platform offered by the ultrasonic standing wave technology makes it an attractive tool for widespread biotechnological applications [2]. In the present study, we numerically demonstrate and experimentally validate a contactless acoustofluidic trapping technique based on the standing bulk acoustic waves (BAW) generated inside a uniquely designed chamber here referred to as the 'shaped trap' that enables the particle to experience axial primary radiation force (PRF) along the flow direction as its main trapping force. Axial PRF opposing the flow (beyond the nodal plane) tends to immobilize the particle eventually getting it trapped at a unique off-node trapping site precisely controlled by extensive variations in particle size (D), flow rate (Q), and acoustic energy density (E_{ac}).

Theory and Experimental

For analysis, the competition between the axial PRF and drag is accounted by considering the acoustic energy and the viscous work scales which are estimated as $E_A \equiv E_{ac}k\phi D^3. D = E_{ac}k\phi D^4$ and $W_V \equiv \eta U D. D = \eta U D^2$, and are further non-dimensionalised (E_A^* and W_V^*) with the initial kinetic energy of the particle. The ratio of the acoustic energy to the viscous work is represented by the dimensionless parameter, $\beta = E_{ac}k\phi D^2/\eta U$, where k is the wave number, ϕ is the acoustic contrast factor, and η is the dynamic viscosity. Trapping is studied numerically across various configurations with different shapes – S, U; resonance modes – M1 (half-wave), M2 (full-wave); standing wave patterns – 1D, 2D; few of which are shown in figure 1d. We validate our simulation model using experiments on S-1D-M1 chamber which is explained through figure 1a-c.
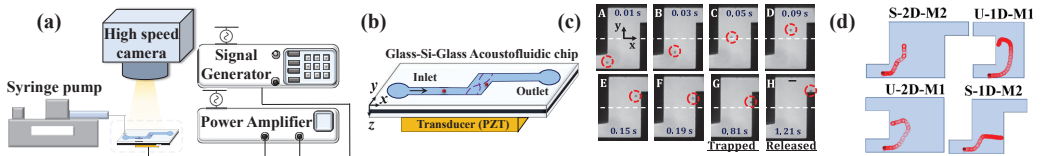

Figure 1: (a) Experimental setup (b) Acoustofluidic chip for S-1D-M1 (c) Experimental time-snaps showing trajectory (instants A to H) of 25 μm particle (circled in red) inside S-1D-M1 chamber. Acoustics is ON from instant A to G, and is off at instant H. Flow is from left to right. White dashed lines represent the pressure nodal plane. Scale bar is 100 μm. (d) Typical particle trajectories are shown in few other trap configurations as labeled in the figure.

Results

The trapping and non-trapping regimes are generalized in terms of the dimensionless parameters, E_A^* and W_V^* as shown in figure 2a. The simulation data pertains to S,U-1D-M1 configurations, as indicated in Fig. 1 for a range of particle sizes, flow rates, and acoustic energy densities, compares well with the experimental data pertaining to S-1D-M1 configuration. $\beta_{cr} = 4$, the critical ratio is the slope of the demarcating line between the two regimes. Hence, trapping for $\beta \geq 4$, and non-trapping for $\beta < 4$, is observed for the S,U-1D-M1 cases. Similarly, for the case of S,U-1D-M2, S,U-2D-M1, and U-2D-M2, a similar regime study reveals $\beta_{cr} \approx 3.5$, 8.5, and 29, respectively as shown in figure 2b in the form of dashed vertical lines. The location of the trapped particle is characterised using y_{TL}^*, which is distance of the trapping site from the nodal plane, non-dimensionalised with the distance from the nodal plane to the location where A-PRF is maximum (i.e. 1/4th of the chamber width). Figure 2b shows a monotonic variation, $y_{TL}^* \sim \beta^{-c}$, where c is a positive constant. Also confirmed by the insets of figure 2b, at higher and lower values of β, acoustics and flow dominates the trapping process, respectively and for the case of $\beta \geq \beta_{cr}$, the competing effects decide
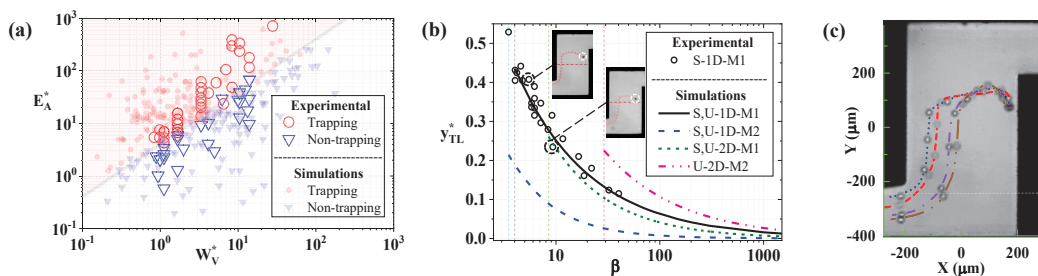
Figure 2: (a) Regime plot showing trapping and non-trapping regimes (b) Characterization of trapping location (c) Effect of particle's initial streamline on the trajectory and trapping location of the particle.

the exact trapping location of the particle. We study the effect of the initial streamline of the particle on particle trajectory and trapping location. As shown in figure 2c, an overlayed image from various experimental data sets shows that although the initial streamline (four different streamlines are compared) affects the trajectory of the particle but eventually leads to the same trapping location because of the fact that the position of zero net force (balance of acoustic and drag force) in the chamber remains unchanged irrespective of the initial streamline of the particle.

Discussion

Previously reported traditional BAW microfluidic trapping platforms utilizing the L-PRF as the main retention force, measured the maximum retention force in the range $0.002 - 1$ nN for a single particle in the size range of 10 - 12 μm operating at a frequency range of 2.5 - 12.4 MHz. Taking advantage of high lateral gradients in the velocity field present over the transducer area, these trapping systems are generally designed to trap particle clusters laterally against the flow. The increased dominance of drag force over L-PRF renders trapping of single-particle difficult as compared to a cluster, which could be attributed to a more exposed surface area to volume ratio [4] in case of a single particle and the inferior size dependency of the retention force, L-PRF ($\sim a^2$) [5,6] as compared to the A-PRF ($\sim a^3$). Based on the experimental findings, the current work utilizing the A-PRF as the main retention force shows a significant increase in the maximum retention force. For a single particle in the size range $15 - 36$ μm for a frequency range of $1 - 2$ MHz, the retention force is found to be of the order 1 nN $-$ 10 nN. Moreover, the maximum retention force for a particle size as low as 12 μm, trapped at a fluid velocity of 12 mm/s with a resonating frequency of 13 MHz, is found to be 3.25 nN, which is at least one order of magnitude higher for similar parameters as reported in the literature. Stronger size dependency of A-PRF is found to produce a retention force in the range 2.5 to 20 nN for larger particle size ($\sim 25 - 36$ μm) even at low frequency (1-3 MHz) operation. Furthermore, with suitable design modifications such as better chamber design and higher frequency operation utilizing multinodal resonance, an improved device could yield an even more promising setup for trapping single particles or high-efficiency particle cluster traps.

Conclusion

The present study [3] provides a fundamental understanding of acoustic trapping of particles in shaped traps. It also offers methods to control the final trapping location through the operating parameters, creating a zone of trapping sites. Our ultrasonic trapping setup highlights the importance of utilizing the A-PRF as the main retention force (which originates from the more dominant potential energy gradients present away from the pressure nodal plane) against the flow unlike the conventional S-BAW trapping systems relying on lateral [2, 7] acoustic energy density gradient (which relies on the smaller lateral acoustic velocity field gradients effective only near the pressure nodal plane), consequently achieving an improved control over the trapping sites and higher retention force which could potentially bring in significant throughput advancements to the existing bioparticle trapping technology, thus opening up new avenues for biochemical applications.

References

[1] T. Laurell, F. Petersson, and A. Nilsson. Chem. Soc. Rev., **36**, 3, 492–506 (2007)
[2] B. Hammarström, T. Laurell, and J. Nilsson. Lab Chip **12**, 21,4296–4304 (2012)
[3] L. Malik, A. Nath, S. Nandy, T. Laurell, and A. K. Sen. Phys. Rev. E, **105**, 035103 (2022)
[4] S. M. Woodside, B. D. Bowen, and J. M. Piret. AIChE Journal **43**, 1727 (1997)
[5] M. Evander and J. Nilsson. Lab on a Chip **12**, 4667 (2012)
[6] M. Groschl. Acustica **84**, 432 (1998)
[7] B. Hammarström, M. Evander, H. Barbeau, M. Bruzelius, J. Larsson, T. Laurell, J. Nilsson. Lab Chip, **10**, 2251-2257 (2010)

Short ultrasonic pulses for acoustic tweezers

Qing Wang[1], Zhixiong Gong[2], Shuhan Chen[1], Jia Zhou[1], Michael Baudoin[2,3], <u>Antoine Riaud</u>[1]

[1]. State Key Laboratory of ASIC and System, School of Microelectronics, Fudan University, Shanghai 200433, China
E-mail: antoine_riaud@fudan.edu.cn
[2] Univ. Lille, CNRS, Centrale Lille, Univ. Polytechnique Hauts-de-France, UMR 8520, IEMN, F59000 Lille, France
[3] Institut Universitaire de France, 1 rue Descartes, 75005 Paris, France

Introduction

The vast majority of acoustic tweezers use monochromatic waves to manipulate small objects. While this simplifies their design, the restriction to a single frequency limits the resolution of the tweezers as well as the type of acoustic sources that can be used. In order to go beyond the monochromatic regime, a theoretical description of the acoustic radiation pressure for complex pulses is required.

Generalization of the Gor'kov theory to small spheres

We propose a generalization of the Gor'kov's theory [1] for small spheres irradiated by a wave of finite duration such as an acoustic pulse. By finite duration, we require all the wave quantities $\tilde{x}$ to satisfy the condition $\tilde{x}(-\tau/2, \mathbf{r}) = \tilde{x}(\tau/2, \mathbf{r})$, where the origin of time is freely chosen and with $\mathbf{r}$ the position vector of the particle (Fig. 1.a). This finite-duration condition allows neglecting the details of the dynamics and focus instead on the momentum exchanged between the incident wave, the particle and scattered wave. The other key assumptions are that the incident wave vibration velocity $\tilde{v}_{in}$ is small ($\tilde{v}_{in} \ll c_0$), that the particle radius a is much smaller than the acoustic wavelength, and that it does not resonate or store acoustic energy over long periods of time.

Given an incident acoustic wave with pressure and velocity fields $\tilde{p}_{in}(t, \mathbf{r})$ and $\tilde{v}_{in}(t, \mathbf{r})$, respectively, the acoustic radiation force acting on the particle is given by $\mathcal{F} = -\frac{4\pi a^3}{3}\left[\left\langle \frac{1}{\rho_0 c_0^2}\tilde{p}_m\nabla\tilde{p}_{in}\right\rangle - \left\langle\rho_0\tilde{\mathbf{v}}_d\cdot\nabla\tilde{\mathbf{v}}_{in}\right\rangle\right]$, where $\tilde{p}_m$ ($\tilde{\mathbf{v}}_d$) is the monopolar pressure (dipolar velocity) contribution to the scattered field. When the particle is much larger than the visco-acoustic and thermo-acoustic boundary layers, the scattered field is simply proportional to the incident field up to two constant scattering coefficients f_1 and f_2, which yields:

$$\mathcal{F} = -\frac{4\pi a^3}{3}\nabla\langle\mathcal{U}\rangle \quad \text{with the dynamic Gor'kov potential:} \quad \mathcal{U} = \frac{f_1}{2\rho_0 c_0^2}\tilde{p}_{in}^2 - \frac{3\rho_0 f_2}{4}\tilde{\mathbf{v}}_{in}^2. \tag{1}$$
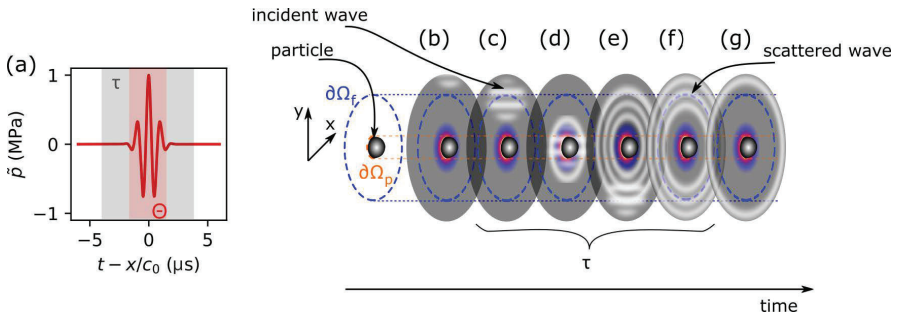

Figure 1: (a) A Gaussian acoustic pulse. The gray region indicates the pulse duration τ, which can be chosen arbitrarily larger than the pulse width θ (in red).(b)-(g) time-lapse of the diffraction of an acoustic wave by a wave packet. At (b-c), a wave packet enters Ω and (d,e,f) generates a scattered field (shown as circular waves) that(g) eventually exits Ω. Neglecting the particle motion, the state of Ω is identical in steps (b) and (g) which allows defining τ as the duration between these two steps.
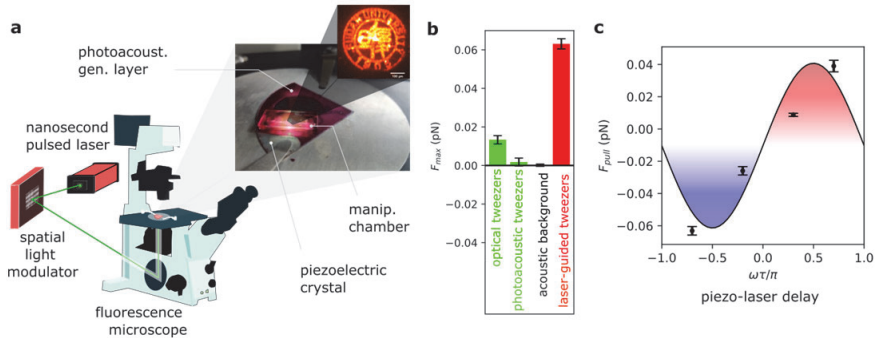
Figure 2: (a) Laser-guided acoustic tweezers: a piezoelectric transducer coated with a photoelastic film is excited by a synchronized electrical signal and a laser pulse. The image formed by the laser pulse can be adjusted with high spatial resolution using a holographic microscopy system. (b) comparison of forces generated by different mechanisms. The force of the tweezers is amplified 30 times compared to the laser alone. (c) reversal of the acoustic radiation force by adjusting the delay between optical and electrical excitations.

Amplification of the acoustic radiation force by field hybridization

Thanks to this generalized theory, the photoacoustic tweezers technology [2] can be improved to exceed the efficiency of optical tweezers. Similar to holographic optical tweezers, photoacoustic tweezers can use spatially-modulated laser beams to create microscale acoustic fields with a megapixel resolution and a high refreshing rate above 60 frames per second, but their low efficiency erases the advantage of using acoustic radiation pressure instead of the optical one. Instead, we propose an amplification mechanism wherein the radiation force of a weak field (L) is amplified by interference with a strong field (Z). In our experiments, the L- and Z-fields are generated by the photoacoustic conversion of a laser pulse and the piezoelectric conversion of an electric burst, respectively. When such interference occurs, the Gor'kov potential (Eq. (1)) reads: $\mathcal{U} = \mathcal{U}^{(ZZ)} + \mathcal{U}^{(ZL)} + \mathcal{U}^{(LL)}$. Because $\tilde{p}^{(L)} \ll \tilde{p}^{(Z)}$, the photoacoustic potential $\mathcal{U}^{(LL)}$ is negligible. Choosing the Z-field as a plane wave $\tilde{p}^{(Z)} = A^{(Z)} \cos(k_z z + \omega\tau - \omega t)$ traveling along the normal to the manipulation plane with τ the delay between the excitation of the laser (L) and the piezoelectric source (Z), we check that $\mathcal{U}^{(ZZ)}$ is a constant and therefore yields no force up to $O(a^6)$. Therefore, only the hybrid potential $\mathcal{U}^{(ZL)}$ remains. After some trigonometry:

$$\mathcal{U}^{(ZL)} = A^{(Z)} \left[\cos(\omega\tau) A_{\cos}^{(L)}(\mathbf{r}) - \sin(\omega\tau) A_{\sin}^{(L)}(\mathbf{r}) \right] \quad \text{with:} \quad A_{\cos}^{(L)} = \left\langle \cos(k_z z - \omega t) \left(\frac{f_1 \tilde{p}^{(L)}(t)}{\rho_0 c_0{}^2} - \frac{3 f_2 \tilde{v}^{(L)}(t)}{2 c_0} \right) \right\rangle,$$

$$(2)$$

and $A_{\sin}^{(L)}$ analog to $A_{\cos}^{(L)}$ after substituting the cos function by a sin. In Eq. (2), the Z-field acts like a uniform gain for the radiation force of the (L)-field. We note that the hybrid potential is actually composed of two orthogonal components $A_{\cos}^{(L)}$ and $A_{\sin}^{(L)}$ that can be selected by adjusting the delay τ between the Z and L fields, and may even be reversed when $\omega\tau = \pi$.

Implementation of laser-guided acoustic tweezers

This amplification method is implemented experimentally (Fig. 2a). The tweezers is a bimodal transducer (inset) made of a piezoelectric crystal coated with a partially transparent photoacoustic generation layer. The laser light is projected onto a spatial light modulator and then shrunk to a millimetric footprint using a microscope objective. We measure that this system amplifies the radiation pressure of the photoacoustic effect of the laser by a factor of 30 (Fig. 2b), and verify the inversion of the sign of the radiation force by modulating τ (Fig. 2c).

Conclusion

These laser-guided tweezers combine the speed and resolution of optical tweezers with 6 times the force, and in a novel way, the ability to switch between attractive and repulsive force.

[1] L. P. Gor'kov, *Doklady Akademii Nauk* (Russian Academy of Sciences, 1961), vol. 140, pp. 88–91.

[2] V. Zharov, T. Malinsky, R. Kurten, *Journal of Physics D: Applied Physics* **38**, 2662 (2005).

Dynamic patterning of microparticles with acoustic impulse control

Luke Cox[1], Anthony Croxford[1], and Bruce W Drinkwater[1]

[1]1Department of Mechanical Engineering, University of Bristol, Bristol, UK
E-mail:luke.cox@bristol.ac.uk, URL: https://www.researchgate.net/profile/Luke-Cox-8/research

Introduction
We present the use of impulse control of acoustic fields to create complex and precise particle patterns and then dynamically manipulate them. We show that the motion of a particle in an acoustic field depends on the applied impulse (i.e. the integral of the applied force over time) and three distinct regimes can be identified; low, high and intermediate. The high impulse regime is the well understood and widely used approach where the particle has sufficient time to reach the force equilibrium of the acoustic field before it is changed. This has been used to pattern particles by optimizing the sound field [1, 2], or by using single traps to move individual particles into a pattern [3, 4]. In the low impulse regime the particle experiences a force field equal to the time weighted average of all the constituent fields. Previously two fields have been combined to obtain new functions such as arbitrarily positioning particle flow location within a channel [5] or stably levitating non-spherical objects [6]. We demonstrate that many fields can be combined to produce more complex user-defined patterns. The intermediate regime is between these two and enables more localized manipulation of particles. By combining the advantages of each of these regimes we create high contrast, complex particle patterns which can be dynamically moved and reconfigured.

Impulse Regimes
To understand the behaviour of particles subjected to an impulse we first conduct simulations using a dynamic time-domain model of the impact of using multiple acoustic fields, each applied for a short duration of time. Consider the scenario shown in Figure 1a in which the pressure field is a simple 1D standing wave with two phase-shifted states where each state is applied for an equal time period, Δt_s. A small, isolated particle in either of these standing wave fields will experience an acoustic radiation force field predicted by the Gor'kov potential and shown in Figure 1b. The range of the particle's motion over $100\Delta t_s$ is plotted on the y-axis of Figure 1c. The x-axis plots variation the applied impulse, i.e. $I_{app} = \max(\mathbf{F_{ac}})\Delta t_s$. This definition is chosen as the maximum acoustic force of each state and the time it is applied for are the two control variables that can be directly set by the user. Figure 1c shows variations in both the switching time, Δt_s, (along the x-axis) and the maximum force (different lines). As can be seen, the lines collapse onto a single line demonstrating that applied impulse is a variable which produces a consistent effect regardless of which component is altered. The different motion ranges also indicate the different impulse regimes, as labelled. In the high impulse regime the particle moves between the two equilbiria defined by the component fields while in the low impulse regime it stays at the effective force field sum of the two fields. In the intermediate regime it travels some, but not all, of the distance between the two.
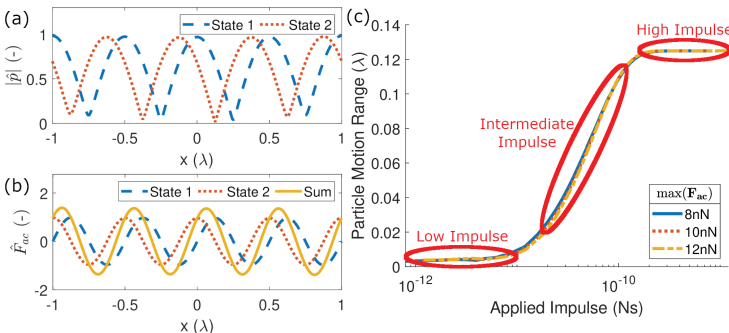

Figure 1: (a) The two normalised absolute 1D pressure of the standing wave fields, $|\hat{p}|$, with one source's phase output offset from the other by $\frac{\pi}{2}$. (b) The normalised acoustic forces, $\hat{F}_{ac}$, generated by the pressure fields in (a) and the sum of these two fields. (c) The variation in particle motion per cycle vs the applied impulse, I_{app}. The different lines indicate different maximum $\mathbf{F_{ac}}$ values which the force field was normalised to and each force was applied with a Δt_s range from 0.1ms up to 100ms.

Figure 2: The forming of a line using 10 twin traps in the low impulse regime. (a) shows the simulated net force field and (b) shows the equivalent experimental particle pattern. (c) shows the experimental results after the application of a clearing and agglomeration sequence. The blue scale bar is 1mm.
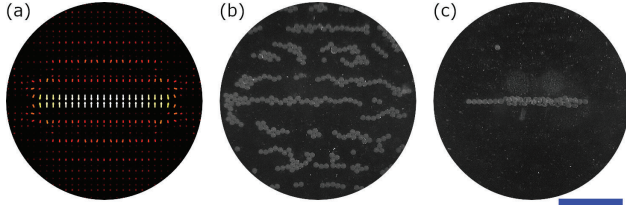
Low impulse patterning and particle clearing

Using the low impulse approach allows us to create complex patterns from the force field summation of multiple simple component pressure fields. In Figure 2 we use a collection of twin traps to make a line of particles. Figure 2a shows the net force field of a 2mm long line formed of 10 twin traps in a 2.33MHz 64-element circular array (see [3] for array). This allows us to create localised force fields and particle patterns, as shown in Figure 2b. A further advantage of our technique is we can combine the patterning with a selection of clearing and agglomeration tools in the high and intermediate impulse regimes to remove extra particles. For example, using progressively increasing order Bessel function shaped fields in the high impulse regime allows us to push excess particles away from the centre, leaving the area around the shape clear. The inverse allows us to create an agglomeration of particles near the centre. We also use intermediate impulse 'sweeping' of a zeroth order Bessel function shaped field to precisely clear a defined area of particles. Using these techniques as a 'toolbox' to remove excess particles allows us to create high contrast patterns like that shown in Figure 2c.

Further Shape Complexity

This technique also allows greater complexity in the fields formed. Figure 3a demonstrates an 'L' shape of particles. This was made by gradually deforming a line of the type shown in Figure 2c. Figure 3b shows a hollow circle patterned by 5th and 9th order Bessel function fields (the order of the Bessel functions determining the circle radius). It was cleared of excess particles using various increasing and decreasing orders of Bessel functions. Finally Figure 3c shows a simulated 'A' pattern, formed and cleared in an ideal device using a variety of 'tools'.
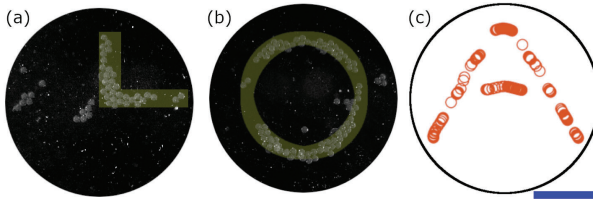

Figure 3: Example particle patterns. (a) shows a 'L' shape made by deforming a cleared line. (b) shows a circle and (c) shows a simulated 'A' shape on an ideal version of this device. Both (b) and (c) are formed directly from a random particle distribution. The blue scale bar is 1mm.

Conclusion

We have shown that the motion of particles under changing acoustic force fields is dependent on the applied impulse. By harnessing the different impulse regimes we can create complex, high fidelity patterns which can be dynamically moved and manipulated.

This abstract is adapted from an open access paper by the authors first published in Scientific Advances [7].

References

[1] K. Melde, A. G. Mark, T. Qiu, and P. Fischer. Holograms for acoustics. *Nature*, 537:518–522, 2016.

[2] J. Greenhall, F. Guevara Vasquez, and B. Raeymaekers. Ultrasound directed self-assembly of user-specified patterns of nanoparticles dispersed in a fluid medium. *Appl. Phys. Lett.*, 108(10310):3, 2016.

[3] Courtney Crp, Demore Cem, H. Wu, A. Grinenko, P. D. Wilcox, S. Cochran, and Drinkwater BW. Independent trapping and manipulation of microparticles using dexterous acoustic tweezers. *Appl. Phys. Lett.*, 104(15410):3, 2014.

[4] A. Riaud, M. Baudoin, O. Bou Matar, L. Becerra, and Thomas J-L. Selective manipulation of microscopic particles with precursor swirling rayleigh waves. *Phys. Rev. Applied*, 7, 2017.

[5] P. Glynne-Jones, R. J. Boltryk, N. R. Harris, Cranny Awj, and M. Hill. Mode-switching: A new technique for electronically varying the agglomeration position in an acoustic particle manipulator. *Ultrasonics*, 50:68–75, 2010.

[6] L. Cox, A. Croxford, B. W. Drinkwater, and A. Marzo. Acoustic lock: Position and orientation trapping of non-spherical sub-wavelength particles in mid-air using a single-axis acoustic levitator. *Appl. Phys. Lett.*, 113:054101, 2018.

[7] Luke Cox, Anthony Croxford, and Bruce W Drinkwater. Dynamic patterning of microparticles with acoustic impulse control. *Scientific Reports*, 12(1):1–14, 2022.

High-performance bulk-wave-acoustophoresis devices driven by lead-free piezoelectric materials

Wei Qiu[1]

[1]Department of Biomedical Engineering, Lund University, Lund, Sweden
E-mail: wei.qiu@bme.lth.se, http://bme.lth.se/research-pages/nanobiotechnology-and-lab-on-a-chip/

Introduction

In bulk-wave-acoustophoresis devices, the acoustic energy can be well confined in the microchannel due to the mismatch of the acoustic impedance of the liquid in the channel and the surrounding solids. High acoustic energy density as well as high throughput can therefore be achieved with low input power when the ideal vibration mode is excited [1]. However, bulk-wave devices are typically driven by lead zirconate titanate (PZT) transducers which contains a high content of lead ($\sim 60\%$ in mass). The lead-containing materials cause severe environmental issues, hence their usage in electronic devices and electrical equipment has been restricted by EU since 2003 [2]. The development of lead-free piezoelectric materials has been boosted since the seminal work by Saito et al. [3], and their piezoelectric properties have now become comparable to those of PZT. In this work, the performance of bulk-wave-acoustophoresis devices driven by lead-free piezoelectric materials is investigated and compared with the devices driven by hard PZT.

Materials and methods

Acoustophoresis devices are operated under resonance conditions, thus high Q-factor and low loss are required for the piezoelectric materials, which is known as the hard-type piezoelectric materials. Here, we select $(\mathrm{Bi, Na})\mathrm{TiO_3}$-$\mathrm{BaTiO_3}$-$(\mathrm{Bi, Na})(\mathrm{Mn, Nb})\mathrm{O_3}$ (BNT-BT-BNMN) [4], which has been commercialized by Honda Electronics. The hard PZT for comparison is the Pz26 from Ferroperm Piezoceramics. The properties of both materials are summarized in Table 1.

For each type of piezoelectric material, three glass chips with the same outer and channel dimensions were tested. The devices were actuated by mounting the transducers to the side, as shown in Fig. 1, which is able to excite the ideal vibration mode and hence achieve high acoustic energy density in the channel [1]. Both PZT and BNT-BT-BNMN transducers have the same length $L_\mathrm{P} = 25$ mm and width $W_\mathrm{P} = 2$ mm. Due to the different frequency constant in the thickness direction, the thickness of the transducer T_P was adjusted to 1 mm (PZT) and 1.2 mm (BNT-BT-BNMN) to match the resonance frequency (~ 2 MHz) of a half-wave standing-wave field in the channel width (y) direction.

Results and discussion

The resonance frequency of each chip was found by flowing 5 µm-diameter polystyrene particles in milli-Q through the channel while the sound field was turned on and the normalized particle-focusing

Table 1: Material properties of BNT-BT-BNMN from Honda Electronics and PZT (Pz26) from Ferroperm Piezoceramics. The obtained material properties from the manufacturers include dielectric constant $\epsilon_{33}^\mathrm{T}/\epsilon_0$, electromechanical coupling factor k_t, piezoelectric charge constants d_{33}, mechanical Q-factor Q_m, dissipation factor $\tan\delta$, and Curie temperature T_C.

	BNT-BT-BNMN	PZT
$\epsilon_{33}^\mathrm{T}/\epsilon_0$	520	1300
k_t	0.41	0.47
d_{33} (PC/N)	110	300
Q_m	500	> 1000
$\tan\delta$ (%)	0.66	0.3
T_C (℃)	260	330

Figure 1: Sketch of the acoustophoresis glass chips (light gray) with a dimension of $70 \times 3 \times 1.1$ mm^3. The long-straight microchannel (light blue) has a dimension of 45×0.403 (at its top) $\times 0.133$ mm^3. The piezoelectric transducer (brown) was mounted to the side of the chip. The half-wave standing-wave field is indicated by the dashed magenta lines.
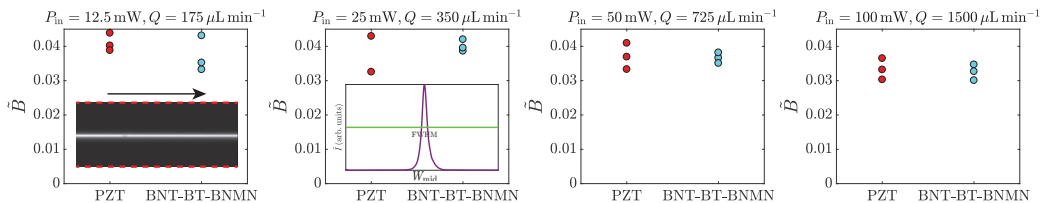
Figure 2: Qualitative comparison of the chip performance using PZT (red) and BNT-BT-BNMN (cyan) transducers under four different conditions, indicated by the normalized particle-focusing bandwidth $\tilde{B}$. The insets in the two left plots are the stacked particle-focusing image and its normalized intensity profile $\tilde{I}$ (purple), which corresponds to $\tilde{B} = 0.033$. Three chips were tested using the same transducer material.
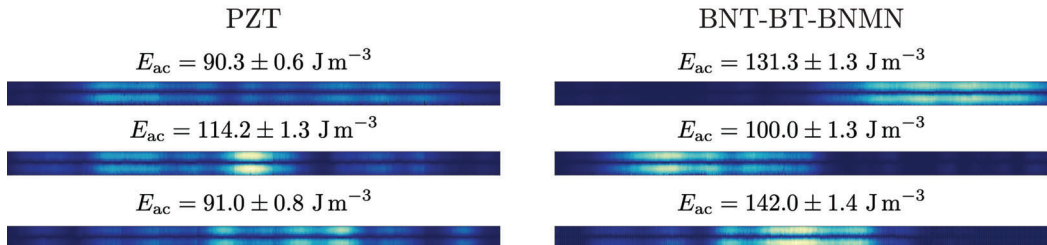

Figure 3: Confocal micro-PIV measurements of the averaged energy density E_{ac} for the devices driven by PZT and BNT-BT-BNMN transducers under 12.5 mW input power P_{in} along the 25 mm-long region where the transducer locates. The color plot shows the particle focusing velocity from 0 (black) to 2.1 mm s^{-1} (white). The width dimension is expanded by a factor of three for better visibility.

bandwidth $\tilde{B} = \text{FWHM}/W_{mid}$ was measured, where FWHM and W_{mid} are the full width at half maxima of the particle intensity profile and the channel width at its mid-height, respectively. The device performance was first qualitatively compared by measuring $\tilde{B}$ under four different combinations of flow rate Q and input power P_{in}. It is found that the devices driven by PZT and BNT-BT-BNMN show similar $\tilde{B}$ under each driving condition, see Fig. 2, indicating similar averaged acoustic energy density E_{ac} and energy conversion efficiency. The devices were driven efficiently by side actuation [1], hence high throughput can be achieved under low P_{in}. Only driven by the function generator (the maximum P_{in} supplied to each device varies due to the different electrical impedance, but around 200 mW or slightly less), it is possible to reach the $\tilde{B} < 0.04$ at $Q = 3100\,\mu\text{L min}^{-1}$ for all the six devices.

The E_{ac} was then quantitatively investigated within the whole actuation zone for the devices driven by PZT and BNT-BT-BNMN transducers at $P_{in} = 12.5\,\text{mW}$ under the stop-flow condition by measuring the amplitude of particle-focusing velocity using confocal micro-particle image velocimetry (micro-PIV), see Fig. 3. Surprisingly, the E_{ac} achieved using BNT-BT-BNMN was even slightly higher than that obtained using PZT, despite the piezoelectric properties of BNT-BT-BNMN are slightly worse than those of PZT. Though experimental variations including the gluing of the transducers are present, the results clearly demonstrate that similar device performance can be achieved using lead-free piezoelectric materials

Conclusion

In this work, we show strong experimental evidence that high-performance acoustophoresis devices can be achieved using lead-free piezoelectric materials. The obtained acoustic energy density, energy conversion efficiency, and throughput are similar to the devices driven by hard PZT transducers. We are currently also testing the devices driven by $(K, Na)NbO_3$-based piezoelectric materials, and the results will be provided in the conference.

References

[1] W. Qiu, T. Baasch, and T. Laurell. Phys. Rev. Appl. **17**, 044043 (2022).
[2] EU-Directive 2002/95/EC. Off. J. Eur. Union **46**, 19-37 (2003).
[3] Y. Saito, H. Takao, T. Tani, T. Nonoyama, K. Takatori, T. Homma, T. Nagaya, and M. Nakamura. Nature **432**, 84-87 (2004).
[4] T. Tou, Y. Hamaguti, Y. Maida, H. Yamamori, K. Takahashi, and Y. Terashima. Jpn. J. Appl. Phys. **48**, 07GM03 (2009).

Sheathless Microflow Cytometry Using Gigahertz Acoustic Streaming

Yaping Wang[1], Wei Wei[1], Yang Yang[1], Wei Pang[1], Xuexin Duan[1]

School of Precision Instrument and Opto-electronics Engineering, Tianjin University, Tianjin, China
E-mail: xduan@tju.edu.cn, URL: http://www.tjumbios.com/

Introduction

Flow cytometry is a high-throughput, multi-parameter instrument for single-cell analysis, which is widely used in life sciences and clinical diagnostics [1]. In the past decade, the rapid development of microfluidic technology promotes the design of flow cytometry to be more tiny, integrated, and inexpensive, namely microfluidic cytometer. It is an important technique for microflow cytometry to focus the particles in the center of the microchannel which can ensure each particle passes through the laser spot one by one achieving consistent optical detection. To data, a variety of techniques have been developed to focus particles. Among them, acoustic focusing has attracted much attention due to its advantages of gentle and sheathless. BAWs and SAWs are the most commonly used acoustic focusing methods [2,3]. However, they all only utilize acoustic radiation to manipulate particles, which has limits on the size of the particles, and it is difficult to achieve 3D focus in nanoscale particles. Recently, a new approach based on acoustic streaming has been developed, which manipulates particles without contact by coupling acoustic waves into fluid to produce acoustic streaming effect [4]. Compared to traditional acoustic-based strategies, acoustic streaming provides more dynamic conditions, and has high resolution biocompatibility on a large number of cells. In this work, we demonstrate a sheathless microflow cytometry for 3D focusing cells by a GHz bulk acoustic wave resonator (GBAW) and integrated it with a reflection confocal fluorescence detection system (RCF). The GBAW resonator captures particles in 3D vortex channels through acoustic streaming and acoustic radiation force and releases them sequentially in a fixed position downstream. The RCF system enables detection with high sensitivity and accurate counting of particles. Microflow cytometry was successfully verified using this system with a coefficient of variation (CV) of 8.1% with standard calibration beads. Its focusing capability has great potential in manipulating biological particles.

References

[1] R.J. Yang, L.M. Fu, H.H. Hou, Review and perspectives on microfluidic flow cytometers, Sens. Actuators B Chem. 266, 26–45 (2018).
[2] Wang C, Ma Y, Chen Z, et al. Sheathless microflow cytometer utilizing two bulk standing acoustic waves[J]. Cytometry Part A, 99(10): 987-998, 2021.
[3] Chen Y, Nawaz A A, Zhao Y, et al. Standing surface acoustic wave (SSAW)-based microfluidic cytometer[J]. Lab on a Chip, 14(5): 916-923. 2014.
[4] Duan X, Yang Y. Manipulation of Single Cells via a Stereo Acoustic Streaming Tunnel (SteAST)[J]. 2022.

Fluido-acoustics: Dynamic Multi-Slit Metamaterial Tuned using Liquid Droplets

Shubhi Bansal[1], Ryuji Hirayama[1] and Sriram Subramanian[1]

[1] Department of Computer science, University College London, United Kingdom
E-mail: shubhi.bansal@ucl.ac.uk, URL: https://sites.google.com/view/shubhi-bansal/home

Introduction

We report an experimental study of a novel active multi-slit acoustic metamaterial (MS-AMM) developed by integrating multiple slits with liquid droplets to manipulate the acoustic field. Each slit is tuned by moving a liquid droplet over it by using the electrowetting-on-dielectric technique. This enables an unexpected tunability, programmability, and reconfigurability to manipulate the output acoustic fields; thus embarking on the field of 'Fluido-acoustics'. Due to the high impedance property of the liquid-air interface, each droplet acts as an acoustic barrier which can tune the acoustic output on demand by leveraging its movement over the slit. We demonstrate the application of the proposed MS-AMM on the acoustic levitator by levitating a bead based on the output acoustic field. Here, we make the levitated bead change its path course (up and down) by blocking the transmitting sound field by covering the slits with liquid droplets. Acoustic wave engineering, including dynamic acoustic switching and continuous acoustic amplitude modulation in space and time, is achieved.

Background

The field of Acoustofluidics deals with moving and manipulating liquid droplets by applying surface acoustic waves (SAW) [1] and other acoustic forcing techniques [2]. However, vice versa, utilizing liquid actuation to manipulate the sound waves for applications like metamaterials has never been investigated. The proposed research embarks on this reverse field of 'Fluido-acoustics'.

Multi-slits metamaterials [3][4] have been proposed in the literature, but most of these designs are static and cannot be reconfigured, which limits their application. In this work, we leverage the use of a microfluidic actuation technique called electrowetting-on-dielectric [5] to implement novel tunable multiple slits-based acoustic metamaterials (MS-AMM).

Device

Each slit with a droplet is referred to as a meta-cell. The slits were fabricated by using a laser cutter. A micropipette was used to place a deionized water droplet (15–30 μL) on the open length of each slit to modulate the transmitting sound field. We used 150 V DC-voltage driving signal for moving the water droplet using patterned actuation electrodes on the side of the slit (Fig. 1A). Each meta-cell is fabricated by using a standard electrowetting device fabrication process (Fig. 1B) involving three steps— 1) Indium tin oxide (ITO) coated PET substrate; 2) Lithography to pattern ITO and subsequently etching patterned ITO using hydrochloric acid (HCl), to make actuation and grounding electrodes. Then, the photoresist is removed by dipping the device in acetone; 3) Coating SU8 dielectric and Teflon for the smooth electrowetting-on-dielectric operation of a moving droplet over the slit gap (see Fig. 1C).

The metamaterial consisted of 16 × 16 slits with each slit of dimension 4.5 mm × 1 mm × 1 mm on an ITO-coated PET substrate (Fig. 2A). The device concept is shown in Figs. 2B and 2C, where each tunable acoustic meta-cell consists of a moving liquid droplet to manipulate the incident sound field, and thereby, together the metamaterial can achieve any desired transmissive sound field pattern.
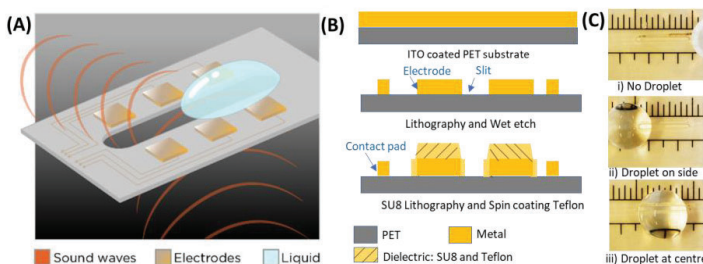

Figure 1: (A) Notion of an acoustic meta-cell consisting of a tunable slit modulated by a liquid droplet. Droplet motion on the tunable slit is achieved using the electrowetting-on-dielectric technique. (B) Process flow for the fabrication of a single acoustic meta-cell. (C) Snapshots of motion of water droplet (15 μL) at 150 V DC voltage over a slit of length 4.5 mm.
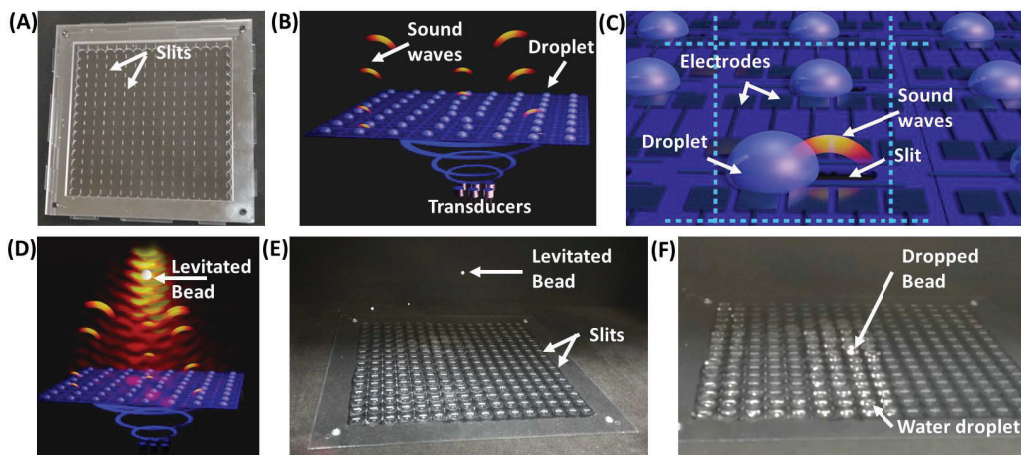
Figure 2: Dynamically programmable multi-slit acoustic metamaterial. (A) Photograph of a multi-slit metamaterial consisting of 16 x 16 slits. (B) Schematic illustration of the concept of acoustic metamaterial with multiple droplets, each controlled individually on multiple slits for acoustic field manipulation. (C) Zoomed-in view of each meta-cell of multi-slit metamaterial shown in Fig. 2B. (D) Schematic illustration of acoustic field focusing for levitation using multi-slit metamaterial. (E) Experimental image of levitating a bead without the presence of any liquid droplet. (F) An experimental image showing a fallen bead caused by covering the slits with water droplets to block the transmitting acoustic field.

Results and discussion

The metamaterial operates at 40 kHz, and a 16×16 transducer board is used as the acoustic source for providing the acoustic field. We show the application of tunable multi-slit acoustic metamaterial for dynamic levitation (Fig. 1D). Without any droplet, the acoustic field through the slits was targeted to create a twin trap (two focal points) to levitate a bead. The bead was successfully levitated using the source acoustic field modulation, as shown in Fig. 1E. When the droplet moves on the open slit, the liquid-air interface blocks sound due to a large impedance mismatch at the air-water interface, thereby modulating the transmitting sound field. To prove the same, we placed multiple liquid droplets (15–30 μL) to fully cover the slits, such that the transmitting sound amplitude was obstructed, and the levitated bead fell (Fig. 1F).

Conclusion

We design and develop a novel dynamically tunable multi-slit acoustic metamaterial by combining the functionalities of passive multi-slit metamaterials with programmable liquid droplets actuation through the electrowetting-on-dielectric technique. We utilize an air-liquid interface as a barrier on an open slit for the manipulation of the transmitted acoustic wave. Future research can deal with employing different shapes and orientations of slits for diverse applications like complex acoustic diffraction grating. The liquid's transparency allows for integrating both acoustic and optofluidic metamaterial designs together. Moreover, these meta-cells can be combined with Helmholtz resonators for automated liquid droplet-based neck width control, enabling tunable and programmable resonators. Thus, this work poses large scope for scientific advancement to enable next-generation tunable and programmable active acoustic metamaterials using Fluido-acoustics.

References
[1]   G. Destgeer and H. J. Sung, "Recent advances in microfluidic actuation and micro-object manipulation via surface acoustic waves," *Lab Chip*, vol. 15, no. 13, pp. 2722–2738, 2015.
[2]   W. Connacher *et al.*, "Micro/nano acoustofluidics: Materials, phenomena, design, devices, and applications," *Lab Chip*, vol. 18, no. 14, pp. 1952–1996, 2018.
[3]   R. Al Jahdali and Y. Wu, "High transmission acoustic focusing by impedance-matched acoustic meta-surfaces," *Appl. Phys. Lett.*, vol. 108, no. 3, p. 031902, Jan. 2016.
[4]   J. Mei *et al.*, "Controllable transmission and total reflection through an impedance-matched acoustic metasurface," *New J. Phys.*, vol. 16, no. 12, p. 123007, Dec. 2014.
[5]   S. Bansal and S. Subramanian, "A Microfluidic Acoustic Metamaterial using Electrowetting: Enabling Active Broadband Tunability," *Adv. Mater. Technol.*, vol. 2100491, p. 2100491, 2021.

On-Chip Localized Microfluidic Pumping Powered by Guided Flexural Waves over Silicon-on-Nothing Membrane Waveguides

Philippe Vachon[1,2], Srinivas Merugu[1], Jaibir Sharma[1], Amit Lal[1,3], Eldwin J. Ng[1], Yul Koh[1], Joshua E.-Y. Lee[1], Chengkuo Lee[2]

[1]Institute of Microelectronics, A*STAR, Singapore,
E-mail: philippe.vachon@u.nus.edu
[2]Department of Electrical and Computer Engineering, National University of Singapore, Singapore
[3]School of Electrical and Computer Engineering, Cornell University, Ithaca, USA.

Introduction

Flexural waves are an interesting alternative to Rayleigh waves for acoustofluidic functions as these can deliver larger amplitudes. Flexural waves classically propagate everywhere within a substrate, making it difficult to localize the actuation. By altering the profile of the substrate such as etching the back of a silicon chip to form suspended membranes, Moroney et al. [1] demonstrated traveling flexural waves for acoustic streaming to drag particles while Vuillermet et al. [2] patterned particles according to the resonant modes of the plate. Liu et al. [3] showcased in-droplet particle control using dimples on the substrate. Recently, using silicon migration to form closed cavities sealed by 2 µm-thick membranes [4], enabling much more complex flexural waveguide patterns than allowed by conventional backport etching, we have demonstrated the ability to perform in-droplet alignment, transportation, and trapping of particles [5] on these devices. This fabrication approach leaves the chip's structural integrity intact, easing the integration of microfluidic channels with the thin membrane-based chip. In this experimental work, we demonstrate highly localized streaming flow, along the membrane waveguide, counteracting pressure flow within a microfluidic channel. This is unique evidence of localized on-chip microfluidic pumping powered by guided flexural waves (GFWs).
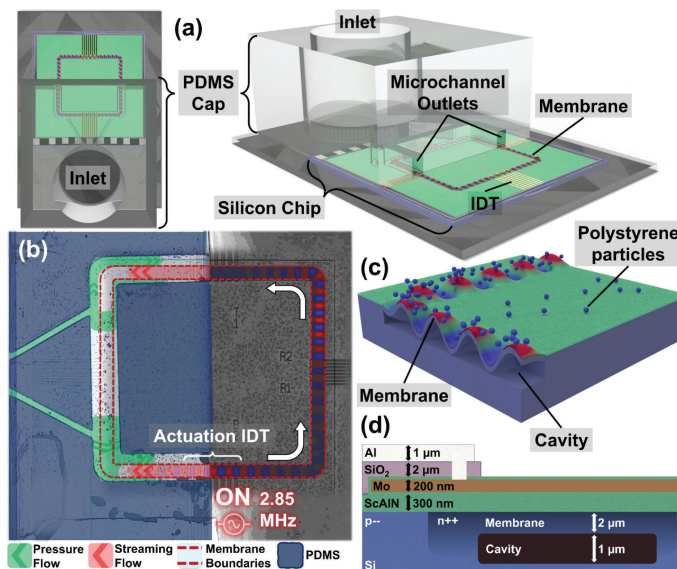

Figure 1: (a) Schematic of device comprising the membrane waveguide chip. Only the left half of the chip is covered by a PDMS cap while the right half is exposed. The microfluidic channels in the PDMS layer are aligned to the membrane waveguide. (b) Top view of the PDMS layer and underlying membrane device as fluid is pumped from the left. IDTs (λ=100 µm) at the bottom of the waveguide loop actuate the membrane, resulting in a burst of traveling waves imaged by LDV. The pressure flow (green) and GFW streaming flow (red) are illustrated on the left half within the microfluidic channel. (c) Schematic rendering of a curved segment of the membrane waveguide with a cross section showing the flexural wave on the waveguide above the cavity. The particles self-align on top of the actuated waveguide and travel in the same direction as the GFWs. (d) Cross section schematic of the membrane chip showing the respective layers.

Description of Device

The microfluidic pumping device in this work comprises two parts: a base silicon chip and a PDMS cap that has been bonded on the former, as shown in Fig. 1(a). The base is a 3 mm × 3 mm microfabricated silicon chip bearing a 2 µm-thick monocrystalline silicon membrane that forms a closed loop as depicted in Fig. 1(b). The thin membrane (also referred as silicon-on-nothing) lies above a seamless cavity, both issued from a silicon migration process, which allows far greater precision in the definition of the membrane shape. On the silicon

membrane is a 0.3 µm-thick piezoelectric layer of scandium-doped aluminum nitride ($Al_{0.85}Sc_{0.15}N$). Molybdenum (Mo) electrodes are patterned on the AlScN layer to define interdigitated transducers (IDTs) for actuating the underlying suspended silicon membrane and thereby generate guided flexural waves (GFWs) propagating along the membrane waveguide. The different fabrication layers are illustrated in Fig. 1(c). The device's cap is a PDMS microfluidic layer with 200 µm-wide main channel that traces the path of the underlying membrane waveguide, such that the walls of the microchannel enclose a part of the membrane waveguide. This main channel is fed by two tributary channels (seen on the left of Fig. 1(b)), which connect the main channel to the inlet on the far left where the fluid and particles are pumped into the microfluidic structure. Note that the patterned microfluidic cap encapsulates only half of the membrane chip (left half as seen in Fig. 1(a)), while the right half of the silicon chip is exposed. Therefore, the ends of the main channel are not sealed but rather exposed to the ambient. As such, fluid that is pumped from the inlet on the left flows toward the right and out of the microfluidic device due to the pressure difference.

Experimental Verification

The device was placed under a microscope and a water solution containing 5 µm polystyrene particles was pumped through the inlet to flow through the main channel from left to right. As the solution is pumped into the device, the IDT at the bottom section of the membrane waveguide was actuated with a 2.85 MHz sine signal, generating traveling GFWs propagating bi-directionally, away from the source IDT. The trajectory of the GFWs, confined within membrane waveguide segments and enclosed within the microchannel, is illustrated in Fig. 1(b). As such, the generated GFWs propagate in the opposite direction of the pressure flow within the microchannel at the top and bottom segments of membrane waveguide. Fig. 2 focuses on the top-left corner of the membrane waveguide. Initially, when the IDT is OFF (Fig. 2(a)), the particles flow naturally from left to right following the established pressure flow (in green). Turning the IDT ON (Fig. 2(b)), particles above the membrane waveguide can be seen flowing "backwards" in a serpentine fashion [5]. This is attributed to a newly formed streaming flow (red) advancing in the same direction as the GFWs' propagation. Turning the IDT OFF again, the counter flow stops and the particles once again drift in the direction of pressure flow.
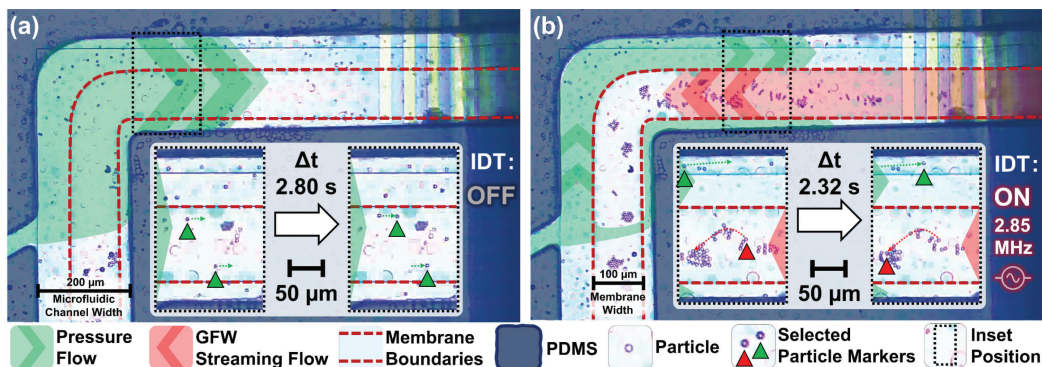

Figure 2: Evolution of flow behavior inside the PDMS microchannels during the acoustofluidic experiment: pressure flow (spanning the width of the microchannel) is indicated in green while GFW streaming flow (spanning only the width of the membrane waveguide) is indicated in red. (a) IDT is OFF initially: Particles drift from left to right everywhere across the width of the channel. (b) IDT is ON: GFWs traveling from right to left. A streaming flow arises and impedes the pressure flow only within the width of the membrane waveguide, as manifested by the particles' trajectory. The insets show two still frames spaced in time (Δt) to highlight the trajectory (indicated by the dotted arrows) of selected particles, each identified by a triangle in the color of the type of flow applied to them.

Conclusion

We have demonstrated that traveling GFWs can be used for highly localized fluid pumping and particle transport inside a microfluidic channel. The reported experimental results reveal acoustic streaming, generated by the traveling GFWs, strong enough to push and move particles against a pre-existing pressure flow. As the streaming itself is highly localized, only particles confined within the membrane waveguide are affected.

Aknowledgement

References

[1] R. M. Moroney, R. M. White, and R. T. Howe. 1990 IEEE Symposium on Ultrasonics, 355–358 (1990).
[2] G. Vuillermet, P.-Y. Gires, F. Casset, and C. Poulain. Phys. Rev. Lett. **116**, 184501 (2016).
[3] P. Liu et al. Sci. Adv. **8**, 1–10 (2022).
[4] J. Sharma et al. 2021 IEEE International Ultrasonics Symposium (IUS), 1–4 (2021).
[5] P. Vachon et al. 2021 IEEE International Ultrasonics Symposium (IUS), 1–4 (2021).

Complex microscale patterning with sub-wavelength acoustic microfeatures

Kirill Kolesnik[1], Philipp Segeritz[1], Daniel J. Scott[2], Vijay Rajagopal[1], David J. Collins[1]

[1]Department of Biomedical Engineering, University of Melbourne, Melbourne, VIC 3010, Australia
E-mail: kkolesnik@student.unimelb.edu.au, URL: https://www.collinsbiomicrosystems.com/
[2]Florey Institute of Neuroscience and Mental Health, University of Melbourne, VIC 3010, Australia

Introduction

Microfluidic cell isolation and patterning is a valuable tool in single cell analysis [1], cell-interaction studies [2], cell fusion [3] and tissue engineering [4]. Cell assembles have further applications for drug screening [5], cellular function studies [6], toxicity testing [7] and patient-specific therapies [8]. While there are a range of approaches that are used for these purposes, these have limited capacity for creating complex biomimetic cell assemblies [9].

In this work we report an approach for generating arbitrary microscale arrangements of particles and cells in sub-wavelength geometric features. These structures are combined with an acoustically resonant structure spanning the entirety of the device, generating acoustic forces that selectively direct suspended cells and particles towards microcavity trapping locations. Unique to this approach is the generation of a uniform device-spanning resonant acoustic field, compared to previous implementations that accomplish this only along lines in thin microchannels [10]. Moreover, careful material and dimensional arrangements permit the production of a unidirectional acoustic field, unlike other resonant devices that result in bidirectional aggregation. This is accomplished via a unique multi-layer cross-sectional structure that results in migration solely in the direction of microwells. By creating nodal positions that occur exclusively within a structured microfeatures, unique particle and cell patterns are generated.

References
[1] Y. Zhou, S. Basu, E. Laue, and A. A. Seshia, Biosens. Bioelectron., vol. 81, pp. 249–258, 2016.
[2] F. Guo et al.. Proc. Natl. Acad. Sci. U. S. A., vol. 112, no. 1, pp. 43–48, 2015.
[3] X. Wang, S. Chen, Y. T. Chow, C. W. Kong, R. A. Li, and D. Sun. RSC Adv., vol. 3, no. 45, pp. 23589–23595, 2013.
[4] B. Guillotin and F. Guillemot. Trends Biotechnol., vol. 29, no. 4, pp. 183–190, 2011.
[5] C. Kim et al.. Adv. Healthc. Mater., vol. 9, no. 7, p. 1901751, 2020.
[6] V. Z. Beachley et al.. Nat. Methods, vol. 12, no. 12, pp. 1197–1204, 2015.
[7] Y. Cong et al.. Micromachines, vol. 11, no. 4, p. 381, 2020.
[8] H.-G. Yi et al.. Nat. Biomed. Eng., vol. 3, no. 7, pp. 509–519, 2019.
[9] C. Tu et al.. Micromachines, vol. 8, no. 1, pp. 1–15, 2017.
[10] J. P. K. Armstrong et al.. Adv. Mater., vol. 30, no. 43, p. 1802649, 2018.

High sensitivity measurements of the acoustic contrast factor of stiffness altered biological cells

Cooper Lars Harshbarger[1,2,3], Alen Pavlic[1], Davide Bernardoni[2,3], Amelie Viol[1], Jess Gerrit Snedeker[2,3] and Jürg Dual[1]

[1]Institute for Mechanical Systems, ETH Zurich, 8092 Zurich, Switzerland
E-mail: hcooper@ethz.ch, URL: http://www.expdyn.ethz.ch/
[2]Department of Orthopedics, Balgrist University Hospital, University of Zurich, Zurich, Switzerland
[3]Institute for Biomechanics, Swiss Federal Institute of Technology Zurich, Zurich, Switzerland

Introduction

Determining the biomechanical response of biological cells is increasingly important in drug classification and discovery [1]. A gold standard method to determine the biomechanical phenotype of a cell are atomic force microscope (AFM) measurements. Despite the widespread adaption of this method, AFM measurements are limited to statically testing adherent cells at a very low throughput. A different experimental method of determining the biomechanical phenotype of a biological cell is measuring the acoustic contrast (AC) factor, whereas the AC is a measure for the density and compressibility of a particle relative to the surrounding fluid. Thus, any change to the biomechanical phenotype of the cell might induce a change of the AC.

Theoretical background

Given a spherical particle in an inviscid fluid with a radius that is much smaller than the acoustic wavelength λ, the acoustic radiation force acting on a particle can be approximated as the negative gradient of the Gor'kov potential

$$\underline{F}_{rad} = -\boldsymbol{\nabla} U \qquad (1) \qquad\qquad U = \frac{4\pi}{3} r^3 \left[f_1(\tilde{\kappa}) \frac{1}{2\rho_0 c_0^2} \langle p_1^2 \rangle - f_2(\tilde{\rho}) \frac{3}{4} \rho_0 \langle v_1^2 \rangle \right] \qquad (2)$$

whereas the variables are the particle radius r, the density of the fluid ρ_0, the speed of sound of the fluid c_0, the time averaged square of the incident acoustic pressure $\langle p_1^2 \rangle$, time averaged square of the incident acoustic velocity $\langle v_1^2 \rangle$, the monopole coefficient $f_1(\tilde{\kappa})$ representing the relative compressibility $\tilde{\kappa} = \kappa_p/\kappa_0$ between the particle κ_p and the fluid κ_0 and the dipole coefficient $f_2(\tilde{\rho})$ representing the relative density $\tilde{\rho} = \rho_p/\rho_0$ between the particle ρ_p and the fluid

$$f_1(\tilde{\kappa}) = 1 - \frac{\kappa_p}{\kappa_0} \quad (3) \qquad\qquad f_2(\tilde{\rho}) = 2\frac{\rho_p - \rho_0}{2\rho_p + \rho_0} \qquad (4)$$

These coefficients can, in the case of a 1D standing wave, be combined to yield the acoustic contrast (AC) factor Φ

$$\Phi = \frac{1}{3} f_1(\tilde{\kappa}) + \frac{1}{2} f_2(\tilde{\rho}). \qquad (5)$$

Methods and Materials

The human bone cancer cell line SaOs-2 was used as a model organism. In addition to measuring the AC of untreated SaOs-2 cells, the SaOs-2 cell line was fixed with formaldehyde, which permanently crosslinks proteins within the cell, thus killing the cell and rendering the cell stiffer [2]. This increased stiffness leads to a decreased relative compressibility and therefore the AC increases. In addition to the cells, 11 μm diameter polystyrene (PS) particles with a known AC ($\phi = 0.165$) were used as reference particles. The setup used for the measurements is custom made and vertical in order to ensure that the cells do not drag along the bottom of the fluidic channel. The chips are a glass-silicon-glass laminate and are therefore see-through. Both the setup and the chips are described in [3]. The cells are mixed with PS particles at a low concentration to reduce particle-particle interactions and are introduced into the chip. The excitation frequency of the driving piezoelectric transducer is set to a frequency previously determined to focus the particles in a $\lambda/2$ mode. The focusing of the cell – PS particle solution is recorded at $14 - 60$ fps using a voltage of $20 - 30$ V_{pp}. The post

processing consists of reducing artefacts and a subsequent particle detection with ilastik, a Fiji plugin, in order to distinguish between the PS particles and the cells of interest. The particle and cell tracks are calculated using TrackMate, also a plugin of Fiji. The particle tracks are evaluated via a custom MATLAB script. As the AC of the reference particles is known, the acoustic energy density can be evaluated. From this, the AC of the cells of interest can be computed, which was first demonstrated by [4].
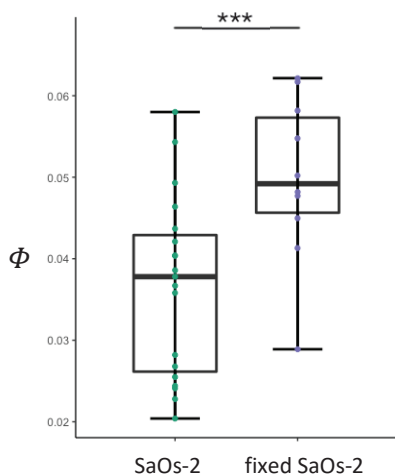
Figure 1: The AC of the SaOs-2 cell line is $\phi = 0.037 \pm 0.011$ (n = 18) and the fixed SaOs-2 cells $\phi = 0.050 \pm 0.010$ (n = 10). There is a large statistically significant difference (***, p = 0.0041 < 0.005) between the untreated and fixed, and thus increased stiffness, SaOs-2 cells.

Results and discussion

Previous work has incorporated a similar method to determine the AC of cells. However, the AC of treated cells was not investigated [5]. The change of the AC of untreated and treated cells was investigated by [6]. However, the compressibility was determined by a dynamic measurement, whereas the density was calculated by a neutrally buoyant selection process, which is a static measurement. The experiment presented here leads to a completely dynamic measurement of the AC of untreated and treated SaOs-2 cells. The results indicate that by increasing the cell's stiffness, a predicted increase in the AC can be observed with high resolution, even for small sample sizes. This increase in the AC is contrary to the decrease of the AC presented in [6], which is potentially due to the difference between the quasi-static measurement presented in [6] compared to the dynamic measurement presented here.

Conclusion

The measurement of the AC is therefore capable to provide insights into the biomechanical phenotype of a cell, which potentially cannot be covered by static measurements. This warrants further investigation into AC measurements. A suggested line of inquiry is how manipulating the cell stiffness through different pharmaceuticals, such as the myosin inhibiting agent Blebbistatin or an actin inhibiting agent Cytochalasin, that are known to reduce the stiffness of a cell, changes the AC. In addition, these experiments could be used together with a numerical model as a prediction tool for the change of the stiffness of biological cells. Thus the potential future application of this method to measure the biomechanical phenotype of cells is demonstrated.

References

[1] Krishnan, Ramaswamy, et al. "Cellular biomechanics in drug screening and evaluation: mechanopharmacology." *Trends in pharmacological sciences* 37.2 (2016): 87-100.
[2] Ling, Yuting, et al. "Effects of fixation and preservation on tissue elastic properties measured by quantitative optical coherence elastography (OCE)." *Journal of biomechanics* 49.7 (2016): 1009-1015.
[3] Harshbarger, Cooper, et al. "Optical feedback control loop for the precise and robust acoustic focusing of cells, micro-and nanoparticles." *Lab on a Chip* (2022).
[4] Barnkob, Rune, et al. "Measuring the local pressure amplitude in microchannel acoustophoresis." *Lab on a Chip* 10.5 (2010): 563-570.
[5] Wang, Han, et al. "Single-cell compressibility quantification for assessing metastatic potential of cancer cells through multi-frequency acoustophoresis." *Microfluidics and Nanofluidics* 22.6 (2018): 1-7.
[6] Cushing, Kevin W., et al. "Ultrasound characterization of microbead and cell suspensions by speed of sound measurements of neutrally buoyant samples." *Analytical chemistry* 89.17 (2017): 8917-8923.

Acoustophoresis-based cell manipulation device for advanced therapy medicinal products manufacturing automation

Florian Jouy[1], Fabien Rémy-Martin[1], Franck Lardet-Vieudrin[1], Alain Rouleau[1], Pauline Bourgeois[1], Rabah Zeggari[1,2], Annie Frelet-Barrand[1] and Jean-François Manceau[1]

[1]Micro Nano Sciences & Systems Department, FEMTO-ST Institute, CNRS/Université Bourgogne Franche-Comté, Besançon, France
[2]FEMTO Engineering, FC INNOV, Besançon, France
E-mail: jfmanceau@femto-st.fr, florian.jouy@femto-st.fr

Introduction

Advanced Therapy Medicinal Products (ATMPs) are emerging medecines for human use based on genes, tissues or cells. This new class of medicinal products offers new opportunities of treatment of severe to life-threatening diseases [1, 2]. These therapies however come at high-reaching financial costs. For instance, the cost for CAR-T cell therapy used for treating acute lymphoblastic leukaemia is estimated to be £528,600 for a single dose [3]. To facilitate ATMPs manufacturing and therefore make it accessible to a wider range of patients, we have developed an all-integrated apparatus able to perform acoustophoresis-based cell manipulations which are part of many ATMPs production cycles [4], including medium renewal, cell washing or sorting. Firstly, the features of the machine and its functions are detailed. Then, the device efficiency is experimentally demonstrated for medium renewal achieved by Bulk acoustic waves acoustophoresis (BAWA) and so is its potential in the event of future clinical applications.

Device architecture and features

The developed apparatus consists of an acoustophoresis module based on a classic BAWA microchannel architecture [5,6] (Figure 1). It is instrumented and controllable in terms of flow rates, input signals and temperature control through a specially designed human-machine interface, including process automation possibilities. Moreover, the apparatus is compatible with microscopy as the general setup illustration depicts in Figure 1.
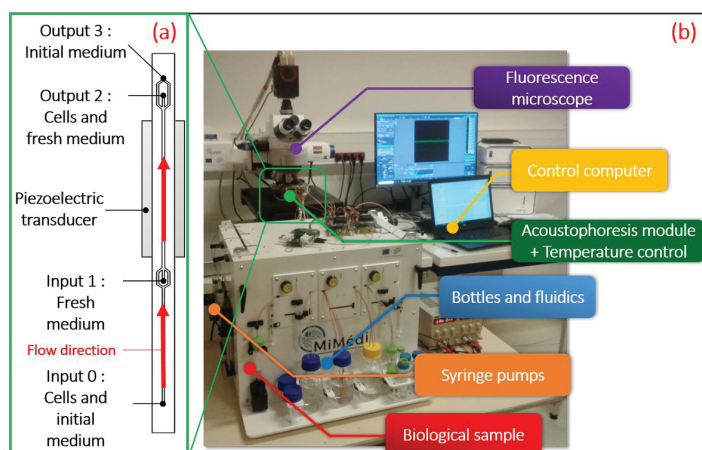

Figure 1:
(a) Microchannel detailed geometry and its configuration while performing medium renewal are displayed.
(b) Overview of the acoustophoresis cell manipulation device (ACMD) (white box in the foreground) and its environment. A fluorescence microscope (Zeiss Axio Imager Vario) is used in order to visualize the acoustophoresis microchannel and the fluorophore-labeled cells flowing through it. The ACMD is fully controllable by a single computer.

Acoustophoresis cell manipulation

Medium renewal of a single type of T lymphoblastic leukemia cell using BAWA at an input flow rate of $400\ \mu L/min$ is tested. The goal of this manipulation is to transfer cells from their current medium to a fresh one. Here, FluoroBrite^{TM} (Gibco^{TM}) is used as initial and final medium. An illustration of

this type of manipulation is displayed in Figure 2a. Cells are concentrated at 9×10^5 $cells/mL$ and labelled using DiOC6 fluorochrome so they can be visualized with fluorescence microscopy. Processed volume is about 10 mL. The cells firstly flow through the channel with no acoustic actuation and are then submitted to acoustic waves acting upon the system. For each case (whether acoustic waves are used or not), Output 2 and 3 (Figure 1) fluids are collected. Four 15 μL samples are observed for each collected output through fluorescence microscopy to get images used for further cell counting. For both configurations (acoustics OFF and acoustics ON), the number of counted cells for each output is compared to the total number of counted cells in both outputs to calculate a ratio called collection efficiency.

Results

The experiment shown here (Figure 2) is representative of 5 different experiments . Figure 2a depicts the cell flux while Figure 2b illustrates collection efficiency. When no acoustics are used, cells remain in their current media and circulate along the channel sides, thus, most of the cells are collected at Output 3 and 96.8 ± 2.3 % are collected. With acoustic waves, cells are directed to the center channel (Output 2) and a collection efficiency of 96.0 ± 2.8 % is obtained, see Figure 2b. The system is efficiently transfering almost all cells in the fresh medium or keeping them in the initial medium, in acoustics ON/OFF configuration, respectively. This demonstrates the performances of the apparatus in the case of medium renewal.
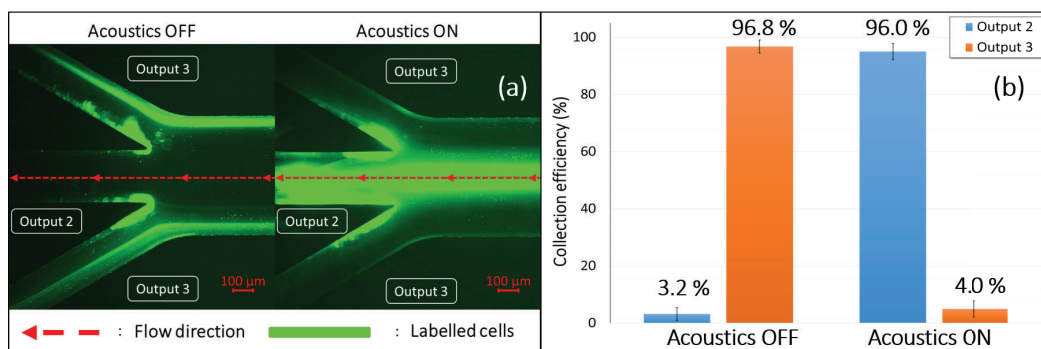

Figure 2: (a) Labelled cells in the current medium (left) and cells in the fresh medium (right). Using BAWA, cells are moving towards the middle of the channel. (b) Collection efficiency in the cases of absence and presence of acoustic waves acting upon the microchannel. Colored bars represent the average efficiency value and the error bars have the full length of a symmetric standard deviation.

Conclusion

In this work, we presented an apparatus designed to perform multiple cell manipulations and we demonstrated its efficiency for medium renewal of T lymphoblastic leukemia cells. As perspectives, we aim to fully automate this process and other cell manipulations required in ATMP production such as sorting of multiple cell types.

Acknowledgements

References

[1] Liras et al. Orphanet Journal of Rare Diseases **7**(97) (2012).
[2] Marofi, F., Motavalli, R., Safonov, V.A. et al. Stem Cell Res Ther **12**(81) (2021).
[3] Hettle R, Corbett M, Hinde S, Hodgson R, Jones-Diette J, Woolacott N, Palmer S. Health Technol Assess **21**(7) (2017).
[4] R. Pörtner. *Stem Cells in Clinical Practice and Tissue Engineering*, IntechOpen (London, 2017).
[5] Augustsson P, Magnusson C, Nordin M, Lilja H, Laurell T. Anal Chem. **84**(18) (2012).
[6] Vitali, V., Core, G., Garofalo, F. et al. Sci Rep **9** 19081 (2019).

Deformation/transportation behavior of non-Newtonian fluid droplet driven by propagating surface acoustic waves

Jikai Zhang, Hossein Abdolnezhad, Luke Haworth, Huiling Ong, Ciro Semprebon, Yong-Qing (Richard) Fu

Faculty of Engineering and Environment, Northumbria University, Newcastle upon Tyne, NE1 8ST, UK, E-mail: jikai.zhang@northumbria.ac.uk

Introduction

Acoustofluidics, with its multiple functionalities, portability, miniaturization, non-contact operation and high biocompatibility, is of great interest in the fields of drug delivery, microscale sample separation, and cell biology in many medical, chemical and biological fields (1,2). However, most of the studies in acoustofluidics are based on the Newtonian liquid (e.g., water solutions, either in sessile droplet or liquid flowing in the microchannel). Non-Newtonian fluids, including those of blood samples, are widely found in various industrial applications ranging from biomedical devices to food industry. They refer to fluids that do not satisfy the Newton's experimental law of viscosity, and show a non-linear relationship between shear stress and shear strain rates (3). The viscosity of a non-Newtonian fluid is a function of the shear strain rate and varies according to the pressure to which it is subjected. With the applying of acoustic wave pressure, these non-Newtonian liquids often show significantly different behaviors as a function of interaction time between waves and liquid (4). However, this is a rather less investigated area, and there are a lot of issues that are not well-understood.

In this study, different concentrations of non-Newtonian fluid droplets (Xanthan solutions with a shear-thinning behavior) were selected to be actuated using propagating surface acoustic waves (SAWs). Deformation and transportation behaviors of these non-Newtonian fluids were evaluated by measuring their deformation angles and transportation speeds.

Experimental design

Comparative experiments were carried out using Xanthan/water solutions at concentrations of 400, 800, 1500 and 2500 ppm, respectively, and compared with glycerin sample with similar initial viscosities. ZnO film coated silicon SAW device with a frequency of 22.175 MHz was used. The SAW device was treated with a layer of CYTOP solution to form a hydrophobic surface. During the tests, a 5 µL droplet was placed at ~5 mm in front of the interdigital transducers (IDT) of the SAW device. The SAW signals were generated from a signal generator and then amplified using an RF amplifier, before applying to the SAW device. The droplet movement was recorded using a video camera.

Results analysis and discussions

Figure 1 shows the variations of viscosities with the shear rate for different concentrations of Xanthan and pure glycerin at 20°C, which shows that the shear-thinning viscosity of Xanthan solutions. The results are contrast to that of glycerin, with a viscosity value of 1.49 Pa·s.

Figure 2 shows the deformation behaviors of Xanthan/water solutions at different concentrations and powers when using a 22.175 MHz SAW device driven for about 0.2 s, e.g., (a) 800 ppm/7W; (b) 800ppm/10W; (c) 800ppm/14W; (d) 1500ppm/7W; (e) 1500ppm/10W; (f) 1500ppm/14W; (g) 2500ppm/7W; (h) 2500ppm/10W; (j) 2500ppm/14W. Figure 3 summarizes

the obtained deformation angles for Xanthan solutions. The deformation angle increases with increasing power for the same concentration of Xanthan droplets driven by the acoustic surface waves. The variations of the deformation following the theoretical Raleigh angles. The variations of deformation of droplets can be attributed to Xanthan's nature of viscosity variations under the large shear stresses induced by SAWs. Although Xanthan has quite large viscosity at zero shear rate, its viscosity reduces remarkably by applying SAW power.
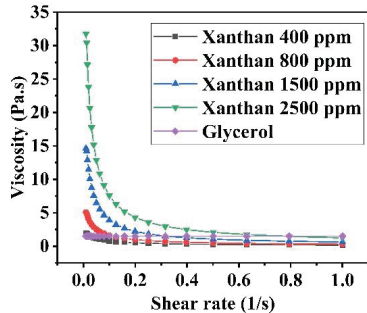
Fig. 1. Variation of viscosities of Xanthan solutions and glycerol as a function of shear rate
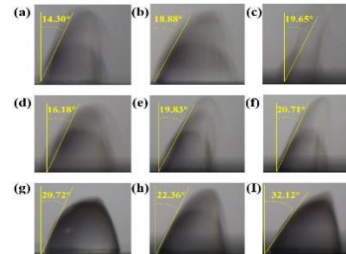
Fig. 2. Selected examples of droplet deformation behaviour at different Xanthan concentrations
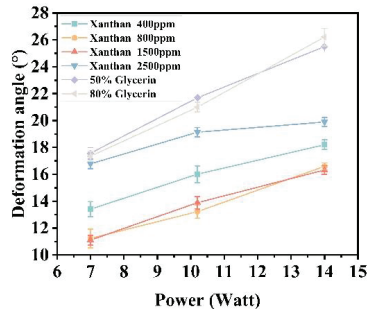
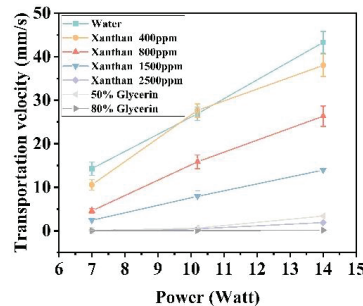Fig. 3. Deformation angle of droplets with various Xanthan concentrations

Fig. 4. Transportation velocities of droplets with different Xanthan concentrations

Figure 4 shows the transportation rates of different droplets with varied Xanthan concentrations. It shows that the rate of movement of droplet of Xanthan 400ppm is closer to that of pure water. The rate of movement of all droplets increases with increasing power.

Summary

This study illustrates that non-Newtonian fluids show different displacement and deformation capabilities than Newtonian fluids driven by the same acoustic surface wave, contributing to the analysis of the principles of motion of microscopic non-Newtonian fluid droplets under non-contact pressure to aid the implementation of non-contact non-Newtonian droplet actuation and applications.

References:

1. Fu, Y. Q., Luo, J. K., Du, X. Y., et al, Recent developments on ZnO films for acoustic wave based bio-sensing and microfluidic applications: a review. *Sens. Actuat. B 143*(2), 606-619.
2. Lu, X., Liu, C., Hu, G., & Xuan, X. (2017). Particle manipulations in non-Newtonian microfluidics: A review. *J. colloid Inter. Sci. 500*, 182-201.
3. Tian, F., Feng, Q., Chen, Q., et al, Manipulation of bio-micro/nanoparticles in non-Newtonian microflows. *Microfluidics Nanofluidics*, *23*(5), 1-9.
4. Zhou, J., & Papautsky, I. (2020). Viscoelastic microfluidics: Progress and challenges.*Microsystems & Nanoengineering*, *6*(1), 1-24.

Dynamic patterning of dielectric particles on a PMUT array.

Bart P. Weekers[1,2], Liesbet Lagae[1,2], Xavier Rottenberg[2], and Veronique Rochus[2]

[1]Department of Physics and Astronomy, KU Leuven, B-3001 Leuven, Belgium
E-mail: bart.weekers@kuleuven.be
[2]imec, Kapeldreef 75, B-3001 Leuven, Belgium

Introduction
Precise manipulation of microscale objects is desired in many applications spanning different fields of science. In life sciences e.g., objects ranging from intracellular components to pluricellular systems require precise manipulation often in a contactless manner [1, 2]. In this work, an array of piezoelectric micromachined ultrasound transducers (PMUTs) is used to dynamically manipulate silica microspheres via a combination of acoustophoresis and dielectrophoresis. The relevant forces are analyzed in detail through finite element analysis and numerical calculations.

Methods
A silicon-based PMUT array is placed at the bottom of a small dish containing high purity water with a suspension of monodisperse silica microspheres (Cospheric, CA, USA) with $7.75 \mu m$ diameter. The PMUT array consists of 30 x 30 circular PMUTs with $100 \mu m$ diameter, $180 \mu m$ pitch and a material stack as shown schematically in Fig. 1. The frequency response of the PMUTs is measured with a Laser Doppler Vibrometer (Polytec MSA500). For the particle manipulation experiments, the PMUTs are actuated per row with a continuous sinusoidal excitation of $10 V_{pp}$ at the fundamental resonance frequency using a function generator.

An axisymmetric finite element model of a single PMUT is constructed in COMSOL Multiphysics®. The model couples the solid mechanics, electrostatics and pressure acoustics interfaces. The dielectrophoretic and acoustic radiation forces are computed explicitly in the model. Numerical calculations are performed in Matlab® to compute the acoustic radiation force and test the validity of the small particle approximation assuming a polynomial velocity profile of the PMUT [5].

Results and Discussion
The fundamental resonance frequency of the PMUTs is $f_{res} = 2.25 \pm 0.01 MHz$ ($N = 25$) such that $ka = 0.04 << 1$ and the velocity amplitude at resonance is $|v_z| = 21.4 \pm 8 mm/Vs$.

Through numerical calculations it is found that the scattering term in the expression for the acoustic radiation force is negligible such that the radiation force can be computed as the gradient of
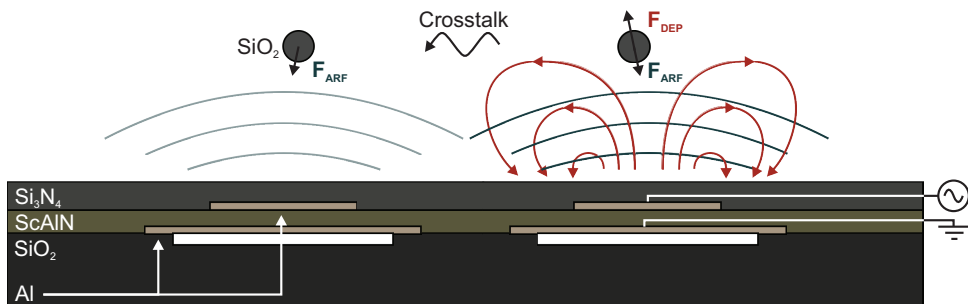

Figure 1: Schematic of the PMUT array and particle manipulation. The top electrode of a PMUT is excited with an electric potential while the bottom electrode in grounded. The particle experiences a force due to the electric field (F_{DEP}) and a force due to the acoustic field (F_{ARF}). Neighbouring PMUTs start vibrating due to crosstalk and emit acoustic waves without electrical excitation.
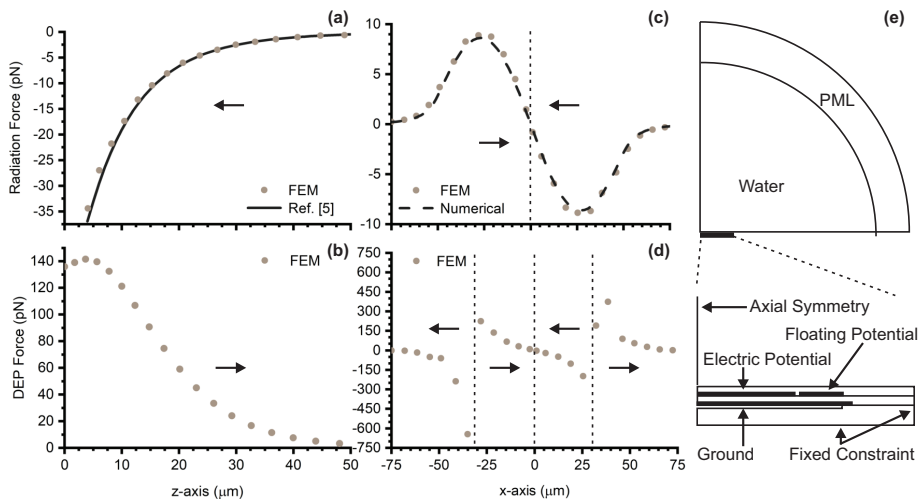
Figure 2: (a,b) Acoustic radiation force and dielectrophoretic force along the symmetry axis of a single PMUT respectively. The small particle approximation is justified by comparing is to the solution of the full scattering problem. (c,d) Acoustic radiation force and dielectrophoretic force $7.75\mu m/2$ above the PMUT in the PMUT plane. (e) Finite element model used for the simulations.
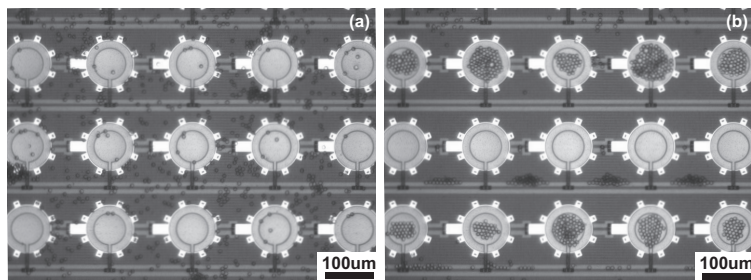

Figure 3: Top view of a section of the PMUT array. (a) Before the excitation the silica particles are randomly distributed on the surface of the PMUT. (b) Silica particles are repelled from the excited PMUT row and trapped on the neighbouring rows.

the well-known Gorkov potential. The computed radiation forces are shown in Fig. 2 (a, c), revealing an attractive force on the silica particles (towards the PMUT center). This attractive force is caused by the dipole term which dominates the monopole term. I.e. the attraction to high velocity amplitudes in the acoustic field dominates the repulsion from high pressure amplitudes which are both located at the center of the PMUT in this case. The computed dielectrophoretic force is shown in Fig. 2 (b, d), revealing a repulsive force on the silica particles (away from the PMUT center) which dominates the acoustic radiation force.

In the experiments, a single PMUT row is actuated. It is clearly observed that the particles are repelled from the actuated PMUTs and are attracted to the neighboring PMUTs (see Fig. 3). These neighboring PMUTs vibrate without electrical actuation due to crosstalk where the dominant mechanism is acoustic coupling through the fluid [4]. It is envisaged that careful design of PMUT arrays utilizing this manipulation scheme, capitalizing on crosstalk, would allow a versatile patterning method applicable to a variety of relevant dielectric particles including biological cells.

Conclusion
Silica particles are dynamically patterned on the surface of PMUT array through a combination of acoustophoresis and dielectrophoresis. The particles are expelled from actuated PMUTs and are attracted to neighbouring PMUTs due to acoustical crosstalk.

References
[1] A. Ozcelik et al. Nature methods, **15**(12), 1021-1028 (2018).
[2] S. Mohanty, I. S. Khalil, and S. Misra. Proceedings of the Royal Society A, **476**(2243), 20200621 (2020).
[3] J. W. S. Rayleigh. *The Theory of Sound (reprinted)*, Dover Publications, Inc. (New York, 1945).
[4] B. P. Weekers et al. EuroSimE Conference IEEE, 1-5 (2021).
[5] B. P. Weekers et al. The Journal of the Acoustical Society of America **151**(6), 3615-3625 (2022).

In-situ investigation of three-dimensional acoustophoretic and acoustothermal effects in SAW-based acoustic tweezers

V.V. Kondalkar[1], Z. Deng[2], A.N. Darinskii[3], R. Weser[1], C. Cierpka[2], J. König[2], and H. Schmidt[1]

[1]SAWLab Saxony, Leibniz Institute for Solid State and Materials Research Dresden, Dresden, Germany
E-mail: h.schmidt@ifw-dresden.de, URL: http://www.ifw-dresden.de
[2]Institute of Thermodynamics and Fluid Mechanics, Technische Universität Ilmenau, Ilmenau, Germany
[3]Institute of Crystallography FSRC "Crystallography and Photonics", RAS, Moscow, Russia

Introduction
Manipulation of cells or particles in fluids at the microscale can be efficiently realized by means of active acoustofluidic devices. Microfluidic devices driven by surface acoustic waves (SAWs) are of particular interest because they allow for very precise manipulation due to small acoustic wavelengths [1-3]. The actuation capability of SAW-driven microfluidics relies on the transfer of momentum from the substrate surface to the fluid and subsequent acoustophoretic effect. Besides mechanical stress mainly induced by acoustophoresis, the dissipation of acoustic energy yields a significant heating of the fluid accompanied by relevant thermal stress on the cells [4]. Both acoustically driven effects need to be taken into account while considering the total stress on cells during manipulations in microfluidics systems.
Acoustophoresis as well as acoustothermal heating have been already intensively investigated. However, two main challenges remain on realizing detailed investigations on SAW-driven microfluidics: (i) the real lateral distribution of SAW displacement amplitude at the substrate-fluid interface that is most relevant for the determination of the transfer of momentum, is hardly known, and (ii) the highly dynamic process of acoustothermal heating is difficult to be investigated by experimental methods due to limitations, i.e. poor spatial resolution or invasive techniques.
Here, we present a comprehensive experimental approach that allows for the in-situ determination of the SAW field at the substrate-fluid interface as well as the dynamic determination of temporal 3D distributions of the position and the temperature of model particles while they are manipulated using a SAW-based single cell separation system. The experimental investigations are based on optical methods that allow a holistic non-invasive investigation of acoustically driven microfluidic devices. Corresponding results yield a high-resolution insight into the fluid volume that was not available so far, which furthermore allows detailed analysis on the acoustophoretic and acoustothermal effects as well as their dynamic behavior.

Experimental setup and methods
Investigations are exemplarily performed for an acoustic tweezers setup driven by a two-dimensional, standing surface acoustic wave field (2DsSAW) [5]. The 2DsSAW is generated by an arrangement of four IDTs (quarter wavelength IDTs with period 120 µm) arranged in two orthogonal propagation directions each with two opposing IDTs. These IDTs are arranged on a 128° rotated Y-cut lithium niobate (128Y LiNbO$_3$) substrate. Furthermore, a microfluidic vessel made from polydimethylsiloxane (PDMS) is attached to the substrate in between IDTs confining a fluid volume with the size of 1.2×1.2 mm² in lateral dimensions and 88 µm in height. The vessel is filled with particles (made from polymethylmethacrylate with a diameter of 10 µm) that are suspended in a glycerol-water mixture to minimize sedimentation while offering sufficient acoustic contrast for manipulation with acoustic waves. In addition, the particles also contain a temperature sensitive phosphorescent dye made from europium (III) thenoyltrifluoroacetonate.
The lateral distribution of SAW amplitude at the substrate-fluid interface was measured using a conventional ultrahigh frequency laser Doppler vibrometer (LDV) with an adapted optical setup to enable access to the fluid loaded substrate surface from the rear side [6]. Furthermore, the volumetric distribution of sound pressure in the fluid was calculated based on the measured SAW displacement amplitude. The three-dimensional particle positions were measured applying the astigmatism particle tracking velocimetry (APTV) [7]. By combining APTV with luminescence lifetime imaging (LLI), the temperature of the particles could be measured simultaneously [8]. It is important to note that above mentioned optical methods are applied to the microfluidic setup using optical transmission of the substrate material (LiNbO$_3$). This enables direct in-situ access to the fluid volume under well-defined conditions, even though the birefringence of the substrate material needs to be compensated appropriately. Details on the different measurement methods will be given in the presentation at the conference.

Results

As expected from acoustofluidic design, the particles are trapped at three different height levels when the SAW field is applied to the microfluidic vessel (Fig. 1, left). A first level was found at $z \approx 5.2$ μm, i.e. the particles are slightly lifted but still in the close vicinity of the substrate surface. A second level was found at $z \approx 26.3$ μm while a third level was observed at a height of 58 μm. With respect to both lower levels, the least particles occupied the top level. The reason for this might be gravitational forces acting already on particles when entering the vessel before the acoustic field was applied. The measured temperature distribution of particles and the corresponding temporal evolution will be discussed at the conference in detail. Two major correlations were revealed: first, the temperature is higher at the second level as compared to the first level, and second, the temperature is higher at the center of the fluid volume as compared to the edges. The latter relationship seems to be plausible because the SAW amplitude is significantly lower at the edges of the chamber and the influence of the anechoic regions also has to be considered, i.e. the sound pressure at the close vicinity of the vessel walls is significantly lower. The position of particles trapped by the standing acoustic wave field reasonably resembles acoustic potential as derived from SAW displacement amplitude in-situ measured by LDV (Fig. 1, right). The comparison between particle positions and the volumetric distribution of sound pressure inside the fluid, calculated on the basis of LDV measurements, will also be discussed at the conference more in detail.
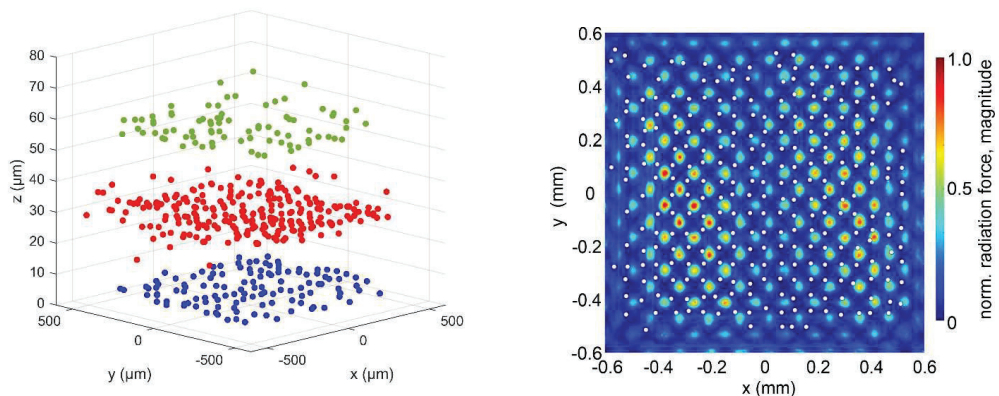

Figure 1: 3D distribution of particles trapped at three heights, measured with APTV (left), and lateral position of particles at the lowest level ($z \approx 5.2$ μm) in direct comparison with the distribution of the acoustic radiation force derived from the SAW displacement amplitude, measured with LDV at the surface (right). The origin of the coordinate system (x=y=z=0) is located at the center of the fluid volume at substrate surface. Total electric power applied to the IDTs was 1.3 W.

Conclusion

We have successfully demonstrated the application of microscopic in-situ methods for non-invasive and high-resolution investigation of the three-dimensional distributions of the acoustic field and of the position and temperature of particles in a SAW-based acoustic tweezers setup. Corresponding results reveal good agreement between the position of particles and the nodal positions in the acoustic field. Moreover, the distribution of particle temperatures shows a significant influence of the particle position with respect to the acoustic field.

The holistic experimental approach yields high-resolution insight into acoustically driven microfluidics that was not available so far. Furthermore, analysis of revealed differences in time scale enables a more detailed consideration not only of the actuation capabilities but also of counter-measures against the thermal stress acting on cells during acoustofluidic manipulation.

References

[1] F. Guo, Z. Mao, Y. Chen, Z. Xie, J.P. Lata, P. Li, L. Ren, J. Liu, J. Yang, M. Dao, S. Suresh, and T.J. Huang. PNAS **113**, 1522 462 (2016).
[2] D.J. Collins, B. Moraha, J. Garcia-Busto, C. Doerig, M. Plebanski, and A. Neild. Nature Comm. **6**, 8686 (2015).
[3] N. R. Skov, P. Sehgal, B. J. Kirby, and H. Bruus. Phys. Rev. Appl. **12**, 044028 (2019).
[4] P. Das, A. Snider, and V. Bhethanabotla. Phys. Fluids **31**, 106106 (2019).
[5] R. Weser, Z. Deng, V.V. Kondalkar, A.N. Darinskii, C. Cierpka, H. Schmidt, and J. König. Lab Chip **22**, 2886 (2022).
[6] R. Weser, H. Schmidt. J. Appl. Phys. **129**, 244503 (2021).
[7] C. Cierpka, R. Segura, R. Hain, C.J. Kähler. Meas. Sci. Technol. **21** 045401 (2010).
[8] J. Massing, C.J. Kähler, C. Cierpka. Exp. in Fluids **59** 163 (2018).

Acoustic microparticle patterning of arbitrary-defined shapes by 3D waveguides

William S. Harley[1], Kirill Kolesnik[1], Daniel E. Heath[1], David J. Collins[1]

[1]Department of Biomedical Engineering, University of Melbourne, Melbourne, VIC 3010, Australia

E-mail: david.collins@unimelb.edu.au, URL: https://www.collinsbiomicrosystems.com/

Introduction

Precise and controllable acoustic manipulation of micron-scale biological objects is a common goal of microfluidic systems, in which particles and cells are concentrated, sorted, or patterned for a variety of diagnostic and biomedical research purposes[1]. Acoustic forces have demonstrated the ability to perform these micro manipulations in a non-contact, biocompatible and on-demand manner, although conventional approaches have been restricted to producing periodic patterns from standing waves or shown to exhibit limited acoustic field complexity. Many advanced processes require the ability to reliably manipulate single-cell scale objects in more complex trajectories and arbitrarily defined patterns. Acoustic-structure interactions is an emerging area of interest that has the potential to generate refined and localized actuation, with sub-wavelength microstructures capable of generating acoustic effects whose gradients can be substantially smaller than the acoustic wavelength [2]. Prior work investigating the effects of vibrating sharp-edge microstructures has found applications in channel mixing, propelling microrobots and nanoparticle concentration[3]. In this work, we demonstrate the capabilities of microstructures for micro rotation, particle transport and arbitrary patterning. We have numerically simulated and experimentally validated such a concept by realizing the patterning of microparticles in complex, non-periodic shapes and as such provide advances in acoustic micromanipulation of biological objects at cellular length scales.

Acknowledgments

References

[1] D.J. Collins, B.L. Khoo, Z. Ma, A. Winkler, R. Weser, H. Schmidt, J. Han, Y. Ai, Selective particle and cell capture in a continuous flow using micro-vortex acoustic streaming, Lab Chip 17(10) (2017) 1769-1777.
[2] K.-W. Tung, P.-S. Chung, C. Wu, T. Man, S. Tiwari, B. Wu, Y.-F. Chou, F.-L. Yang, P.-Y. Chiou, Deep, sub-wavelength acoustic patterning of complex and non-periodic shapes on soft membranes supported by air cavities, Lab on a Chip 19(21) (2019) 3714-3725.
[3] Y. Zhou, Wang, H., Ma, Z., Yang, J. K. W., Ai, Y., Acoustic Vibration-Induced Actuation of Multiple Microrotors in Microfluidics, Advanced Materials 5(9) (2020).

On-chip particle centrifuge using spiral surface acoustic waves on ZnO/glass substrate

Zhihao Zhu, Xiasheng Guo

Key Laboratory of Modern Acoustics (MOE), Department of Physics, Collaborative Innovation Center of Advanced Microstructure, Nanjing University, Nanjing 210093, China
Email: 944750257@qq.com

Introduction

We have implemented a glass-based, highly efficient and controllable particle concentration device. A circular interdigital transducer with spiral electrodes is fabricated on a composite substrate of ZnO film and quartz glass (QG), generating an omnidirectional spiral surface acoustic wave field. A vorticity field is generated in a sessile droplet and controlled concentrations of polystyrene particles with different diameters and Hela cells in the droplet is achieved. Compared to a similar device prepared on a LiNbO3 substrate, it is observed that, benefiting from the isotropic substrate, the working area of the proposed centrifuge is both controllable and predictable, and the achieved particle concentration is more stable. The ZnO/QG-based centrifuge shows good performance in enriching micron/submicron particles and cells and is compatible with optical tools, offering good promise in enriching low abundance micro- and nanoparticles, especially in rare samples.
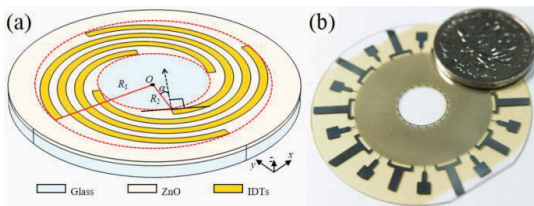
Methods

Figure 1: Schematic diagram of the ZnO/QG-based SAW centrifuge. (a) illustrates an example of four electrodes required for a simple IDT. on a composite substrate made of ZnO (light yellow) and quartz glass (light blue), the electrodes (gold) made of Aluminum is located within a circular area having inner and outer radii R1 and R2. At any arbitrary azimuthal angle, the generated SAWs propagate along a direction orthogonal to the spiral lines, or at an angle of α to the corresponding radial direction. (b) shows the actual device we designed, where the IDT consists of n/2=36 electrodes.

To concentrate acoustic energy into the droplet, a spiral IDT is prepared on a ZnO/QG substrate to generate omni- directional spiral SAWs. Figure 1 shows the structure of the device. The waves converge to a circular region from all directions, thereby driving particles in a sessile droplet at the substrate center. [1]
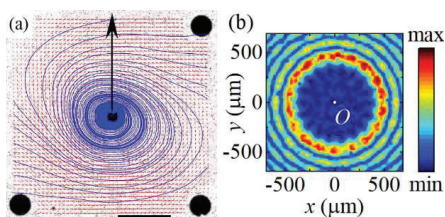

Figure 2: Device characterization results. (a)Two-dimensional streaming distribution in the central potential well, where the red arrows indicate vector velocities, blue lines are flow lines, and the black shadings at the center and four corners are opaque calibration points on the substrate; VP-P=60 mV, scale bar: 200 μm. (b) laser vibrometer scan results giving the off-plane displacement amplitude of SAW vibrations in a rectangular area centered at the origin.

The streaming field at the bottom of the droplet is given in Fig. 2(a), where the four opaque circular spots at the center and corners of the field of view are calibration spots fabricated on the substrate. The red arrows indicate the streaming velocity, and the resulting blue flow lines indicate the formation of vortices in the droplet. The center of the vortex essentially overlaps with the center of the device. In the $\varphi = 0°$ direction as indicated by the black arrow in Fig. 2(a), the maximum value of the streaming velocity is recorded as v_m and this value is then examined for different excitation voltages. A laser vibrometer is used to scan the central area of the device to obtain the 2D distributions of amplitude (A_{vib}). Using this method, the operating frequency of our

centrifuge is chosen to be f = 22.70 MHz, and the laser vibrometry measurement results in Fig. 2(b) show a concentric ring-shaped SAW field generated on the device surface, and a circular potential well with low vibration amplitude is formed in the innermost part of the field.

Results

In Fig. 3(a), the device has not yet started working and the particles are uniformly distributed in the stationary droplet; the shaded points at the corners are calibration spots on the substrate. As SAWs generate an azimuthal flow in the droplet, the particles move along inwardly spiraling trajectories, see the 1-s state in Fig. 3(b). When the local particle concentration is high enough, shear-induced migration generates inward radial forces.[3] As observed in Fig. 3(c), under the radial force, the PS particles gradually migrate and accumulate to the central region. Figure 3(d) shows the final state of the process, where almost all the particles are concentrated at the central region marked by the red circle.
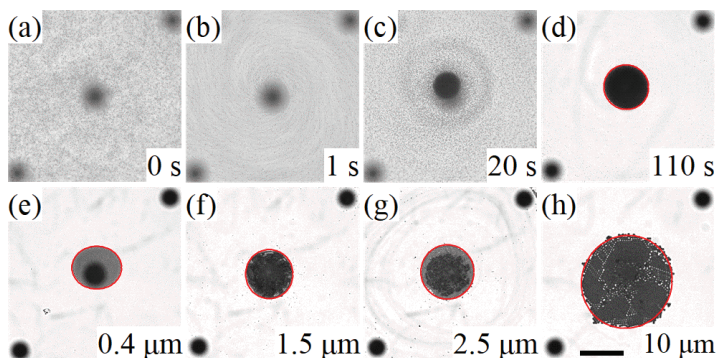

Figure 3: Concentration results for PS particles of different sizes. (a)-(d) show the concentration process of 1 μm particles, where (a) is the initial state before the operation of the device, and the circular dark spots are calibration points on the substrate; (b)-(d) are the states at 1, 20 and 100 s after the SAW field was activated, respectively, and in (d) the particles were aggregated in the red circle; (e)-(h) are the concentrated states of 0.4, 1.5, 2.5 and 10-μm particles. VP-P=80 mV, SV=150, CB=3% (w/v), scale bar: 200 μm.

Then, the final concentrated states of 0.4, 1.5, 2.5, and 10-μm particles are shown in Figs. 3(e)-3(h), respectively, with particles of different sizes clustered near the central calibration spot. According to the particle boundaries marked by red circles, larger particles end up occupying larger circular areas, as clusters formed by larger particles have more voids at the same concentration. The results presented here show that the ZnO/QG-based SAW centrifuge can effectively concentrate particles in a large size range (at least from 0.4 to 10 μm), which is preferred for biomedical applications. For example, bacteria and viruses are typically at the submicron level, while biological cells are at the micron size. In particular, manipulation of submicron particles previously relied on high operating frequencies or the construction of acoustic resonators. With the present device, this can be achieved at operating frequencies around 20 MHz, and no resonance structure is necessary.

Conclusion

In this paper, a ZnO/QG-based SAW centrifuge is pro- posed. At an operating frequency of 22.70 MHz, an omnidirectional spiral IDT generates asymmetrically propagating SAWs that produce inward rotating vorticity fields in the droplet, and shear action concentrates 0.4-10 μm PS microspheres and Hela cells to the device center. The concentration efficiency can be optimized by controlling the driving voltage and in turn the streaming velocity in the droplet. Compared to LN-based on-chip centrifuges, the ZnO/QG-based device offers better stability and optical compatibility, with results that are both controllable and predictable.

References

[1] N. Zhang, J. P. Zuniga-Hertz , Lab Chip, 2021, 21, 904-915.
[2] D. J. Collins, Z. Ma, J. Han and Y. Ai, Lab Chip, 2016, 17, 91-103.
[3] H. Li, J. R. Friend and L. Y. Yeo, Biomed Microdevices, 2007, 9, 647-656.

Characterization and control of a broadband acoustic cavity: Application to cells spheroids manipulation.

Nathan Jeger-Madiot[1], Xavier Mousset[1,2], Chloé Dupuis[1,2], Lucile Rabiet[1,3], Mauricio Hoyos[1], Jean-Michel Peyrin[2] and Jean-Luc Aider[1]

[1]Laboratoire de Physique et Mécanique des Milieux Hétérogènes, Unité Mixte de Recherche 7636 Centre National de la Recherche Scientifique, École Supérieure de Physique et de Chimie Industrielles de la Ville de Paris, Paris Sciences et Lettres University, Sorbonne Université, Université de Paris 1, Paris, 75005, France
[2]Sorbonne Universités, Faculté des Sciences et Ingénierie, CNRS UMR 8246, INSERM U1130, Neurosciences Paris Seine, Institut de Biologie Paris Seine, Paris, 75005, France
[3]Unité de Thérapie Cellulaire, APHP, Hôpital Saint-Louis, Université de Paris, Inserm U976 et CIC de Biothérapies CBT501, 75010 Paris, France

Introduction

The acoustic energy density E_{ac} is a key parameter for the acoustophoretic devices and applications. It determines the magnitude of the acoustic radiation force (ARF) applied on small objects like particles or cells. The prior knowledge of the experimental E_{ac} over a large frequency spectrum gives fundamental information on the device and allow many different applications like moving the axial position of the acoustic levitation plane just by changing the acoustic frequency [1]. In this work we present an acoustofluidic chip working with bulk acoustic standing waves. The chip is designed to produce several acoustic nodes and to allow lateral optical access. It is characterized using Particle Image Velocimetry (PIV) measurements. It allows us to assemble cells spheroids while applying a constant acoustic force over a wide frequency, just by frequency tuning.

Background

The acoustic cavity is modelized as a 1D multilayer system in order to estimate the acoustic field properties from the particles velocities. Three layers, composed by water, glass and air, are considered. By applying the matrix formulation given by [2] and implementing the boundary limits we can compute the theoretical acoustic velocity and pressure. A standing wave is generated in the system and leads to interactions with the small polystyrene particles about 15μm, suspended in the liquid. The Gorkov and Yosioka model can be used [3] as the Rayleigh condition is verified and the ARF can be calculated:

$$F_{rad} = 4\pi r_p^3 \beta k E_{ac} \sin(2kz + 2\phi)$$

with β the acoustic contrast factor, r_p the particle radius.
In order to measure the acoustic energy density, the particle motions are linked to the ARF. According to the Newton's second law, and neglecting the inertial effect and the buoyancy force, we can express the velocity of the particle moving toward the acoustic pressure node as:

$$v_p(z) = \frac{1}{3\eta} 2\beta r_p^2 k E_{ac} \sin(2kz + 2\phi)$$

Measuring the velocity magnitude and knowing the particle diameter and physical properties, we access to the mean of the acoustic energy density.

Experimental setup and PIV methods

The setup has been designed to be fully automated in order to carry out large parametric studies [4]. It allowed the measurement of the acoustic energy over a wide range of frequency with a small frequency step. For each acoustic frequency the particle suspension is mixed inside the acoustic cavity using a controlled syringe pump. Once the fluid is settled, a digital microscope and the ultrasound transducer are simultaneously triggered. The motions of the particles are then recorded until they reach the levitation plane.

Using the successive snapshots, the PIV could be used to measure the polystyrene particles velocities. The velocity fields are computed using PIVlab [5], a 2D cross-correlation software. A velocity vector is computed on each interrogation windows (Fig. 1) leading to 2D velocity fields, which are averaged in the spanwise direction, allowing the computation of the maximum axial velocity of the particles.
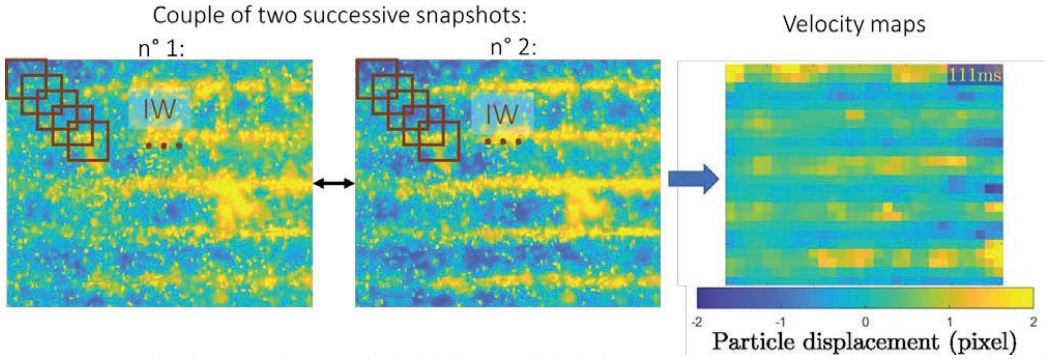
Figure 1: Example of two snapshots acquired with the USB digital microscope. Interrogation windows (IWs) are defined in order to compute 2D cross correlation. From global particle displacement, we obtained the velocity maps of the axial velocity of the particles moved by the ARF. This experiment was repeated many times to obtain robust characterization of the acoustic energy density.

Acoustic energy measurements over a wide frequency range

We measured the evolution of the acoustic energy density for a given voltage (7Vpp) and for 2400 frequencies ranging from 1 to 3 MHz (Fig. 2a). Several resonance peaks can clearly be observed. It corresponds to the creation of new pressure nodes and to continuous shifting of the axial location of the levitation planes. The maxima of E_{ac} reaches $1.75\ J.m^{-3}$.
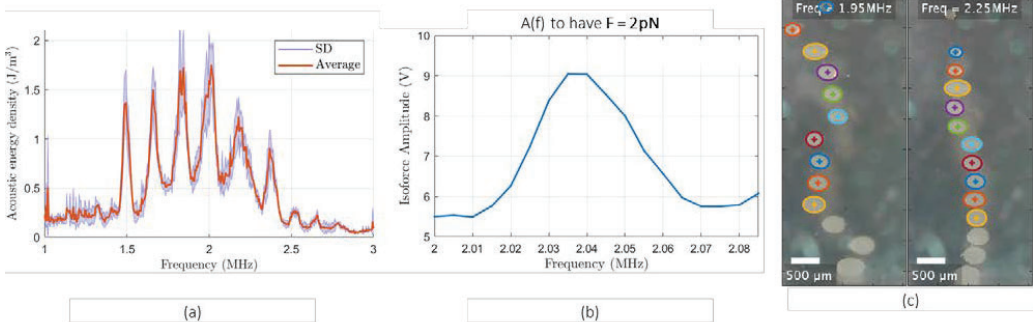

Figure 2: (a) Estimation of the acoustic energy density as a function of the frequency for a voltage of 7Vpp. (b) Calculation of the voltage amplitude to supply the transducer with a constant ARF on the particles. (c) Variation of the spheroid positions with frequency tuning. Two snapshots are showed but this manipulation was continuous.

Isoforce manipulation of cell spheroids

The measurement of $E_{ac}(F_{ac})$ provided the predefined pattern of the applied forces as a function of the frequency and the amplitudes of the generator signal. Using this knowledge, it was possible to change the amplitude of the signal to obtain a constant amplitude of the ARF while changing the frequency (Fig. 2b). The cell spheroids could then be moved closer to each other, and even assembled, just by tuning the acoustic frequency (Fig. 2c).

Conclusion

One application of this work is the manipulation and merging of cell spheroids in acoustic levitation. After the self-organization of the cells in acoustic levitation, it was possible to bring them closer and closer just by varying the acoustic frequency. This manipulation allows the interaction between two spheroids in acoustic levitation.

References

[1] Dron, O., and Aider, J.-L., Ultrasonics 53 (7), 1280-1287. (2013).
[2] Folds, D. L., and Loggins, C. D. J. Acoust. Soc. Am. 62 (5), 1102–1109. (1977).
[3] Karlsen, J. T., and Bruus, H. Phys. Rev. E 92(4), 043010. (2015).
[4] Jeger-Madiot, N., et al, J. Acoust. Soc. Am. 151 (6), 4165–4179. (2022).
[5] Thielicke, W., and Stamhuis, E. J. Open Res. Softw. 2, e30. (2014).

Transverse mode of bulk acoustic wave for sub-100 nm nanoparticles manipulations

Wei Wei[1], Zhaoxun Wang[1], Xuexin Duan[1]

School of Precision Instrument and Opto-electronics Engineering, Tianjin University, Tianjin, China
E-mail: xduan@tju.edu.cn, URL: http://www.tjumbios.com/

Introduction

Manipulations of sub-100 nanoparticles with high accuracy and stability still present as one of the major challenges in current acoustofluidic field, which is due to the fact that the acoustic radiation force decreases rapidly when particle size is below 100 nm[1]. To solve this issue, several strategies have been developed: combining the acoustic streaming force and the radiation force[2]; enhancing acoustic radiation force through oscillating nanocavities[3]; modulating the physical properties of the flow field by introducing additives in the solution[4]; increasing acoustic radiation force by designing nanoparticles with special properties[5]; and combing other fields, such as electrical or magnetic fields[6]. Here, we proposed a novel acoustofluidic approach for particles manipulations based on transverse mode of thin film bulk acoustic wave resonator (TBAW). TBAW can generate independent multi-mode resonances at different frequency and eventually induce different types of acoustic streaming patterns. Here, we investigated the possibility of TBAW for nanoparticles manipulations at different resonant modes. As a proof of concept, this single-chip TBAW is used to trap 70 nm nanoparticles and pattern them into rectangle shapes.

Experimental setup and working mechanism

TBAW was designed and fabricated through standard MEMS process, which has a resonant frequency of 2.60 GHz. From 2.4 to 2.6 GHz, multiple resonant modes can be identified (Fig. 1a). The displacement plan view of the device in the transverse mode were shown in Fig. 1b-d. In these modes, the vibration of the device is distributed periodically from the center, and the dynamic operation of particles can be realized by inducing different positions of vibration nodes and anti-vibration nodes (Fig. 2). It creates arrays of stagnation zone so called potential well due to the opposing streaming vortex flows, where defines the position of the trapped nanoparticles. The fluid stagnation zone in the middle of the vibration region is verified by finite element analysis (Fig. 2), where streaming velocity is close to 0. It is observed that the nanoparticles follow the fluid motion and eventually stop in the static zone due to the balance of the drag and radiation forces. Fig. 3a present the particles trapping setup, where a simple microfluidic channel was mounted on top of the device. 70 nm polystyrene nanoparticles were delivered into the channel. When turning on the device, TBAW can produce stable streaming patterns, the nanoparticles were been trapped in the potential well. At typical resonant modes, rectangle pattern shape were realized.

Conclusion

TBAW has been demonstrated as a promising tool for sub-100nm nanoparticles manipulation. A single chip can parallelly achieve quasi-static particles trapping and reconfigurable surface patterning at different resonant frequency. It has no strict restrictions on the density and acoustic impedance of nanoparticles and the solvents. In addition, the TBAW works at extremely low power range, which has high biological compatibility.
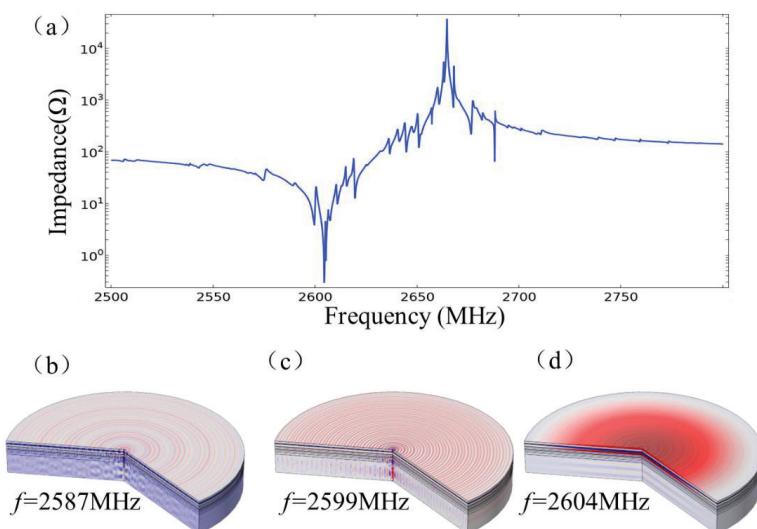
Figure 1: (a) 2.6GHz circular TBAW impedance characteristic curve. (b), (c) the displacement plan view of the device in the transverse mode near the main mode, and (d) the working state of the device in the main mode.
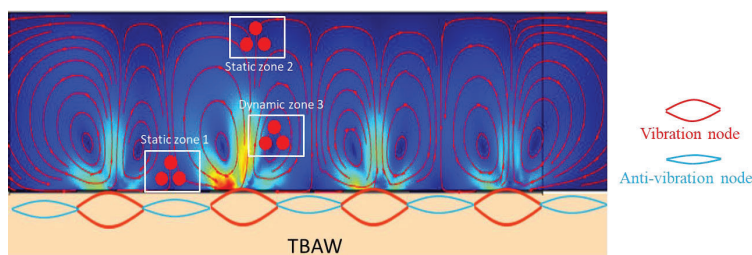

Figure 2: Graphical working principle and simulation streamline of acoustic fluid tweezers: red and blue marks represent vibration nodes and anti-vibration nodes respectively. And there are three different particle capture sites between the vortex and the vortex.
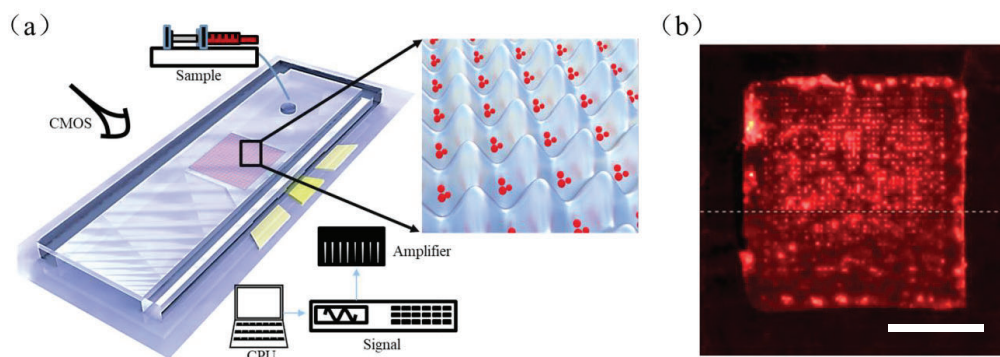

Figure 3: (a) Illustration of the TBAW system; (b) 70 nm red fluorescence polystyrene beads are patterned on square shapes. Scale bar: 50 μm;

References

[1]Xie Y, Rufo J, Zhong R, et al. ACS Nano, 2020, 14(12): 16220–16240.
[2]Collins D J, Ma Z, Han J, et al. Lab on a Chip, 2017, 17(1): 91–103.
[3]Tayebi M, O'Rorke R, Wong H C, et al. Small, 2020, 16(17): 2000462.
[4]Zhao L, Niu P, Casals E, et al. Lab on a Chip, 2021, 21(4): 660–667.
[5]Zhou W, Chen M, Liu X, et al. Lab on a Chip, 2019, 19(20): 3387–3396.
[6]Zhang P, Rufo J, Chen C, et al. Nature Communications, 2021, 12(1).

3D cell rotation based on a vibration-induced flow

Hiroyasu Kobayashi, Yuha Koike, and Takeshi Hayakawa

Department of Precision Engineering, Chuo University, Tokyo, Japan
E-mail: hayaka-t@mech.chuo-u.ac.jp, URL: https://www.mech.chuo-u.ac.jp/~hayakawalab/

Introduction

  The techniques of on-chip 3D cell rotation benefit various fields such as medicine and transgenic animal researches. Conventionally, on-chip cell rotation methods using acoustic streaming were proposed [1,2]. However, it is difficult to access to target cells from outside of the chip due to their closed structure. Moreover, 3D cell rotation in a stable position is difficult with these methods. Therefore, we propose a method to enable 3D cell rotation in a stable position with an opened chip which is easily accessed from outside of it. Therefore, we propose 3D cell rotation method with opened chip structure by using vibration-induced flow, in this study.

Method

  A vibration-induced flow (VIF) is a local flow that occurs around microstructures when vibrations of $\approx$ 100 Hz are applied to the microstructures. This phenomenon occurs even in an opened chip. By applying circular vibration to a micropillar, a rotational flow is generated around the structure, as shown in Fig. 1 (a-1). This flow can be used for two-dimensional manipulation like a horizontal cell rotation [3]. Moreover, applying rectilinear vibration causes a flow in a height direction of the micropillar, as shown in Fig. 1 (a-2). This out-of-plane flow makes vertical rotation of a cell possible. Therefore, by combining these horizontal and vertical rotations 3D cell rotation become possible with opened chip, as shown in Fig. 1 (b).

  In this study, we analyzed the out-of-plane flow that occurs when rectilinear vibration is applied to a single pillar. From the analyzed results, we designed microstructures to realize a 3D cell rotation and succeeded in the 3D cell rotation using a VIF. Moreover, we demonstrated an orientation control of a mouse oocyte.
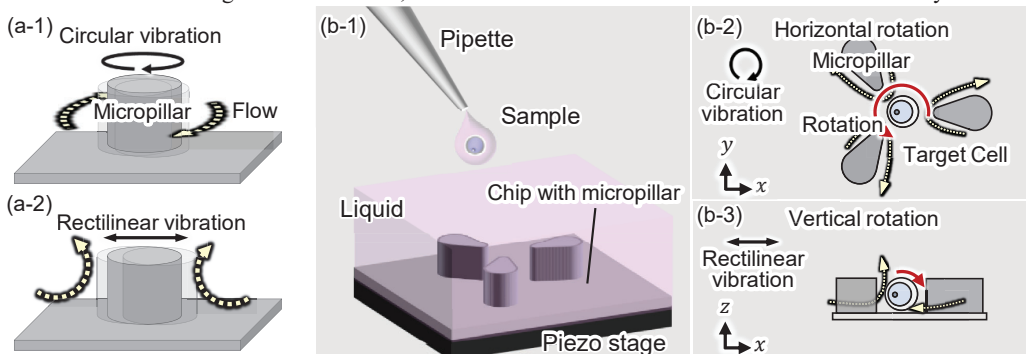

Figure 1: Concept, (a) VIF with circular and rectilinear vibrations, (b) Concept of the 3D cell rotation.

Particle Image Velocimetry (PIV) analysis

  We fixed a chip to a chamber and attached the chamber to a piezo stage on a microscope. In addition, the chamber was filled with a water mixed with fluorescent particles. We irradiated a sheet laser to excite the fluorescent particles on the observation plane, as shown in Fig. 2 (a). PIV analysis software (KATO KOKEN, Flow Expert) was used for analysis of the flow.

  Micropillar were fabricated with a diameter of 150 μm and a height of 200 μm. The applied frequency was 300 Hz, and the applied voltage was 120 V. When x-axis vibration was applied to the pillar, an out-of-plane flow is generated in the direction toward the pillar, as shown in Fig. 2 (b-1). When y-axis vibration was applied to the pillar, an out of plane flow was generated in the direction away from the pillar, as shown in Fig. 2 (b-2).

  We fabricated microstructures for 3D cell rotation, as shown in Figure 2 (c). The applied frequency was 300 Hz, and the applied voltage was 25 V. Figure 2 (d-1) shows the result of PIV of a flow which is generated when x-axis vibration is applied. From Fig. 2 (d-1), we can confirm that the flow can rotate a cell in clockwise (CW) direction in the vertical plane. Similarly, when y-axis vibration is applied to the structures, the induced flow can rotate a cell in counterclockwise (CCW) direction, as shown in Fig. 2 (d-2).
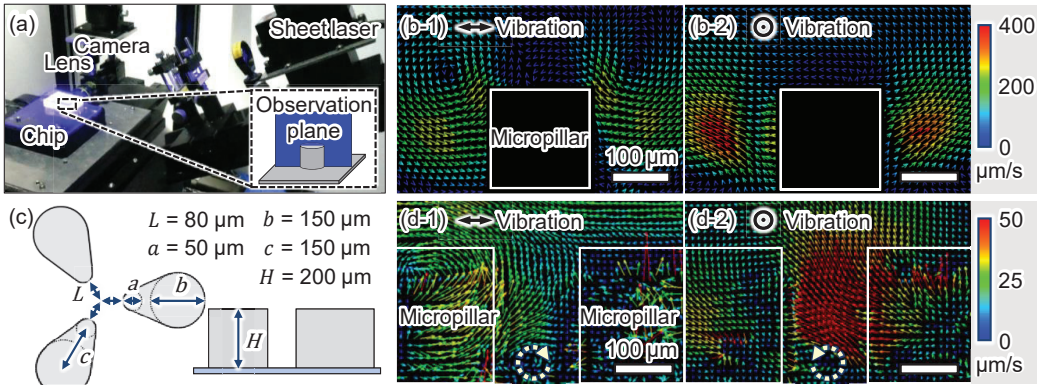
Figure 2: Experiments and results, (a) Experimental system, (b) Results of PIV analysis around a micropillar, (c) Design of the microstructure for 3D cell rotation, (d) Results of PIV analysis around the microstructures for 3D cell rotation.

3D cell rotation

Horizontal rotation of a mouse oocyte was realized by applying circular vibration to the designed microstructures, as shown in Fig. 3 (a). We also evaluated angular velocities of the rotation when voltages corresponding to amplitudes of vibrations were changed, as shown in Fig. 3 (b). The angular velocity increased as the voltage increased. Both CW and CCW rotation were achieved by switching the direction of applied circular vibration. We also succeeded in vertical rotation of a mouse oocyte by applying rectilinear vibration to the designed microstructures, as shown in Fig. 3 (c). In addition, it was confirmed that the angular velocity increases as the voltage increases, as shown in Fig. 3 (d). We succeeded in switching the direction of cell rotation in the vertical plane by switching the direction of rectilinear vibration, as explained in Fig. 2 (d).

Finally, we demonstrated an orientation control of a mouse oocytes. We succeeded in positioning of a nucleus of the cell by combining horizontal and vertical rotations, as shown in Fig. 3 (e).
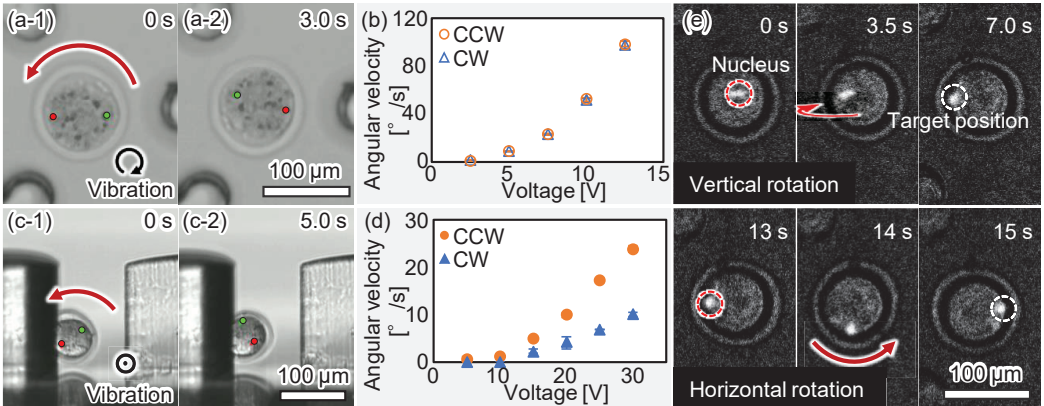

Figure 3: Experimental results of rotation of a mouse oocyte, (a) microscopic images of a horizontal rotation (300 Hz, 10 V), (b) angular velocities of horizontal rotations with various input voltages, (c) microscopic images of a vertical rotation (300 Hz, 25 V), (d) angular velocities of vertical rotations with various input voltages, (e) fluorescent images of nucleus during the demonstration of an orientation control.

Conclusion

We succeeded in analyzing out-of-plane flow and switching horizontal and vertical rotation by switching the vibration pattern from circular vibration to rectilinear vibration. In addition, we succeeded in switching the direction of rotation by switching the direction of vibration. This study showed that 3D cell rotation can be performed with an open chip structure by using VIF.

References
[1] Ozcelik, Adem, et al. small **12.37**, 5120-5125 (2016).
[2] Läubli, Nino F., et al. Nature communications **12.1**, 1-11 (2021).
[3] Hayakawa Takeshi, Shinya Sakuma, and Fumihito Arai. Microsystems & nanoengineering **1.1**, 1-9 (2015).

High Performance Acoustofluidic Particle Focusing in Silicon-Based and Polymer-Based Devices Using Lateral Modes of Plate Transducers

Andreas Fuchsluger[1], Annalisa De Pastina[2], Norbert Cselyuszka[2], Nikolai Andrianov[2], Ali Roshanghias[2], Rafael Ecker[1], Tina Mitteramskogler[1], Thomas Voglhuber-Brunnmaier[1], Mohssen Moridi[2], Bernhard Jakoby[1]

[1]Institute for Microelectronics and Microsensors, Johannes Kepler University Linz, Linz, Austria
E-mail: andreas.fuchsluger@jku.at, URL: https://www.jku.at/ime
[2]Silicon Austria Labs, Microsystems, Villach, Austria

Introduction

We present the employment of lateral modes of piezoceramic plate transducers using the transverse piezoelectric effect for rapid acoustophoretic particle focusing in both silicon-based and polymer-based microfluidic chips. Based on the results of numeric simulations, we designed and fabricated high-performant silicon/glass chips capable of particle focusing in the experiment with an acoustic energy density E_{ac} of more than 100 J m^{-3} at 22 V$_{pp}$ and 544 kHz actuation. In a polymer-based device we observed particle focusing with E_{ac} reaching about 15 J m^{-3} at 22 V$_{pp}$ and 508 kHz actuation. Here, we are able to solve the paradox of particle focusing—which is assumed to require an anti-symmetrical pressure wave inside the channel—in a completely symmetric and symmetrically actuated system with the help of simulations. Although our models and investigations are similar to other work, e.g. [1-5], to the best of our knowledge, we are the first who explicitly employ lateral modes of piezoceramic plate transducers for acoustofluidic particle manipulation.

The Device

Our acoustofluidic devices (Fig. 1) in the simulation as well as in the experiment consist of a ca. 1 mm thick PZT plate transducer attached to microfluidic chips that are made out of silicon/glass or polymethylmethacrylate (PMMA). We use glycerol as acoustic coupling medium between the chip and the transducer. The channel is filled with water and in the experiment, we additionally use polystyrene (PS) or PMMA beads as tracer particles and a small amount of detergent. The PZT is actuated symmetrically by two electrodes (bottom and top electrode) or anti-symmetrically by a three-electrode design (two bottom electrodes and electrically floating top electrode).

Simulation Results

Our numerical simulations reveal very pronounced Lamb-wave-like oscillations of the PZT transducer (Fig. 2) where the material is vibrating in the horizontal plane (indicated by arrows) with n nodes (blue regions). For a silicon/glass chip, we use anti-symmetric actuation to drive the $n = 2$ lateral mode of the PZT (Fig. 2a) resulting in a flexural mode in the chip material. We observe a "roof mode" (indicated by arrows) where the roof of the channel performs a beam-like vibration towards the channel floor, which is leading to a pressure distribution inside the channel (Fig. 2a inset) that has minimal amplitude (i.e. a pressure node) in the center of the channel and would lead to particle focusing in the middle of the channel in our experimental setting. For PMMA chips we also find stable (i.e., not an artifact due to discretization of the problem) particle focusing pressure distributions when actuating the PZT symmetrically, e.g., in $n = 3$ mode (Fig. 2b). This is surprising, because if one assumes a one-dimensional standing half pressure wave (which is anti-symmetric) inside the channel, this should not be possible in our totally symmetric system. So, the one-dimensional assumption is not valid here and what we see in the inset in Fig. 2b is the amplitude of a two-dimensional standing pressure wave that is generated through top and bottom channel wall oscillations (indicated by arrows).
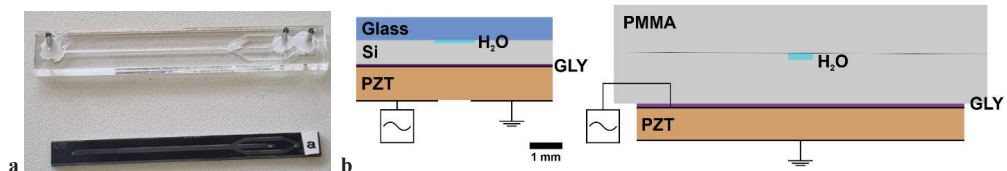

Figure 1: (a) Photograph of the silicon/glass chip (bottom) and the PMMA chip (top). (b) Composition and operational principle of the silicon/glass device with anti-symmetric actuated PZT (left) and the PMMA device with symmetrically actuated PZT (right). A thin film of glycerol (GLY) is used as acoustic coupling medium.
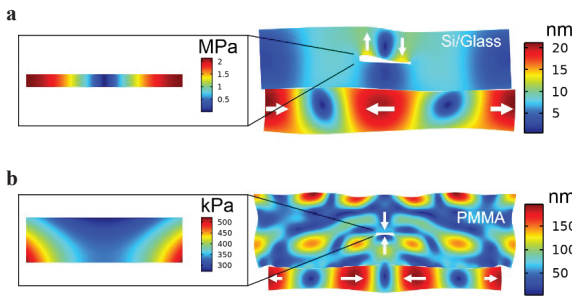
Figure 2: Simulations of (a) a 6 mm wide silicon-glass chip with a 1240 μm wide channel using the n = 2 lateral mode of a 6 mm wide PZT plate at 20 V_{pp} and 539 kHz and (b) a 11.4 mm wide PMMA chip with a 700 μm wide channel using the n = 3 lateral mode of a 10 mm wide transducer at 20 V_{pp} and 518.5 kHz. The color map represents the root mean square displacement in the chip and transducer. The deformation scale factor is (a) 5,000 and (b) 1,000. Instantaneous movement in the material is indicated by arrows. The insets show the pressure amplitude inside the channels.

Experimental Results

With a chip design based on the numerically optimized geometry for a lateral mode of the plate transducer, we fabricated high-performant silicon-based microfluidic chips enabling rapid and accurate acoustofluidic particle focusing (Fig. 3a,b). The transparency of our particles does not allow to apply the intensity-based method presented in [6] for measuring E_{ac}. However, with the focusing time of 0.4 s and using the underlying formulas from [6], we can estimate that the acoustic energy density is exceeding 100 J m^{-3} in the silicon-based chip. Here, we did not observe significant heat generation of the device, indicating low damping of the lateral mode of the PZT, which is also visible in low attenuation of the resonance peak in the admittance spectrum of the mounted transducer compared to that of the free transducer. Using an infrared camera, we measured an increase in temperature of less than 5 K over 5 minutes with a flattening curve without fluid flow in the channel nor ventilation of the chip. By experimentally exploring different PMMA based chips, we encountered good particle focusing capability for a system where the transducer is actuated symmetrically (Fig. 3c,d). The unexpected high acoustic energy density of around 15 J m^{-3} can be explained by the simulation above.
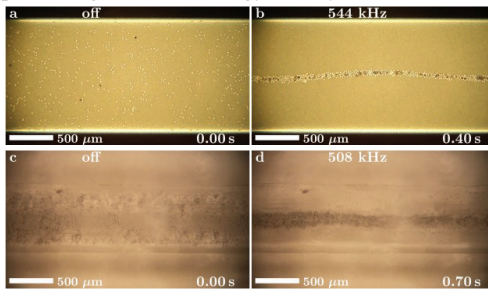

Figure 3: Experimental results: (a,b) Focusing of 20 μm PS beads in a 6 mm wide silicon-glass chip with a 1.24 mm wide channel in 0.40 seconds using the anti-symmetric n = 2 lateral mode of the PZT transducer. The dark spots are shadows of particles that are floating above the channel ground. (c,d) Focusing of 20 μm PMMA beads in a 11.4 mm wide PMMA chip and 0.7 mm wide channel in 0.7 seconds using the symmetric n = 3 lateral mode of the PZT transducer.

Conclusion

Via numerical simulations and experiments, we demonstrated for the first time, the application of lateral modes of piezoceramic plate transducers for acoustofluidic particle focusing in silicon-based and polymer-based microfluidic chips. The employment of this lateral modes is very promising to lead to high performant acoustofluidic devices which furthermore do not suffer from serious thermal problems due to heat generation. In the near future, we expect that refining our numerical model along with device optimization will allow an increase in the acoustic energy density by a factor of two for the silicon-based chips, achieving more than 200 J m^{-3}. According to simulations, using anti-symmetric actuation as well and adapting the geometry of the chip, the possible improvement for the PMMA-based device is even higher—reaching up to 3 MPa difference in the pressure amplitude inside the channel—compared to the results using symmetric actuation that were presented here with 0.25 MPa pressure difference. But we tend to be careful with declarations made in advance for PMMA, because we observed that polymer-based devices are less predictable and simulation results can be less reliable with respect to silicon-based chips. Nonetheless, we have found some amazing results, which we are looking forward to presenting for the international acoustofluidics community at the *Acoustofluidics 2022 in person Conference* on 19 - 21 October 2022.

References

[1] M. Bora and M. Shusteff. Lab Chip 15, 3192-3202 (2015).
[2] F. Garofal, T. Laurell, and H. Bruus. Physical Review Applied 7, 054026 (2017).
[3] R. P. Moiseyenko, and H. Bruus. Physical Review Applied 11, 014014 (2019).
[4] A. Tahmasebipour, L. Friedrich, M. Begley, H. Bruus, and C. Meinhart. J. Acoust. Soc. Am. 148, 359-373 (2020).
[5] F. Lickert, M. Ohlin, H. Bruus, and P. Ohlsson. J. Acoust. Soc. Am. 149, 4281-4291 (2021).
[6] R. Barnkop, I. Iranmanesh, M. Wiklund, and H. Bruus. Lab Chip 12, 2337-2344 (2012).

In-flow measurement of acoustic mobility

Thierry Baasch[1], Linda Péroux[1], Andreas Lenshof[1] and Thomas Laurell[1]

[1]Department of Biomedical Engineering, Lund University, Lund, Sweden
E-mail: Thierry.baasch@bme.lth.se

Introduction

The acoustic mobility is the most important parameter for acoustophoresis based separations. Assessing the acoustic mobility and thus the acoustic properties of particles or cells has long been a challenging procedure. Many approaches are tedious and rely on focusing experiments in stopped flow that require the tracking of individual particles [1, 2]. While the focusing experiments under stopped flow have the potential to measure properties on single particle/cell level, the procedure is time consuming, and many repeats are necessary to acquire statistically relevant data. Here, we present a very simple and fast method to measure the acoustic mobility inflow.

Method

The acoustic mobility, which is intrinsic to the manipulated particles, is proportional to the acoustophoretic migration velocity and therefore defines the motion of particles inside an acoustic field. Acoustic particle separation relies on differences in acoustic mobility to separate one species from another. Here, we exploit the particle trajectories and especially the relative position of two particle species of different acoustic mobility to directly measure the ratio between their respective acoustic mobilities. For our procedure, **no knowledge or measurement of the viscosity of the surrounding medium, flowrate or acoustic energy is needed**. The two particle types are introduced into the separation device (Fig. 1) at a sample flowrate of 30 µL/min and a concentration of 0.001 % w/v each. The mobility ratio between a species 1 (contrast factor Φ_1 and radius a_1) and a species 2 (contrast factor Φ_2 and radius a_2) can then be found by

$$\text{mr}(1,2) = \frac{\Phi_1 a_1^2}{\Phi_2 a_2^2} = \frac{\int_{y_0}^{y_{e1}} \frac{v_x(y)}{\sin(2ky)} dy}{\int_{y_0}^{y_{e2}} \frac{v_x(y)}{\sin(2ky)} dy},$$

where y_0, y_{e1} and y_{e2} are defined in Fig. 2. One measurement consists of collecting y_0, this can be done without any actuation in the main channel and then increasing the actuation voltage to measure the whole separation curve (Fig. 3). The maximum of the separation curve then gives the most reliable mobility ratio measurement. We performed the measurements with 6 different particle types (summarized in Table 1).

species 1	red 9.89	red 9.89	red 7.76	red 7.76	**red 7.76**
species 2	green 7.81	green 5.18	red 4.99	green 5.18	**green 5.00**
meas. mr(1,2)	1.50, 1.51, 1.50	3.31, 3.36, 3.12	2.20, 2.23, 2.22	2.1, 2.12, 2.14	**2.27, 2.33, 2.28**
expected mr(1,2)	1.60	3.64	2.42	2.24	**2.41**
green 7.81	green 7.81	red 9.89	red 9.89	red 9.89	green 7.81
red 4.99	green 5.18	red 7.76	red 4.99	green 5.00	green 5.00
2.14, 2.29, 2.22	2.08, 2.16, 2.15	1.49, 1.47, 1.47	3.48, 3.18, 3.39	3.69, 3.28, 3.22	2.39, 2.24, 2.24
2.45	2.27	1.62	3.92	3.91	2.44

Table 1: Summary of the acoustic mobility ratios for different colored fluorescent polystyrene particles. All particles are obtained from the Microparticles GMBH, with exception of the 5 µm green particles which were obtained from Thermofisher. The expected mobility ratio is based on the manufacturer data of the particle diameter only.

Conclusion

We have developed a novel and fast measurement technique to measure the acoustic mobility ratio between two species of particles in flow, without any knowledge of the buffer viscosity, flowrate, or acoustic energy density. The measured values are in a 10% range of the expected values calculated from the particle sizes. The variation could be explained by manufacturing variability of the different particle types.

Acknowledgements

References
[1] D. Hartono, Y. Liu, P. L. Tan, X. Y. S. Then, L. Y. L. Yung, and K. M. Lim. Lab on a Chip **11**, 4072-4080 (2011).
[2] T. Baasch, P. Reichert, S. Lakämper, N. Vertti-Quintero, G. Hack, X. Casadevall I Solvas, A. de Mello, R. Gunawan, J. Dual. Biophysical journal **115**, 1817-1825 (2018).
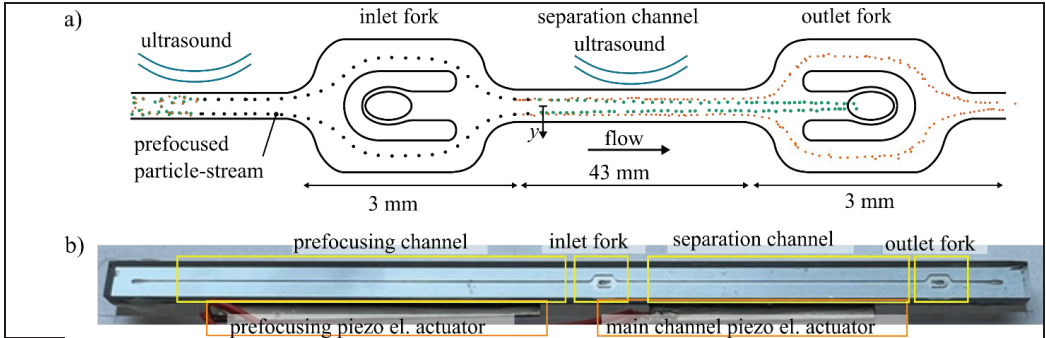
Figure 1: The figure shows a schematic (a) and photograph (b) of the acoustophoretic separation device that was used to measure acoustic mobility ratios of polystyrene particles. The channels are etched into silicon and sealed by a bonded glass slide. The acoustic fields are actuated by piezo-electric actuators. The particles enter the device through the pre-focusing channel inside which two acoustic modes focus them into two thin bands at channel ½-height. The separation takes place in the main (separation) channel. Here, the have wavelength mode is actuated in the y direction. The particles migrate at velocities proportional to their respective acoustic mobilities towards the pressure nodal plane at y=0.
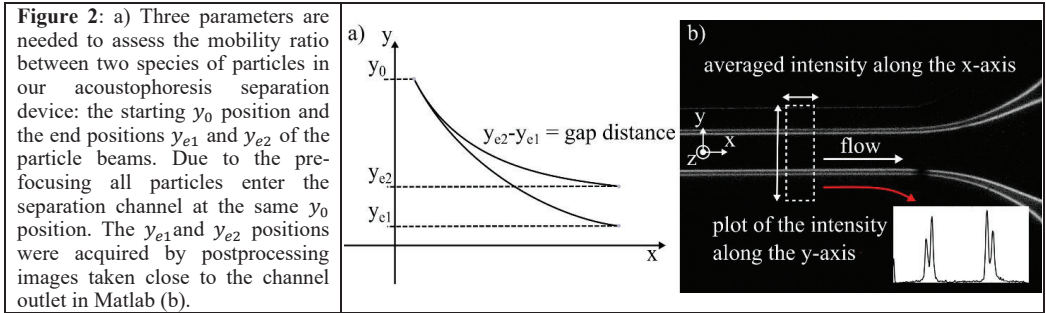

Figure 2: a) Three parameters are needed to assess the mobility ratio between two species of particles in our acoustophoresis separation device: the starting y_0 position and the end positions y_{e1} and y_{e2} of the particle beams. Due to the pre-focusing all particles enter the separation channel at the same y_0 position. The y_{e1} and y_{e2} positions were acquired by postprocessing images taken close to the channel outlet in Matlab (b).
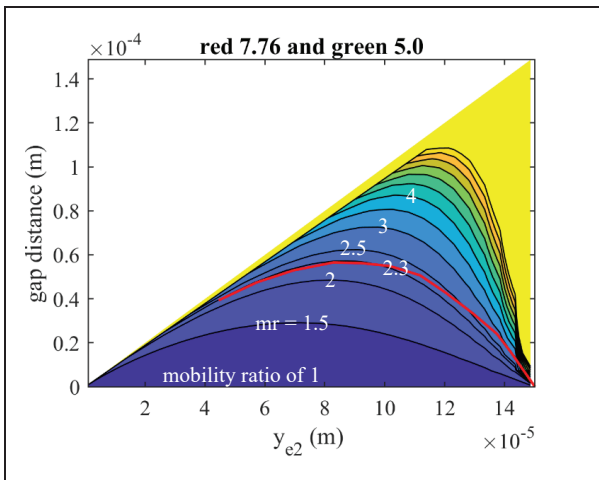

Figure 3: The figure is a graphical representation of eq. 1. The black isolines and the colored background are theoretical calculations while the red line is data obtained from measurements with red 7.76 μm PS (microparticles GMBH) and green 5 μm PS (Thermofisher) particles. Every of the black isolines corresponds to a specific mobility ratio and shows the gap distance as a function of y_{e2}. Some care is required when the separation curve (red) is to be used as a measurement of the acoustic mobility ratio. For small gap distances the error propagation is very large, i.e. small measurement errors lead to large deviations in the measured mobility ratio. This can be counteracted by taking the maximum of the separation curve as the final measurement. A summary of many measurements, based on maxima of the separation curve, is shown in Table 1.

Constant voltage versus constant power in acoustofluidic applications

Fabian Lickert, Henrik Bruus, and Massimiliano Rossi

Department of Physics, Technical University of Denmark, Kongens Lyngby, Denmark
E-mail: fabianl@dtu.dk, URL: www.fysik.dtu.dk/microfluidics

Introduction
The acoustic energy density for a given voltage amplitude is a commonly used performance indicator for many acoustofluidic devices. Often, however, the corresponding literature only states the actuation voltage without specifying how this value was measured. In recent studies comparing device performances [1], a constant-power approach has been used, where the power dissipation rather than the actuation voltage is kept constant. In this work we explore how different actuation methods, such as constant power versus constant voltage, impact particle focusing at various frequencies.

Experimental setup
Experiments were performed on a glass capillary tube (VitroTubes, VitroCOM), filled with with a neutrally-buoyant solution containing 10-μm-diameter polystyrene particles. The glass capillary was glued on a disk-shaped piezoelectric transducer (Pz27, Meggitt A/S) using UV-curable glue (NOA 86H, Norland Products). An overview of the experimental setup is shown in Fig. 1. The acoustic focusing was studied using 3D particle tracking performed with the general defocusing particle tracking (GDPT) method [2]. The GDPT setup used a cylindrical lens and 200 images recorded at 25 frames per second at frequencies in the range from 3.3 to 4.3 MHz in steps of 10 kHz. Using the four-probe setup sketched in Fig. 1(a), the voltage amplitude φ_{pzt} directly across at the transducer and the voltage amplitude φ_{gen} of the signal generator were both recorded during the measurements. First, measurements of the particle trajectories were performed with the transducer voltage amplitude stabilized at $\varphi_{\mathrm{pzt}} = 0.5$ V. In a second measurement, the average power dissipation of the transducer was kept constant at $\langle P_{\mathrm{diss}} \rangle = 50$ mW. Using the toolbox *defocustracker* [2], we obtain the x-, y-, and z-coordinates of the particles at each frame and frequency. The average particle velocity is then calculated as $\langle v_z^{\mathrm{exp}} \rangle = \partial_t \langle s_z \rangle |_{t=t_{\mathrm{exp}}}$ at time $t_{\mathrm{exp}} = 40$ ms (after turning on the acoustics), where $\langle s_z \rangle (t)$ is the average cumulative particle displacement in the z-direction.

Numerical simulations
A quarter of the actual device geometry was simulated using the finite-element software *COMSOL Multiphysics*, as seen in Fig. 1(c) and (d), with dimensions and parameters matching the experimental setup. To simulate the lack of reflected waves from the end of the long capillary tube, a perfectly-matched layer (PML) was implemented at the end of a shorter version of the tube. In our simulation a frequency sweep from 3.3 to 4.3 MHz was performed in steps of 10 kHz. Using the *Particle Tracing for Fluid Flow* module, we computed the particle trajectories of 1000 randomly distributed particles. We then calculated the average particle velocity $\langle v_z^{\mathrm{sim}} \rangle = \frac{1}{N} \sum_{i=1}^{N} |v_z(t_{\mathrm{sim}})|$ at time $t_{\mathrm{sim}} = (40 t_{\mathrm{foc}}^{\mathrm{sim}}/t_{\mathrm{foc}}^{\mathrm{exp}})$ ms, where $t_{\mathrm{foc}}^{\mathrm{sim}}/t_{\mathrm{foc}}^{\mathrm{exp}}$ is the ratio between the numerical and experimental focusing time at resonance.
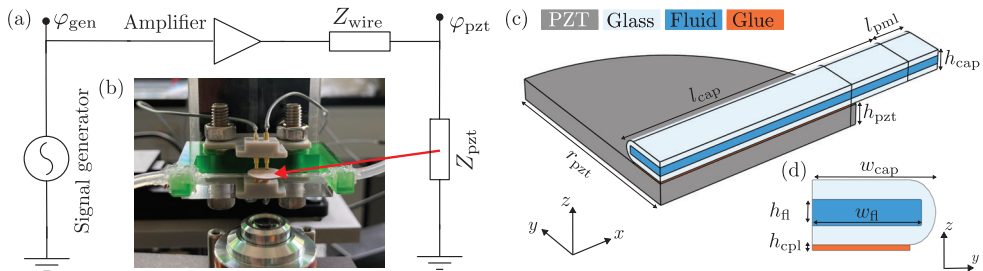

Figure 1: (a) Schematic drawing of the electrical circuit consisting of signal generator, amplifier, parasitic wire impedance Z_{wire} and the piezoelectric transducer with impedance Z_{pzt}. (b) Overview of the experimental setup. (c) Sketch of the quarter-geometry that was simulated in COMSOL with dimensions $r_{\mathrm{pzt}} = 5.02$ mm, $h_{\mathrm{pzt}} = 506$ μm, $w_{\mathrm{fl}} = 2060$ μm, $h_{\mathrm{fl}} = 200$ μm, $h_{\mathrm{cpl}} = 39$ μm, $w_{\mathrm{cap}} = 2324$ μm, $h_{\mathrm{cap}} = 483$ μm, $l_{\mathrm{cap}} = 6.44$ mm, and $l_{\mathrm{pml}} = 839$ μm. (d) Cross-sectional view of the capillary tube and coupling layer in the yz-plane.
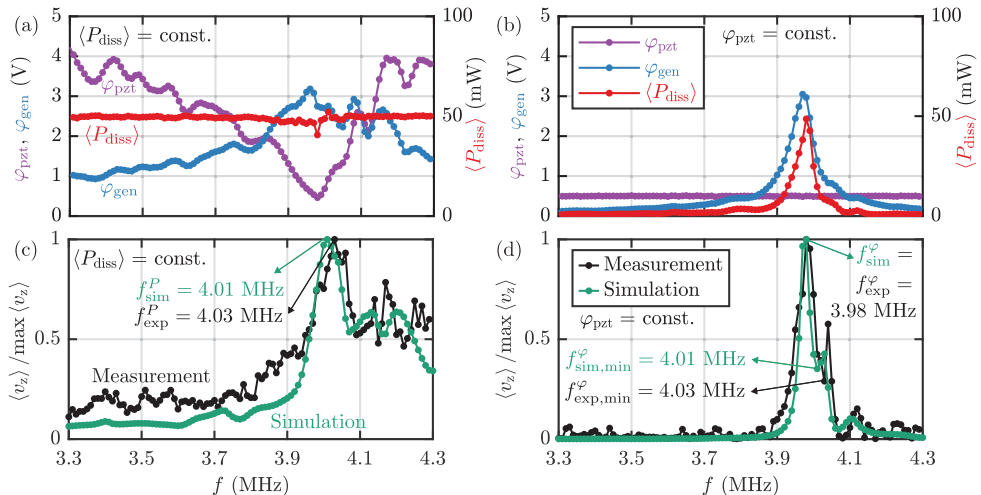
Figure 2: (a) Measured generator voltage φ_{gen} (blue), transducer voltage φ_{pzt} (magenta), and power dissipation $\langle P_{\text{diss}} \rangle$ (red) plotted versus frequency f at constant-power dissipation $\langle P_{\text{diss}} \rangle = 50$ mW. (b) Same as (a) but at constant transducer voltage $\varphi_{\text{pzt}} = 0.5$ V. (c) The experimental (black) and simulated (green) normalized average particle velocity $\langle v_z \rangle / \max \langle v_z \rangle$ versus frequency f at constant-power dissipation $\langle P_{\text{diss}} \rangle = 50$ mW. (d) Same as (c) but at constant transducer voltage $\varphi_{\text{pzt}} = 0.5$ V.

Experimental and numerical results

Going from constant power to constant voltage, our experiments (shown in Fig. 2) reveal a clear change in the particle-velocity spectrum and a slight 40-kHz downward shift of the system's resonance frequency near 4 MHz. In Fig. 2(c)-(d), we find good agreement between the simulated and the measured resonance frequencies: For constant $\langle P_{\text{diss}} \rangle = 50$ mW, the simulated and measured resonance frequencies are found at $f_{\text{sim}}^{P} = 4.01$ MHz and $f_{\text{exp}}^{P} = 4.03$ MHz respectively. For constant voltage $\varphi_{\text{pzt}} = 0.5$ V, we find the resonance frequency $f_{\text{exp}}^{\varphi} = f_{\text{sim}}^{\varphi} = 3.98$ MHz to be coinciding with the point of lowest impedance or correspondingly the point of highest power dissipation. Fig. 2(a)-(b) emphasize the need of monitoring φ_{pzt} and $\langle P_{\text{diss}} \rangle$ and specifying which of them are kept constant. When the electrical impedance $|Z_{\text{pzt}}|$ falls below the parasitic wire impedance $|Z_{\text{wire}}|$ more than half of the input power is lost on the wire, so to maintain a constant power in the piezoelectric transducer the input voltage needs to be adjusted depending on the frequency. Further parasitic effects such as non-linear gain of the amplifier contribute to big discrepancies between theoretical voltage output at the amplifier and actual voltage amplitude at the transducer. It appears that operating in the local minimum found in the constant-voltage measurement (Fig. 2(d)) at $f_{\text{sim,min}}^{\varphi} = 4.01$ MHz and $f_{\text{exp,min}}^{\varphi} = 4.03$ MHz is the most power-efficient, as the resonances shown in Fig. 2(c) confirm. Operating directly at the transducer resonance at $f_{\text{sim}}^{\varphi} = f_{\text{exp}}^{\varphi} = 3.98$ MHz is problematic due to the low impedance of the transducer and the resulting high power dissipation at this frequency.

Conclusion

Monitoring voltage and power dissipation of the piezoelectric transducer is important and helpful for understanding and optimizing the system performance. Constant-power dissipation of the piezoelectric transducer appears to be a better measure to compare device performance across frequencies, as this compensates for the decrease of impedance at the transducer resonance. Constant-voltage measurements often result in high power dissipation at the resonance frequency of the transducer. Acoustofluidic applications, however, are often limited by power-limitations of the frequency generator or the amplifier, as well as heating of the transducer. Constant-power measurements can help to identify the most power-efficient frequencies leading to the desired acoustic response and allow a more fair comparison of the different resonances across the frequency spectrum.

Acknowledgments

References

[1] Wei Qiu, Thierry Baasch, and Thomas Laurell, Phys. Rev. Applied **17**, 044043 (2022). [doi]
[2] R. Barnkob and M. Rossi, J. Open Res. Softw., **9**(1), 22 (2021) [doi]

Acoustic microstreaming induced by a substrate-attached acoustic microbubble

Claude Inserra[1], Maxime Fauconnier[1], Jean-Christophe Béra[1], Cyril Mauger[2], Alexander Doinikov[2] and Philippe Blanc-Benon[2]

[1]LabTAU, University of Lyon, Université Claude Bernard Lyon 1, Lyon, France
E-mail: claude.inserra@inserm.fr
[2]INSA Lyon, Ecole Centrale de Lyon, Ecully, France

Introduction

Microbubbles can serve as actuators for the stretching, rupture and lysis of biological cells in microfluidic devices [1]. In this context, they are commonly maintained at stable location as being attached to a substrate, which significantly modifies the bubble interface dynamics through the emergence of asymmetric shape instabilities [2]. These shape oscillations are favored as being responsible of steady fluid flow, called microstreaming, in the vicinity of the bubble interface. In this study, we investigate the correlation between the dynamics of the bubble shape interface with its induced microstreaming in the case of a bubble experiencing asymmetric shape oscillations.

Materials and methods

A microbubble is nucleated by electrolysis by means of a signal generator (Agilent 33210A, squared signal, peak-to-peak amplitude 4 Vpp, offset 2 Vpp, 50% duty cycle). A three-axis hydraulic micromanipulator (Narishige MMO-203) allows the positioning of the microbubble at the bottom of a polymethyl methacrylate tank filled with pure water (Milli-Q® IQ 7000) with added NaCl as a concentration of 24 mg/L $\pm$ 1 mg/L. The bubble is then driven by a 30-kHz Langevin transducer (Reson®, 30-kHz nominal frequency, high-voltage gain amplifier Trek 50/750) with acoustic pressures up to 40 kPa, supplied by a signal generator (Agilent 33220A). Above a certain pressure threshold, shape instabilities of the bubble interface are triggered, a phenomenon that results in microstreaming. The microstreaming pattern is obtained by tracking seeded microparticles (Fluoro-max red beads 3.2 µm, Fisher ThermoScientific) in the vicinity of the bubble interface. Thence, the time-resolved bubble dynamics and the resulting fluid motion are captured by an ultra-fast camera that alternates between two recording frame rates (67 kHz and 900 Hz) in order to observe the two mechanisms quasi-simultaneously. We have recently developed an original image processing technique based on a spatiotemporal Fourier transform that allows the extraction of the modal content of a wall-attached bubble from its top-viewed contour [3].

Results

The variety of asymmetric shape oscillations make the analysis of the bubble interface complex in a 2D visualization. However, a class of asymmetric modes linked to particular spherical harmonics $Y_{nm}(\theta, \phi)$, called sectoral modes, are easily recognizable from a top-view observation of the bubble. Such a sectoral bubble possesses an azimuthal that correspond to a $\cos(m\phi)$ function where $n = m$ corresponds to the mode order. In Figure 2 (left), a substrate-attached bubble is oscillating on a sectoral mode $n = m = 5$, for instance. Such a bubble may produce two typical microstreaming signatures (Figure 2): one is a lobe-type pattern with close curved trajectories of the particles that start and end at the bubble interface, the other is a star-shape pattern where particles are ejected far from the bubble interface with a high velocity. It is known that microstreaming results from the interaction between two modes oscillating at the same frequency [9]. Since the sectoral mode we observed is produced through parametric instability, and hence oscillate at half the driving frequency, no possible interaction with the radial mode may explain the generated fluid flow. As a consequence, the microstreaming may arise only from the self-interaction of a sectoral mode with itself or form the interaction of a sectoral mode with another shape mode. By quantifying the modal content of the bubble interface for the two microstreaming patterns shown in Figure 2, we revealed that star-shape patterns are obtained in the case of the interaction between a zonal (axisymmetric mode with $m = 0$) and the sectoral mode, while the lobe-type pattern results mainly from the self-interacting sectoral oscillation.

We have also performed a particle tracking velocimetry analysis on several dataset in which a zonal and sectoral modes were exciting and interacting, from degrees $n = 3$ to $n = 6$. This investigation arises from the desire to find the best way of generating intense flows, and reaching high streaming velocities. This analysis demonstrated that interaction of zonal and sectoral modes results in a powerful streaming flow in comparison to the flow resulting from each mode taken separately, zonal only or sectoral only.
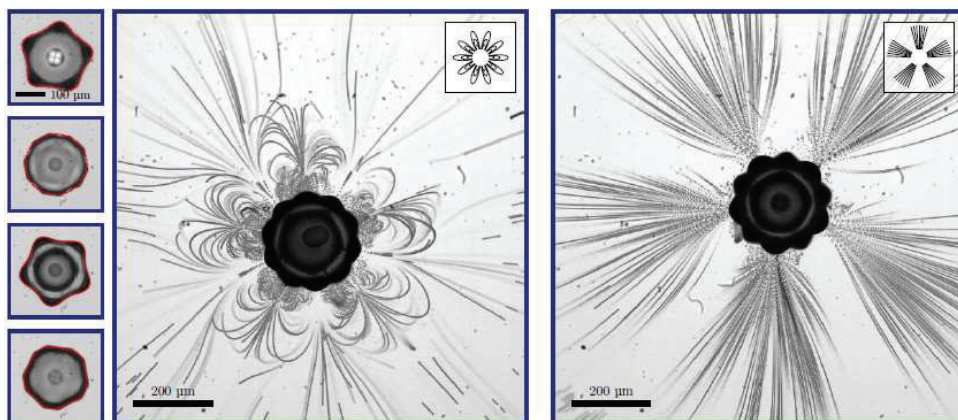
Acoustofluidics 2022, 19 - 21 October
Glasgow, Scotland, UK

Figure 1: Left row: nonspherical contour of a bubble experiencing a sectoral mode n=m=5. This oscillation may give rise to the appearance of two microstreaming patterns, a lobe-type pattern (middle row) or a star-shape pattern (right row).

Conclusion

The formation of specific microstreaming patterns induced by a wall-attached microbubble undergoing asymmetric shape oscillations is analyzed with respect to the resolved dynamics. We have revealed a powerful streaming flow with an original star-shape pattern that arises when a sectoral mode interacts with a zonal one. We expect that these results may be beneficial to applications where enhanced intensity and directivity of streaming are required, such as ultrasound-mediated targeted drug delivery, for instance.

References

[1] W. Lauterborn and T. Kurz. Reports on Progress in Physics **73**, 106501 (2010).
[2] W. Xi and F. Cegla. The Journal of the Acoustical Society of America **135**, 1731 (2014).
[3] M. Fauconnier, JC. Bera and C. Inserra. Physical Review E **102**, 033108 (2020).

Looking for the missing mass: insights on surface-acoustic-wave-driven droplet centrifuging

Shuren Song[1], Jia Zhou[1], Antoine Riaud[1]

[1]. State Key Laboratory of ASIC and System, School of Microelectronics, Fudan University, Shanghai 200433, China
E-mail: antoine_riaud@fudan.edu.cn

Introduction

Surface acoustic waves (SAW) can concentrate micro-particles in droplets within seconds [1]. Although the operation is straightforward, the mechanism for particle aggregation is not firmly established [2]. We analyze the collective dynamics of particles in sessile droplets of vastly varying viscosities. Depending on the fluid composition and particle size, three different dynamics are observed: the particles remain dispersed in the entire droplet (cloud), the particles are only observed outside a trapping radius (cavities) and the particles aggregate in a small dot (aggregates). Unlike previous studies, we take a holistic view of these phenomena and use the scaling laws of the cavities to shed light on the aggregation mechanism.

Experimental method and results

In order to simplify the analysis, we design the experiment to rule out the effects of the acoustic radiation force. This is done by using acoustic vortices instead of the plane waves used in most previous experiments. Acoustic vortices can conveniently be synthesized from the radiation of swirling SAW which can be generated using spiraling transducers [3] (Fig. 1(a)). While in our experiment the vortex is imposed by the design of the transducers, it is plausible that asymmetric actuation using plane SAW can excite a circulating Stoneley wave or a whispering gallery mode in the droplet reminiscent of an acoustic vortex.

Axisymmetry shows that a topological protection ensures that the acoustic field at the center of the droplet is null regardless of the scattering in the droplet. To vary the viscosity, we mix glycerol and water by various amounts. We note that glycerol-water mixtures are denser than the polystyrene particles used here, such that the particles cannot be trapped except in pure water according to Bourquin et al. [4]. This enables the formation of cavities that have been helpful in understanding the formation of particle aggregates.

The dynamics of particles with different diameters (d_p = 20 nm, 100 nm, 450 nm, 1 μm, 5 μm, 10 μm) dispersed in water are shown in Fig. 1. Three types of pattern are observed: cloud (the particles are continuously distributed (b)), cavity (not particles are observed at the center of the droplet (c)), and aggregate (all the particles are concentrated at the center (d)). Over a range of viscosities and particle sizes, the cavities are the most common patterns found in our experiments. While cavities have occasionally been observed in previous studies, and in this regard are not exclusive to acoustic vortex actuation, we are not aware of studies dedicated to this particular pattern.
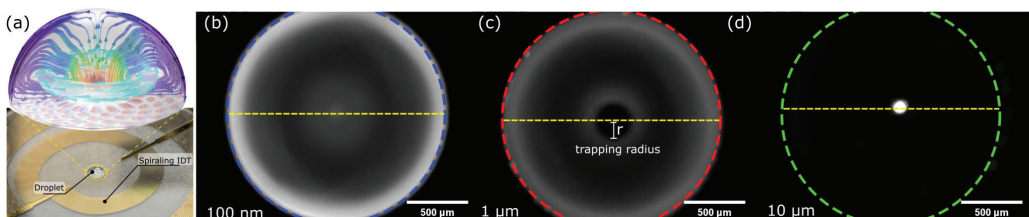

Figure 1: (a) Experimental setup (b-d) particles of various diameters forming a cloud (100 nm), a cavity (1 μm) and an aggregate (10 μm).
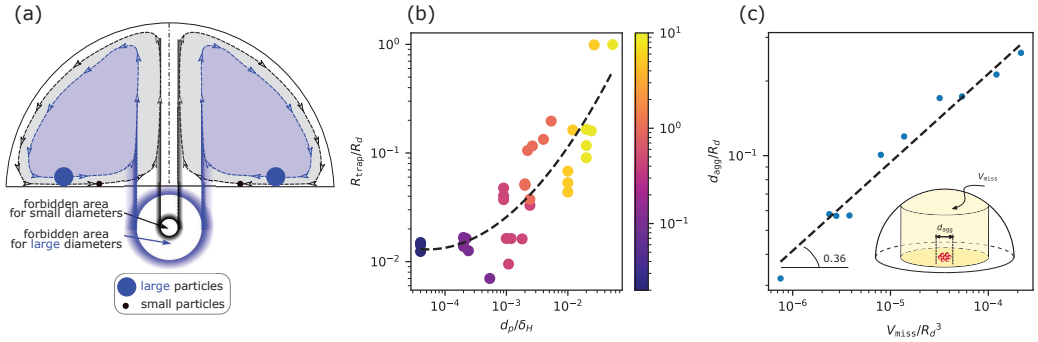
Figure 2: (a) Proposed generation mechanism for the cavities. Unlike small particles, large particles are unable to flow along the streamlines that go closest to the solid substrate, and therefore cannot reach the center of the droplet, which results in a forbidden area. At low viscosity (high droplet Reynolds number), the streamlines at the bottom of the droplet are squeezed into a thin boundary layer, such that large particles are prevented to access a much larger area. (b) Trapping radius of the cavity depending on the ratio between the particle diameter and the hydrodynamic layer thickness (the color indicates the particle diameter in μm). (c) Aggregate diameter depending on the missing volume.

Scaling laws and postulated mechanism

Because the cavities continue to exist even at very high viscosities, a force balance analysis suggests that they are formed via a purely kinematic mechanism. We postulate that particles are carried to the center of the droplet via some poloidal streamlines (see Fig. 2 (a)). The closer the streamline to the axis of the droplet, the closer it also flows next to the solid substrate. Therefore, large particles cannot flow along the streamlines closest to the center of the droplet, which results in large cavities for 5 and 10 μm diameter particles. If the cavities are truly formed due to the contact between the particles and the solid surface, then the trapping radius of the cavities should only depend on the droplet radius and the ratio of the particle size to the hydrodynamic boundary layer thickness (we recall that in water $Re \simeq 100$). The experimental relationship between the trapping radius of the cavities to the ratio between the particle size and the boundary layer thickness shown in Fig. 2(b) supports such kinematic mechanism for cavity formations.

The existence of cavities suggest that some amount of particles have been withdrawn from the flow circulation in the droplet. Similar to cavities, The size of the aggregates increases with the particle size and with the droplet rotation speed. Therefore, we use the cavity model to extrapolate the cavity sizes to the case where aggregates are formed, deduce the volumes V_{miss} of the missing particles and compare it to the size of the aggregates obtained with 1, 5 and 10 μm particles in water using different power levels (Fig. 2(c)). We find a clear correlation between the experimental aggregate diameter $d_{\mathrm{agg,exp}}$ and the missing volume which suggests that the missing particles form the aggregate.

Conclusion

We have found that particles tend to organize as hydrodynamic cavities where the center of the droplet is empty of particles. We propose a model where the geometry of these cavities is dictated purely by geometric constraints. The largest particles are physically forbidden to reach the center of the droplet as they touch the solid substrate before doing so. When the particles are lighter than the liquid, they gradually detach from the solid and escape by buoyancy, whereas particles heavier than the liquid continue to roll toward the center of the droplet and may form an aggregate.

[1] H. Li, J. R. Friend, L. Y. Yeo, *Biomedical microdevices* **9**, 647 (2007).

[2] H. Ahmed, S. Ramesan, L. Lee, A. R. Rezk, L. Y. Yeo, *Small* **16**, 1903605 (2020).

[3] A. Riaud, M. Baudoin, O. B. Matar, L. Becerra, J.-L. Thomas, *Physical Review Applied* **7**, 024007 (2017).

[4] Y. Bourquin, *et al.*, *Angewandte Chemie International Edition* **53**, 5587 (2014).

Ultrafast acoustofluidic handling of human blood

<u>Md Ehtashamul Haque</u>[1], Alvaro Conde[2], Harikumar Kuzhikkattu Chandrasekharan[1], William N. MacPherson[1], Stephen Knight[3], Richard Carter[1] and Maïwenn Kersaudy-Kerhoas[1]

[1] School of Engineering and Physical Sciences, Heriot-Watt University, Edinburgh, UK
[2] Micronit B.V., The Netherlands
[3] Usher Institute, University of Edinburgh, UK

Introduction

Many blood-based assays need some form of treatment of human blood cells, which may include extracting, isolating, or lysing cells. Biological cells can be precisely and quickly manipulated using bulk acoustic waves (BAW), including for lysis, separation, and manipulation [1]. Using microstreaming flow produced by oscillating bubbles powered by BAW from a piezoelectric actuator, we have built an economical, low-power micromixer. Our mixer has several benefits including the capacity to focus the acoustic streaming force where needed, a simple reversible coupling with the actuator, and the absence of soft-lithography-based and cleanroom-based fabrication. These advantages are all made possible by an independent soft polymer slab enclosed in a rigid chip (Fig. 1A). The micromixer is appropriate for static or continuous operation. Here, we demonstrate the use of this mixer to mix and lyse blood and viscous fluid under static conditions.

Experimental

Laser-cut cell-cast polymethyl methacrylate (PMMA) sheets (Clarex) and polydimethylsiloxane (PDMS – Sylgard 184, Dow Corning) casting onto SLA-3D printed moulds were used to create microfluidic chips and acoustic slabs, respectively, as described in [2]. A function generator (TG215, Thurlby Thandar Instruments) was used to drive a piezoelectric diaphragm (7BB-15-6L0, Murata Electronics) at 4 ± 0.5 kHz and 20 Vpp. Under the Scottish National Blood Transfusion Service's local ethical approval, human blood samples were collected. Image analysis on Image J was used to do the mixing analysis. Using a hematology analyzer, full blood counts were collected (Sysmex XP-300). Spun samples were examined using a spectrophotometer (Jenway 7315) for free hemoglobin (Hgb).

Results and discussion

Mixing inside microfluidic devices relies on diffusion and may be slow. This issue is exacerbated by the use of highly viscous fluids, which further reduces the rate of mixing. To demonstrate the effectiveness of the acoustofluidic micromixer with highly viscous fluids, the mixing chamber was filled with 130 µL of 0%, 20%, or 40% glycerol solutions, half of which was fluorescein tagged (5% fluorescein v/v), (Fig 1.B.i). Full mixing of water-based solutions (0%) and 20% glycerol solutions was accomplished in less than 60 seconds, while the 40% glycerol solution, which has a viscosity of 4.8 cP = 4.8 mPa.s (4.8 times the viscosity of water at 20°C), mixed completely in less than 2 minutes (Fig. 1. B.ii), which is comparable to the results reported with other BAW mixers [1]. Comparatively, diffusion-only mixing would need several hours to achieve full mixing [2].
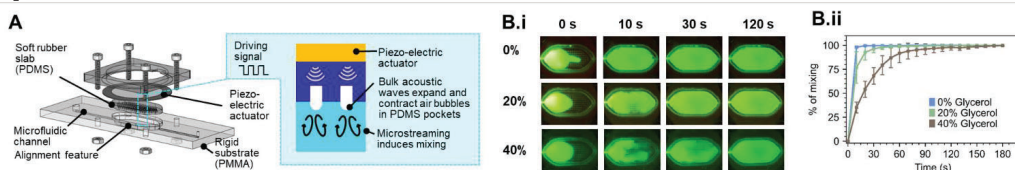

Figure 1: (A) The acoustic microbubble mixer detailed in [1]. All designs available on https://github.com/MaiwennKsKh/BubbleMicromixer B.i) Video screenshots of 0, 20 and 40% glycerol solution (half fluorescein tagged) at various time points B.ii) Analysis of mixing performance. All data acquired in triplicate.

The mixing efficiency of human blood at various hematocrit (Hct) levels was then investigated. Normal Hct range between 36 to 45% for women, and 40 to 50% for men, corresponding to viscosities at low shear rates between 5 to 100 cP [3]. Hct at birth ranges from 42 to 65%, so we evaluated four Hct (35, 45, 55, and 65%) to account for the complete human range. Complete mixing of 65 µL of whole blood with 65 µL of PBS buffer was accomplished at all Hct in under 60 s, whereas mixing rates above 80% was accomplished in under 30 s (Fig. 2B and C). Next, we measured the amount of free-Hgb after 1, 3, or 5 minutes of mixing of whole blood sample to look into the impact of the acoustic microbubble mixer on blood cells (45% Hct). Red blood

cells (RBCs) count (Fig. 2D), white blood cells (WBCs) count (Fig. 2E), and free Hgb (Fig. 2F) all revealed no evidence of cell lysis for up to 5 minutes throughout the mixing process, proving that the mixer is gentle to blood cells.
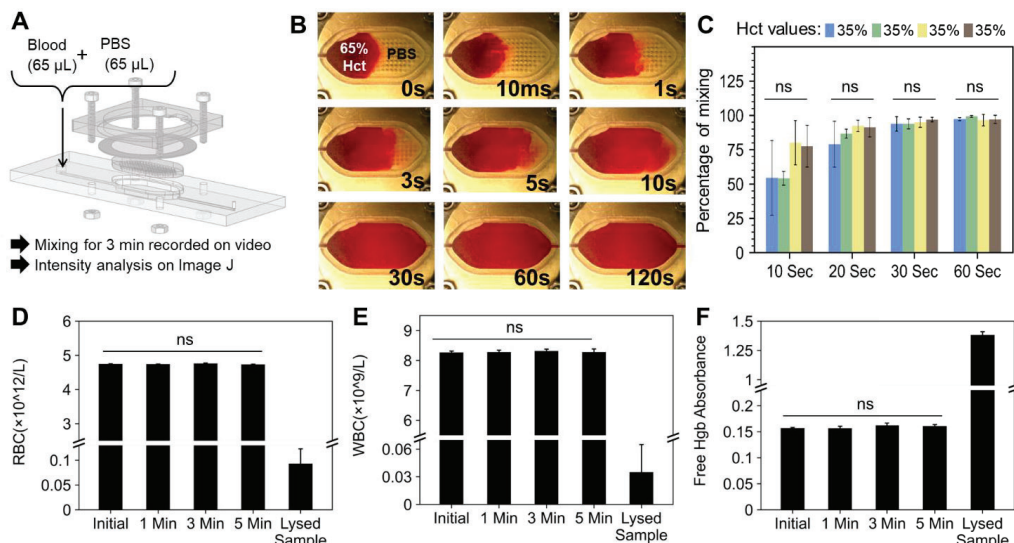

Figure 2: A) Blood mixing set-up B) Screenshots of 65% Hct blood sample mixing with PBS C) Percentage of mixing for various Hct level and time points D) RBCs count E) WBCs count and F) Free-Hgb measurements demonstrating absence of lysis for up to 5 min of continuous mixing. Statistical analysis: Annova test. n.s=non-significant . All data acquired in triplicate.

Finally, we looked at chemical lysis on human blood samples. Cell lysis is an essential step in many bioassays, including drug assays and molecular tests for viruses, bacteria, and other organisms. Therapeutic drug monitoring assays necessitate comprehensive RBC lysis since preventative medications like tacrolimus have a high affinity for binding to RBCs. 21.6 μL of human blood (Hct=42%) and 108 μL of chemical lysis solution (Product 11814389001, Roche) were pipetted in the acoustic mixer (Fig 3A). Just 15 seconds of mixing resulted in 80% lysis rate, whereas 60 seconds of mixing on the device is required to attain a mixing level comparable to the bench control (Fig 3B).
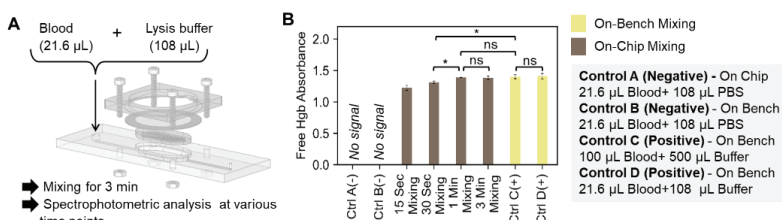

Figure 3: A) Blood cell lysis set-up B) Free Hgb measurement on lysed samples. All controls use the manufacturer recommended time of 10 min. Statistical analy-sis: Student's t-test. *in-dicates $p > 0.05$. All data acquired in triplicate.

Conclusion

Our microstreaming acoustofluidic mixing method allows for quick and lysis-free mixing of human blood while also producing rapid chemical-assisted cell lysis (80% cell lysis in less than 15 seconds), making it a module ideal for point-of-care applications.

References

[1] J. Rufo, F. Cai, J. Friend, M. Wiklund & T.J. Huang Nature Reviews Methods Primers 2(30), 2022).
[2] A. J. Conde, I. Keraite, A. E. Ongaro, et al, Lab Chip, vol. 20, no. 4, pp. 741–748, 2020
[3] D. E. Brooks, J. W. Goodwin, and G. V. Seaman, J. Appl. Physiol., vol. 28, no. 2, pp. 172–177, 1970.

Contact

* M.K.K; phone: +44 131 451 4171; m.kersaudy-kerhoas@hw.ac.uk

Diced microchannels and automated design optimization: a promising combination for affordable nm-particle trapping

Michael Gerlt[1,2], Nicola Hagger[1], and Jürg Dual[2]

[1]Department of Department of Chemistry and Applied Biosciences, ETH Zurich, Zurich, Switzerland
E-mail: mgerlt@ethz.ch, URL: https://bit.ly/3zGuX4l
[2]Department of Mechanical and Process Engineering, ETH Zurich, Zurich, Switzerland

Introduction

Acoustofluidic devices typically consist of microscale cavities such as microfluidic channels in which particles are manipulated. The production of these microscale cavities typically requires a cleanroom environment. For bulk acoustic wave (BAW) devices, e.g., etching into silicon is used, whereas for surface acoustic wave (SAW) devices, the channels are produced in PDMS; both device types require photolithography. An elegant alternative with high potential is an acoustically excited glass capillary. [1] However, by using glass capillaries, one relies on the precision and dimensions provided by the supplier. Further, advanced functionalities such as sorting are challenging to realize. In this work, we present a new production procedure: diced microfluidic channels. By dicing the channels with a standard wafer saw into a silicon substrate, we are much more flexible in design while achieving an easy production procedure, not requiring any cleanroom equipment. Further, we developed a COMSOL optimization procedure that can automatically evaluate the best dimensions of the microfluidic cavity and the piezoelectric transducer to achieve high acoustic forces inside the device. Finally, we demonstrate the trapping of polystyrene particles as small as 450 nm in diameter.

Materials and Methods

For the dicing of the microchannels, we used a standard dicing saw (DAD3221, Disco Corporation) with a 45 µm thick blade (FTB R46 45130, Disco Corporation). After dicing the channels, we sealed them by anodic bonding of a glass plate. We used this process for demonstration purposes, but it could easily be replaced by gluing or clamping the glass layer. Finally, we inserted fused silica capillaries (164 ± 6 µm outer diameter, 100 ± 6 µm inner diameter, Molex) into the sides of the device and fixed them with a two-component glue (5-minute epoxy, Devcon). The dimensions of the devices were optimized using a combination of COMSOL Multiphysics version 6 and Matlab. The COMSOL model has 217961 degrees of freedom and needs ~4 min to find the optimal frequency using the optimization module. For experimental evaluation, we used PS particles (5 µm and 0,45 µm diameter, Microparticles Gmbh).

Results and Discussion

Before device production, we were interested in the best device design. Therefore, we created a numerical model in COMSOL Multiphysics and verified its correct representation by experimental verification. Afterwards we improved the performance of the devices numerically. We used the optimization module in COMSOL to find the frequency with the highest energy density within 2 minutes. The result was then fed back to an evolution algorithm in Matlab, which would determine the next geometry to be evaluated and send it back to COMSOL. After roughly 24 h, we found the best solution for 5 design parameters (Figure 1).
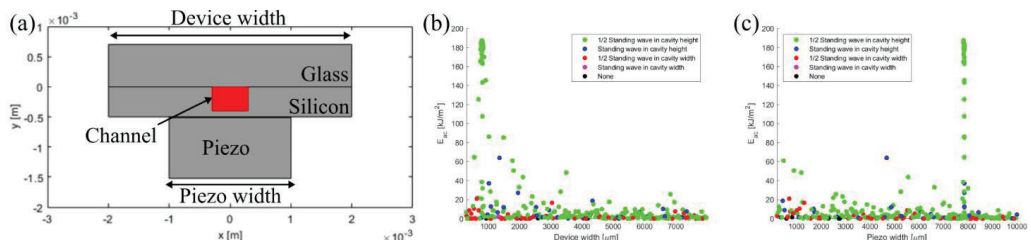

Figure 1: Automated design optimization. (a) Numerical model of the device. (b/c) Results of the automated procedure for the device design for (b) the device width and (c) the piezo width.

Knowing the theoretical optimal design, we used a wafer saw to dice the microfluidic channels into the silicon with a precision of ± 2 μm in width and ± 2 μm in depth. The shape could not be chosen straight due to the shape of the blade. However, as demonstrated by wet etched channels which are rather round than straight, [2] the shape of the channel has no significant influence on the particle manipulation abilities. We were able to move 5 μm PS particles into the z-center plane within 100 ms using an excitation frequency of 1.94 MHz and an input voltage of 9 V. Further, the particles were pushed against the wall, which most probably is a result of acoustic streaming. We verified this hypothesis by demonstrating trapping of 0.45 μm PS particles at a flow rate of up to 40 μL/min.
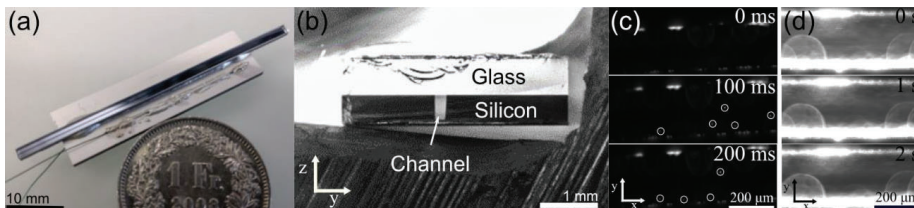

Figure 2: Optimized device performance. (a) Photograph of the fabricated optimized device. (b) Microscope picture of the cross-section of a diced microchannel, demonstrating the fabrication accuracy. (c) Focusing of 5 μm PS particles to the z-center plane within 100 ms. (d) Trapping of 0.45 μm PS particles at the channel walls at a flow rate of 40 μL/min. The trapping effect is visible by a reduced fluorescent intensity in the center of the device and a significant increase at the edges. The device was excited at 1.9 MHz with 9 V_{pp}.

Using analytical approximations and experimental particle focusing, we were able to determine the acoustic radiation force on the particle to be ~ 17pN. Adjusting the numerical model to this value allowed us to predict the acoustic pressure inside the device to be ~1.3 bar which is remarkable given the low input power.
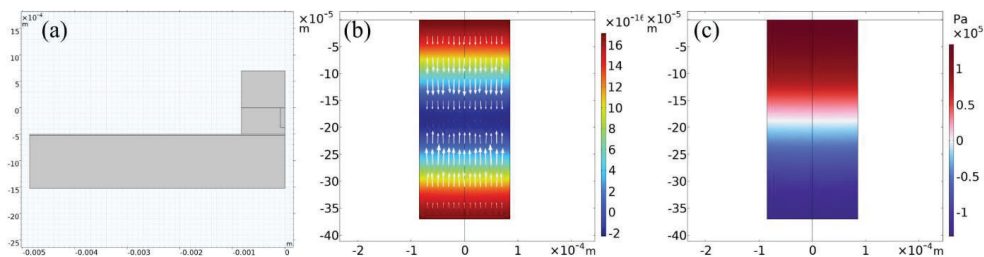

Figure 3: Experimental parameter fitting. (a) Geometry of the optimized design in COMOSL. (b) Gorkov potential with acoustic radiation force as white arrows. Particles are pushed towards the center plane of the device. (c) Acoustic pressure inside the device.

Conclusion and Outlook

In this work, we present a facile and cheap method to produce precise microchannels that are flexible in design. Further, we optimized the device design using an automated procedure comprising of a COMSOL Multiphysics model together with a Matlab evolution algorithm. With this automated procedure, we were able to show remarkable particle manipulation abilities – focusing of 5 μm PS particles within 100 ms and trapping 450 nm PS particles.

In the future, we plan to dice microfluidic channels into glass wafers to produce see-through devices that can be used in transmitted light microscopy, which is currently rather challenging for the production of BAW devices. Further, we will test the production of microfluidic channels directly into the piezoelectric element to achieve even higher acoustic energy densities.

References

[1] M. S. Gerlt, A. Paeckel, A. Pavlic, P. Rohner, D. Poulikakos, and J. Dual, Phys. Rev. Applied, 2022, 17, 014043
[2] M. Evander, A. Lenshof, T. Laurell, and J. Nilsson, Anal. Chem. 2008, 80, 13, 5178–5185

Acoustic mobility of fluorescent polystyrene particles

Thierry Baasch[1], Alexander Edthofer[1], Andreas Lenshof[1] and Thomas Laurell[1]

[1]Department of Biomedical Engineering, Lund University, Lund, Sweden
E-mail: Thierry.baasch@bme.lth.se

Introduction

Polystyrene particles are often used as reference particles when assessing the acoustic energy density in channels and assessing the performance of acoustophoresis devices [1 – 4]. Their popularity as reference particles is partly due to their acoustic properties being close to those of cells, their availability in several fluorescent and non-fluorescent colors, and their low density, thus long sedimentation times. However, their acoustic properties are usually assumed to be known and have never been studied thoroughly. In the underlying study we compared the acoustic mobility of different types (size, color) of polystyrene particles. We have found a significant variation in acoustic mobility that can not be explained by size variations only. This indicates that some care needs to be taken if quantitative values of the acoustic energy density are reported based on particle image or tracking velocimetry measurements with polystyrene particles.

Methods and results

Our experiments are performed in a simple single channel device, sketched in Fig. 1. Two piezo-electric transducers are glued to the device that excite the half-wavelength mode in width of the height of the device. Our measurements are performed in two steps: 1. levitation and 2. migration. The half-wavelength mode in height (levitation) is used to levitate the particles into the optical focus and minimize the influence of the channel top and bottom walls. In a next step, the particles are focused towards the channel center by the half-wavelength mode along the width direction and their tracks are recorded. The velocity profiles are then extracted from the recorded particle trajectories by the general defocusing particle tracking GDPT software [5]. The two-step focusing procedure is summarized in Fig. 2. When fitting the experimentally obtained velocity profile to the theoretical sinusoidal curve, both the acoustic energy density and the properties of the focused particles are generally unknown. The state-of-the-art procedure requires to perform a first measurement (two-step focusing experiment) with a known reference particle to calibrate for the acoustic energy density in the manipulation channel. In a next step, the approach is repeated under the same conditions with the unknown particle. In fact, mathematically, one measures the acoustic mobility ratio between the known and unknown particles by this method. The acoustic mobility denotes the square of the particle radius times its acoustic contrast factor and therefore depends on the particle size and material properties. We present all our results as the ratio of the acoustic mobility of the measured particle with respect to our reference particle (5.18 μm polystyrene, Microparticles GMBH). As the acoustic migration behavior of the particles is highly dependent on their sizes, i.e., the acoustic mobility is proportional to the square of the particle radius, we performed Coulter counter measurements, shown in Fig. 3, to verify the sizes given by the manufacturer. An example of a sinusoidal fit is shown in Fig. 4. We filtered out all the slow particles to remove data of particles that are stuck at the channel walls from the dataset. The resulting acoustic mobility ratios are shown in Table 1. The variation in acoustic mobility can partly be explained by the variation of the particle's sizes. However, in a few cases, for example in the case of the red fluorescent 4.99 μm and the red fluorescent 9.89 μm particles, the particle size cannot explain the measured mobility ratio. From the theory, we would expect the acoustic migration velocity, and hence the acoustic mobility, of the red 4.99 μm particles to be smaller than the acoustic migration velocity of the green 5.18 μm reference particles, which, to our surprise, was not confirmed by the experiments. While the red 4.99 μm particles appeared to be faster than expected, the red 9.89 μm were significantly slower.

Conclusions

We have measured the acoustic mobility ratio of several sizes and colors of fluorescent polystyrene particles with respect to 5.18 μm green-fluorescent polystyrene particles (Microparticles GMBH). From the theory we would expect the material properties of the different polystyrene particles to be comparable, hence motivating their choice as reference particles. In that case the acoustic mobility ratio will be dominated by the squared diameter ratio. However, our results indicate that this is not the case for all particles. Therefore, some care is needed if polystyrene particles are used to quantify the acoustic energy density of acoustophoresis devices or to assess the properties of cells and a deviation of up to 15% from the expected acoustic mobility and thus measured acoustic energy density can occur.
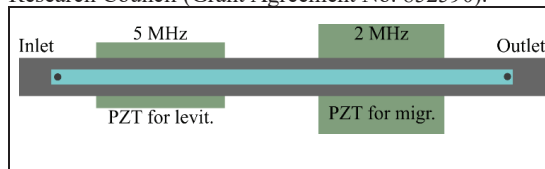
Fig. 1 shows a schematic of our acoustophoretic manipulation device. The channel was dry etched in silicon and sealed by an anodically bonded glass lid. Two piezoelectric transducers were used to actuate the levitation and migration mode, respectively. The channel dimension is 375 μm × 150 μm (width × height).
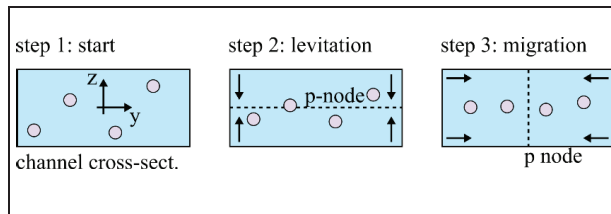

Fig. 2 shows the channel cross-section during the measurement procedure. First (step 1) the particles are flushed into the device. Then, in step 2, the particles are levitated to minimize the distance towards the top and bottom walls. The third step is the measurement step. Here the half wavelength mode is applied and the particle paths are recorded while they migrate towards the channel center.
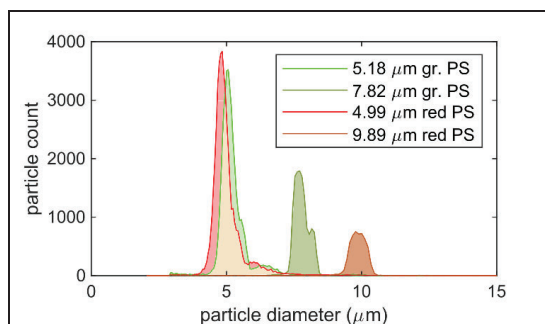

Fig. 3 shows Coulter counter measurements of the sizes for four types of the assessed polystyrene particles. The results are summarized in table 1. The manufacturer's claims are very close to the data obtained from the Coulter counter. The size variation can not explain the variation in acoustic mobility.
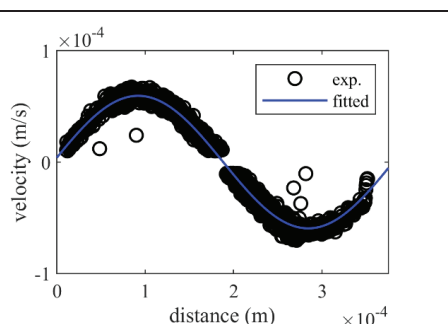
Fig. 4 shows velocity data as a function of the position obtained from migration experiments with the 5.18 μm green polystyrene reference particles (Microparticles GMBH). The blue curve is the sinusoidal fit. To improve the accuracy of the fit we neglected data from slow particles. This filter excludes, for example, particles that are stuck.

particle manufac. Size	mobility ratio (mean)	95% confidence interval	N datapoints	expected from size	size (mean ± sd) by Coulter counter
fluor. green 5.18 μm (ref.)	1 (by definition)	0.99 – 1.07 (ref. exp.)	769	1 (ref)	5.21 μm
fluor. green 7.81 μm	2.31	2.24 – 2.39	1565	2.24	7.76 μm
fluor. green 9.98 μm	3.15	2.98 – 3.31	361	3.71	not assessed yet
fluor. red 4.99 μm	1.07	1.05 – 1.10	980	0.93	5.00 μm
fluor. red 7.76 μm	2.31	2.12 – 2.50	292	2.22	not assessed yet
fluor. red 9.89 μm	2.90	2.85 – 2.95	378	3.33	9.52 μm

Table 1 Summarizes our results. For most measured particles their mobility ratio is in a range that was expected from their size measured by the Coulter counter. The mobility ratio for the red 4.99 μm and red 9.89 particles seems to be off. Although, the mobility ratio for the green 9.98 μm particles seems to be off also, we will first confirm their size distribution by Coulter counter measurements. The particles were all purchased from the Microparticles GMBH.

References

[1] D. Hartono, Y. Liu, P. L. Tan, X. Y. S. Then, L. Y. L. Yung, and K. M. Lim. Lab on a Chip **11**, 4072-4080 (2011).
[2] T. Baasch, P. Reichert, S. Lakämper, N. Vertti-Quintero, G. Hack, X. Casadevall I Solvas, A. de Mello, R. Gunawan, J. Dual. Biophysical journal **115**, 1817-1825 (2018).
[3] P. Augustsson, J. T. Karlsen, H. W. Su, and H. Bruus, Nature communications **7**, 1-9 (2016).
[4] A. Urbansky, F. Olm, S. Scheding, T. Laurell, and A. Lenshof, Lab on a Chip **19**, 1406-1416 (2019).
[5] R. Barnkob, and M. Rossi. *Experiments in Fluids* **61**, 1-14 (2020).

Acoustofluidics 2022
19-21 October 2022
University of Glasgow, Scotland

Acoustofluidic tweezer inside circular glass capillary using traveling surface acoustic waves

Qiaoyun Wang[1,2], Jikai Zhang[2], Hui Ling Ong[2], and Yong-Qing (Richard) Fu[2]

[1]College of Information Science and Engineering, Northeastern University, Shenyang, Liaoning Province 110819, China
[2]Faculty of Engineering and Environment, Northumbria University, Newcastle upon Tyne, NE1 8ST, UK
E-mail: qiaoyun.wang@northumbria.ac.uk/jikai.zhang@northumbria.ac.uk

Introduction

Microfluidic technologies have been used extensively to manipulate the micron-size or nanometer particles (1, 2). Recently surface acoustic waves (SAWs) technology has been integrated into microfluidic system due to their advantages of precise control, non-invasive, low loss, label-free and biocompatible (3, 4). There are numerous studies about the mechanisms and principles of particle manipulation inside rectangular capillary tubes or polydimethylsiloxane (PDMS) microchannel using both standing waves and propagating waves (5). A detail study of patterning and alignment of particles inside glass capillary with different cross-section and different angles relative to the direction of the interdigital transducers (IDTs) have also been reported [6] using the standing acoustic waves. Whereas there are no any reports using traveling SAWs with a single IDT.

In this study, we demonstrated patterning and alignment of microparticles inside a circular glass capillary using a single IDT with an aluminum plate based thin film SAW device. Figure 1(a) shows the schematic view of a SAW device which consists of a ZnO film coated Al plate, Au IDT and a circular glass capillary tube. When a sinusoidal signal amplified by the amplifier is applied to the IDT, the generated SAWs will propagate along the surface and through a water layer propagate into the glass capillary. Due to the acoustic radiation force (ARF) generated into particles in the capillary, which are concentrated into the center of the capillary, the particles suspended in the mixture fluid are formed with a good pattern. Figure 1(b) shows a cross-section illustration of the manipulation principle.
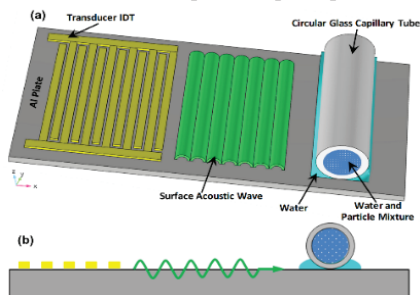

Figure 1: (a) Schematic of acoustic fluidic micromixer with a SAW device and circular glass capillary; (b) Principle of SAW with single IDT in a cross-section

Figure 2: A Schematic of experimental platform

Patterning experimental designs with circular glass capillary

The SAW device was fabricated by depositing ZnO film (with a thickness of $\sim 5 \mu m$) onto an aluminum substrate (thickness of 0.5mm) using a direct current (DC) magnetron sputter (NS3750, Nordiko). The IDT (made from 20/100 nm thick of Cr/Au) of the SAW device was fabricated using a standard photolithography and lift-off process. The designed IDT had a frequency of 6 MHz, 17 MHz and 27 MHz. The polystyrene microspheres (SIGMA- ALORICH, $3 \mu m$) were diluted by the deionized (DI) water and introduced into the capillary by a syringe. These particles have the density of ~ 1900 kg/m³. Then the mixtures were injected into the round glass capillary (OD=1mm, ID=0.7mm) with a length of ~ 20mm. The round glass capillary was placed on the surface of the SAW device. In order to improve the efficiency of acoustic coupling, the DI water was put between the round glass capillary and the SAW device. The experimental setup is shown in Figure 2. The radio frequency (RF) sinusoidal signal from the function generator (AIM-TTI Instruments TG5011A) was transferred into the power amplifier (Amplifier Research 75A) and the amplified signals were applied to the IDT. A video camera (iDS, UI-3880CP-C-HQ-R2) was used to record the patterning results. Software ImageJ

(NIH, USA) was used to process the experimental images and measuring the requires data. The additional lights were provided additional illumination.

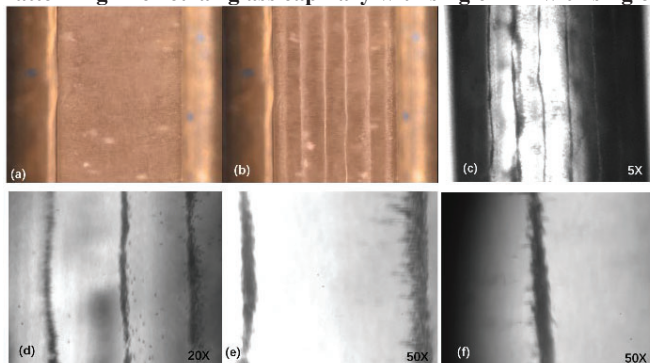**Patterning in circular glass capillary with single IDT with single IDT**

Figure 3: Micrograph of the pattern in circular glass capillary (OD=1.0mm) with sing IDT. (a) the microparticles micrograph suspended in the DI water without the SAW. (b) the pattern micrograph of the microparticles in the DI water with the SAW. (c) the pattern micrograph of the microparticles under oscilloscope with 5X. (d) the pattern micrograph of the microparticles under oscilloscope with 20X. (e) the pattern micrograph of the microparticles under oscilloscope with 50X. (f) the pattern micrograph of the microparticles under oscilloscope with 50X.

The polystyrene microspheres (SIGMA- ALORICH, $3\mu m$) was diluted by the ID water and agarose gel. The concentration of the agarose gel is about 0.1% V/V. The mixture was injected into the capillary. The top view of the capillary is shown in Figure 3(a) and the round glass capillary is driven at 0.8Vpp to form the pattern with single IDT. When the SAW is produced, the microparticles are moved to the acoustic pressure nodes and focused to certain positions. The top view of the patterning in the circular glass capillary is shown in Figure 3(b). It shows that the microparticles are concentrated and patterned into lines along the capillary. About 5 minutes later, the pattern will be fixed in the capillary. The particles inside the capillary were observed using the oscilloscopes (Nikon ECLIPSE LV100) and the images are shown in Figure (c)-(f). From the imagines we can know that the line is concentrated and agglomerated well.

We then tested with patterning of particles within a few glass capillaries which are located on the same SAW device. The polystyrene microspheres (SIGMA- ALORICH, $3\mu m$) was diluted by the DI water, and three circular glass capillaries (OD=0.7mm) were applied parallel to form patterns. The SAW signal was applied from right hand and the patterning was form when the capillaries. The output of the signal generator was 0.8Vpp, and the DI water was applied to transfer the SAW energy into the capillary. The results are shown in Figure 4. Figure 4(a) is the top view without applying the SAWs. Two circular glass capillaries were separated with a width of 0.2 mm. When the SAW was actuated from the right hand of the photograph, the patterning in the two capillaries can eb clearly seen as shown in Figure 4(b). When three capillaries were separated by a given distance of 0.2mm, Figure 4(c) shows the image of patterns without applying the SAWs. When the SAWs were applied, the patterning can be seen clearly in the circular glass capillaries as shown in Figure 4(d).
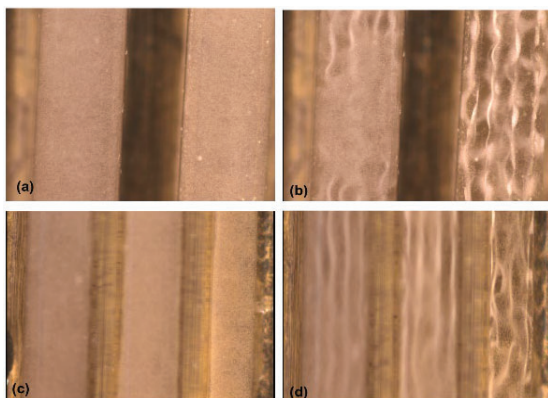

Figure 4: Top view of patterning in multiple circular glass capillaries. (a,c) top views of the two/three circular glass capillaries separated with two rectangle capillary without SAW actuator. (b,d) Patterning in three circular glass capillaries separated by one/two rectangle capillary.

Conclusion: Patterning in the round glass capillary with single IDT was researched. The results shown that the pattering formed by the microparticles is concentrated and patterned into lines along the capillary. Compared with the standing SAW device, this structure is simple. Then the patterning in the multiple round glass capillary is researched. The results show that patterning in multiple round glass capillaries is focused well. This work can serve as focusing of cell in blood.

References
[1] MS Gerlt, A Paeckel, et al., Physical Review Applied. 17(1):014043(2022)
[2] Z Li, P Li, et al., Biomedical Microdevices **22**(2), 1-12(2020)
[3] W Qiu, T Baasch, et al., Physical Review Applied **17**(4), 044043(2022)
[4] A Fornell, T Baasch, et al., Journal of Physics D: Applied Physics **54**(35), 355401(2021)
[5] T Peng, M Zhou, et al., Applied Mathematical Modelling **101**, 517-32(2022)
[6] S Maramizonouz, C Jia, et al., International Journal of Mechanical Sciences **214**,106893(2022)

Single focused-beam acoustical tweezers

Zhixiong Gong[1], and Michael Baudoin[1,2]

[1]CNRS, UMR8520 IEMN, Lille, France
E-mail: zhixiong.gong@iemn.fr, michael.baudoin@univ-lille.fr
[2]Institut Universitaire de France, Paris, France

Introduction

The first three-dimensional (3D) trapping of microparticles with a single beam was demonstrated in the field of optics by the Nobel prize laureate Arthur Ashkin's group in 1986 with a tightly focused laser beam [1]. As an analogy to the optical method, Wu explored in 1991 [2] the possibilities offered by acoustic focused beams to trap particles. In his seminal paper, he demonstrated trapping of latex particles and clusters of frog eggs with two counter-propagating collimated focused beams. Later on, Shung's group explored the trapping capabilities of a single focused beam. They were able to demonstrate 2D lateral trapping with different types of particles, but with no axial trap [3]. Recently, Silva *et al.* showed numerically the possibility to trap silicone-oil droplet in 3D in the Rayleigh regime regime [4]. However, the results on 3D trapping with focused beams remain relatively scarce and 3D selective trapping beyond the Rayleigh regime has not been reported yet. In this work [5], we conduct extensive numerical exploration of 2D and 3D trapping capabilities of a focused beam *in and beyond* the Rayleigh regime for a large set of parameters (particles size and material) with numerical simulations based on the angular spectrum method [6]. We demonstrate that 3D trapping is possible *in and beyond* the Rayleigh regime for specific particles.

Design of an interdigitated transducer (IDT) for a focused beam with finite aperture

In this work, the field is produced by concentric circle IDTs of opposite polarities (see Fig. 1) designed to produce focused wave at 40 MHz frequency. A large aperture (60°) was chosen to improve 3D trapping capabilities, as is classically done in optics. The electrodes constitute a phase hologram of a focused beam descretized on two levels. Such active hologram based on IDTs can be easily produced in a clean room by using traditional lithography fabrication technique [7,8].

Acoustic radiation force formulas

The angular spectrum method [6] is applied to compute the 3D radiation force with our homemade Matlab codes published in Ref. [8]. When the particle size is in the Rayleigh regime, the radiation force includes the gradient force and a small scattering contribution, as re-organized by Eq. (6) in Ref. [5]. The corresponding scattering coefficients for different materials are briefly reviewed in [5].

Trapping ability in and beyond the Rayleigh regime

The trapping ability of the designed single focused beam is studied *in and beyond* the Rayleigh regime, for materials of either positive (such as PolyStyrene, PS) or negative contrast (such as PDMS) factors.

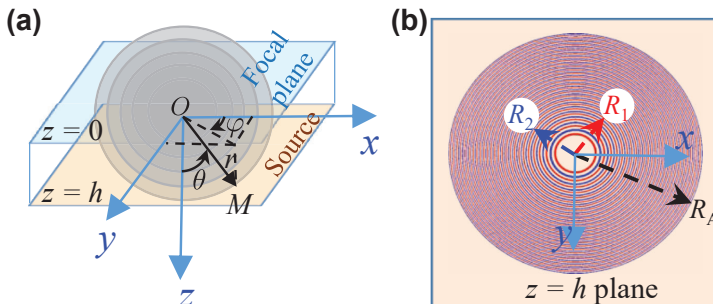**Figure 1:** (a) Design principle of the IDT for a focused beam. The source plane $z = h$ is used to cut the spherical waves to obtain the structures of two sets of electrodes on the piezoelectric transducer. (b) The structures of two sets of equiphase electrodes are described by R_1 and R_2. $R_A = 1.72$ mm is the aperture radius, leading to the aperture angle $\approx 60°$ with the focal length of 1 mm at the frequency 40 MHz.
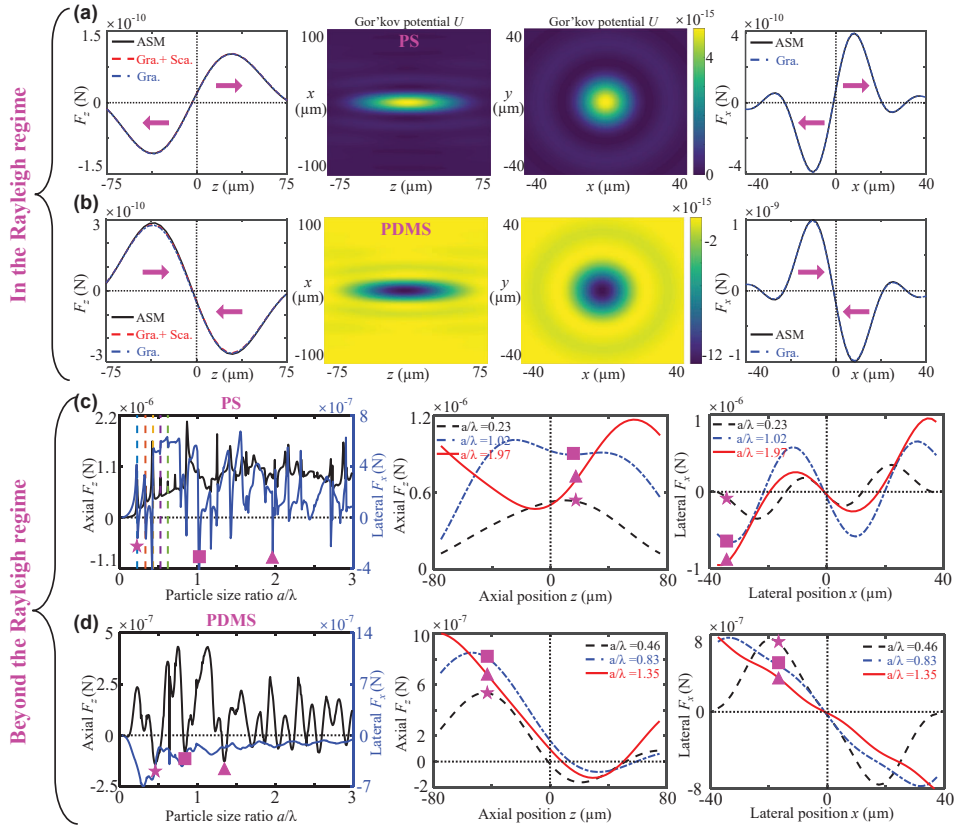
Figure 2: Materials with positive (PS) or negative (PDMS) contrast factors in the Rayleigh (Fig. 2a,b with particle radius $1\mu m \ll$ wavelength $37.5\mu m$) and beyond (Fig. 2c,d) the Rayleigh regime. In the Rayleigh regime in (a) and (b), the second and third columns are the Gor'kov potential in xz and xy planes, and the first and fourth columns are the axial and lateral radiation forces versus the spatial positions. Beyond the Rayleigh regime in (c) and (d), the first column is the axial (left y-axis) and lateral (right y-axis) radiation forces versus the partial size ratio at fixed axial and lateral positions, respectively. The second and third columns are the axial and lateral radiation forces versus spatial positions for selected particle size ratios.

Fig. 2 illustrates the results obtained for PS and PDMS particles, while a large set of materials was explored in [5]. These results show that PS particles can be only trapped laterally in 2D *beyond* the Rayleigh regime. Indeed, the axial radiation force in the first and second columns of Fig. 2c are always positive, which means there may be no negative restoring force for the trapping in the axial direction. While Figs. 2b and 2d show that the 3D trapping is possible for PDMS particles both *in and beyond* the Rayleigh regime.

Conclusion

This work demonstrates (i) that 3D trapping of particles with negative contrast factors with focused beams is possible *in and beyond* the Rayleigh regime, and (ii) that classic particles with positive contrast factors (such as PS) can only be trapped in 2D *beyond* the Rayleigh regime by using the particle resonances. The readers are suggested to read our recent preprint for more details if interested [5].

References

[1] A. Ashkin, *et al.* Optics Letters **11**, 288-290 (1986).
[2] J. Wu. J. Acoust. Soc. Am. **89**, 2140-2143 (1991).
[3] J. Lee, *et al.* Appl. Phys. Lett. **95**, 073701 (2009).
[4] G.T. Silva, *et al.* IEEE Trans.Ultrason., Ferroelectr., Freq. control **64**, 576-583 (2015).
[5] Z. Gong, and M. Baudoin. arXiv preprint arXiv:2205.10033, submitted to J. Acoust. Soc. Am. (2022).
[6] O.A. Sapozhnikov, and M.R. Bailey. J. Acoust. Soc. Am. **133**, 661-676 (2013).
[7] M. Baudoin *et al.* Science Adv. **5**, eaav1967 (2019).
[8] M. Baudoin *et al.* Nature Commun. **11**, 4244 (2020).

Amplification of secondary Bjerknes forces using microbubble arrays for precise acoustofluidic manipulation

Rahul Goyal[1], Athanasios G. Athanassiadis[1,2], Zhichao Ma[3] and Peer Fischer[1,2]

[1]Max Planck Institute for Medical Research, Heidelberg, Germany
E-mail: goyal@is.mpg.de
[2]Institute for Molecular Systems Engineering and Advanced Materials, Heidelberg University, Heidelberg, Germany
[3]Shanghai Jiao Tong University, Shanghai, China

Introduction

Sound waves provide a pathway to controlled manipulation and assembly of objects through acoustofluidic forces, such as streaming and radiation forces. Bubbles, which are subwavelength resonant scatterers, can be used to generate these forces at small scales, but have traditionally been limited for larger objects. Larger-length structures would require long-wavelengths of sound for robust manipulation but high frequency fields are necessary for precise control, introducing a trade-off for large structures. A way around this trade-off is to use secondary radiation forces between bubbles. However, such forces are typically very weak - on the order of 10 nN for micron-scale bubbles. In this work we demonstrate how to amplify secondary Bjerknes forces for use in acoustofluidic manipulation, by patterning microbubbles into arrays [1]. By embedding microbubble arrays into larger structures, sound waves of 50 cm wavelength can be used to rotate cm-scale objects and position them with an accuracy of 15 μm. The results are quantitatively described by a theoretical model and a numerical analysis is performed to show that the amplified secondary Bjerknes forces are at least one order of magnitude stronger than the dipole-dipole interaction of magnetic counterpart. These results lay the foundation for using secondary Bjerknes forces in integrating novel capabilities into acoustofluidic devices.

Scaling of secondary Bjerknes force

Primary radiation forces - which are directly exerted on objects and particles by the acoustic field - comprise the majority of the research on the acoustic assembly. We present an alternative approach based on the secondary radiation force between microbubbles in a sound field. The secondary Bjerknes force on a bubble with radius R_0 at the origin, from an identical bubble at position $\vec{r}$, is given by $\vec{F}_B = 2\pi\rho R_0^4 \omega^2 \delta^2 \vec{r}/r^3$ where, ρ is the density of the liquid, ω is the angular oscillation frequency, and δ is the radial oscillation amplitude of the bubble. By patterning bubbles into arrays, this force can be amplified to scales relevant for micromanipulation (Fig. 1 (a)). The amplification of force is a monotonic increasing function of the number of microbubbles N in an array, however it is not linearly dependent on the N instead grows superlinearly as approximately $F \sim N^{1.6}$ for small N, transitioning to an asymptotic scaling $F \sim N$ for large N. We calculated that a microbubble array of dimensions 10×10 ($N = 100$) amplifies the secondary radiation force $\approx 13\times$ over N independent bubble pairs, generating nearly 0.1 mN of force. We further showed that the secondary acoustic forces between microbubble arrays scales more effectively than those from a comparable magnetic array (Fig. 1 (a)). While for close-range interactions, the magnetic arrays produce higher forces, the scaling of forces
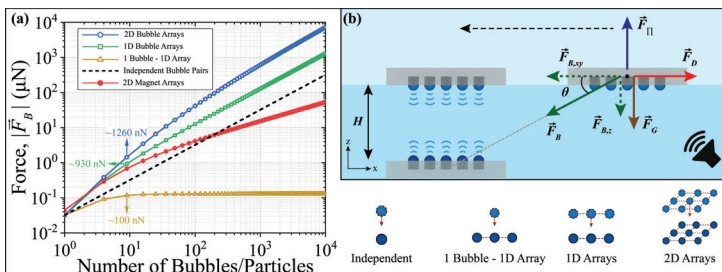

Figure 1: Patterning bubbles amplifies their interactions. (a) Force scaling for bubble arrays as a function of array size in different geometries. (b) Forces acting between two structures with embedded bubble arrays in a sound field. The floating structure moves due to the lateral component of the secondary Bjerknes force $\vec{F}_{B,xy}$. Figure is adapted from [1].
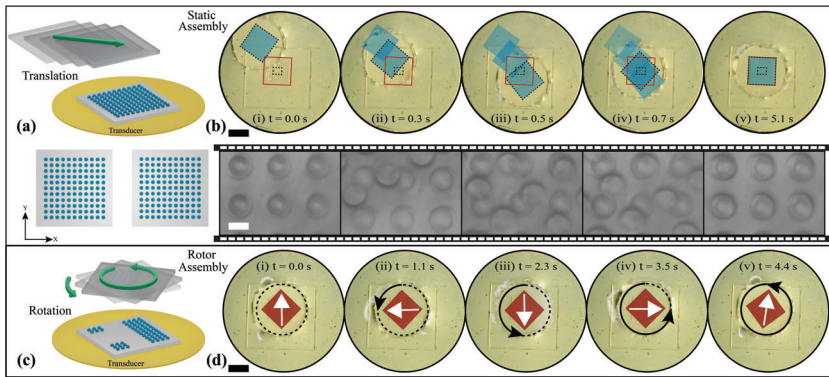
Figure 2: Assembly and alignment of sound-activated structures. (a) Schematic of the assembly experiment. (b) Experimental images of the alignment of the floating array (blue square) with respect to the fixed array (red square). The microscope images below show the central region of the fixed array, demonstrating precise alignment. Acoustic rotation of structures. (c) Schematic of asymmetric bubble arrays for rotation of the free structure. (d) Experimental images of acoustically-driven rotation of structure. Red colored rectangle and white colored arrow indicate the instantaneous position and orientation of the mobile structure, respectively. Scale bars: 5 mm (black) and 300 μm (white). Figure is adapted from [1].

between the microbubble arrays is more favourable with N and for long-range interactions. We show this arises because of the longer range forces between bubbles, which scale as $F \sim r^{-2}$, compared to r^{-4} for magnetic dipoles.

Experimental assembly and manipulation of structures

We patterned microbubbles into 11×11 arrays to experimentally demonstrate manipulation with the secondary Bjerknes forces. We fabricated cylindrical cavities of diameter $2R_0 = 300$ μm and height $L = 275$ μm on planar PDMS structures using soft lithography. The cavities are uniformly spaced with a pitch $\Delta = 500$ μm. The immersion of PDMS structures in water trapped air in the cavities, forming bubbles, due to the small size of the cavity and the hydrophobicity of PDMS. We fixed one structure to the bottom of the reservoir while the other structure floated freely on the air-water interface (Fig. 1 (b)). Switching on an acoustic transducer at the bubble resonance generated secondary acoustic forces on the bubble arrays large enough to drive assembly of the floating PDMS structures (Fig. 2 (a) and (b)). We measured an alignment accuracy of 14 μm ± 4 μm, which corresponds to an accuracy of 0.1% relative to the size of objects, and 0.003% relative to the acoustic wavelength. We developed a numerical model based on the dynamics of the objects under the influence of secondary Bjerknes forces. The model shows excellent agreement with the experimental results, demonstrating that only secondary Bjerknes forces are responsible for the motion. Finally, we realized a rotor-assembly by arranging the microbubbles asymmetrically in the arrays. When excited by sound, the secondary Bjerknes forces drive the free structure in a continuous rotation while simultaneously producing a central trap to maintain the coaxial alignment of the arrays (Fig. 2 (c) and (d)). The absence of common axis of symmetry in the patterns of the two structures skew the force distribution, and generates a torque depending on the relative angular position of the structure. The acoustic rotor spins at a rate of $1.4 \, \text{rad s}^{-1}$, or about $14 \, \text{RPM}$ and we expect that more complex manipulations could be realized by further arranging the microbubble arrays.

Conclusion

We have introduced a unique assembly mechanism based on the secondary Bjerknes force between arrays of microbubbles which can be used to drive translational or rotational motion of sound-activated structures. The assemblies form within seconds of the application of an external sound field, and persist as long as the sound field is applied, indicating the switchable nature of the assembly technique. The all-acoustical strategy using activated bubble arrays could be integrated with acoustofluidic devices and chips to pave the way for potential applications.

Acknowledgement

References

[1] R. Goyal, A. G. Athanassiadis, Z. Ma, and P. Fischer, Amplification of acoustic forces using microbubble arrays enables manipulation of centimeter-scale objects, Phys. Rev. Lett. **128**, 254502 (2022).

OSAFT: A Python Library for Acoustofludics

Jonas Fankhauser[1], Christoph Goering[1], Merrill Gutzwiller[1], and Jürg Dual[1]

[1]Institute for Mechanical Systems, Department of Mechanical and Process Engineering, ETH Zürich, Zürich, Switzerland
E-mail: fankhauser@imes.mavt.ethz.ch, URL: https://expdyn.ethz.ch

Introduction

The **O**pen-**S**ource **A**cousto**F**luidics **T**heories (OSAFT) library is a Python library for acoustofluidics [1]. The OSAFT library contains a growing list of theories for the computation of the acoustic scattering, the acoustic radiation force (ARF), and soon the acoustic streaming for a single particle suspended in a fluid and subjected to an ultrasonic field.

Currently, six different models are available and four more will be released in the upcoming months. The unified interface that is used across all implemented theories allows for a straight-forward comparison of different models. With the included plotting capabilities, the user can quickly illustrate their results. The library serves as a tool for researchers to analyse their experimental results, validate numerical simulations, or design acoustofluidic devices. It is in particular suitable for research projects, since it is fully open-source and available for free through Python's package index PyPi [2]. The following two sections are short demonstrations of the functionalities of the OSAFT library.

Computation of Acoustic Scattering Field

One of our main goals during the development of OSAFT was that the library is easy to use, even for people unfamiliar with the Python programming language. We are demonstrating this ease of use in a minimal example shown in Fig. 1. In the example the theory from Yosioka and Kawasima [3] is used to compute the acoustic scattering field around a polystyrene particle. Using the plotting capabilities of OSAFT different quantities of the scattering field can be displayed and even animated, e.g. the pressure, the velocity amplitude, or the velocity potential.

Scattering plots can be generated for any theory implemented in OSAFT, if the corresponding article provides the linear scattering coefficients for the acoustic field or if they can be inferred from the theory. Often the underlying scattering process can give some intuition about the resulting ARF, in particular for the direction of the force and the contributing modes of vibration of the particle. Therefore, we

```python
from matplotlib import pyplot as plt
import osaft

yosioka = osaft.yosioka1955.ScatteringField(
    f=1e6, R_0=1e-6,
    rho_s=1020, c_s=2350,
    rho_f=997, c_f=1498,
    p_0=1e5,
    wave_type=osaft.WaveType.STANDING,
    position=osaft.pi/4)

plot = osaft.FluidScatteringPlot(
    yosioka, r_max=4e-6)
plot.plot_pressure(incident=False)

plt.show()
```
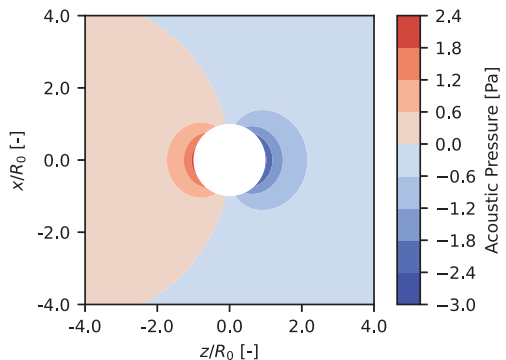

Figure 1: A short (but complete) OSAFT example: The Python code on the left generates a plot of the scattered pressure field due to an incident plane standing wave ($f = 1\,\mathrm{MHz}$, $p_0 = 1\,\mathrm{bar}$) around a polystyrene particle ($R_0 = 1\,\mu\mathrm{m}$, $\rho_s = 1020\,\mathrm{kg/m^3}$, $c_s = 2350\,\mathrm{m/s}$) suspended in water ($\rho_f = 998\,\mathrm{kg/m^3}$, $c_f = 1498\,\mathrm{m/s}$). The particle is positioned half-way between pressure node and pressure anti-node ($d = \pi/4$). Note, pressure plots are available in OSAFT from version 1.2.0, scheduled for release mid-August 2022.

Figure 2: ARF on a polystyrene particle in water: The plot of the ARF on a polystyrene particle in a standing wave field for different particle radii has been created using the OSAFT library. The frequency is $f = 5\,\mathrm{MHz}$, all other parameters are the same as in Fig. 1.
Note, the model from Hasegawa [5] and the source code for this example are available in OSAFT from version 1.1.0, scheduled for release early August 2022.

believe that the OSAFT library can also serve as an excellent tool for teaching acoustofluidics theory.
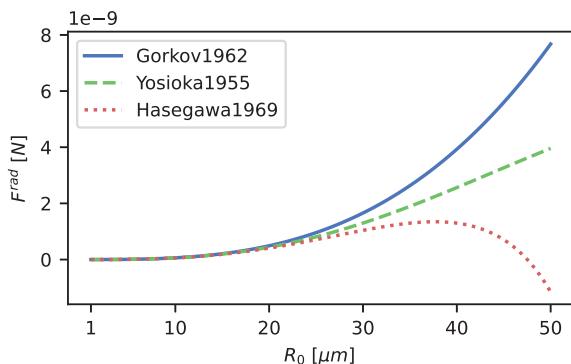
Comparing the ARF in Different Theories

Arguably more relevant for applications in acoustofluidics than the computation of scattering fields is the computation of the ARF. The OSAFT library can simplify the analysis of different ARF theories. In particular, the plotting functionalities that allow the evaluation of the ARF over a range of input parameters makes the comparison of multiple models straight-forward.

In Fig. 2 we investigate the ARF on a polystyrene particle in water in a $5\,\mathrm{MHz}$ standing wave field. In this example we compare three theories of increasing complexity: Gor'kov [4], Yosioka and Kawasima [3], and Hasegawa [5]. Gor'kov's model describes the particle as an inviscid droplet and the theory is limited to the long-wavelength regime. Also in the article by Yosioka and Kawasima the particle is assumed to be an inviscid droplet, however, droplet modes of all orders are included and the model is thus not limited by the long-wavelength approximation. In the most complex expression for the ARF in our example, the solution by Hasegawa, the particle is modelled as a linear-elastic solid. The parameters of the solid have been set such that the compressibility of the particle matches in all models. The surrounding fluid is assumed to be inviscid in all three cases.

For small particle radii the model from Gor'kov is in excellent agreement with the other two solutions. In this regime only the monopole and the dipole mode contribute to the ARF as predicted by Gor'kov. For a larger radius, higher-order modes start contributing to the ARF, and all three models begin to diverge. While the model by Yosioka and Kawasima includes higher-order modes, it still fails to predict the ARF accurately. Our example suggests that for an elastic solid like a polystyrene particle, the shear stresses inside the particle, included in the model by Hasegawa, strongly influence the ARF for larger particles and high-frequency excitations.

Getting Started with OSAFT

To get started with OSAFT, we provide a full documentation of the library on our website [6] including an installation guide and many examples for possible use-cases. The website also contains information for OSAFT users that are interested to contribute to the project.

References

[1] Jonas Fankhauser, Christoph Goering, and Jürg Dual. Osaft library: An open-source python library for acoustofluidics. *Frontiers in Physics*, page 445, 2022.

[2] Jonas Fankhauser and Christoph Goering. Pipy website of the *OSAFT* library. Online, 2022. https://pypi.org/project/osaft/.

[3] Katsuya Yosioka and Yukihiko Kawasima. Acoustic radiation pressure on a compressible sphere. *Acta Acustica united with Acustica*, 5(3):167–173, 1955.

[4] L.P. Gor'kov. On the Forces Acting on a Small Particle in an Acoustical Field in an Ideal Fluid. *Soviet Physics Doklady*, 6:773–775, 1962.

[5] Takahi Hasegawa. Acoustic radiation force on a sphere in a quasistationary wave field—theory. *The Journal of the Acoustical Society of America*, 65(1):32–40, 1979.

[6] Jonas Fankhauser and Christoph Goering. Readthedocs.org website of the *OSAFT* library. Online, 2022. https://osaft.readthedocs.io/en/stable/.

Electrical impedance spectroscopy for acoustofluidic applications

William N. Bodé[1], Fabian Lickert[1], Per Augustsson[2], and Henrik Bruus[1]

[1]Department of Physics, Technical University of Denmark, Kongens Lyngby, Denmark
E-mail: winabo@dtu.dk, URL: www.fysik.dtu.dk/microfluidics
[2]Department of Biomedical Engineering, Lund University, Lund, Sweden

Introduction

Numerical simulations of acoustofluidic devices require precise knowledge of several material parameters. However, there is a lack of the complex-valued elastic moduli especially in the case of polymers. To overcome this hurdle, we have developed a simple and low-cost method, named ultrasound electrical impedance spectroscopy (UEIS) [1], to determine the elastic moduli of polymers and other materials by measuring the electrical impedance spectrum $Z(f)$. The method relies on numerically fitting of the unknown material parameters to obtain the best possible agreement between the measured and the simulated impedance spectrum. The method extends previous work [2-4] by enabling an automated determination of both the real and imaginary part of the elastic moduli.

Theory

For an elastic solid, the governing equation for the time-harmonic displacement field $\boldsymbol{u}$ is given by $\boldsymbol{\nabla} \cdot \boldsymbol{\sigma} = -\rho \omega^2 \boldsymbol{u}$. In Voigt notation, the stress $\boldsymbol{\sigma}^\mathsf{T} = (\sigma_{xx}, \sigma_{yy}, \sigma_{zz}, \sigma_{yz}, \sigma_{xz}, \sigma_{xy})$ and the strain $\boldsymbol{s}^\mathsf{T} = (\partial_x u_x, \partial_y u_y, \partial_z u_z, \partial_y u_z + \partial_z u_y, \partial_x u_z + \partial_z u_x, \partial_x u_y + \partial_y u_x)$ for an isotropic solid, e.g. a polymer, are connected through $\boldsymbol{\sigma} = \boldsymbol{C} \cdot \boldsymbol{s}$ by the stiffness tensor

$$\boldsymbol{C} = \begin{pmatrix} C_{11} & C_{12} & C_{12} & 0 & 0 & 0 \\ C_{12} & C_{11} & C_{12} & 0 & 0 & 0 \\ C_{12} & C_{12} & C_{11} & 0 & 0 & 0 \\ 0 & 0 & 0 & C_{44} & 0 & 0 \\ 0 & 0 & 0 & 0 & C_{44} & 0 \\ 0 & 0 & 0 & 0 & 0 & C_{44} \end{pmatrix}, \quad C_{12} = C_{11} - 2C_{44}. \tag{1}$$

$\boldsymbol{C}$ is determined by the two complex-valued elastic moduli $C_{11} = C_{11}' + \mathrm{i} C_{11}''$ and $C_{44} = C_{44}' + \mathrm{i} C_{44}''$.

Materials and methods

After precise measurements of their geometry, a polymer ring and a PZT transducer disk are glued together using the UV-curable glue NOA 86H, see Fig. 1. The PZT transducer disk is electrically contacted by two spring-loaded pins, allowing impedance measurements while minimizing the clamping force. The measurement procedure is performed in two steps: First the unloaded PZT disk is characterized, and then the polymer-ring-loaded PZT disk is measured and fitted. The electrical impedance spectrum $Z(f)$ is measured using a Vector Network Analyzer Bode 100 (OMICRON electronics GmbH, Klaus, Austria) in the frequency range from 500 Hz to 5 MHz. The cost function $\mathcal{C}$, which is minimized in the fitting procedure by varying the four unknown polymer material parameters C_{11}', C_{11}'', C_{44}' and C_{44}'', is defined as $\mathcal{C} = \sqrt{\sum_i \left[\log_{10}\big(|Z_{\mathrm{exp}}(f_i)|\big) - \log_{10}\big(|Z_{\mathrm{sim}}(f_i)|\big) \right]^2}$.
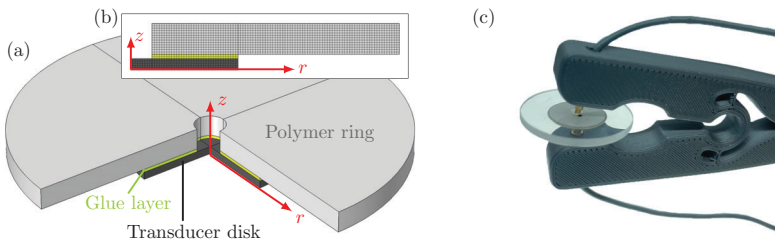

Figure 1: (a) Overview of the 3D system consisting of a polymer ring, glue, and a piezoelectric transducer disk. (b) 2D cross-section in the r-z plane representing the axisymmetric domain used in the numerical simulations. (c) Image of the transducer-glue-polymer stack mounted between two spring-loaded pins.
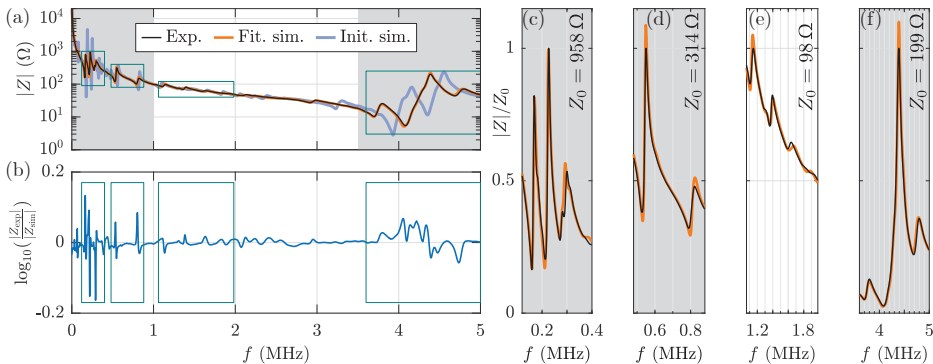
Figure 2: (a) Semilog plot of the measured (black), the UEIS-fit-simulated (orange), and initial-value-simulated (blue) impedance spectrum $|Z(f)|$ of a PMMA ring glued to a PZT disk. The gray regions indicate the frequency ranges used in the fitting. (b) Plot of the logarithm to the relative difference $\Delta_{\rm sim}^{\rm exp} = \log_{10}(|Z_{\rm exp}|/|Z_{\rm sim}|)$ between the experimental and the simulated impedance spectrum. (c)-(f) Zoom-in on different regions showing the same as (a) but on a linear scale normalized by Z_0. The positions of the four zoom-ins are indicated by the four rectangular frames inserted in both panel (a) and (b).

Results of the parameter fitting

The measured and fitted impedance spectrum $|Z(f)|$ in Fig. 2 show a good agreement, indicating that the correct material parameters have been found. Zoom-ins on regions, with the largest relative deviations $\Delta_{\rm sim}^{\rm exp} = \log_{10}(|Z_{\rm exp}|/|Z_{\rm sim}|)$ between experiment $|Z_{\rm exp}(f)|$ and simulation $|Z_{\rm sim}(f)|$, show that even in those regions small features of the signal are captured well. In Table 1, UEIS results for C_{11} and C_{44} are shown for a PMMA sample. Compared to reference values measured by ultrasonic-through-transmission (UTT), we found deviations as low as -1.10 % and 0.5 % for the real parts C_{11}' and C_{44}'. Due to a lower sensitivity of the impedance signal to changes in the imaginary parts, the fitting of these is less accurate with deviations of 3.8 % for C_{11}'' and -11.7 % for C_{44}'' compared to the UTT values. The method shows good precision, as the relative standard deviation of the mean $\hat{\sigma}_{\rm UEIS}$ is low, below 1 % and 7 % for the real and imaginary parts, respectively.

Table 1: The elastic moduli of PMMA (Diakon TD525, Lucite International), determined by the UEIS procedure and measured using UTT at 24 ℃, with a measured density $\rho = 1162(4)$ kg/m^3. $\hat{\sigma}_{\rm UEIS}$ is the relative standard deviation of the UEIS mean. $\Delta_{\rm UEIS}^{\rm UTT}$ is the deviation of the UTT values relative to the UEIS values.

Param.	Unit	UEIS	$\hat{\sigma}_{\rm UEIS}$ (%)	UTT	$\Delta_{\rm UEIS}^{\rm UTT}$ (%)
C_{11}'	GPa	7.18(4)	0.6	7.1(1)	-1.1
C_{11}''	GPa	$-0.183(5)$	2.9	$-0.19(1)$	3.8
C_{44}'	GPa	1.553(8)	0.5	1.56(1)	0.5
C_{44}''	GPa	$-0.111(7)$	6.3	$-0.098(6)$	-11.7

Conclusion

By providing precise values of the elastic moduli, the UEIS method enables more accurate simulations of acoustofluidic devices. This is especially relevant for obtaining improved agreement between measurements and design simulations of polymer-based devices, for which these moduli govern the all-important whole-system acoustic resonance modes. The UEIS method is simple to execute: It takes 4 min to measure $Z(f)$ and 1 min to upload the result and execute our automated fitting software. The resulting UEIS-fitted spectrum and the values for C_{11} and C_{44} are picked up after 10 hours.

Acknowledgments

References

[1] W. N. Bodé, F. Lickert, P. Augustsson, and H. Bruus. ArXiv/2204.06464 **submitted** (2022). [pdf]
[2] J. Ilg, S. J. Rupitsch, A. Sutor, and R. Lerch. IEEE T. Instrum. Meas. **61**, 3031 (2012). [doi]
[3] J. Maynard. Physics Today **49**, 26 (1996). [doi]
[4] A. G. Steckel, H. Bruus, P. Muralt, and R. Matloub. Phys. Rev. Applied **16** 014014 (2021). [doi, pdf]

Thermoviscous corrections to the acoustic radiation force on a spherical particle including scattering and microstreaming

Bjørn G. Winckelmann and Henrik Bruus

Department of Physics, Technical University of Denmark, Kongens Lyngby, Denmark
E-mail: winckel@dtu.dk, URL: http://www.fysik.dtu.dk/microfluidics

Introduction

Recent theoretical work on the acoustic radiation force (ARF) on spherical particles in viscous [1] and thermoviscous [2] fluids have studied corrections to the ARF on small particles compared to ideal-fluid results [3]. However, these studies neglected the steady microstreaming generated around the sphere by thermoviscous losses in the boundary layers and in the bulk fluid. ARF with thermoviscous microstreaming was previously studied analytically by Doinikov in general [4], and his results were validated numerically for viscous fluids by Baasch, Pavlic, and Dual [5]. We extend this theory [4] by taking into account temperature and density dependencies of material parameters in thermoviscous fluids hitherto neglected. We identify experimentally relevant regimes that require the inclusion of all thermoviscous effects to accurately predict the ARF.

The acoustic radiation force (ARF) in the long wavelength limit

The oscillatory velocity $\boldsymbol{v}_1^{\text{in}}$ and pressure p_1^{in} of an axisymmetric, but otherwise arbitrary, acoustic incident wave in a thermoviscous fluid far from any sound transducer are determined from its compressional potential ϕ_c^{in}, which generally can be written as a partial wave expansion,

$$\phi_c^{\text{in}} = \sum_{n=0}^{\infty} A_n j_n(k_c r) P_n(\cos\theta), \qquad \boldsymbol{v}_1^{\text{in}} = \boldsymbol{\nabla}\phi_c^{\text{in}}, \qquad p_1^{\text{in}} = \mathrm{i}\omega\rho_0\phi_c^{\text{in}} - \left(\eta_0^{\text{b}} + \frac{4}{3}\eta_0\right)k_c^2\phi_c^{\text{in}}. \qquad (1)$$

Here, j_n denote spherical Bessel functions, P_n are Legendre polynomials, k_c is the damped compressional wave number of the fluid, η_0 is the dynamic viscosity, η_0^{b} is the bulk viscosity, ρ_0 is the density, and ω is the angular frequency of the incident wave. The axis of symmetry is z, illustrated in Fig. 1.

Denoting the drag force from the incident wave $\boldsymbol{F}_{\text{drag}}$, the general form of the total steady force $\boldsymbol{F}_{\text{rad}}$ on a spherical particle centered at $r = 0$ in such a wave can be written as [4],

$$\boldsymbol{F}_{\text{rad}} = -\boldsymbol{e}_z 3\pi\rho_0 \sum_{n=0}^{\infty} \frac{n+1}{(2n+1)(2n+3)}\text{Re}\big[A_n A_{n+1}^* D_n\big] + \boldsymbol{F}_{\text{drag}}, \qquad (2)$$

where D_n are coefficients known analytically and containing all quadratic combinations of scattering coefficients. In the long wavelength limit characterized by $x_0 = |k_c a| \ll 1$, where a is the particle radius, only the first two terms in this sum contribute to leading order in x_0. Using the definitions in Eq. (1) and the properties of j_n and P_n, we have derived the following identity to leading order in x_0,

$$\boldsymbol{F}_{\text{rad}} = -\pi a^3 \left(\frac{2\kappa_s}{3}\text{Re}\left[\frac{9(D_0 + D_1^*)}{2x_0^3}p_1^{\text{in}}\boldsymbol{\nabla}p_1^{\text{in}*}\right] - \rho_0\text{Re}\left[-\frac{9D_1}{2x_0^3}(\boldsymbol{v}_1^{\text{in}}\cdot\boldsymbol{\nabla})\boldsymbol{v}_1^{\text{in}*}\right]\right)\Bigg|_{r=0} + \boldsymbol{F}_{\text{drag}}, \qquad (3)$$
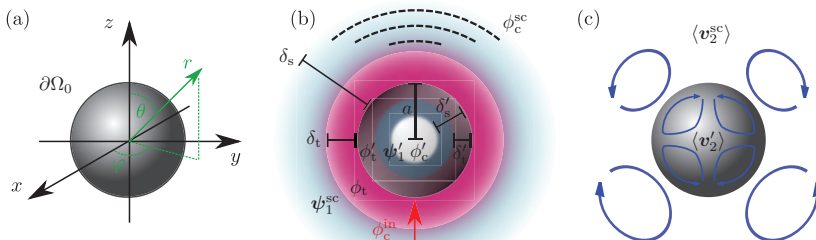

Figure 1: Sketch of the radiation force calculation. (a) The sphere and the coordinate systems. (b) The 1st-order scattering problem. (c) The steady, 2nd-order microstreaming generated in- and outside the sphere.

where κ_s is the adiabatic compressibility of the fluid. Eq. (3) reveals the analogy between the theories derived from the method used by Gorkov [3], Settnes and Bruus [1], and Karlsen and Bruus [2], and the theory by Doinikov [4]. The analytically known constants $9(D_0 + D_1^*)/(2x_0^3)$ and $-9D_1/(2x_0^3)$ correspond to the monopole and dipole coefficients in Refs. [1-3]. Their analytical expressions are very complicated when the contributions of the acoustic microstreaming $\langle \boldsymbol{v}_2 \rangle$ are included.

We extend the work of Doinikov by including the effects of temperature and density dependency in the fluid parameters, and furthermore, for a fluid particle, by including the acoustic streaming inside the sphere, Fig. 1. All these effects contribute to leading order in x_0 to the ARF on small particles.

Results
For the important case of an incident standing plane wave $p_1^{\mathrm{in}} = p_0 \cos[k_c(z + d)]$, we have to leading order in x_0 derived the following identity for the ARF,

$$\boldsymbol{F}_{\mathrm{rad}} = \boldsymbol{e}_z 4\pi \Phi_{\mathrm{ac}} a^3 k_0 E_{\mathrm{ac}} \sin(2k_0 d), \qquad \Phi_{\mathrm{ac}} = \frac{3}{2x_0^3}\mathrm{Re}[D_0 - 2D_1], \qquad k_0 = \frac{\omega}{c_0}, \qquad E_{\mathrm{ac}} = \frac{1}{4}\kappa_s p_0^2. \quad (4)$$

Here, we have introduced a generalization of the usual acoustic contrast factor Φ_{ac}, and defined the the wave number k_0 by the fluid sound speed c_0, and the acoustic energy density E_{ac} of the incident wave. Φ_{ac} includes the thermoviscous dependency of the magnitude and sign of the ARF, and controls how fast a given particle is focused in pressure nodes, $\Phi_{\mathrm{ac}} > 0$, or anti-nodes, $\Phi_{\mathrm{ac}} < 0$.

The contrast factor Φ_{ac} of a copper sphere in oil was studied numerically in Ref. [5], where a sign reversal for small particles was identified. Karlsen and Bruus also found a sign reversal for the case of a small water droplet in air [2]. In Fig. 2, the contrast factors for these two cases are replicated as a function of particle radius with the five different analytical theories by Gorkov [3], Settnes [1], Karlsen [2], Doinikov [4], and Winckelmann [present work]. The case of a copper sphere in oil shows a sign reversal in the contrast factor Φ_{ac} for small particles for both theories that include the microstreaming contributions (Doinikov [4] and Winckelmann [here]), albeit it happens at significantly larger particle sizes, when parameter temperature and density dependencies are taken into account. For a water droplet in air, the microstreaming theories also predict a sign reversal in Φ_{ac}, but the phenomena is seen at much higher particle radii, than what was found by Karlsen and Bruus [2], who did not include the acoustic microstreaming in their model.
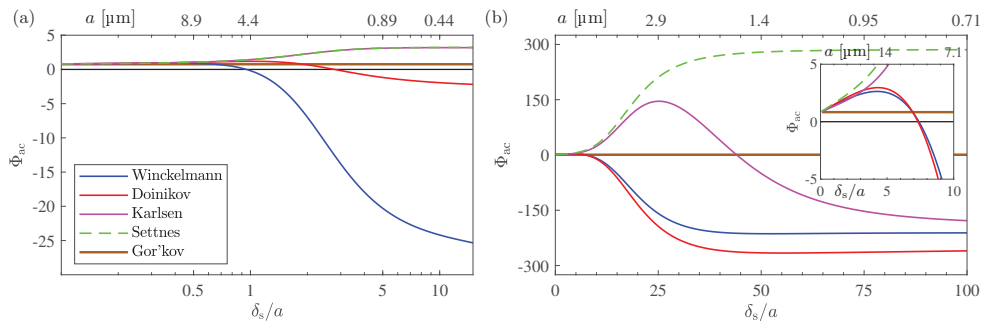

Figure 2: The contrast factor Φ_{ac} computed by Eq. (4) and plotted versus particle radius a (upper axis) and the normalized viscous-boundary-layer thickness δ_s/a (lower axis). (a) A copper sphere in oil at $f = 1\,\mathrm{MHz}$. (b) A water droplet in air at $f = 1\,\mathrm{kHz}$.

Conclusion
We have derived an analytical theory for the acoustic radiation force including microstreaming on spherical particles in an axisymmetric wave in a thermoviscous fluid. The theory extends the work of Doinikov [4] by including temperature and density dependencies of all parameters and (for droplets) the acoustic streaming inside the particle. These effects are found to greatly enhance the force on microparticles in experimental relevant cases, such as heavy particles in oil and water droplets in air.

References
[1] M. Settnes and H. Bruus. Phys. Rev. E **85**, 016327 (2012). [doi, pdf]
[2] J. T. Karlsen and H. Bruus. Phys. Rev. E **92**, 043010 (2015). [doi, pdf]
[3] L. P. Gorkov, Soviet Physics - Doklady, **6**, 773 (1962). [Doklady Akademii Nauk SSSR **140**, 88 (1961).]
[4] A. Doinikov. J. Acoust. Soc. Am. **101**, 713 (1997). [doi]
[5] A. Pavlic, T. Baasch, and J. Dual. J. Acoust. Soc. Am. **148**, 2784 (2020). [doi]

Interfacial evolutions and phase changes of rime ice activated by thin-film surface acoustic waves

Deyu Yang[1], Luke Haworth [2], Xianghui Hou[1], and Yong-Qing (Richard) Fu[2]

[1]Faculty of Engineering, University of Nottingham, Nottingham, NG7 2RD, UK
[2]Faculty of Engineering and Environment, Northumbria University, Newcastle upon Tyne, NE1 8ST, UK
E-mail: deyu.yang@nottingham.ac.uk/luke.haworth@northumbria.ac.uk

Introduction

Icing accretion on structural surfaces is one of the critical hazards in aerospace, power transmission, offshore platform, and wind turbine sectors (1,2). The efficiency and sustainability of current ice mitigation technologies have significant limitations (3,4). Thin film-based SAWs have been demonstrated to generate both acoustic wave vibrations and thermal effects directly onto the structural surfaces, thus offering great potentials for both anti-icing and de-icing with high efficiency (5,6). However, interfacial behaviours, ice removal, and prevention mechanisms for both anti-icing and de-icing of the rime under propagating SAWs have never been explored. There is a lack of in-depth investigations on the interfacial responses and phase changes driven by SAWs during the icing and de-icing processes, which restricts the further exploration of SAW devices for ice mitigation.

This study is focused on the anti-icing and de-icing mechanisms of porous rime ice on a structural surface (aluminum plates) using integrated ZnO thin film SAWs. We first propose theoretical mechanisms and models for interactions of SAWs with the rime ice and/or liquid/ice mixtures. Then we focus on the experimental studies of anti/de-icing performance for rime ice using the thin film SAW devices. The evolution of ice morphology and phase changes at different humidity levels in icing conditions and different SAW powers are investigated, from which the de-icing and anti-icing mechanisms using thin film SAWs are deduced.

Figure 1. Schematic illustration of interfacial behaviors between rime ice and propagating SAWs
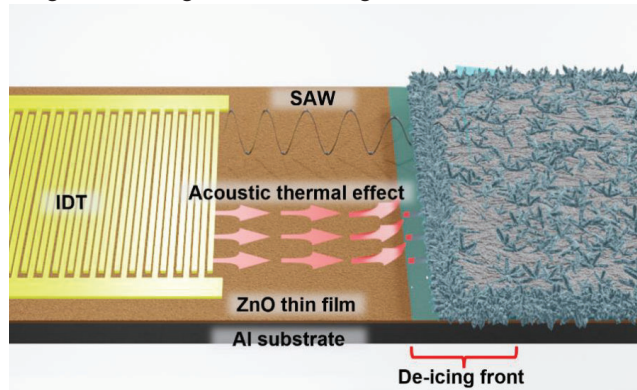
SAW device and anti/de-icing experiments

A ZnO film of ~5 μm thick was deposited on 1.5 mm-thick Al plates using the DC magnetic sputtering technique. The DC power was 400 W and the Ar/O2 gas flow was 10/15 (in the unit of sccm). The interdigital transducers (IDTs) were patterned on top of ZnO thin film through a conventional photolithography and lift-off process. A bilayer of Cr/Au with thicknesses of 20 nm/100 nm was prepared using a thermal evaporator (EDWARDS AUTO306) as the electrode. The IDTs were designed with a wavelength of 400 μm, comprising 30 pairs of electrodes.

The anti/de-icing experiment was conducted in a freezing chamber that was built based on a cold plate (Para Cooler A, Para Cooler O, Weinkauf Medizintechnik, Germany) with a sealed resin shield. The accurate humidity was achieved using an atomizer (Omron Ultrasonic Nebulizer NE-U17) that generated water aerosols with controlled vaporizing power and imputing speed. The SAW device was cooled down in the chamber for 20 minutes in advance. Then, the icing process was carried out with various icing humidity levels and SAW powers, respectively. An IDS camera with Navitar 12X objective lens and a high-speed camera (HotShot 1280 CC) with Navitar 6.0X zoom lens and 1.5X objective lens were used to record the ice morphology from the top and side views of the device.
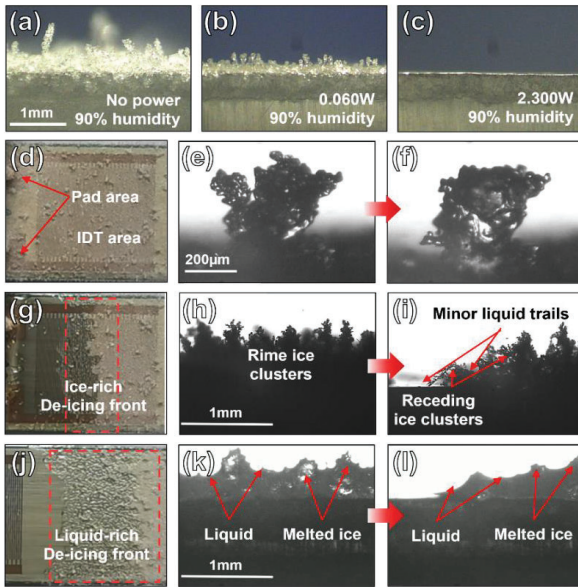
Anti/de-icing performance under SAWs

Figure 2 Cross-sectional surface or ice morphology after 20-minute anti-icing process: (a) with no SAW power in 90% humidity, (b) with the SAW power of 0.060W in 90% humidity, and (c) with the SAW power of 2.300W in 90% humidity. The changes of ice morphology or ice crystals before the occurrence of possible phase changes with the propagation of SAW in the de-icing process: (d) surface morphology of the iced SAW device (in the IDT area, top view), (e) the ice crystal before the application of SAW power, and (f) the ice crystal after the application of SAW power. The de-icing phenomenon of the ice-rich de-icing front: (g) the image of the real situation, (h) the morphology of ice clusters before application of SAW power, and (i) the morphology of the ice-rich receding de-icing front. The de-icing phenomenon of the liquid-rich de-icing front: (j) the image of the real situation, (k) the morphology of melted ice clusters before the reaching of the de-icing front, and (l) the morphology of the liquid-rich receding de-icing front.

The phenomena in Figures 2(a) to 2(c) prove that the icing was restrained effectively with the application of SAWs in 90% humidity. With the increase in SAW power, better anti-icing performance was obtained with higher SAW power. For the attached supercooled droplets, the SAWs prevent ice nucleation and accretion by restricting the size of ice embryos to be smaller than the critical nucleolus radius and increasing the critical free energy of heterogeneous ice nucleation. The hybrid effect of acoustic vibration and thermal effect offers an advanced platform for acoustofluidics to enhance the further anti-icing performance. The attached droplets are easily activated, jetted, or evaporated before the ice nucleation happens, thus significantly preventing or delaying ice formation and accumulation.

Figure 2(d) to Figure 2(l) show three different stages in the SAW de-icing process. The first stage in Figure 2(d) to Figure 2(f) shows no macroscopical changes in ice morphology, while the acoustic wave vibration induced by SAWs led to dramatic changes in the single ice crystal. After the phase change due to the acoustic thermal effect, an ice-rich de-icing front can be observed in the second de-icing stage (Figure 2(g) to Figure 2(i)). The acoustic vibration and thermal heating provide enough energy to locally melt ice clusters into a liquid layer, which is then merged with the ice clusters. These large ice clusters are often seen to collapse into the thin liquid layer. With the enhanced exchange of mass and heat induced by the acoustic streaming force, this liquid/ice crystal de-icing front is seen to gradually move along the direction of SAW's propagation. The third stage in Figure 2(j) to Figure 2(l) occurs in zones that are often far away from the IDT area. The de-icing front becomes much wider. The ice crystals shrink significantly without clear ice cluster morphologies. The liquid layer becomes more apparent, which forms a liquid-rich front. The acoustic streaming inside the liquid enhances the heat transfer, and also causes significant pumping, jetting, or nebulization effects.

Conclusion The anti-/de-icing mechanisms of rime ice using thin film SAW technology were studied. Both good performances of anti/de-icing were achieved even in the severe frozen environment with high humidity. Both acoustic wave vibration and acoustic heating play key roles. The surface vibration led to the break-up and collapse of ice crystals or clusters. The accumulation of heat led to the melted liquid that absorbed the SAW waves and led to the internal streaming to enhance the exchange of mass and heat. The formation and movement of the de-icing front in the de-icing process were enhanced accordingly.

References
[1] A Kudzys, Engineering Structures. **28**(5): 682-689(2006)
[2] C Ryerson, et al., Cold Reg Sci Technol **65**(1), 97-110(2011)
[3] Y Shen, et al., Progress in Materials Science **103**, 509-507(2019)
[4] L Fay, et al., Water, Air, & Soil Pollution **223**(5), 2751-2770(2012)
[5] D Yang, et al., Advanced Materials Interfaces **8**(2), 2001776(2021)
[6] X Zeng, et al., Langmuir **37**(40), 11851-11858(2021)

ANALYSIS OF ACOUSTIC RELOCATION OF IMMISCIBLE FLUIDS IN A MICROCHANNEL

Varun Kumar Rajendran[1], Aravind Ram S P, Karthick Subramani[1]

[1]Indian Institute of Information Technology, Design and Manufacturing, Kancheepuram.
E-mail: mdm20d010@iiitdm.ac.in

Introduction

Earlier Deshmukh et al.[1] experimentally proved that the relocation phenomena in an inhomogeneous fluid are dependent on acoustic impedance. The theoretical analysis along with experimentation for relocation and streaming suppression of miscible inhomogeneous fluid was first developed by Karlsen et al.[2]. However, these studies do not involve immiscible inhomogeneous fluid. Hemachandran et al.[3] experimentally studied the dynamics of coflowing immiscible fluids under acoustic fields and found that surface tension affects relocation but did not report the threshold force or energy density that is required for relocation. In this study, we report the critical acoustic energy density that is required to overcome the surface tension force for relocation of immiscible fluid in a microchannel under acoustics and also study the relocation phenomenon using numerical analysis.

Theoretical Analysis

For an inhomogeneous fluid, the relocation body force due to acoustics can be approximated as[4]

$$f_{ac} = -E_{ac}\cos(2k_a x)\Delta\hat{Z} \tag{1}$$

Where E_{ac} is acoustic energy density, Z is impedance, $\hat{Z} = Z/Z_{avg}$ and, k_a is wavenumber. For standing acoustic half-wave $k_a = \pi/W$. The instability analysis in a single-mode disturbance on the x-y plane for a domain of inhomogeneous immiscible fluid in a microchannel of differing impedance Z_1 and Z_2, separated by an interface of surface tension T with an imposed perturbation as shown in Fig.1 yields the eigenvalue

$$n = \sqrt{kF\left(\frac{Z_2 - Z_1}{\rho_2 + \rho_1} - \frac{k^2 T}{F(\rho_2 + \rho_1)}\right)} \tag{2}$$

Where $F = \frac{E_{ac}\sin(2k_a x)2k_a}{Z_{avg}}$, $k = \pi/H$ and ρ is density. The critical acoustic energy density E_{cr} required for relocation of immiscible fluids under acoustic fields is obtained as

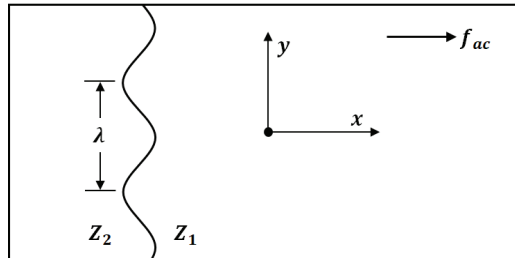$$E_{cr} = \frac{k^2 T Z_{avg}}{\sin(2k_a x)2k_a(Z_2 - Z_1)} \tag{3}$$

Figure 1: Inhomogeneous fluid (of different impedance Z_1 and Z_2) separated by a perturbed interface.

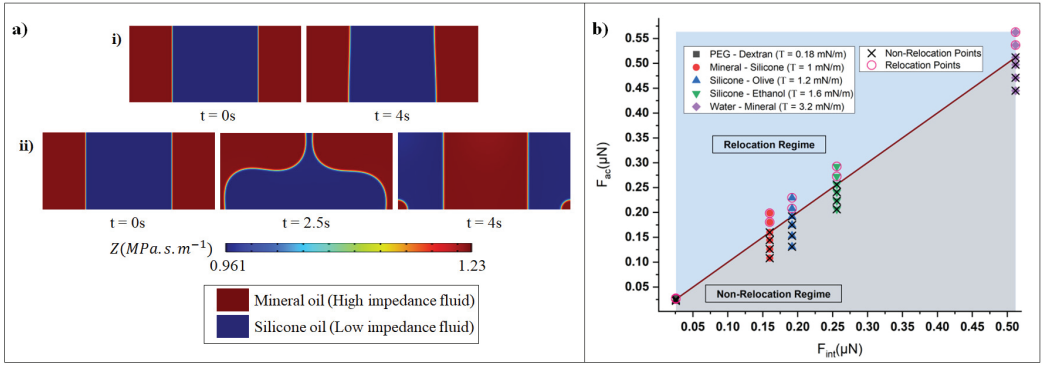**Figure 2:** **a)** Non-relocation and relocation of mineral-silicone oil in a microchannel. **(i)** No relocation when $E_{ac} = 80 \ J/m^3 < E_{cr}$ **(ii)** Relocation occurs when $E_{ac} = 100 \ J/m^3 > E_{cr}$. **b)** Plot showing relocation and non-relocation regimes for different immiscible fluids. Crossed points in the box indicate non-relocation points, points on the dark green line are critical points, and solid points are relocation points. Light blue and light gray areas indicate relocation and non-relocation regimes respectively.

Results and Discussion

When an inhomogeneous-immiscible fluid is subjected to a standing acoustic half-wave, the fluid relocation takes place only when the acoustic force overcomes the surface tension force. An immiscible fluid combination of mineral-silicone oil in a microchannel of width 380 μm and height 160 μm with a surface tension of 1 mN/m is considered for the study. The critical energy density required for relocation (using Eq.3) is found to be 88.87 J/m^3. Hence the relocation of mineral-silicone oil in the microchannel takes place only if the applied acoustic energy density is greater than 88.87 J/m^3. The numerical analysis of the relocation phenomenon is studied in COMSOL Multiphysics 6.0. It can be seen from Fig.2.a-i) that for an acoustically unstable configuration, the relocation of immiscible fluids does not take place if the applied energy density ($E_{ac} = 80 \ J/m^3$) is less than the critical energy density. Whereas if the applied energy density is more than the critical energy density ($E_{ac} = 100 \ J/m^3 > E_{cr}$), then the high impedance mineral oil moves to the center (node) from the sidewalls, and the low impedance silicone oil moves to the sidewalls (antinodes) from the center as shown in Fig 2.a-ii). These results of the relocation of immiscible fluids in a microchannel are well in agreement with previous experimental studies[3]. To characterize the relocation and non-relocation regime in a microchannel for immiscible fluids, we define the capillary acoustic number (Ca_{ac}) as

$$Ca_{ac} = \frac{2k_a E_{ac} \Delta Z \sin(2k_a x)}{k^2 T Z_{avg}} \tag{4}$$

The critical Ca_{ac} is found to be 1 for interfaces that are located at 90 μm away from the center of the microchannel on either sides, indicating that relocation of immiscible fluids takes place only above this value. This number helps in differentiating relocation and non-relocation regimes as shown in Fig.2.b.

Conclusion

An expression to find the critical acoustic energy density to cause relocation and a new acoustic capillary number that differentiates relocation and non relocation regimes for immiscible fluids in a microchannel is proposed. This study of the relocation of immiscible fluids under acoustic fields can be helpful in immiscible fluid manipulation in microscale systems.

References

[1] Deshmukh. S, Brzozka. Z, Laurel. T, and Augustsson. P, "Acoustic radiation forces at liquid interfaces impact the performance of acoustophoresis," *Lab Chip*, vol. 14, no. 17, pp. 3394-3400, Sep. 2014.
[2] J. T. Karlsen, P. Augustsson, and H. Bruus, "Acoustic Force Density Acting on Inhomogeneous Fluids in Acoustic Fields," *Phys. Rev. Lett.*, vol. 117, no. 11, pp. 1-6, 2016.
[3] E. Hemachandran, S. Karthick, T. Laurell, and A. K. Sen, "Relocation of coflowing immiscible liquids under acoustic field in a microchannel," *Epl*, vol. 125, no. 5, 2019..
[4] V. K. Rajendran, S. Jayakumar, M. Azharudeen, and K. Subramani, "Theory of nonlinear acoustic forces acting on inhomogeneous fluids," *J. Fluid Mech.*, vol. 940, Aug. 2022.

Measurement of the acoustically induced fluid flow in a 2DsSAW tweezer and its influence on single cell patterning

Zhichao Deng[1], Hagen Schmidt[2], Christian Cierpka[1], and Jörg König[1]

[1]Institute of Thermodynamics and Fluid Mechanics, Technische Universität Ilmenau, Ilmenau, Germany
E-mail: Joerg.Koenig@tu-ilmenau.de URL: http://www.tu-ilmenau.de/ttd
[2]Leibniz Institute for Solid State and Materials Research Dresden, SAWLab Saxony, Dresden, Germany

Introduction

Acoustic tweezers have been demonstrated as a versatile toolset for the precise manipulation of abiotic particles, biological cells or exosomes. Even single cells can be trapped utilizing a two-dimensional standing surface acoustic wave (2DsSAW) with a wavelength in the same order as the cell dimensions [1,2]. In this case, the acoustic radiation force (ARF) mainly governs the three-dimensional particle pattern. Besides, the drag force exerts on the particles due to a fluid flow induced by the acoustic streaming effect, which may cause particles to be displaced from locations predicted solely by considering the AR, [3]. Since both forces scale differently with respect to the ratio of particle size and acoustic wavelength, differences in the three-dimensional particle pattern result. In order to shed more light into the interplay between both forces originating from a complex 2DsSAW, detailed knowledge is gained by measuring the three-dimensional velocity distribution within the chamber applying astigmatism particle tracking velocimetry (APTV) [4].

Experimental

Investigations were performed for an acoustic tweezer setup based on a 2DsSAW field excited by two pairs of opposing interdigital transducers (IDTs) deposited on a 128° rotated Y-cut lithium niobate substrate. Both IDT pairs were arranged in orthogonal direction and driven by a common resonance frequency of 32.4 MHz. In between, a microfluidic chamber made of Polydimethylsiloxan (PDMS) with an inner lateral size of $1.2\,\mathrm{mm} \times 1.2\,\mathrm{mm}$ and a height of about $55\,\mu\mathrm{m}$ was positioned. The chamber was filled with deionized water. To measure the acoustically induced fluid flow, fluorescently labeled polystyrene particles of 450 nm in diameter were suspended as tracer particles. Details about the APTV setup used and reliability of fluid flow measurements in sSAW-devices can be found in Sachs et al. [5]. During the measurements, resonance frequency and power were kept constant. The electric power applied corresponds to an acoustic power of 100 mW within the microfluidic chamber estimated by in situ measurements using laser Doppler vibrometry [3].

Results and discussion

Figure 1 illustrates the spatially and time averaged velocity field measured at the center of the microfluidic chamber. Since the lateral size of the measurement volume amounted to $660\,\mu\mathrm{m} \times 680\,\mu\mathrm{m}$ approximately, the 3D velocity distribution was measured only at the central part of the chamber. Within this region acoustically induced 3D vortex structures exist, resembling in lateral direction the distribution of the 2DsSAW field measured inside the chamber [3]. While regions of positive u_z-velocities in height direction coincide with regions with maximum displacement amplitude of the 2DsSAW, negative u_z-velocities can be seen at positions with minimum displacement amplitude. The latter correspond to positions of acoustic force potential wells, where particles or cells of appropriate size can be trapped [1-3]. However, the actual particle positions within these regions depend on the balance of the ARF and the drag force. Moreover, the strength of the acoustically induced fluid flow varies over the chamber width due to slight local variations of the displacement amplitude caused by acoustic diffraction [3]. According to Fig. 1c) and d), counter-rotating vortices evolve in both directions having an extent of half the wavelength of both superimposed SAWs approximately. In addition, maximum vorticity was found at almost center height and in close vicinity to positions corresponding to locations with maximum displacement amplitude of the 2DsSAW. This complex three-dimensional flow causes particles to be displaced from positions with local sound pressure minima not only in lateral but also in height direction [3].

Conclusion
The structure of the acoustically induced fluid flow in a microfluidic chamber of an acoustic tweezer based on a 2DsSAW has been characterized experimentally by applying APTV. These investigations revealed a complex 3D vortex structure within the chamber, with a formation and extension of the vortices that agree well to the 2DsSAW field measured at the fluid-substrate interface. As particle trapping locations are governed by the balance of ARF and drag force, the induced fluid flow causes different trapping positions depending on the size of the particles and the acoustic wavelength. During the conference, measurements not only of the fluid flow but also of particle patterning will be presented for different acoustic wavelengths and particle sizes, which provide important information for facilitating a more precise manipulation of particles or cells in acoustic tweezer devices.
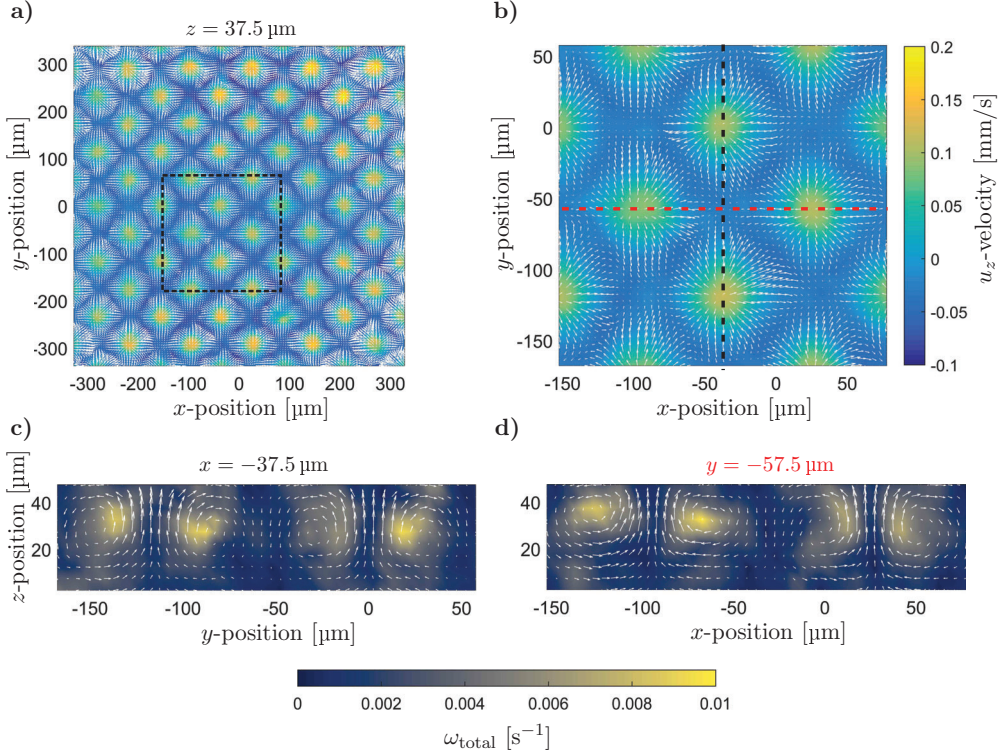

Figure 1: (a) Top view of the flow velocity field measured inside the microfluidic chamber at a height of about $z = 37.5\,\mu\mathrm{m}$. (b) Detail view of Fig. 1(a). Arrows indicate flow direction in the corresponding lateral plane, while color coding represents the u_z-component in height direction. (c) and (d) cross section along $x-$ and $y-$direction as marked in Fig. 1(b). Arrows indicate velocity direction within the corresponding vertical plane. Color coding represents total vorticity $\omega_{\mathrm{total}} = \sqrt{\omega_x^2 + \omega_y^2 + \omega_z^2}$.

References
[1] D.J. Collins , B. Morahan , J. Garcia-Bustos , C. Doerig , M. Plebanski, and A. Neild. Nat. Commun. **6**, 8686 (2015).
[2] X. Ding, S.-C.S. Lin, B. Kiraly, H. Yue, S. Li, I.-K. Chiang, J. Shi, S.J. Benkovic, and T.J. Huang. Proc. Natl. Acad. Sci. U.S.A. **109**, 11105-11109 (2012).
[3] R. Weser, Z. Deng, V.V. Kondalkar, A.N.Darinskii, C. Cierpka, H. Schmidt, and J. König. Lab Chip **22**, 2886-2901 (2022).
[4] C. Cierpka, R. Segura, R. Hain, and C.J. Kähler. Meas. Sci. Technol. **21**, 045401 (2010).
[5] S. Sachs, M. Baloochi, C. Cierpka, and J. König. Lab Chip **22**, 2011-2027 (2022).

Formation of micron sized drops from low viscosity liquid films under the action of surface acoustic waves

Niladri Sekhar Satpathi[1] and Ashis Kumar Sen[1]

[1]Department of Mechanical Engineering, Indian Institute of Technology Madras, Chennai, India
E-mail: piyushsatpathi962@gmail.com

Introduction

Surface acoustic waves (SAWs) have been used for decades in various domains of engineering. In recent years interest has spiked in the interaction of SAWs with thin liquid films [1,2]. Previously, works have explained the formation of soliton like wave pulses through understanding the formation of capillary ridges in films dominated by Rayleigh streaming [1]. However, the interaction SAWs with low viscosity liquids ($\mu \sim 1$ mPas) is still not fully understood. In this work we discuss the formation of micron sized drops from the formed ultrathin films of the order of ~ 1 μm. By considering the ultrathin film to be in Schlichting streaming domain, as the film does not move opposite to the direction of SAW (x - direction) as in Rayleigh streaming domain, from theory we show drops form from the ultrathin film at specific spatial interval equal to the wavelength ($'\lambda^*_{SAW}'$) of the SAW.

Experimental setup

Cr/Au Interdigitated Transducers (IDTs) of resonance frequency of 29.9 MHz, were patterned on the surface of a 128° Y-cut X propagating lithium niobate ($LiNbO_3$) substrate using standard photolithography techniques. The substrate is cleaned using isopropanol and water. Nitrogen gas is used to dry clean the substrate. Droplets of the working fluid (kerosene) were deposited on the substrate using a pipette. Upon deposition the drop spreads on the substrate as a film/thin puddle. The SAWs are actuated on the surface using a signal generator (SMC100A, Rohde and Schwarz) and amplifier (75A250A, Amplifier Research). The working fluid is having a low viscosity of 1 mPas. The surface tension and density are 25 mN/m and 780 kg/m^3 respectively.
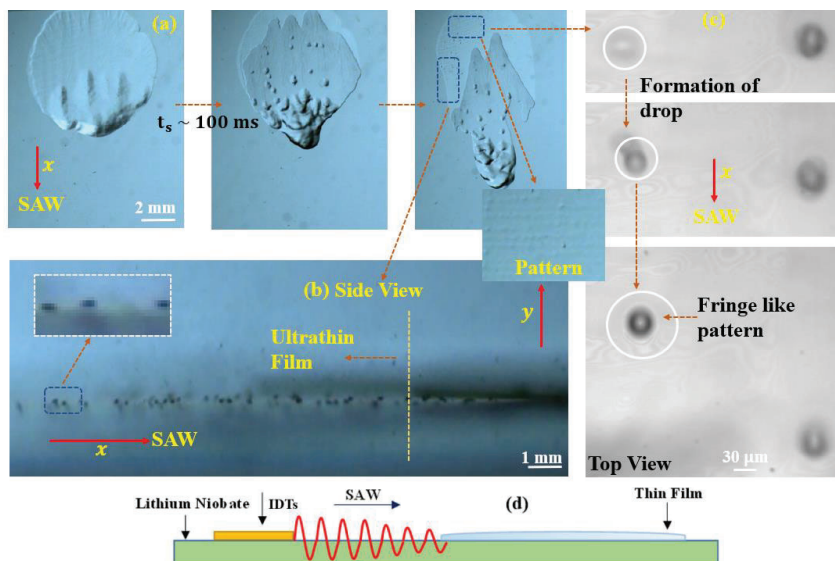

Figure 1: **(a)** Film getting actuated under SAW and separating into thick and ultrathin film at 100 ms **(b)** Side view of the ultrathin film showing the micron sized droplets on the ultrathin film and the mist layer over it **(c)** Zoomed in top view of the ultrathin film showing the formation of drops on it **(d)** Experimental setup schematic.

Results and Discussion

Initially a 1 μL droplet of kerosene is dispensed on the LiNbO$_3$ substrate. Upon SAW actuation the droplet takes $'t_s'\sim 100$ ms to separate and form thick and ultrathin films (Figure 1 (a)). The drop takes this time to overcome the pinning force (F_P). The time scale $'t_s'$ can be found by comparing the SAW force ($'F_S'$) with the pinning force ($'F_P'$). On the ultrathin film we observe a pattern of parallel lines forming and fading in the direction of SAWs (Figure 1 (a)). We also observe ~ 30 μm sized droplets forming out of the ultrathin film from the parallel line patterns (Figure 1 (b) & (c)). From the asymptotical flow variables expansion method given in [2], for this ultrathin film we write the final non-dimensionalized stream function as $-\psi = (\psi_{-1}/\eta) + \psi_0 + (\epsilon\psi_1/\eta)$. Here, $'\epsilon'$ represents the Mach number of the SAW propagating in solid, $'\eta'$ is the ratio of viscous penetration length scale $'\beta^{*^{-1}}'$ and the wavenumber of the SAW in solid $'k^{*^{-1}}'$. Henceforth, the $'*'$ represents dimensional quantities. The expressions for ψ_{-1}, ψ_0 and ψ_1 can be found in [2]. Direction coordinates $'x^{*'}$ and $'y^{*'}$ are non – dimensionalized with $k^{*^{-1}}$ and $'\beta^{*^{-1}}'$ respectively. From the stream function formulation, we derive the y – direction liquid velocity $'v'$ at the liquid – air interface $'v\,|\,y = h'$ using $v = -\partial\psi/\partial x$ which is non – dimensionalized using $'\eta U^{*'}$ where $'U^{*'}$ is the velocity magnitude of the SAW in the solid. Here we take the film thickness $'h'$ to be equal to the viscous penetration length scale $\beta^{*^{-1}}$. Using an inhouse MATLAB code we find the variation of $v\,|\,y = h$ with x (direction of SAW) as shown in figure 2. We find the dimensionalized peak-to-peak distance to be $'\lambda_{SAW}^*'$. Also, from the experimental snaps we find the parallel line patterns to be located approximately $'\lambda_{SAW}^*'$ apart from each other. Hence, as $'v\,|\,y = h'$ maximizes at $'\lambda_{SAW}^*'$ intervals, the ultrathin film thickens at these particular zones and forms the parallel line patterns and these patterns fade away with $'x'$ as the peak-to-peak magnitude of $'v\,|\,y = h'$ decreases with $'x'$. These patterns form micron sized drops that hover over a very thin air film formed over the ultrathin liquid film and move in the direction of SAWs. The fact that these are drops and not capillary ridges can be confirmed from a number of observations. Firstly, capillary ridges move continuously upon formation without any stoppages whereas these drops move in a stop and go fashion when seen from the top view. Secondly, these drops form a fringe like pattern around them when hovering over the thin air film which is reminiscent of fringe patterns millimeter sized droplets form when hovering over thin air film as shown in [3]. Also, the ultrathin film moves with a layer of submicron to micron sized drops over it, confirming the tendency of the film to form droplets instead of ridges.
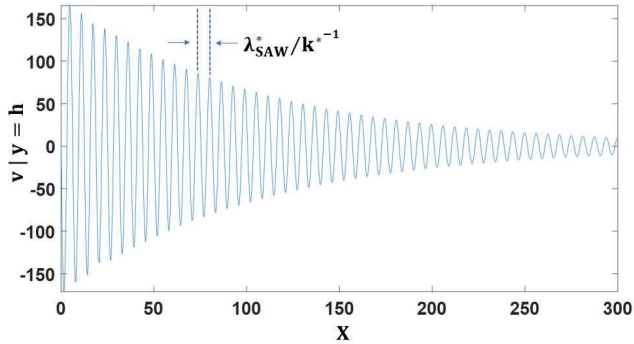

Figure 2: The plot compares non – dimensional y – velocity at the liquid – air interface $'v\,|\,y = h'$ with the non – dimensional direction coordinate $'x'$.

Conclusion

In conclusion we discuss the mechanism of micron sized drop formation from the interaction of a low viscosity ultrathin film with SAWs. We show from theory and experiments that the distance between the parallel line patterns is equal to the wavelength of the SAW($'\lambda_{SAW}^*'$) and it corresponds to the spatial periodic maxima of the y – directional velocity of the liquid at the liquid – air interface $'v\,|\,y = h'$.

References

[1]   A. R. Rezk, O. Manor, J. R. Friend, and L. Y. Yeo, Unique Fingering Instabilities and Soliton-like Wave Propagation in Thin Acoustowetting Films, Nat. Commun. **3**, 1 (2012).

[2]   O. Manor, A. R. Rezk, J. R. Friend, and L. Y. Yeo, Dynamics of Liquid Films Exposed to High-Frequency Surface Vibration, Phys. Rev. E **91**, 53015 (2015).

[3]   J. De Ruiter, R. Lagraauw, D. Van Den Ende, and F. Mugele, Wettability-Independent Bouncing on Flat Surfaces Mediated by Thin Air Films, Nat. Phys. **11**, 48 (2015).

Self-induced radiation force on a moving monopolar source

M. Baudoin[1], A. Roux[1], J.P. Martishang[1]

[1]Univ. Lille, CNRS, Centrale Lille, Univ. Polytechnique Hauts-de-France, UMR 8520, IEMN, F59000 Lille, France
E-mail: michael.baudoin@univ-lille.fr, URL: .https://pro.univ-lille.fr/michael-baudoin/parcours/

Introduction

Since the seminal work of Rayleigh, Langevin, and Brillouin, many expressions of the acoustic radiation force have been derived for different types of particles and wavefields, and with different levels of approximations (see e.g. [1] for a review). Nevertheless, all the expressions derived so far have been calculated for a steady particle, hence neglecting its motion. Yet, the displacement of the particle induces an asymmetry of the radiated wavefield (Fig. 1) due to Doppler effect, which can in turn produce a self-induced radiation force. In this work [2], we derive the expression of the radiation force exerted on a translating monopolar source. We show that the translation of the source induces a force opposite to its motion and that this force can be of the same order of magnitude as the Stokes drag for millimetric bubbles translating in cryogenic liquid such as Nitrogen.

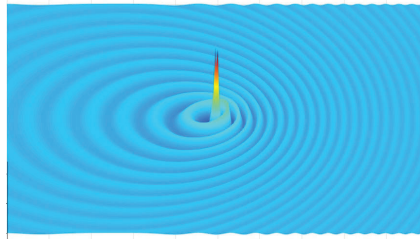**Wavefield radiated by a translating monopolar source**

Figure 1: Sketch illustrating the asymmetry of the acoustic field synthesized by a translating monopolar source. The normalized field is calculated with eq. (3) and for the sake of illustration, the asymmetry is magnified by choosing a Mach number M = 0.5.

The first step to compute the radiation force exerted on monopolar source translating at a constant speed $\mathbf{U} = U\,\mathbf{x} = Mc_o\,\mathbf{x}$ along a fixed axis $\mathbf{x}$ (with M the Mach number, c_o the sound speed) is to compute the field radiated by this source. For this purpose, the wave equation with a punctual translating source must be solved:

$$\Delta \psi_1 - \frac{1}{c_0^2}\frac{\partial^2 \psi_1}{\partial t^2} = -q(t)\delta(x - Mc_0 t)\delta(y)\delta(z), \tag{1}$$

with ψ_1 the velocity potential, and $q(t)$ the instantaneous mass flow rate created by this source. The solution of the wave equation for a punctual steady source ($M = 0$) is well known:

$$\psi_1(r, t) = \frac{q(t \pm r/c_0)}{4\pi r}. \tag{2}$$

To solve the moving source problem, it would be interesting to find a transformation which leaves the wave equation unchanged, while moving into a reference frame wherein the source does not translate. This can be achieved with the Lorentz transformation, whose ability to leave the wave equation unchanged is at the core of the special relativity. With this transformation, the wavefield radiated by a translated source can be computed [3] (see Fig. 1 for an illustration):

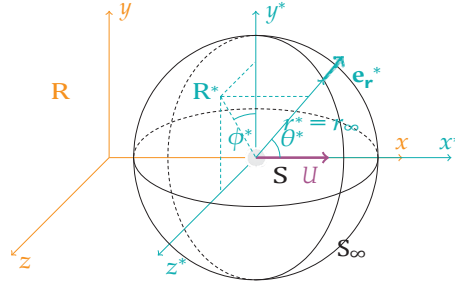$$\psi_1(r, t) = \frac{q(t - R/c_0)}{4\pi R_1}, \tag{3}$$

Figure 2: We make the change of variables corresponding to the Galilean transformation from R to R* and then use the local spherical coordinates (r^*, θ^*, ϕ^*).

with:

$$R = \frac{M(x - Mc_0 t) + R_1}{1 - M^2} \quad \text{and} \quad R_1 = \sqrt{(x - Mc_0 t)^2 + (y^2 + z^2)(1 - M^2)}. \tag{4}$$

Integral expression of the radiation stress in the far field

The next step is to compute the time averaged radiation force $\langle \mathbf{F}_{rad} \rangle$ exerted on the translating source, which is nothing but the integral of the stress tensor $\bar{\sigma}$ scalar the normal $\mathbf{n}$ over the particle surface $S(t)$:

$$\langle \mathbf{F}_{rad} \rangle = \left\langle \iint_{S(t)} \bar{\sigma} \cdot \mathbf{n} \, dS \right\rangle. \tag{5}$$

with $\langle f \rangle = \frac{1}{T} \int_t^{t+T} f(t) dt$ the time average of the function f. While the expression looks simple, a well known difficulty to compute it is that the surface of the object $S(t)$ is itself vibrating. To solve this problem, this integral is generally converted into an integral over a closed surface at rest surrounding the object in the far field by using the divergence theorem and Reynolds transport theorem (see. e.g. [1]). An additional difficulty here, is that the particle is also translating. To solve this issue, our integral of the stress on the surface of the object is transposed into an integral over a spherical surface S_∞ of radius $r_\infty \gg \lambda$, centered on the source, and hence translating at the velocity $\mathbf{U}$ in R (see Fig 2). We obtain the following integral expression of the radiation force as a function of the first order pressure p_1 and velocity field $\mathbf{v}_1$:

$$\langle \mathbf{F}_{rad} \rangle = \left\langle \iint_{S_\infty} \left(\rho_0 \frac{v_1^2}{2} - \frac{1}{\rho_0 c_0^2} \frac{p_1^2}{2} \right) \bar{I} - \rho_0 \mathbf{v}_1 \otimes \mathbf{v}_1 \; \mathbf{n} \, dS \right\rangle + \left\langle \iint_{S_\infty} (\mathbf{U} \cdot \mathbf{n}_\infty) \rho_1 \mathbf{v}_1 \, dS \right\rangle. \tag{6}$$

Final computation

The last steps to compute the radiation force is to compute the pressure p_1 and velocity $\mathbf{v}_1$ velocity field from the velocity potential ψ_1 and to compute the previous integral. We finally obtain, the following expression of the radiation force in the weak mach number approximation:

$$\boxed{\langle \mathbf{F}_{rad} \rangle = - \frac{\langle q'^2 \rangle M}{4\pi \rho_0 c_0^2} \mathbf{x}.} \tag{7}$$

Conclusion

In this work we computed the self-induced radiation force exerted on a translating monopolar source. We showed that the radiation force resulting from the translation of the source is opposite to its motion (as can be seen from the minus sign in the final expression (7)), and proportional to the intensity of the radiated wavefield $\langle q'^2 \rangle$ and the Mach number M. Estimation of this force carried out in [2] shows that it can be of the same order of magnitude as the Stokes drag for millimetric bubbles oscillating in cryogenic liquids.

References

[1] M. Baudoin and J.-L. Thomas, Ann. Rev. Fluid Mech. **52**, 205-234 (2020).
[2] A. Roux, J.P. Martishang, and M. Baudoin arXiv preprint arXiv:2205.09346 (2022)
[3] P.M. Morse. and K.U. Ingard. Theoretical acoustics. New York: McGraw-Hill book company (1968)

Effects of wettability in relocation of coflowing immiscible liquids exposed to bulk acoustic wave

Sazid Z. Hoque[1], and Ashis K. Sen[1]

[1]Department of Mechanical Engineering, IIT Madras, Chennai, India
E-mail: ashis@iitm.ac.in, URL: http://www.ashislab.in

Introduction

The physics of acoustic radiation forces acting on immiscible fluid interfaces when exposed to bulk acoustic wave (BAW) has not been received much attention. It is well known that sound exerts radiation pressure on the interface due to the impedance difference between the fluids [1]. Recent experiments show that the higher impedance liquid relocates towards the center of the microchannel via exposure to bulk acoustic wave (BAW) [2,3].

The evolution of an immiscible fluid-fluid interface inside a microchannel when exposed to a BAW is not well understood in the literature. Specifically, the effects of wettability of the fluids on the relocation dynamics is not available. In the present study, we provided a theoretical explanation of the above phenomena using simulations based on the two-phase flow model. We developed an expression for acoustic radiation pressure acting on an immiscible fluid-fluid interface exposed to a BAW. We showed that depending on the wettability even the low impedance fluid relocates to the center of the microchannel.

Theoretical modelling

Classically, the mean Lagrangian pressure difference across the immiscible fluid-fluid interface defines the acoustic radiation pressure acting on an immiscible fluid interface [5]. let us consider an immiscible fluid interface located at $x = w_1$ between two fluids a and b and the system is exposed to bulk acoustic wave. The acoustic radiation pressure across the interface can be written as the Lagrangian pressure difference,

$$\langle \Delta P^L \rangle = -\langle E_{ac} \rangle \left[\left(e^{+i2k_a x} + \Delta \widehat{z}^2 e^{-i2k_a(x-2w_1)} \right) - \frac{\rho_b}{\rho_a} (1 - \Delta \widehat{z})^2 e^{+i2k_a w_1} e^{-i2k_b(w_1-x)} \right] \tag{1}$$

where, $\langle E_{ac} \rangle$ is the average acoustic energy density defined as, and $\Delta \overline{Z} = \frac{z_b - z_a}{z_b + z_a}$. The acoustic impedance for fluid a and fluid b are defined as $z_a = \rho_a c_a$ and $z_b = \rho_b c_b$, where ρ_a and ρ_b are the density and c_a, c_b represents the speed of sound in fluid a and fluid b respectively. Further, k_a and k_b are the wave number of the acoustic wave in fluid a and fluid b. The acoustic radiation force per the interface area, A is given by [5],

$$F_{ac}/A = \langle \Delta P^L \rangle \mathbf{n} \tag{2}$$

where, $\mathbf{n}$ is the normal vector pointing from fluid a to fluid b. The eqn.[2] is modeled as a body force term in Navier-Stokes equation to incorporate the effect of the bulk acoustic wave in case of immiscible fluids. Further, the interface between the two fluids are captured using the phase field method. Sufficiently fine uniform mesh is created to capture the interface deformation through out the fluid domain.

Results and discussion

The effects of the wettability of the the fluids in a coflow configuration is investigated in terms of the contact angle. The contact angle (θ) is defined as the angle between the tangent to the interface at the wall and the wall on the low impedance fluid side. The temporal evolution of the interface between two fluids with impedance difference $\Delta Z = 0.24$ and $Z_a > Z_b$ for contact angles $\theta = 30°, 90°$, and $150°$ are presented in Fig. 1. The density and the speed of sound for fluid a and fluid b are $\rho_a = 1000$ kg/m^3, $c_a = 1440$ m/s and $\rho_b = 910$ kg/m^3, $c_b = 970$ m/s, respectively. The initial interface curvature depending on the contact angle is shown at $t = 0$ s. The interface starts deforming and reaches a new equilibrium position when exposed to bulk acoustic wave.

For $\theta = 30°$, fluid a having higher impedance and lower wettability bulges out into fluid b and finally relocates to the channel center. On the other hand, for $\theta = 150°$, fluid b having higher impedance

and lower wettability bulges out into fluid a and finally relocates to the channel center through the middle of the channel. In case of the straight interface (i.e., $\theta = 90°$), complete flipping of the phase is observed. The results clearly demonstrated that the relocation dynamics predominantly depends on the wettability of the fluids. The result is summarized in a regime plot between impedance and contact angle of the two fluids as shown in Figure 1(d). The higher impedance fluid (i.e., fluid a) relocates towards the center of the microchannel for contact angle less than $70°$. However, for contact angle higher than $110°$, fluid b with lower impedance relocates towards the center. We observed that, the contact angle in the range $70° < \theta < 110°$, a complete flipping of the fluid streams is observed. For the three different contact angle (i.e., $theta = 30°, 50°$ and $90°$), the variation of fluid pressure (P_F), acoustic radiation pressure (P^L), and Laplace pressure (P_{IFT}) after the relocation is presented in Figure 2. In the final equilibrium, the fluid pressure (P_F) variation is balanced by the sum of the acoustic radiation pressure (P^L) and Laplace pressure (P_{IFT}). In the case of a straight interface, i.e., $\theta = 90°$, the P_F across the interface is balanced by the P^L at the initial and final equilibrium positions since the P_{IFT} is zero.
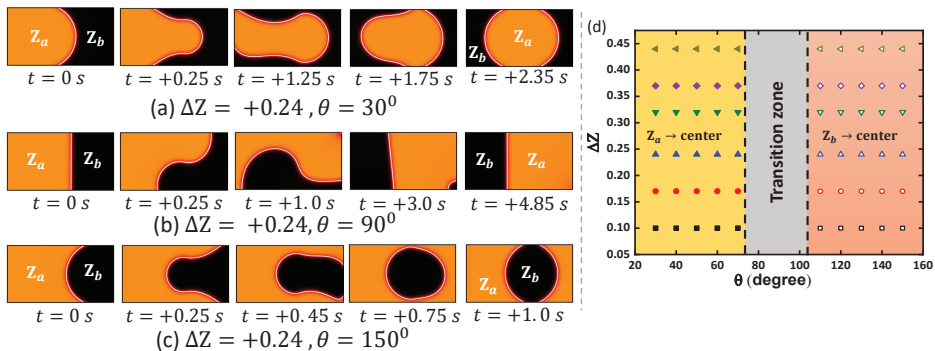

Figure 1: The transient dynamical motion of the immiscible fluid interface (yellow, Z_a; Black, Z_b, $Z_a > Z_b$) for different wall contact angle, (a) $\theta = 30°$, (b) $\theta = 90°$, and (c) $\theta = 150°$, (d) The different relocation regimes in coflow systems as a function of impedance difference and contact angle.
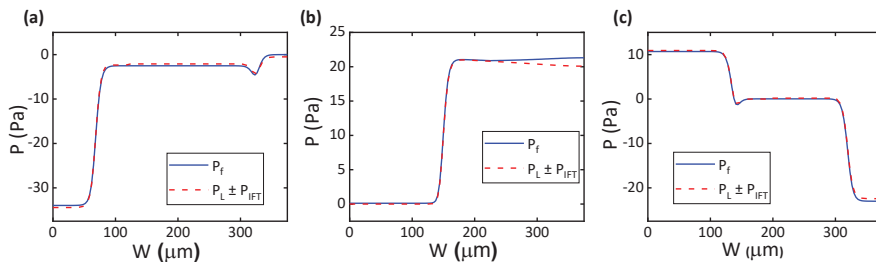

Figure 2: The variation of fluid pressure, acoustic radiation pressure, and Laplace pressure along a horizontal line at the middle of the microchannel, for different wall-fluid contact angle (a) $\theta = 30°$, (b) $\theta = 90°$, and (c) $\theta = 150°$. Impedance difference $\Delta Z = 0.24$ and $Z_a > Z_b$.

Conclusion
We examined the effects of the wettability of the fluids in the relocation dynamics in coflowing configuration. We observed that even lower impedance fluid relocates towards towards the center of the microchannel with lower wettability. Our study reveals new physics regarding the relocation dynamics of immiscible fluids exposed to a BAW which may find relevance in microfluidics.

References
[1] G. Hertz and H. Mende, Z. Phys. 114, 354 (1939).
[2] E. Hemachandran, S. Z. Hoque, T. Laurell, and A. K. Senf, Phys. Rev. Lett. 127, 134501 (2021).
[3] E. Hemachandran, S. Karthick, T. Laurell, and A. K. Sen, Europhys. Lett. 125, 54002 (2019).
[4] C. P. Lee and T. G. Wang, J. Acoust. Soc. Am. 94, 1099 (1993).
[5] J. T. Karlsen, P. Augustsson, and H. Bruus, Phys. Rev. Lett. 117, 114504 (2016).

Liquid Layer Evolution Characterization using GHz Ultrasonic Pulses: Linear and Nonlinear Effects

Rohan Sanghvi[1], Justin Kuo[2], and Amit Lal[2]

[1]Mechanical and Aerospace Engineering, Cornell University, Ithaca, USA
E-mail: rs2577@cornell.edu
[2]Electical and Computer Engineering, Cornell University, Ithaca, USA

Introduction

The effects of radiation forces and streaming are often a strong function of the film thickness due to the reflecting and absorbing boundary conditions that control the acoustic profile and its gradients. Herein, we demonstrate the capability to interrogate thin liquid film thickness using GHz ultrasonic pulse reflectometry owing to the complex reflection of high frequency and short ultrasonic pulses that reflect from the free liquid surface and the transducer-liquid interface. This work provides a method for quantification and real time monitoring of evaporation and nonlinear acoustofluidic effects in sub-100 um thin liquid films. Furthermore, the data collected suggests the possibility of using ultrasonic radiation forces to delaminate and release droplets from ultra-thin liquid layers at GHz frequencies.

Reflectometer structure and operation

In recent years we have developed AlN transducers integrated with CMOS for highly compact GHz ultrasonic platforms. Our platform has yielded applications such as imaging [1,2], microfluidic mixing, and particle manipulation [3]. This work utilizes an Aluminum Nitride (AlN) based GHz transducer (Figure 1 (a)), operated in the bulk acoustic wave (BAW) mode to transmit and receive short acoustic pulses. The device is configured as a Fresnel transducer using concentric AlN rings with varying inner radii and widths. The Fresnel transducer is designed to focus the acoustic energy within a very small area ($5\mu m$ radius) on the opposite side of the silicon chip ($725\mu m$ thick). This transducer yielded a peak displacement amplitude of 250pm, equivalent to 1.7 kW/cm^2 intensity for a 5 Vpp RF input [3]. When a thin layer of liquid is placed on top of the opposite side of the transducer, the pulse partially reflects back from the silicon-liquid interface. The pulse transmitted into the liquid layer consequently reflects from the fluid-air interface. The effect of the liquid layer on the net reflection can be calculated using the transmission line model of the thin liquid layer, which yields the impedance into the liquid layer to be $\boldsymbol{Z_{ll}} = Z_{liquid}tan(\boldsymbol{\beta}l)$ where $\boldsymbol{\beta}$ is the complex propagation wavenumber for liquid at the GHz frequencies. This impedance results in the overall reflection coefficient at the transducer-liquid interface to be $\Gamma = |(\boldsymbol{Z_{ll}} - \boldsymbol{Z_{Si}})/(\boldsymbol{Z_{ll}} + \boldsymbol{Z_{Si}})|$. Since Γ is a function of the acoustic impedance of the liquid film (Figure 1(b)), the variations in film thickness during evaporation result in changes in the amplitude of the reflected wave (Vpp-first echo). These changes are recorded over time to study the evolution of film thickness.
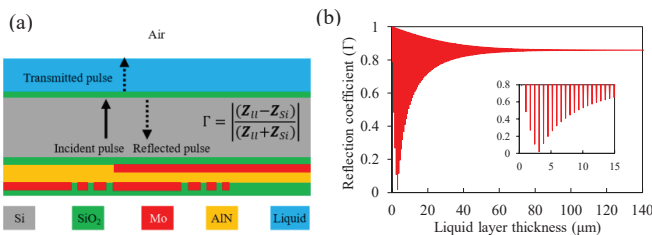

Figure 1: (a) Schematic showing the reflectometer cross section and operation mechanism. Pulse launched by the transducer at the bottom reflects partially at the chip-liquid interface and reaches the transducer back as echo; (b) Theoretical reflection coefficient (Γ) as a function of the liquid layer thickness (inset: zoomed in graph shows Γ as low as 0.2 for sub-5μm thin films)

Experimental setup

The experimental setup (Figure 2) consists of (1) electrical characterization system, (2) high-speed optical camera, and a (3) motorized nanoliter droplet dispenser. Nanoliter droplets are deposited on top of the chip with the droplet dispenser and the high-speed camera allows visualization of the droplet evaporation process. A python program was developed to interface the various instruments and conduct real-time synchronized recording of the ultrasonic echo data from oscilloscope and optical images with 40 ms temporal resolution.
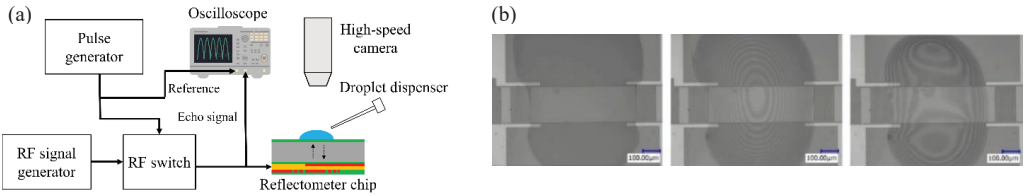
Figure 2: (a) Schematic of the experimental setup for simultaneous acoustic and optical characterization of thin film evaporation; (b) High speed camera images showing optical interference effects caused during thin film evaporation

Acoustic characterization of evaporating thin liquid films

The transducer was driven by 50ns pulses at 1.08GHz carrier frequency, with drive voltage amplitudes (V_{RF}) from $0.5 - 2$ Vpp. The first echo ($V_{pp\text{-first echo}}$) amplitude was recorded every 40ms, as 14 nL droplet of 50% v/v solution of DI water and IPA evaporated from the chip surface. Over time, as the liquid layer grew thinner due to evaporation, we observe the expected oscillations in the reflection amplitude with consecutive troughs corresponding to half-wavelength reduction in liquid thickness (Figure 3). The echo amplitude decreases until an inflection point where the liquid is completely removed from the chip surface and then increases sharply owing to the large impedance mismatch between SiO_2 and air. This sharp rise represents the possibility of previously undiscovered non-linear acoustofluidic phenomena where thin liquid layer is ejected due to radiation forces.
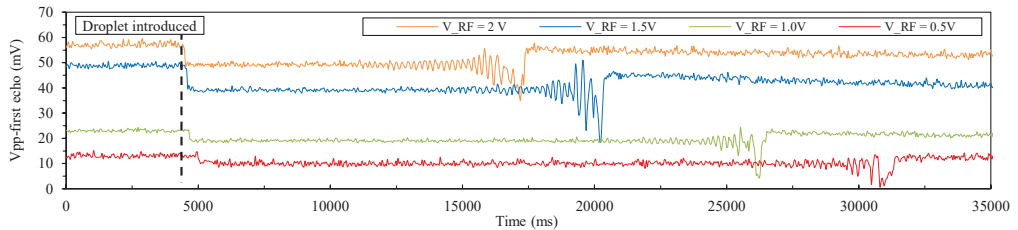

Figure 3: Experimental variation in first echo amplitude during evaporation of liquid film for various drive amplitudes

Analysis of liquid film evaporation

The time-domain echo amplitude data is post-processed yielding the evolution of liquid film thickness for various transducer drive voltages. From Figure 4 it is evident that the droplet takes longer to completely evaporate for a lower RF drive voltage. This can be attributed to accentuation of thermal transfer into the liquid film for higher ultrasound drive voltages due to RF and US absorption in the transducer platform. Additionally, the rate of film thickness decrease accelerates as the film gets thinner, which correlated to the rate of fringes passing over the transducer observed under the high-speed microscope camera. Furthermore, the graph indicates that the liquid film is able to reach a lower reflection coefficient, and hence a lower layer thickness, before ejection for a smaller drive amplitude ($3.5\mu m$ for 0.5 V as opposed to $12.8\mu m$ for 2 V).
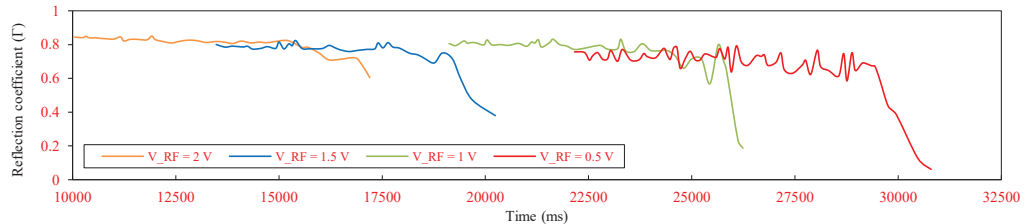

Figure 4: Variation of chip-liquid interface reflection coefficient (Γ) over time for various drive amplitudes

Conclusion

We have presented, for the first time, a GHz ultrasonic reflectometry based approach to characterize thickness and non-linear acoustofluidic effects in sub-$100\mu m$ thin liquid films. The approach has been applied to study the evolution of evaporating liquid thin films with time. Finally, we investigate effects of high radiation pressures on films with thickness comparable to the acoustic wavelength. Correlation of the experimental data with theory suggests a possibility of liquid droplet ejection at GHz drive frequencies.

References

[1] M. Abdelmejeed. *pp. 807-810, 2019 International Electron Devices Meeting, IEDM*, San Francisco, 7 - 11 Dec 2019.
[2] M. Abdelmejeed. *pp. 1967-1970, 2019 IEEE International Ultrasonics Symposium, IUS*, Glasgow, 6-9 Oct 2019.
[3] A. Ravi. *pp. 310-313, Solid-State Sensors, Actuators and Microsystems Workshop*, Hilton Head, 3-7 Jun 2018.

Thermoacoustic Streaming Induced by Asymmetric Laser Heating

Franziska Martens, Wei Qiu and Per Augustsson

Department of Biomedical Engineering, Lund University, Lund, Sweden
Email: franziska.martens@bme.lth.se
https://bme.lth.se/staff/augustsson-per/research/thermal-acoustofluidics/

Introduction

Inhomogeneities, such as density and compressibility gradients [1] are essential for influencing the acoustic streaming effects in acoustofluidics. A thermal gradient, altering those acoustic properties, can be generated using LED- [2] or laser-light [3], the latter with a µm-precision.

Previous work achieved heating by LED resulting in a thermal inhomogeneity that is large compared to the channel dimensions [1], and we have recently investigated the temporal decay of the streaming field after turning the laser off for a symmetric thermal field [3]. In this work, we investigate the static 3D thermoacoustic streaming field resulting from a laser-induced thermal gradient for symmetric and asymmetric illumination.

Materials and Methods

The setup (Fig.1) comprises an inverted Galilei telescope to prepare the 785 nm laser spot before being focused through a 10x objective. It excites the Indo-Cyanin green (ICG) dye at its absorption peak. The light enters continuously at the bottom of the silicon glass channel (375 µm wide, 150 µm high) with a spot size of 50 µm. The dye absorbs 86% of the laser-light. To excite fluorescence of the 1 µm sized, green fluorescent polystyrene tracer particles (ex. 468 nm, emi. 508 nm) a 470 nm LED illuminates from the top. The $\lambda/2$ acoustic pressure field across the width of the channel is generated with a piezo-electric transducer, driven with 3 V and 1.9 MHz. Each experiment was repeated 10 times, recording 1000 frames at a frame rate of 20 fps, resulting in approximately 4000 trajectories per set.

Results and Discussion

The resulting streaming fields arise from an interplay of boundary acoustic streaming and thermoacoustic body forces due to light absorption and the thermal conductivities and geometry of the acoustofluidic system (see Fig.2). The thermal gradient originates from the laser heating and the cooling through the thermally conducting silicon channel walls and the colder liquid along the channel's x-axis. Comparing heated to non-heated experiments, the acoustic streaming velocity increases from about $50 - 60\,\mu m/s$ (not shown) without laser heating to $150 - 200\,\mu m/s$ with laser heating. The effect the thermal gradient has on the streaming velocity and pattern can be explained with the acoustic body force (f_{ac}) induced by the density and compressibility difference between hot and cold regions in the fluid. Due to high absorption coefficient, most of the light is absorbed in a thin liquid layer upon entering the channel leading to the acoustic body force pointing towards the heat maximum located at the laser spots' center at the channel floor. The liquid in that area heats up, moves away from the heat source, pushing liquid out of its way. Afterwards, it cools down until it is pulled towards the hot region again (Fig. 2 b-g).
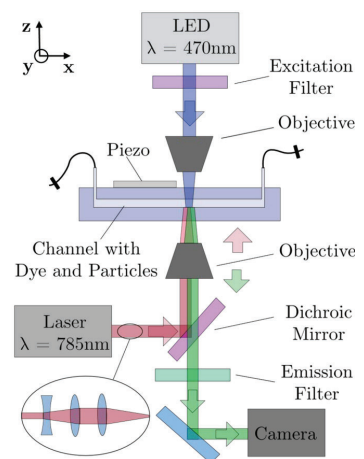

Figure 1: Dye molecules absorb the 785 nm laser-light (red). A 470 nm LED (blue) excites the 1.1 µm sized particles' fluorescence (green).
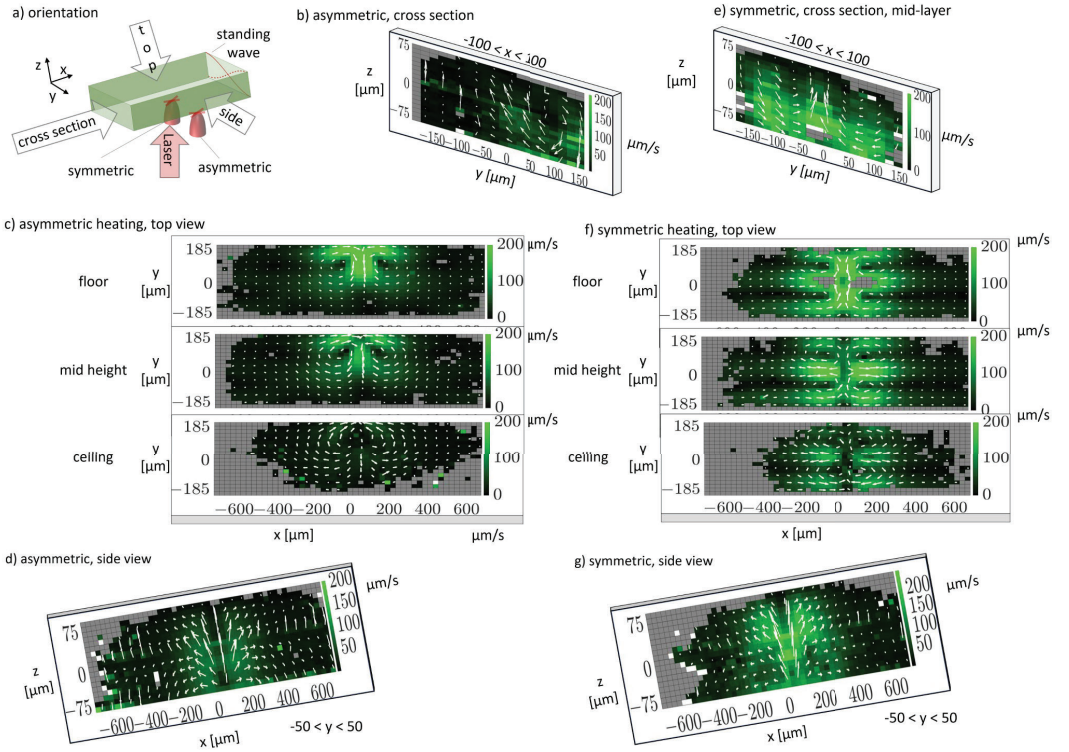
Figure 2: (a) Orientation and indication of the laser spot position. (b-d) Streaming fields for asymmetric heating for an off-centered laser spot, projected onto the (b) y-z, (c) x-y and (d) x-z plane. (e-g) Streaming fields for symmetric heating for a centered laser spot, projected onto the (e) y-z, (f) x-y and (g) x-z plane.

Juxtaposing the streaming patterns of the non-centered and the centered heat source, the streaming rolls alter from one to two rolls when viewed along x (Fig. 2 b and e) and from two to four rolls when viewed from the top (Fig.2 c and f). In the asymmetric case, the liquid moves away from the hot side-region after being heated at the edge of the channel, pushing away colder liquid to the center. The symmetric case exerts this pushing motion along the middle of the channel, which results in more rolls. The peak velocity at the hot side of the channel is similar to that of the center-heated case with $\sim 250\,\mu\mathrm{m/s}$. The velocity decreases towards the cold region which is more obvious in the asymmetric case. The thermal gradient has more space to flatten out, since it progresses over the full width of the channel. The symmetric gradient has only half of the space and therefore its lowest velocity of $100 - 150\,\mu\mathrm{m/s}$ is higher than the lowest velocity of $0 - 50\,\mu\mathrm{m/s}$ in the asymmetric case. The side view along the y-axis proved to have similar velocity fields for both cases when measured in the center (Fig. 2 d and g).

Conclusion
The symmetry of a thermal gradient influences the thermoacoustic streaming pattern but not the maximum velocity. With these experiments we could show that the positioning of the laser spot with regards to the channel walls can break the symmetry of the acoustic streaming field. It leads to transport of suspended particles through the acoustic pressure node at the channel's center. Further investigations utilizing light-patterning techniques, altering the shape of the laser spot, could lead to interesting, fast and non-invasive flow manipulation option.

References
[1] J. T. Karlsen, W. Qiu, P. Augustsson, and H. Bruus *Phys. Rev. Lett.* **120**, 054501 (2018)
[2] W. Qiu, J. H. Joergensen, E. Corato, H. Bruus, P. Augustsson *Phys. Rev. Lett.* **127**, 064501 (2021)
[3] F. Martens, W. Qiu, A. Ehn, P. Augustsson *Acoustofluidics Conference 2021* **Abstract**, (2021)

Acoustic near-resonance modes in a cylindrical half-wavelength microcavity

Glauber T. Silva

Physical Acoustics Group, Institute of Physics, Federal University of Alagoas, Maceió, Brazil
E-mail: gtomaz@fis.ufal.br, URL: www.if.ufal.br/~gaf

Introduction

Acoustic manipulation in cylindrical half-wavelength resonators can simultaneously levitate and aggregate microparticles or cells [1]. An aggregation is formed by means of the primary and secondary radiation forces. Some normal modes form a radiation force potential well in the levitation plane [2]. These trends suit developing cell culture methods with individual cell monitoring [3]. Moreover, rich dynamics of metal microrods are observed, including fast axial motion, in-plane loops, chain assembly, and pattern formation [4].

We aim to discuss the acoustic normal modes (vortex and nonvortex) near-resonant states that can be induced in a viscous fluid-filled cylindrical microcavity. We also derive the primary acoustic radiation force exerted on subwavelength particles immersed in the microcavity. To carry out this task, we use the fluid conservation equations to obtain the Helmholtz equations for the compressional and shear wave components. The boundary conditions for pressure consider viscous boundary-layer effects [5]. The results show that the acoustic energy density and radiation force are amplified by the squared quality factor (Q factor) of the microcavity, which primarily depends on dissipation effects within the boundary layer.
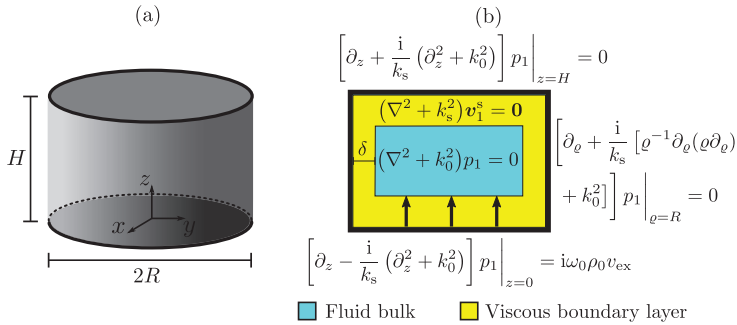

Figure 1: (a) Cylindrical microcavity of height H and radius R. (b) Lateral cross-section with the top, bottom, and lateral surfaces, with their respective boundary conditions in cylindrical coordinates. The boundary-layer thickness is denoted by δ.

Physical model

We consider a cylindrical microcavity resonator of radius R and height H filled with a quiescent viscous liquid, as depicted in Fig. 1. Our analysis is restricted to pillbox cavities in which $\frac{H}{R} \ll 1$. The microcavity boundaries are assumed to be rigid walls. The unperturbed state of the liquid is described by a density ρ_0, speed of sound c_0, adiabatic compressibility $\kappa_0 = 1/\rho_0 c_0^2$, and dynamic η_0 and bulk ζ_0 viscosity. These parameters remain constant for the analysis under consideration.

The normal mode is induced in the microcavity through a harmonic oscillation at the bottom surface with angular frequency ω_0. By considering that the bottom surface moves like a rigid piston along the z axis, we express the excitation velocity in cylindrical coordinates (ϱ, φ, z) as

$$v_{\text{ex}}(t) = -\mathrm{i}\omega_0 d_0 J_n(q_\varrho^{nm}\varrho)\,\mathrm{e}^{\mathrm{i}n\varphi}\mathrm{e}^{-\mathrm{i}\omega_0 t}, \quad q_\varrho^{nm} = \frac{j'_{nm}}{R}, \tag{1}$$

where i is the imaginary unit, t is time, d_0 corresponds to the peak displacement, J_n is the Bessel
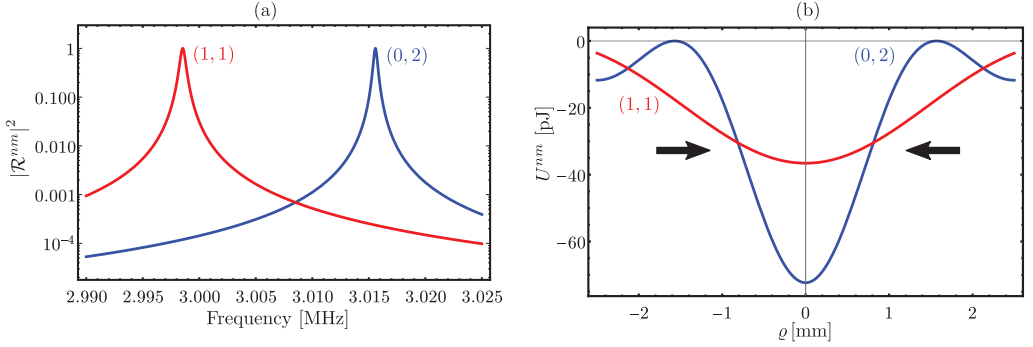
Figure 2: The results for the $(0,2)$ mode (nonvortex) and $(1,1)$ mode (vortex). (a) The resonance function versus frequency. (b) The Gor'kov radiation force potential for a rigid particle ($f_\rho = 1$) with a $10\,\mu$m radius. The black arrows illustrate the radiation force direction.

function of order $n = 0, 1, 2, \ldots$, j'_{nm} is the mth-zero of $\mathrm{d}J_n(j'_{nm})/\mathrm{d}j'_{nm} = 0$, with $m = 1, 2, \ldots$ Note that $j'_{01} = 0$ so in $(0,1)$ mode, the radial pressure distribution is suppressed, $q^{01}_\varrho = 0$.

Results

After solving the Helmoltz equation for the linear pressure p_1 as depicted in Fig. 1, we find near a resonance $\omega \approx \omega^{nm}_0$,

$$p^{nm}_1 = \rho_0 c^2_0 \frac{2d_0 Q^{nm}}{H} \mathcal{R}^{nm}(\omega_0) \cos(q_z z)\, J_n\!\left(q^{nm}_\varrho \varrho\right) \mathrm{e}^{\mathrm{i}n\varphi}, \quad Q^{nm} = \frac{1}{\Gamma^{nm}_\delta}, \tag{2a}$$

$$\mathcal{R}^{nm}(\omega_0) = \frac{\frac{1}{2}\omega^{nm}_0 \Gamma^{nm}_\delta}{\omega_0 - \omega^{nm}_0 + \frac{\mathrm{i}}{2}\omega^{nm}_0 \Gamma^{nm}_\delta}, \quad \Gamma^{nm}_\delta = 2\left[\frac{1}{1 - \left(\frac{n}{j'_{nm}}\right)^2} + \delta_{n,0}\delta_{m,1}\right]\frac{\delta}{\lambda}\frac{H}{R} \tag{2b}$$

After solving the Helmholtz equation for the linear pressure p_1 as depicted in Fig. 1, we, where $q_z = \pi/H$ is the axial wavenumber, $\mathcal{R}^{nm}$, is the microcavity resonance function, and Γ^{nm} is the boundary-layer damping factor, λ is the wavelength, and δ_{nm} is the Kronecker delta function. For a typical acoustofluidic microcavity with $H = 250\,\mu$m and $R = 10H$, filled with water at $25\,°$C, we have for the zeroth- and first-order modes $Q^{0m} = 8089.24$ and $Q^{11} = 5718.98$. The energy density scales as $E^{nm} \sim |p^{nm}_1|^2 \sim (d_0 Q^{nm}/H)^2 \rho_0 c^2_0$. Thus, we obtain $E^{02}, E^{11} \sim 10^4\,\mathrm{J\,m^{-3}}$. This result should be considered an upper limit since we assumed that the vibration pumped into the microcavity could not propagate through the rigid boundaries. The Gor'kov potential [6] (which is related to the radiation force on a particle of radius a, compressibility κ_s and density ρ_s), can be expressed near a resonance $\omega \approx \omega^{nm}_0$ by

$$U^{nm} = -2\pi^3 \rho_0 c^2_0 a^3 \left(\frac{d_0 Q^{nm}}{k_0 H^2}\right)^2 |\mathcal{R}(\omega_0)|^2 f_\rho \left[J_n\!\left(q^{nm}_\varrho \varrho\right)\right]^2, \quad f_\rho = 2\frac{\rho_s - \rho_0}{2\rho_s + \rho_0}, \tag{3}$$

where $k_0 = \omega_0/c_0$ is the compressional wavenumber. The Gor'kov potential is also amplified by the cavity quality factor squared. In Fig. 2, we show the results for the $(0,2)$ mode and the $(1,1)$ mode. Panel (a) show that resonances occur, respectively, at $3.015\,$MHz and $2.9985\,$MHz. In Panel (b), we see a potential well in the levitation plane ($z = H/2$).

Conclusion

We partially presented some results of acoustic normal modes induced in a cylindrical microcavity. With obtained result for pressure in Eq. (2a), we can also calculate the spin-torque on nonspherical particles caused by the vortex modes.

References

[1] J. F. Spengler and W. T. Coakley, Langmuir 19, 3635 (2003).
[2] J. P. Leão Neto, M. Hoyos, J.-L. Aider, and G. T. Silva, J. Acoust. Soc. Am. 149, 285 (2021).
[3] H. D. A. Santos et al., Adv. Eng. Mat. 23, 2170040 (2021).
[4] W. Wang, L. A. Castro, M. Hoyos, and T. E. Mallouk, ACS Nano 67, 6122 (2012).
[5] J. S. Bach and H. Bruus, J. Acoust. Soc. Am. 144, 766 (2018).
[6] L. P. Gor'kov, Sov. Phys.-Dokl. 6, 773 (1962).

Stable, Obstruction-Free, Audible-Frequency Acoustic Microstreaming by a Pinned Oscillating Membrane

Anthony Mercader[1] and Sung Kwon Cho[1]

[1]Department of Mechanical Engineering and Materials Science, University of Pittsburgh, Pittsburgh, USA
E-mail: ALM287@pitt.edu

Introduction

We present an investigation into a new configuration to generate strong acoustic streaming in a microchannel at audible frequency with thorough characterization of the flow field and its mechanism via advanced measurement techniques. Fig. 1 shows a schematic diagram of the overall concept and fabrication. When a PDMS channel is formed with a membrane as the bottom wall and that membrane is bonded to a glass slide so that the channel 'hangs' off exposing the membrane to open air, an acoustic signal sent through the glass via a piezo buzzer causes strong vortex flow patterns bound where the membrane is pinned to the glass edge. Such a configuration does not suffer from any stability issues related to dissolution of the driving mechanism as with bubble microstreaming [1]. Compared to sharp edge streaming, the effect is stronger and does not require obstructions protruding into the channel [2].

Advanced measurement techniques are used to characterize this new flow in order to get a complete picture of the flow field and to investigate the driving mechanisms. A system of co- or counterrotating vortices spans the area of membrane oscillation which takes shape as a superposition of standing and travelling waves. These boundary oscillations are applied to a CFD simulation, and the resulting time-averaged velocity field shows good agreement with the micro PIV measured velocity field, lending evidence that the membrane oscillation is the primary mechanism driving the streaming vortices.

The novel acoustic streaming flow studied in this work is relatively inexpensive to fabricate and operate, meaning it can be integrated into certain existing microchannel devices. Due to the necessity of an exposed membrane and vertical orientation of the mixing, gas transfer toward microfluidic artificial lung devices is seen as a potential application [3]. The vortices may be used to enhance mass transfer, which would normally be limited by diffusion within the microchannel.
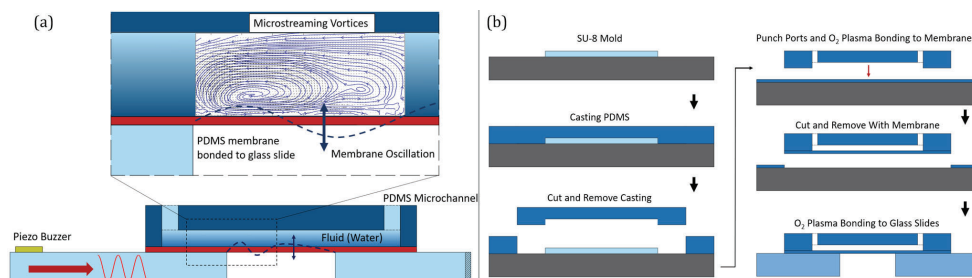

Figure 1: (a) Schematic diagram of the new configuration for acoustic microstreaming. (b) Fabrication process flow

Laser Doppler Vibrometry (LDV)

LDV measurement was performed on the section of the membrane exposed to open air to characterize its oscillation pattern in magnitude and phase. The microchannel is filled with water and sealed shut. The underside of the membrane is aligned with the view of the microscope objective and a grid of measurement points is specified over the area of interest. The observed pattern is a superposition of travelling and standing waves starting at the glass edge from which the acoustic waves originate. The travelling wave component dominates near that same edge and gives way to a standing wave dominant portion close to the opposite glass edge, evidenced by the steady decrease in phase starting from the leading edge and a flattening out of the plot on the opposite side. The largest velocity gradient and magnitude appear nearest the primary glass edge, which corresponds to the main vortex and fastest velocity observed in the below PIV experiments. The displacement magnitude varies approximately linearly with voltage, and the peak displacement observed was 18.5 μm for a 20 V_{pp} input. The wavelength seen in this membrane oscillation close to 1.5 mm is much shorter than the acoustic wavelength in PDMS, which would be 196 mm at the actuation frequency of 5.5 kHz, indicating that

the pattern is mechanical in nature, not acoustic. This can be seen as a reason the acoustic streaming occurs at this lower frequency in this experiment compared to ultrasound configurations.

Particle Image Velocimetry (PIV)

A 600 μm x 600 μm microchannel fabricated as described above was seeded with fluorescent particles and a sine wave acoustic signal is sent through. The particles are illuminated by laser light reflected by a right-angle prism to generate a side view. For two separate pulses with known time delay, two images corresponding to those laser pulses are correlated by PIV software, generating a velocity vector field in that field of view.

The PIV data shown in Fig. 2 give a clear picture of the streaming patterns for the entire channel height and within approximately 1.5 mm down the channel length based on the field of view of the system. In the case of 3 mm length of membrane determined by the gap between glass slides, a single strong vortex is captured in that field of view which spans the height of the channel with the highest velocity located near the membrane. For the 1.5 mm long membrane case, a view of the entire flow field is possible which reveals a three-vortex system. There is a similar main vortex spanning the height of the channel, a much slower corotating vortex within the main one, and a third counterrotating vortex bound by the opposite glass. Noting the maximum velocity at the bottom of the main vortex, the scaling with input voltage is approximately quadratic. At 20 V_{pp}, a maximum velocity of 47 mm/s was measured.

Simulation

A CFD simulation was executed with the CFX solver in ANSYS to further investigate the driving mechanism of the streaming flow. Geometry was created with dimensions to match the fabricated channels. Boundary conditions were applied to this geometry where the inlet and outlet were left open, the top and side walls were set to no-slip, and the bottom wall representing the membrane was set as a no-slip wall with specified displacement in time corresponding to the magnitude and phase data from LDV. The streaming flow is visualized by calculating the time average of the velocity field over the time steps in the final acoustic period.

The simulation results shown in Fig. 2 show good agreement in pattern and magnitude to the PIV results, providing evidence that the mechanical oscillation of the membrane is the driving mechanism of the acoustic streaming vortices. The three-vortex system is correctly predicted by simulation for the 1.5 mm gap case. The input amplitude of displacement for the simulation is related to the input voltage in the PIV experiment through the LDV results and show similar quadratic scaling. The velocity was predicted well, though slightly higher than experiment by close to 15% at higher input amplitudes, potentially due to sample-to-sample variation.

Conclusion

We have demonstrated here a novel configuration to generate acoustic microstreaming at audible frequency. Through advanced measurement techniques and simulation, we characterize the flow and provide evidence of the driving mechanism being the oscillating membrane. Future work is planned by the group for more complete understanding, optimization, and application. The interaction of these patterns with streamwise flow and the effect of orientation of the oscillation will be studied. The configuration may be applied to gas transfer towards a micro artificial lung device and the group plans to demonstrate this with an experiment showing higher concentration of gas transferred through the membrane into/out of the liquid channel when the acoustic actuation is applied and the vortex flows are present.
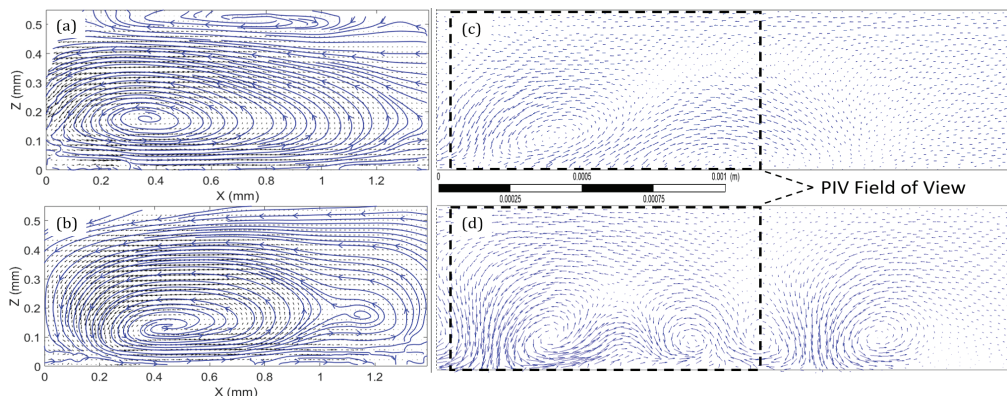

Figure 2: Acoustic streaming velocity vector field and streamlines measured by PIV for (a) 3 mm gap and (b) 1.5 mm gap case compared to CFD results given membrane oscillation as input for (c) 3 mm and (d) 1.5 mm gap case.

References
[1] P. Tho, R. Manaseh, and A. Ooi. *Journal of Fluid Mechanics* **573**, 191-233 (2007).
[2] P.-H. Huang *et al. Lab on a Chip* **13** no. 19, 3874-3852 (2013).
[3] J. A. Potkay. *Lab on a Chip* **14** no. 21, 4122-4138 (2014).

Abstracts - Poster Session I

Biomarker Protein Capture and Acousto-microfluidic separation Using Functional Microparticles

Song Ha Lee[1], Jinsoo Park[1]*

[1]Department of Mechanical Engineering, Chonnam National University, Gwangju, Republic of Korea
E-mail: thdgk14@jnu.ac.kr

Introduction
Cardiovascular disease (CVD) is the leading cause of death worldwide and the main cause of sudden death. Early diagnosis and prevention of CVD is one of the top priorities in public health to reduce the CVD mortality rate. C-reactive protein (CRP) [1] and Thrombin (Thr) [2] were chosen as CVD biomarker proteins because CRP and Thr are important biomarkers of cardiovascular disease. DNA aptamer-functionalized poly styrene (PS) microparticles of different diameters were designed and fabricated to selectively capture their corresponding biomarker proteins. We confirmed the binding of the functionalized microparticle-aptamer-protein by scanning electron microscopy (SEM). Two kinds of protein-aptamer-microparticle complexes can be separated from platelets when exposed to traveling surface acoustic wave (TSAW)-induced acoustic radiation force (ARF). Unlike our previous studies [3.4], our research developed to re-use and high throughput.

Experimental
Microparticles are surface modified with aptamer designed to selectively bind target biomolecules. Two kinds of the aptamers were designed for CRP and Thr. Particle-aptamer-protein complex is formed by binding to aptamer and protein from an immune reaction This complexes were then spiked in human serum to imitate a CVD patient-derived plasma sample (Figure 1a).
The two different-sized elastic polymer particles be separated by TSAW-induced ARF. Finally, two PS microparticles-aptamer-protein complexes were separated from platelets in plasma, and result to three trajectories in microchannel (Figure 1b).
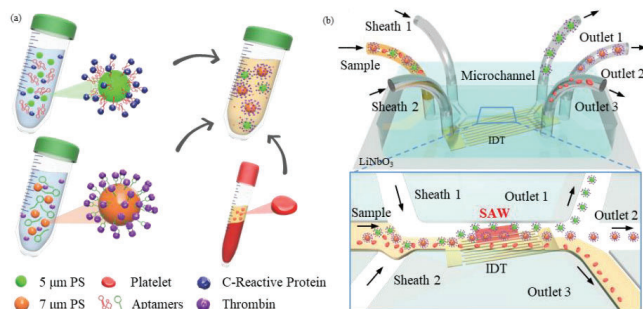

Figure 1: schematic diagram of the process. (a) shows the process of forming a complex by binding the aptamer to the particles and then binding the 5 µm particles and 7 µm particles with CRP and Thr protein. (b) shows to separate two particle by TSAW-induced ARF in the acoustofluidic device.

Results and discussion
To validate the formation for protein-aptamer-microparticle complexes, we performed SEM analyses. Figure 2 indicate the SEM micrographs of bare (a) 5 µm diameter polystyrene microparticles (PS5), (d) 7 µm diameter PS microparticles (PS7), (b) AptC-conjugated PS5 (PS5-AptC), (e) AptT- conjugated PS7 (PS7-AptT), (c) CRP-conjugated PS5-AptC (PS5-AptC-CRP), and (f) Thr-conjugated PS7-AptT (PS7-AptT-Thr) (Figure 2.) The streptavidin-coated PS microparticles in Figures 2(a) and 2(d) observe to be bare microspheres with approximate diameters of 5 and 7 µm. The two DNA aptamers coated onto the streptavidin conjugated microspheres through streptavidin-biotin interactions can be visually verified by the roughened surfaces with white dots on the microspheres in Figures 2(b) and 2(e). The two target biomarker proteins, CRP and Thr, conjugated with their corresponding aptamer-functionalized PS microparticles can be verified by the protein-aptamer-microparticle complexes in Figures 2(c) and 2(f).
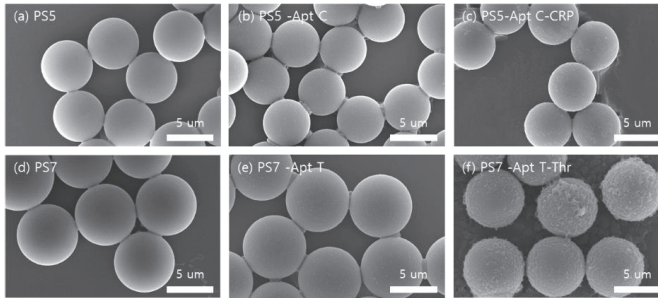
Figure 2: SEM images of streptavidin-conjugated PS microparticles with (a) 5 μm (PS5) and (d) 7 μm (PS7) in diameter; (b) AptC-functionalized PS5 (PS5-AptC); (e) AptT-functionalized PS7 (PS7-AptT); (c) CRP-conjugated PS5-AptC (PS5-AptC-CRP); (f) Thr-conjugated PS7-AptT (PS7-AptT-Thr)
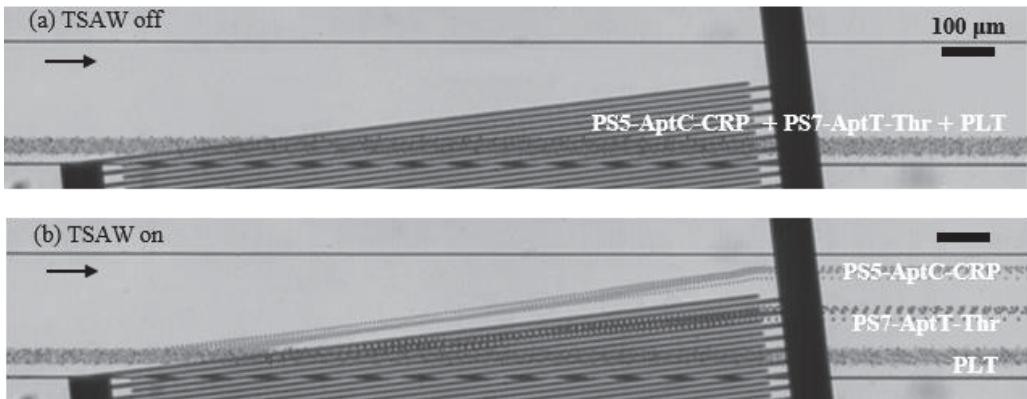

Figure 3: microscope images of separation in microchannel with ARF. (a) TSAW off bind (b) TSAW on.

5 μm PS particle-AptC-CRP and 7 μm PS particle-AptT-Thr were separated by a single-frequency acoustic field using interdigital transducer (IDT). separation of particles was confirmed that PS particle-aptamer-target protein moved to influence of ARF in the channel. (Figure 3).

Conclusion
Cardiovascular disease biomarker CRP and Thr were bound to particles, and particle-aptamer-protein complex were collected by TSAW. Separation of particle-aptamer-protein complex could to diagnose cardiovascular diseases in patients by checking the presence or absence of CRP and Thr.
Also, capture of particle-aptamer-protein complex can be expected to increase the accuracy of cardiovascular disease diagnosis.

References
[1] CDC/AHA Workshop, *Circulation*, 2004, 110, 25, 560-567
[2] Russell P., et al. Thrombin, Inflammation, and Cardiovascular disease. *CHEST*, 2003, 124, 49S-57S
[3] Afzal M., et al. *Anal. Chem*., 2021, 93, 8309-8317
[4] Ahmad R., et al. Anal. *Chem*., 2017, 89, 13313-13319

Using acoustofluidics for continuous patterning of cells within a hydrogel

Dhananjay V. Deshmukh[1,2], Peter Reichert[1], Joel Zvick[3], Céline Labouesse[2], Valentin Künzli[1], Oksana Dudaryeva[1], Ori Bar-Nur[3], Mark W. Tibbitt[2], and Jurg Dual[1]

[1] Institute for Mechanical Systems, Department of Mechanical and Process Engineering, ETH Zürich, 8092 Zürich, Switzerland
E-mail: deshmukd@ethz.ch
[2] Macromolecular Engineering Laboratory, Department of Mechanical and Process Engineering, ETH Zürich, 8092 Zürich, Switzerland
[3] Laboratory of Regenerative and Movement Biology, Department of Health Sciences and Technology, ETH Zürich, 8603 Schwerzenbach, Switzerland

Introduction

Tissues in our body have unique spatial arrangement. Conventional 3D encapsulation of cells for tissue engineering often fails to capture this structural complexity of native tissues. To engineer tissues ex vivo, it is often critical to mimic not only the biochemical cues through biomaterials but also the complex cellular organization. For example, parallel alignment of myotubes enables uniaxial muscle contraction. These myotubes are formed by the fusion of muscle progenitor cells (myoblasts), a process in which cell–cell contact is known to be important. [1]

In our work, we have used acoustofluidics to pattern muscle cells within a hydrogel to mimic the structure of skeletal muscle tissue while increasing the local cell density to promote myotube formation. We used a glass capillary-based device to achieve acoustic patterning, while a Teflon tube inside the capillary ensured continuous and smooth extrusion of patterned cells in the hydrogel fiber. We observed formation of myotubes and their spontaneous twitching indicating the functionality of the tissue constructs.
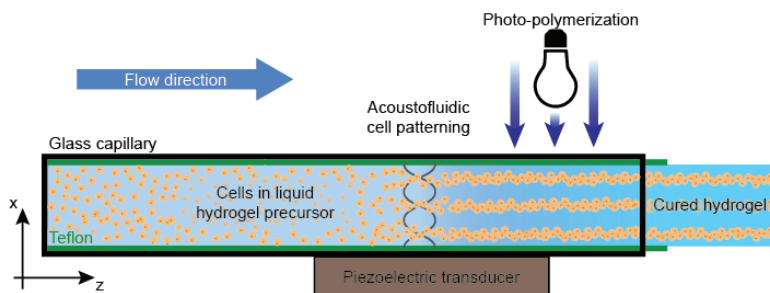

Figure 1: Cells in a liquid hydrogel precursor solution are patterned using an acoustic field, the patterned cell positions are retained by photo-polymerization of the hydrogel. The continuous flow in the device results in extrusion of the hydrogel fiber with patterned cells.

Results

For continuous extrusion and patterning, we used a Teflon-in-glass capillary device with a piezoelectric transducer (PZT) glued onto a square glass capillary (Figure 1a). [2] The operating frequencies for the device were identified using tracer particles (polystyrene, Ø = 15 μm). Varying the operating frequency gave us control over the spacing between the lines of cells. (Figure 2a) To externally trigger the polymerization of hydrogel, we used gelatin methacrylate (GelMA), a photo-polymerizable hydrogel that was polymerized using a light trigger ($\lambda = 405$ nm). Cells patterned in the hydrogels maintained their positions after extrusion. (Figure 2b)

a. Tunable acoustic patterning

f = 2490 kHz
d ≈ 300 µm
n = 5

f = 2900 kHz
d ≈ 250 µm
n = 6

f = 6820 kHz
d ≈ 110 µm
n ≈ 13
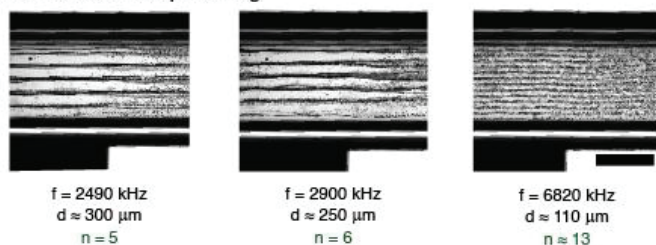
b. Patterning of the cells
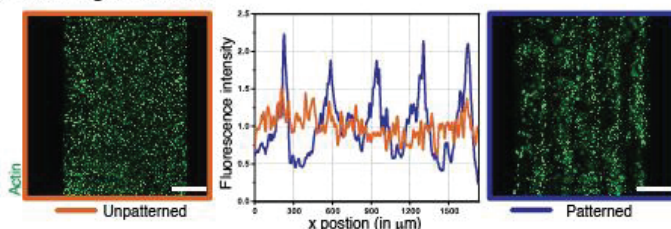
Actin

— Unpatterned   — Patterned

Figure 2: Patterning frequencies and patterned cells (a) Acoustofluidic device enables tunable positioning by varying the operating frequency. Scale bar, 1 µm (b) Cell positions were analyzed in unpatterned (left, orange) and patterned (right, violet) hydrogel fibers. Cells were stained for actin and the fluorescence intensity was calculated from maximum intensity projection of a z-stack. The plots were normalized against the total fluorescence in each image. Scale bar, 500 µm

Finally, primary murine myoblasts were patterned in a previously optimized hydrogel formulation using our device. [3] The samples were collected and allowed to proliferate in myoblast growth medium in a cell incubator. Three days post patterning, the samples were transferred to myoblast differentiation medium to initiate myotube formation for seven additional days. Spontaneous twitching was observed from 7 days post patterning to indicate presence of myotubes in the sample. The samples were stained for myosin heavy chain, a marker for mature muscles. The acoustically patterned samples showed presence of myotube all through the bulk of the hydrogel, whereas unpatterned samples only had myotubes on the surface. (Figure 3)
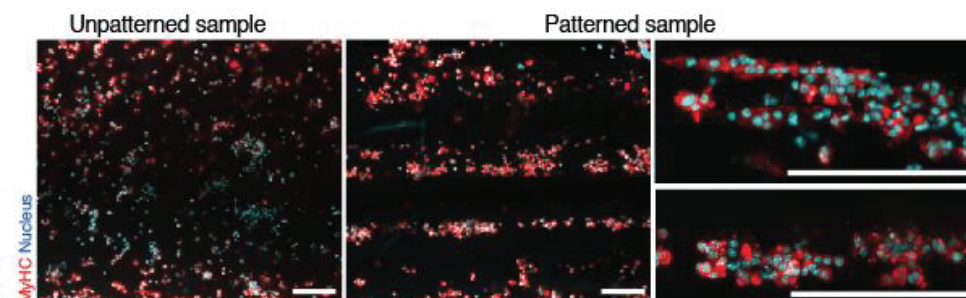

Unpatterned sample   Patterned sample

MyHC Nucleus

Figure 3: Myotube formation in unpatterned and patterned hydrogel samples. MyHC+ cells were observed in regions of high localized cell density in the patterned samples whereas myotubes were only present on the surface of the gel in the unpatterned samples. Scale bar, 200 µm

Conclusion

We have developed a device which allows for robust patterning of cells inside a hydrogel. Leveraging acoustofluidics, we showed control over cell spacing by changing the operating frequencies. We used our device to pattern myoblasts in our hydrogel and could observe their fusion into myotubes. Since this technology is label-free, we can use this device for other tissues which require structural anisotropy. The small size of the device and continuous extrusion can enable the use of this device as a nozzle for 3D bioprinting.

References
[1]   R. S. Krauss, G. A. Joseph, A. J. Goel, *Cold Spring Harb. Perspect. Biol.* **2017**, *9*.
[2]   D. V. Deshmukh, P. Reichert, J. Zvick, C. Labouesse, V. Künzli, O. Dudaryeva, O. Bar-Nur, M. W. Tibbitt, J. Dual, *Adv. Funct. Mater.* **2022**, 2113038.
[3]   D. V. Deshmukh, N. Pasquero, G. Rathore, J. Zvick, O. Bar-Nur, J. Dual, M. W. Tibbitt, *Bioeng. Transl. Med.* **2020**, *5*.

Mass-producible SAW chips for blood cell sorting

M. Colditz[1], A. Fakhfouri[1], K. Ivanova[1], U. Weißker[1], R. Kronstein-Wiedemann[2], S. Hartmann[1], R. Brünig[3], T. Tonn[2], A. Winkler[1]

[1] Group Acoustic Microsystems, SAWLab Saxony, Leibniz Institute for Solid State and Materials Research Dresden, Dresden, Germany
E-mail: m.colditz@ifw-dresden.de, URL: https://www.sawlab-saxony.de/
[2] Institute for Transfusion Medicine, DRK-Blutspendedienst Nord-Ost gGmbH, Dresden, Germany
[3] BelektroniG GmbH, Freital, Germany

Introduction

Sorting of biological cells from body fluids is of increasing importance in liquid biopsies and personalized medicine, as it provides useful information about the stage and progression of a disease and can enable precision treatments. The analysis of complex fluids, such as blood, often requires a prior sample preparation to differentiate its components. In analysis of the blood, for instance, pure blood plasma, cells indicative of diseases, and even nanometer-sized particles are interesting for subsequent analysis. As such, there is a great need for novel methods capable of a pure and gentle sorting of target components. Surface acoustic wave (SAW)-based acoustofluidics is a promising technology to meet this demand, since cells and particles can be manipulated, separated and sorted in an acoustic field purely based on their intrinsic properties such as size, density, compressibility and shape.

At SAWLab Saxony, we demonstrate a breakthrough technology for fabrication of mass-producible acoustofluidic cell sorting chips and the miniaturization of "lab-around-the-chip" to enable potential real-life applications in biomedicine. Furthermore, we demonstrate the separation of blood cells with higher throughput and higher purity compared to current state-of-the-art microfluidic methods.

Mass-producible SAW-based acoustofluidic chips

The gold standard method for fabrication of the channels used in SAW-based acoustofluidics chips is currently polydimethylsiloxane (PDMS) replica molding and bonding. Whilst passive microfluidic systems increasingly use roll-to-roll and injection moulding methods suitable for mid and large-scale production, the fabrication procedure of SAW-based acoustofluidics was so far limited to the laboratory environment due to the use of piezoelectric substrates and thus reduced possibilities for channel integration. PDMS microfluidic channels, besides their poor biochemical properties, are poorly reproducible, not very precise in positioning, costly to manufacture and not suitable for (automated) production at an industrial level, which is why their use represents a major limitation to acoustofluidics.

At SAWLab Saxony we develop methods for production of acoustofluidic chips based on the next generation materials and their analysis, including epoxy polymers and dry film resists [1,2]. We demonstrate, that the co-integration of interdigital transducers (IDT) and microchannels at the wafer-level is possible (see Figure 1a). Here, we report on an improved technology to produce structures down to resolutions of 5 μm, large aspect ratios of 1:10 as well as several cm long channels closed with a continuous cover and in- and outlets. The fabricated channel walls are consistent in their thickness and of highly defined geometry, while the microchannel cover has a flat surface without bending. We demonstrate SAW-acoustofluidic chips produced on 4" wafers combining physical vapor deposition, lift-off technology, etching and resist technology. We analyze the chips regarding their geometry and their electric and acoustic performance, before they are used in microfluidic applications.

Demonstrator and miniaturization

A major challenge in microfluidics is the size and control of the whole setup consisting mainly of the chip holder, fluid supply, tubing, valves, connectors and SAW generator, the so called "lab-around-the-chip". Development of the microfluidic technologies, especially for point-of-care applications and portable stand-alone or handheld devices, can only be successful when chip and miniaturized components are developed together.

Our developments so far lead to different versatile and compact lab demonstrators comprising miniaturized components like pumps, valves and signal sources combined with application tailored chip platform. With this flexibility and reduced size, the complexity of the laboratory setup is minimized and, depending on the area of the application, various functions can be realized at the same time. For the electrical and fluid connection, a platform technology has been developed that enables easy chips exchange. It comprises a task-specific metal

holder, suited as well for passive/active heat management, fluid connections, and printed circuit boards for chip connection via spring pins. Together with miniaturized components, we develop task-specific demonstrators allowing a simple handling for trained staff and reliable standalone usage in partner laboratories.

Blood cell sorting

Various applications have been tested with the described chips and demonstrator, in particular the separation of blood cells (see Figure 1b, c), which is highly interesting for a range of biomedicine applications. In order to achieve a separation of different fractions, an arrangement with two IDT pairs, with wavelength of 300 µm, and a channel with 150 µm width and 50 µm height is used. Two pressure nodes close to the channel walls are generated to create two successive blood cell separation stages. The sorting technology indicates a high throughput of 25 – 50 µL/min, gentle sorting with low applied powers (< 1.5 W) and a high separation efficiency and purity of the desired fraction (86% [2] - >99%).
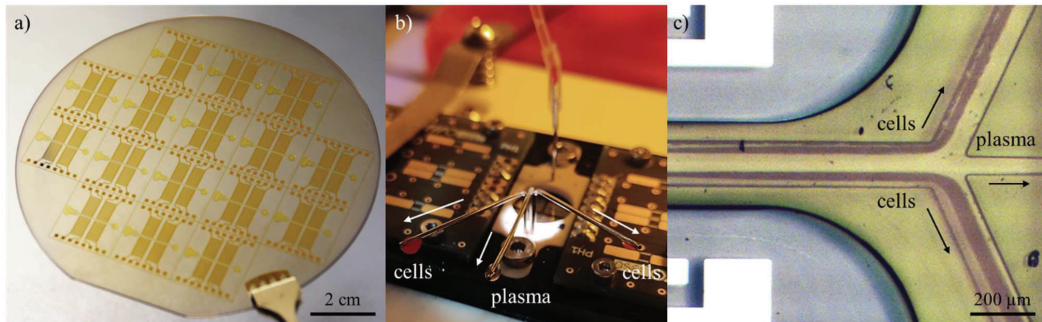

Figure 1: a) Lithographically cointegrated interdigital transducers and on-chip microchannels on 4" LiNbO3 wafer, b) chip in chip holder with fluid and electrical connectors; blood inserts the chip at the inlet, it gets separated in cells and blood plasma and the blood cells where collected at the side outlet, the plasma at the middle outlet c) insight in microfluidic channel at the outlet junction; blood cells are deflected to channel walls and were separated from plasma

Conclusion

At SAWLab Saxony of IFW Dresden, our aim is to make SAW-based acoustofluidics accessible to industry. We have been able to realize truly mass-producible SAW-based acoustofluidic chips with high precision and reproducibility, a chip platform for easy fluidic and electric connection to external device components, a portable and easy-to-use demonstrator with miniaturized components and further efforts towards automation, as well as blood cell sorting.

References

[1] M.M. Roos, A. Winkler, M. Nilsen, S.B. Menzel, S. Strehle, International Journal of Precision Engineering and Manufacturing-Green Technology 9, 43–57 (2022)
[2] C. Richard, A. Fakhfouri, M. Colditz, F. Striggow, R. Kronstein-Wiedemann, T. Tonn, M. Medina-Sánchez, T. Gemming, A. Winkler, Lab on a Chip 19, 4043-4051 (2019)

A holistic solution to icing by acoustic waves on piezoelectric plates

Jaime del Moral,[1] Laura Montes,[1] Víctor J. Rico,[1] Carmen López-Santos,[1,2] Stefan Jacob,[3] Manuel Oliva,[1,4] Jorge Gil-Rostra,[1] Armaghan Fakhfouri,[3] Shilpi Pandey,[3] Miguel Gonzalez del Val,[5] Julio Mora,[5] Paloma García-Gallego,[5] Pablo F. Ibáñez-Ibáñez,[6] Miguel A. Rodríguez-Valverde,[6] Andreas Winkler,[3] Ana Borrás[1] and Agustín R. González-Elipe[1]

[1] Nanotechnology on Surfaces and Plasma Lab, Materials Science Institute of Seville (CSIC-US), c/ Américo Vespucio 49, 41092, Seville (Spain)
E-mail: anaisabel.borras@icmse.csic.es; URL: https://sincaf.icms.us-csic.es
[2] Departamento de Física Aplicada I, Escuela Politécnica Superior, Universidad de Sevilla, C/ Virgen de Africa 7, 41011, Seville (Spain)
[3] Leibniz IFW Dresden, SAWLab Saxony, Helmholtzstr. 20, 01069 Dresden (Germany)
[4] Departamento de Física Atómica, Molecular y Nuclear, Universidad de Sevilla, Avd. Reina Mercedes s/n, 41012, Seville (Spain)
[5] National Institute for Aerospace Technology (INTA), Ctra. Ajalvir km. 4, 28850, Torrejón de Ardoz (Spain)
[6] Departamento de Física Aplicada, Universidad de Granada, Avd. de Fuente Nueva s/n, 18002, Granada (Spain)

Introduction

Icing has become a hot topic both in academia and in the industry given its implications in strategic sectors such as transport, robotics, wind turbines, photovoltaics, and electricity supply. Recently proposed de-icing solutions involving the propagation of acoustic waves (AWs) at suitable substrates may open the path for a sustainable alternative to standard de-icing or anti-icing protocols.[1] Herein we experimentally unravel some of the basic interactions that contribute to the de-icing and/or hinder the icing (ice accretion) on AW-activated substrates. The response toward icing of a model substrate system consisting of piezoelectric plates AW activated by radio-frequency (rf) signaling has been characterized both at a laboratory scale and in an icing wind tunnel under forced convection conditions. Additional experiments have shown that the piezoelectric substrate surfaces modified with perfluoromolecules, fluorinated ZnO thin film, or a ZnO/CFx bilayer present anti-icing functionality and a synergistic response when activated with AWs.

Experiment description

The piezoelectric substrates utilized in the experiments consisted of double-side polished, single-crystalline commercial available plates with 0.5 mm thickness, 1x2 cm^2 or 1.5x3 cm^2 size. Icing tests were carried out either using the bare piezoelectric substrates or onto these substrates functionalized by the deposition of various thin layers modifying the wetting and passive anti-icing response of the examined substrates. The activation protocol was based on the holder system and conditions detailed in ref. 2.

Polycrystalline ZnO thin films were deposited by plasma enhanced chemical vapor deposition (PECVD) at room temperature in an ERC MW plasma reactor as detailed elsewhere.[30–32] Typical thicknesses of the ZnO thin films varied between 500 to 1500 nm, a range for which no significant differences were found in the de-icing and active anti-icing experiments.[3]

CFx, Teflon like thin films. CFx thin films have been prepared at ambient temperature by PECVD in an rf parallel plate reactor. Full details of the preparation procedure of these thin films have been reported elsewhere.[4] CFx thin films with thicknesses in the range of 100 to 200 nm were deposited directly onto the LiNbO3 plates or onto ZnO coated plates. Hereafter, this bilayer arrangement will be named ZnO/CFx.

PFOTES molecular grafting. The bare or ZnO-coated LiNbO3 plates were functionalized by the grafting of perfluorooctyltriethoxysilane (PFOTES).[5]

The icing tests consisted of de-icing and active anti-icing experiments under controlled conditions in an icing wind tunnel, lab-scale icing set-up, and using the environmental chamber of an OCA WCA system. Pulling-off ice adhesion characterization was carried out on a custom-made system emplaced in a freezing chamber.

De-icing and active anti-icing with Acoustic Waves.

Experiments have been performed with well-defined piezoelectric substrates consisting of piezoelectric single crystal plates where standing acoustic plate waves with a majority shear character are generated by rf

activation. The wetting properties of this ideal system could be readily modified by surface functionalization without altering the AW resonance conditions. In particular, we show how the modification of the plate with a ZnO(F) thin film or ZnO/CFx multilayer renders the substrate surface hydrophobic while leaving unaffected the AW excitation. The experiments present a well-founded assessment of the influence of the wetting behavior and surface roughness of the plate surface on phenomena such as the adhesion and accretion of ice, or the ice melting phenomena. In general, surface hydrophobicity favors the anti-icing character of the piezoelectric chip devices, reducing the AW power required to induce de-icing or prevent icing (active anti-icing). Regarding the ice adhesion, a higher roughness of the functionalized devices appears to be detrimental for an effective detachment and contributes to increasing the adhesion strength of ice onto the modified piezoelectric substrates. Comparison between ferroelectric and non-pyroelectric piezoelectric plates has served to discard that, to a first approximation, pyroelectric activity plays a significant role in the AW de-icing processes, thus supporting previous hypotheses relying on pure mechano-acoustic mechanisms for the melting of ice aggregates by AWs.

Particular attention is paid to the freezing/melting behavior of water droplets. Specifically, our experiments show the ice-particle interface melting constitutes the first stage in the overall de-icing process for the wave mode studied here. For intermediate states, with both water and ice coexisting in partially melted aggregates, water seems to effectively wet the remaining ice core, providing a liquid diffusion layer over which the ice core can slide and be naturally removed by the action of natural forces such as gravity or wind (this latter as demonstrated in the icing wind tunnel experiments).

Conclusions. In this communication, we explore the suitability of AWs generated in piezoelectric plates to induce ice-phobicity, including de-icing, active anti-icing, and low ice adhesion. We have unraveled the role played by different anti-icing terminations on the icephobic performance of the devices, for the thin films and multilayers showing higher efficiency in the case of de-icing and active anti-icing while the grafting of anti-icing fluorinated molecules on the bare plates being addressed as the best solution for achieving ultra low ice-adhesion. We trust that proving the effectiveness of the AWs de-icing concept in close to real scenarios should open the way for future industrialization and applications of evolved versions of systems based on this principle.

References
[1] Yang, D.; Tao, R.; Hou, X.; Torun, H.; McHale, G.; Martin, J.; Fu, Y. Adv. Mater. Interfaces 8 (2), 2001776 (2021).
[2] García-Valenzuela, A.; Fakhfouri, A.; Oliva-Ramírez, M.; Rico-Gavira, V.; Rojas, T. C.; Alvarez, R.; Menzel, S. B.; Palmero, A.; Winkler, A.; González-Elipe, A. R. Mater. Horiz. 8 (2), 515–524 (2021).
[3] García-Casas, X.; Ghaffarinejad, A.; Aparicio, F. J.; Castillo-Seoane, J.; López-Santos, C.; Espinós, J. P.; Cotrino, J.; Sánchez-Valencia, J. R.; Barranco, Á.; Borrás, A. Nano Energy 91, 106673 (2022).
[4] Rico, V. J.; López-Santos, C.; Villagrá, M.; Espinós, J. P.; de la Fuente, G. F.; Angurel, L. A.; Borrás, A.; González-Elipe, A. R. Langmuir 35 (19), 6483–6491 (2019).
[5] Rico, V.; Mora, J.; García, P.; Agüero, A.; Borrás, A.; González-Elipe, A. R.; López-Santos, C. Appl. Mater. Today 21, 100815 (2020).

Facilely fabricated, flexible ultrasound sensor as a non-invasive approach for pulse and blood pressure monitoring

Yuyang Li[1], Jia Zhang[1]*

[1]Key Laboratory of Microsystems and Microstructures Manufacturing, Ministry of Education, Harbin Institute of Technology, Harbin 150080, China
*Corresponding Author, E-mail: zhangjia@hit.edu.cn, URL: http://homepage.hit.edu.cn/zhangjia

Introduction

According to WHO, cardiovascular diseases are seen as imminent threats of mankind. An estimated 17.9 million people died from CVDs in 2019, representing 32% of all global deaths [1]. Inspired by the development of electronic materials, manufacturing technology and wireless communication technology, flexible, miniaturized and intelligent devices are becoming the focus of routine medical care. One of the most promising applications is flexible devices or systems for medical imaging and monitoring, such as ultrasound transducer, which has better skin fitting property than traditional rigid ultrasonic equipments and consequently it is suitable for continuous detection of physiological indicators of the human body. This paper will briefly introduce a flexible piezoelectric sensor in medical application from perspectives of the numerical design logic and experimental results.

Description of the sensor

The sensor consists of a matching, backing, electric bonding layer, flexible electrodes and a 4×4 array of 1-3 piezoelectric composites, which contain PZT-5H (40%) and epoxy resin (60%). Compared with conventional isotropic piezoelectric ceramic, epoxy resin have the characteristics of reducing transverse vibration and thus 1-3 composite concentrates the energy mainly on the longitudinal vibration. The center frequency in this study is 3 MHz. According to the sound attenuation coefficient of human tissue 0.5 ± 0.05 dB/cm·MHz, low-frequency ultrasound has stronger capability of depth penetration into the superficial tissue than high-frequency ultrasound. Low temperature solder paste $Sn_{48}Bi_{52}$, of which melting point 138 °C is significantly lower than the Curie temperature of PZT, namely 160°C , is selected as the bonding layer, because it ensures good conductive as well as adhesive performance, even when the sensor works at largely deformed conditions, such as repeatedly bent or stretched (up to 30%). The flexible electrode is designed with an island-bridge structure, that can also withstand the deformation as mentioned. The independent excitation control for each row, column and seperate elements of sensor array is realized by the orthogonal layout of upper and lower electrodes. Finally, the ACF cables from electrodes are reserved for data communication.
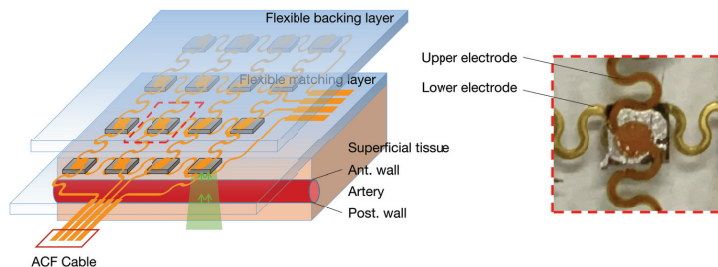

Figure 1: Schematic diagram of design and principle of the flexible ultrasound sensor. Schematic of ultrasound device and working principle. When piezoceramic is stimulated, the echos from ant. wall and post. wall of antery, as shown by green arrows, will be received by the same ceramic (left). Optical image of a single subunit in partial enlarged view (right).

The core area of the device is a square with length of 25 mm and only weights 34.2 g. Since the filling material PDMS possesses good flexibility, the device is completely covered comfortably on the skin surface. The fabrication process is also relatively facilely. The electrodes were pasted on the flexible backing layer and the matching layer, respectively. After the solder paste was uniformly smeared and solidified, as shown in enlarged view of Fig. 1 and the sensor was then encapsulated with PDMS, under the condition, namely 70°C and 5 hours. The fabrication was utterly completed.

Design logic

According to Huygens-Fresnel principle, ultrasonic sensors in the form of array have strong transmission performance compared with its in a single sub-unit. However, subject to the coherent cancellation, it is essential to determine the interval between each piezoceramic. Fig. 2 demonstrates the ultrasound transmission in a spherical human tissue region with a radius of 10 mm and given sound attenuation. The outermost spherical shell with a thickness of 2 mm is a perfect matching layer (PML).
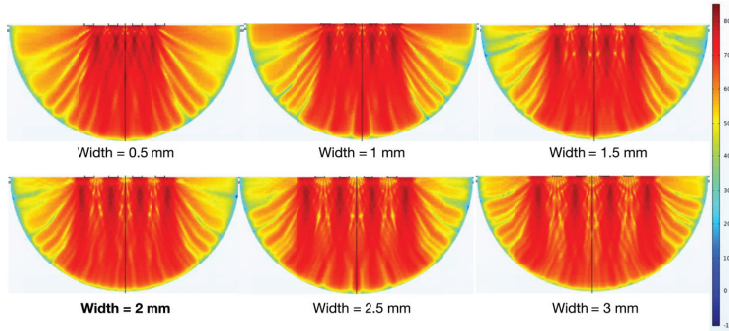

Figure 2: Numerical simulation results in 1×4 sensor array (yOz- cross section), in which different intervals between adjacent piezoceramics are illustrated. All subgraphs share the same colorbar.

Because of immerse calculations of transient simulation, stationary simulation is highly recommended. Under the same excitation condition, compared with the stationary, side lobe shown as sound pressure level in the transient is relatively small, so this simulation focuses mainly on the transmission of the main lobe in human tissue. The following conclusions can be drawn: The dark red area in the image increases gradually with the increase of width, and no longer increases when the width is above 2 mm. The sound field with intervals inside 2 mm is holistic, which means the sensor will operate as a whole. Nevertheless the sound field with intervals above 2 mm is independent, which means the sensor will operate as multiple subunits.

Results

There is a strong correlation between sub-units and rows or columns. With the comparison of signals from medical equipment and this sensor, data in this work is accurate (absolute error 5mmHg). The legnth of a complete cycle was 0.78 s. Therefore, the estimated heart rate is in the normal (76.9 BPM). The diastolic peak of the cardiac cycle, as shown in red dash line of Fig (e), however is low, it means that the elasticity of the artery is weaken, the closing function of the aortic valve is abnormal.
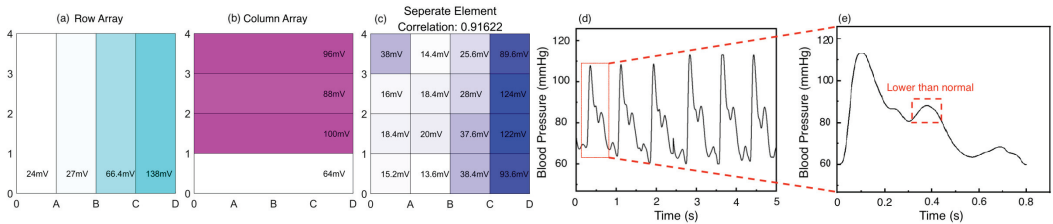

Figure 3: A sensor with voltage peak-peak 240 mV and central frequecy 3 MHz. Subplots are results from row (a) and column (b) array as well as correlation coefficient (c) between subunits and those arrays. Blood pressure waveform from 25-year-old male volunteer, diagnosed as hypertension and atherosclerosis, detected by medical device (d). Blood pressure waveform recorded simultaneously using this sensor (e).

Conclusion

Exploring the relationship between flexible ultrasonic sensors and cardiovascular diseases is a promising work. The sensor in this work can routinely monitor diseases such as atherosclerosis and hypertension so that people can take better care of themselves.

References

[1] WHO Fact Sheets. https://www.who.int/news-room/fact-sheets/detail/cardiovascular-diseases-(cvds)

Application of living probes to assess SAW-based acoustofluidic device performance

Advaith Narayan[1*], Mingyang Cui[1,2], and J. Mark Meacham[1†]

[1]Department of Mechanical Engineering and Materials Science, Washington University in Saint Louis, Saint Louis, MO 63130, USA
[*]E-mail: narayan@wustl.edu, [†]E-mail: meachamjm@wustl.edu, URL: https://meachamlab.wustl.edu/
[2]Department of Electrical Engineering and Computer Science, Massachusetts Institute of Technology, Cambridge, MA 02139, USA

Introduction

Numerous experimental methods have been proposed to characterize acoustofluidic device performance, including the application of motile cells for qualitative and quantitative assessment of bulk acoustic wave (BAW) devices.[1,2] Unlike passive particles, swimming *Chlamydomonas reinhardtii* cells redistribute throughout a fluidic domain when not under the influence of an acoustic field, which allows us to rapidly determine optimal device operating conditions and to map evolving pressure fields. In the reported work, we demonstrate the flexibility of the method to assess substrate acoustic wave (SAW) devices operating at higher frequencies. Resonance identification and relative field strength analysis are performed for glass-based straight channels and circular chambers driven at 6, 10, and 20 MHz (note we apply the conventional abbreviation SAW to include any substrate acoustic waves, e.g., Rayleigh, Lamb, etc., due to our substrate thickness and operating frequency range). We first summarize the concept and experimental protocols used to implement the method. We then identify optimal device operating parameters by visually observing distributions of swimming *C. reinhardtii* cells, comparing our results with electrical impedance measurements. Finally, we map evolving cell distribution densities to characterize relative field strengths in 1D straight channels and 2D circular chambers. Though the actuation mechanism differs, results are similar to those previously reported for BAW devices, suggesting wide applicability of our approach for operating frequencies up to at least 20 MHz.

Background and experimental protocols

Particle motion in an acoustic field is influenced by two second-order acoustic effects, the acoustic radiation force and acoustic streaming. The acoustic radiation force dominates for particles larger than ~2 μm.[3] *C. reinhardtii* are ~8 μm in diameter, so we expect that acoustic streaming effects are negligible relative to the primary acoustic radiation force and the intrinsic propulsive capability of the cells. Assuming cells can be approximated as spherical, the acoustic radiation force $\boldsymbol{F}^{\mathrm{rad}}$ can be represented as the gradient of a potential U

$$\boldsymbol{F}^{\mathrm{rad}} = -\boldsymbol{\nabla} U = -\frac{4\pi}{3} a^3 \boldsymbol{\nabla} \left[f_0 \frac{1}{2} \kappa_{\mathrm{o}} \langle p_1^2 \rangle - f_1 \frac{3}{4} \rho_{\mathrm{o}} \langle v_1^2 \rangle \right], \tag{1}$$

where a is the cell radius, κ is compressibility, and ρ is density. Thus, $\boldsymbol{F}^{\mathrm{rad}}$ depends only on the pressure and velocity fields, and the fluid and cell properties. At locations with large gradients in acoustic potential, $\boldsymbol{F}^{\mathrm{rad}}$ is higher, causing cells to be trapped and concentrated at higher densities in potential minima. The cell distribution density is easily observed, reflecting the shape and strength of the acoustic field.

A variety of hybrid BAW/SAW devices were used to demonstrate our method: 6 and 20 MHz straight channels and 6, 10, and 20 MHz circular chambers. Devices comprised a wet-etched glass superstrate on a 500-μm thick lithium niobate (LiNbO3) substrate, with interdigitated transducers (IDTs) fabricated using conventional photolithographic, thermal vapor deposition, and lift-off microfabrication processes to pattern the chromium/gold IDT geometry (Fig. 1A). IDT finger width and spacing dictated the design frequency as is typical of SAW devices; however, due to the hybrid nature of SAW actuation driving BAW field development, the superstrate channel geometry largely determined the optimal operating frequency and mode shapes.

Cells were loaded into the channels, and a function generator and amplifier were used to actuate the device during a frequency sweep at constant input power to identify the optimal device resonance(s). Examples of desired mode shapes with concentric rings and a central node for 6, 10, and 20 MHz nominal circular chambers are shown in Fig 1B. Cell distributions were recorded at 10 fps, and maxima in correlation coefficient of subsequent images were used to isolate potential operating conditions. After locating an optimal resonant frequency, we swept the drive amplitude (at fixed frequency) to map the relative field strength as a function of position. As the cells were focused, images were taken at 10 fps and pixel densities throughout the channel were analyzed to construct heat maps using MATLAB.

Resonance identification

Impedance measurements revealed optimal IDT operation where the measured impedance was nearest 50 Ω; however, this operating condition did not necessarily correspond to a channel/chamber resonance dictated by the BAW. These 'true' resonances were identified using the image correlation (Fig 1C) with the desired operating frequency selected from those with the highest correlation coefficient (e.g., filtering f_{ac} from f_1^* and f_2^* in Fig. 1C). Using this method, we identified the optimal resonant frequencies for each of the devices and channel geometries as shown in Table 1.

Table 1: Design and operating frequency for each device.

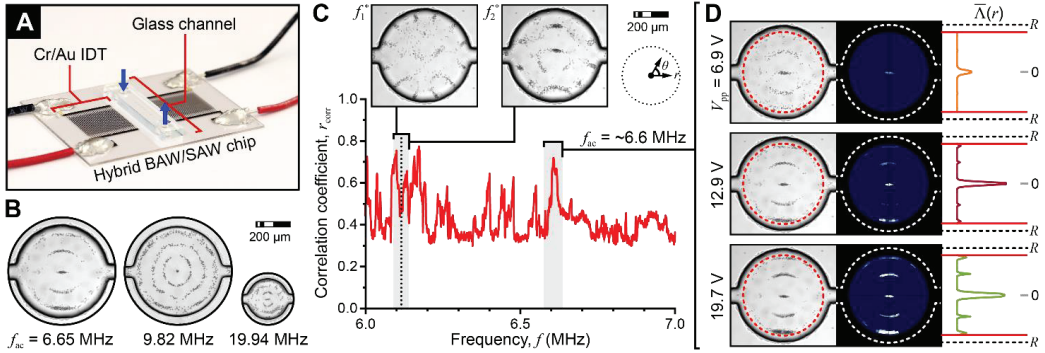| IDT design frequency	Straight channel resonance	Circular chamber resonance
6 MHz	6.39 MHz	6.65 MHz
10 MHz		9.82 MHz
20 MHz	19.25 MHz	19.94 MHz

Figure 1: SAW-based device characterization using motile cells as measurement probes. (**A**) and (**B**) overview of hybrid BAW/SAW device and operation of circular chambers at various BAW resonant frequencies. (**C**) Identification of optimal chamber resonance for a 6 MHz nominal device. (**D**) Evolution of the swimming cell distribution with increasing field strength at f_{ac} = 6.65 MHz. Cell distributions are averaged over time to create distribution density maps, which are then averaged over space to create line plots of average distribution density as a function of radial position $\overline{\Lambda}(r)$.

Relative field strength characterization

Holding the operating frequency constant and gradually increasing the input voltage allowed us to visualize the relative increases in field strength within a channel/chamber. Brightfield images were averaged over time to create a heat map of the cell distribution density which was then spatially averaged to create a line plot of average distribution density versus radial position about the center of the circular chamber (Fig 1D). A similar analysis was performed for straight channel devices to characterize nodal bands oriented along the channel. As expected, increasing the input voltage yielded an increase in cell density in the trapping regions, while elucidating the complex field shape arising from the inlet/outlet structures, slight misalignment of the channel/chamber to the IDTs, and driving a 2D field with 1D transducers. Importantly, experiments were performed in rapid succession since the cells quickly redistribute during off-resonance operation.

Conclusion

While the use of passive particles requires flowing new particles through the channel after every actuation, motile cells swim freely to redistribute throughout the channel enabling comprehensive performance characterization without manual reloading of cells. We have established broadly applicable experimental protocols for cell preparation and qualitative device assessment. To prove these capabilities, we used our previously reported method to identify resonances and rapidly determine the relative field strengths for SAW-based microfluidic devices with different actuators and microfluidic architectures. Though the SAW actuation is inherently different than that of a typical BAW device, the cell behavior and analysis are consistent with our earlier results.[1,2] As before, resonances are easily identified visually, and cell distribution densities capture irregularities associated with real devices (e.g., the slight mode shape asymmetry in the circular chamber device), which are difficult if not impossible to predict using computational methods.

References

[1] M. Kim, R. Barnkob, and J.M. Meacham. J Acoust Soc Am **150**, 1565-1576 (2021).
[2] M. Kim, P.V. Bayly, and J.M. Meacham. Lab Chip **21**, 521-533 (2021).
[3] R. Barnkob, P. Augustsson, T. Laurell, and H. Bruus. Phys Rev E **86**, 056307 (2012).

Deformation of Thalassaemia Minor and Major Red Blood Cells Induced by Surface Acoustic Waves

Mustafa Zaimagaoglu[1], Andreas Link[1], and Thomas Franke[1]

[1]Department of Biomedical Engineering, University of Glasgow, Glasgow, UK

Email: Mustafa.Zaimagaoglu@glasgow.ac.uk

Introduction: We present an experimental study for Thalassaemia Minor and Major RBC elasticity. In previous research, it was found that using Surface Acoustic Waves (SAW) is a distinctive method to perform for investigating the D-Taylor values of RBCs. [1] On the other hand, as diseased RBCs are more fragile and challenging to find for research purposes; there is a gap in the literature for Thalassaemia RBC morphology properties. This disease`s chemical and biological properties were well investigated in previous years but physical property-wise; our paper will give a better understanding on the diseased RBCs` behaviour under stress. There are various methods to investigate the physical properties of RBCs, our approach involves analysis at a single cell level rather than an analysis that is done with a group of cells. [2] Our method gave us a chance to pay more attention to each individual cell with a detailed analysis. Our interpreted results are parallel with our theoretical knowledge and expectations. It can be seen that both Thalassaemia Minor and Thalassaemia Major RBCs are less deformable than Healthy RBCs under the same powers(dBm). Our research also showcased that Thalassaemia Minor patients have more microcytes than Thalassaemia Major patients which showcases that RBC deformation in Thalassaemia minor is lower than Thalassaemia Major due to the node/cell ratio.

Abstract: We demonstrate an acoustic device to mechanically probe a population of Thalassaemia Minor and Major RBCs at the single cell level. The device operates by exciting a surface acoustic wave in a microfluidic channel creating a stationary acoustic wave field of nodes and antinodes. RBCs are attracted to the nodes and are deformed. Using a stepwise increasing and periodically oscillating acoustic field we study the static and dynamic deformation of individual RBCs one by one.
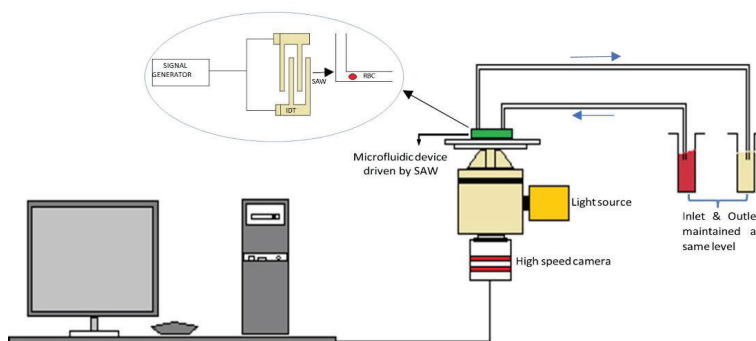
Experimental Set-up:

Figure 1: Diagram providing an understanding of the process involved in examining the deformation of RBCs using SAW. The electrical signals produced from the signal generator was applied across the metallic fingers of the Interdigital Transducer (IDT) to generate SAW. The SAW was then utilised to trap and deform the cell to study the elastic properties of the cell. An inverted light microscope with 60x objective lens and Photron fast camera with 250 frames per second was used to observe and record the behaviour of RBCs in response to SAW. The inlet syringe comprises the sample and the outlet syringe comprise the PBS/ BSA (10 mg/ml) solution, and a pressure pump is used for the movement of fluid and flushing mechanism during the experiment. The inlet and

outlet are maintained at the same level using height reservoir to bring the fluid flow to absolute zero and the pressure pump was used for flushing mechanism and to move RBCs towards the microfluidic channel. Then, the cell is trapped and deformed with 2 different power sweeps with the help of SAW. The whole setup was handled using the LabView software and it also helps to transfer the data to other software efficiently for analysis purposes. The data acquired from the SAW experiment was analysed using the ImageJ and Origin Lab software. The ImageJ allows to smoothen, to establish a threshold and analyse the particles in an image. The Origin Lab software can handle a large amount of data and was used to analyse the data by plotting scientific graphs in order to understand the behaviour of cells effectively.
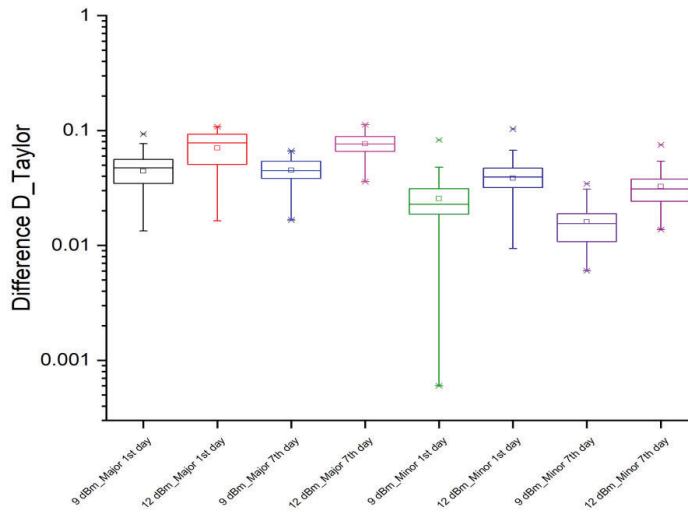
Results and Conclusion:

Figure 2: Deformation difference of the Major and Minor RBCs with 2 different power sweeps (9dBm, 12dBm). The data is gathered after 5 elongations for 9dBm and 5 elongations for 12dBm. It can be seen that 12dBm deformed the RBCs more than 9dBm. On the 7th day the range of elasticity decreased when we compare it with the 1st day, which shows that; The cells left after a week have mostly the same elasticity range rather than a wider ability to deform. boxplot shows Beta-Thalassaemia Major RBCs are more deformable than Beta-Thalassaemia Minor RBCs. This might be a result of the Microcyte population in Beta-Thalassaemia Minor.

Anisocytosis is the medical term for having red blood cells (RBCs) that are unequal in size. Normally, a person's RBCs should all be roughly the same size. Anisocytosis is usually caused by another medical condition called anaemia. With lack of oxygen throughout the body RBCs may lose their intracellular dense which will end up with microcytosis. [3] Having deficient RBCs caused by Thalassemia comes with challenges for both Minor and Major types of the disease. In our experimental investigation, we showcased the morphological properties of these RBCs and contributed to the literature why/how Thalassaemia RBCs are less deformable than the healthy ones and how badly aging effects the RBCs in life and dead conditions.

References:

[1] Link, A.; Franke, T. Acoustic erythrocytometer for mechanically probing cell viscoelasticity. Lab Chip 2020,20, 1991–1998.

[2] H. Bow , I. V. Pivkin , M. Diez-Silva , S. J. Goldfless , M. Dao , J. C. Niles , S. Suresh and J. Han , *Lab Chip*, 2011, **11** , 1065 —1073

[3] Iolascon A, De Falco L, Beaumont C. Molecular basis of inherited microcytic anemia due to defects in iron acquisition or heme synthesis. *Haematologica*. 2009;94(3):395-408.

Generation of various cell patterns with millimeter scale with standing waves on a liquid surface

Kohei MORITA, Takeshi HAYAKAWA

Department of Precision engineering, Chuo University, Tokyo, Japan
E-mail: hayaka-t@mech.chuo-u.ac.jp, URL: https://www.mech.chuo-u.ac.jp/~hayakawalab/

Introduction

Cell aggregation is an important manipulation for tissue engineering. Our group has proposed a cell manipulation system to generate cell patterns from ≈100 μm to ≈10 mm sizes by using fluid-vibration interactions. The system uses two phenomena that are vibration-induced flow and Faraday waves for different seizes of cell patterns. Vibration-induced flow that have been studied in our group generates patterns of several hundred μm sizes, including cell spheroids. Faraday waves that are nonlinear waves on liquid surface generate patterns of ≈1-10 mm sizes. In this study, we confirmed that generating cell patterns of ≈1-10 mm sizes by Faraday waves. By changing a direction of applying vibration and chambers shape, cell patterns were changed.

Background

In recent years, researches on cell manipulations have been vigorous in biomedical research fields. Specifically, cell aggregation is one of the most important manipulations being studied. For example, cell spheroids are formed by aggregating single cells and used for a drug screening, cancer models and evaluations of liver function[1]. Previously, we proposed a method of forming cell spheroids with a vibration-induced flow[2]. Vibration-induced flow is a local flow induced around microstructures by applying vibration to the structures. We successfully used vibration-induced flow to form cell spheroids of approximately ≈100 μm sizes. However, since vibration-induced flow is a localized flow, it is difficult to form cell patterns of mm sizes by using vibration-induced flow even though actual human tissues have sizes of ≳10 mm. Therefore, we also use Faraday wave for formation of cell patterns of ≈1-10 mm sizes with a same system as a vibration-induced flow. Faraday waves that are nonlinear waves on liquid surface are generated in chamber by applying vibrations with piezoelectric stage, as shown in Fig.1 (a). Our goal is combining these phenomena in one system and generating multi-scale cell patterns that are more similar to actual human tissues by using the proposed system.

Method

Fig.1 (b) shows concept of a proposed system. When vibration of ≈100-1000 Hz is applied, vibration-induced flow occurs in several hundred μm area around microstructures patterned on a chip. Therefore, vibration-induced flow can form cell spheroids of ≈100 μm sizes, as shown in Fig.1 (c). On the other hand, Faraday waves are generated by applying vibration of ≈10-100 Hz. This phenomenon generates a flow across the entire liquid chamber. Because of that, using Faraday wave can generate cell patterns of ≈1-10 mm sizes, as shown in Fig.1 (d). By combining these two phenomena, the proposed system can achieve generating cell patterns from sizes of ≈100 μm to ≈10 mm by changing vibration frequencies. In this study, we confirmed differences of cell patterns by changing vibration directions and shape of chambers with Faraday wave.
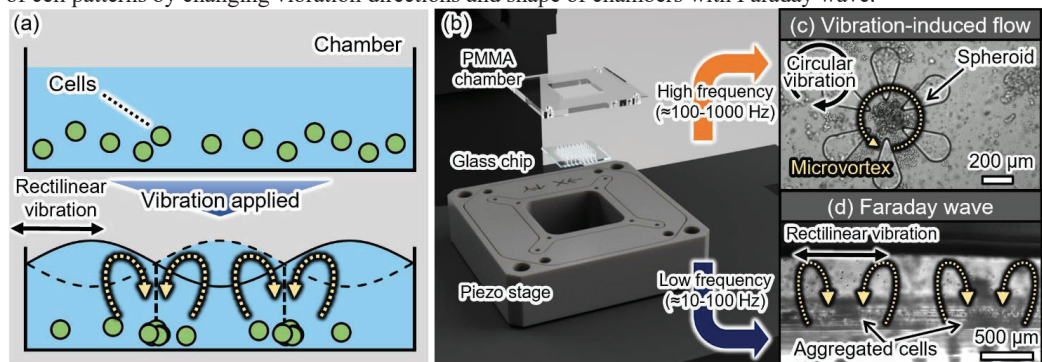

Figure 1: (a) Principle of Faraday wavers (b) Concept of the proposed system (c) Vibration-induced flow (d) Side-view of Faraday waves

Experiments

The experimental system consisted of a glass chip that has patterned microstructures for vibration-induced flow, a PMMA chamber, and a piezoelectric XY stage (PK2H100-030U, THK PRECISION) on a microscope stage. The chip that was glued on the PMMA chamber fixed on the XY stage. The microstructures shaped micropillars with diameter of 100 μm and height of 40 μm patterned on the chip. HepG2 cell suspensions were used for experiments of formation of cell patterns.

Results

Firstly, we confirmed that cell patterns in a rectangle chamber with vibrations of various directions. When vibrations were applied in the x axis and y axis directions, stripe patterns were generated in the chamber, as shown in Fig.2 (a) and (b). And when the vibrations were applied in the right oblique upward direction, two circular patterns were generated at the center, as shown in Fig.2 (c). When circular vibration was applied, a lattice dot pattern was generated in the chamber, as shown in Fig.2 (d).
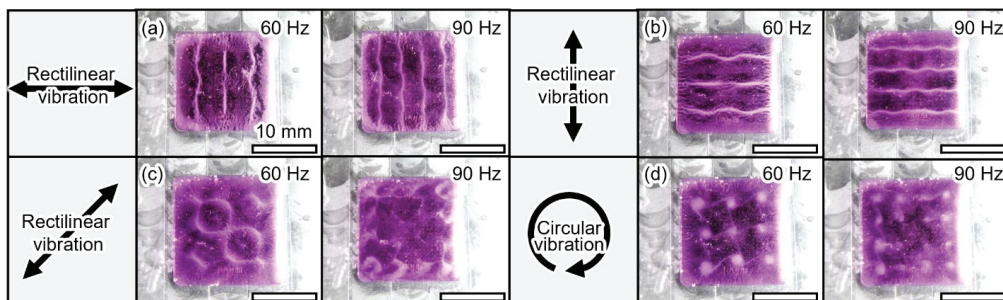

Figure 2 The results of generating pattern in a rectangle chamber (a) x axis (b) y axis (c) oblique (d) circular vibrations

Secondly, we confirmed cell patterns in a circular and triangular chambers, as shown in Fig. 3. In case of a circular chamber, when x axis, y axis, and oblique vibrations were applied, arc-shaped patterns were generated perpendicular to the direction of each vibration, as shown in Figs. 3 (a)-(c). It was also confirmed that circular patterns were generated when circular vibration was applied, as shown in Fig. 3 (d). In case of a triangular chamber, the x axis vibrations generated regular patterns in the chamber, as shown in Fig. 3 (a). When vibrations were applied in the y axis and oblique vibrations were applied, stripe patterns were generated. Moreover, it was confirmed that circular vibrations generated a mesh-like pattern with a hexagonal shape in the chamber, as shown in Fig. 3 (d).
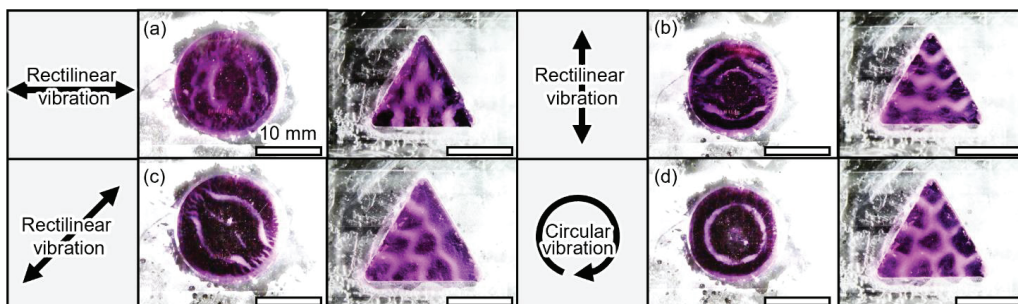

Figure 3 The results of generated patterns in a circular and triangular chamber
(a) x axis (b) y axis (c) oblique (d) circular vibrations

Conclusion

In this study, we propose a system for formation of multi-scale cell patterns from ≈100 μm to ≈10 mm sizes. We succeeded in generating cell patterns of ≈10 mm sizes with a Faraday waves generated by applying rectilinear and circular vibrations. It was also confirmed that different patterns were generated depending on vibration direction, vibration frequency, and the shape of the chamber. In the future, we perform generation of ≈10 mm patterns of spheroids by using faraday wave to realize large and complex tissues.

References

[1] A. S. Nunes, et al., *Biotechnology and Bioengineering*, 116, 206-226 (2019).
[2] N. Minoshima, T. Hayakawa, *The proceedings of MicroTAS 2019*, 292-293 (2019).

Acoustofluidics 2022
19-21 October 2022
University of Glasgow, Scotland

Size-selective separation and enrichment of nano/microparticles using GHz acoustic streaming

Shen Sihong[1], Shen Xiaotian[1], and Duan Xuexin[1]

[1]School of Precision Instrument and Opto-electronics Engineering, Tianjin University, Tianjin, China
E-mail: xduan@tju.edu.cn, URL: http://www.tjumbios.com/

Introduction

Separation of particles is of great importance in diagnostics, chemical and biological analyses, food and chemical processing and environmental assessment [1]. Trapping and enrichment of biological particles is a fundamental preprocessing step in biomedical and biochemical assays, where enriched samples increase diagnostic and therapeutic efficacy [2]. There is a significant unmet need for methods that can perform fractionation of small volumes of multicomponent mixtures [3]. Microfluidic sorting platforms require smaller sample volume, which has several benefits in terms of reduced cost of reagents, analysis time. The approach of particle separations contains of passive and active methods. In active fields, magnetic [4], acoustic [5,6] and dielectrophoretic [7,8] forces are promising tool to manipulate particles. Acoustic forces are potential in biomedical application due to their biocompatible nature and ease in microfluidic integration. In this study, we demonstrated an acoustofluidic platform for trapping particles of different diameters by a GHz bulk acoustic resonator to fixed locations in microchannel. The acoustofluidic device is capable of separation of 10 μm and 300 nm polystyrene particles. Simultaneously, the concentration of 300 nm particles was achieved. This acousticfluidic shows potential in immunological detection based on multiple particles.

Experimental

In this work, the acoustofluidic platform consisted of two pentagon-shaped solid mounted resonator (SMR) and a straight polydimethylsiloxane(PDMS) microchannel. The resonant frequency of the SMR is 2.45 GHz. The width of microchannel is 150 μm and the height of that is 100 μm to match the resonator. The microchannel was loosely aligned on top of the SMR without plasma bonding. A sample mixture of particles containing 10 μm polystyrene particles (fluorescent red) and 300 nm polystyrene particles (fluorescent green) was added to the inlet with a syringe pump. The 10 μm and 300 nm beads were separately trapped in upstream and downstream resonators respectively which is shown in Figure 1a.
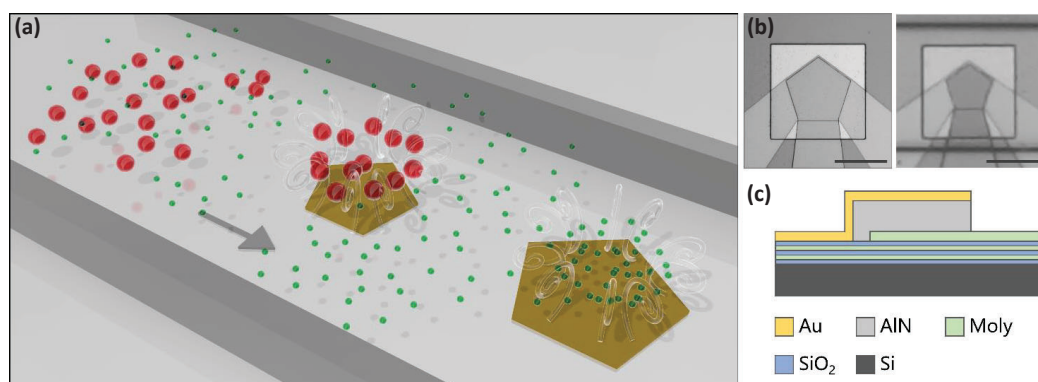

Figure 1: (a) schematic of the separation and concentration of particles using acoustic streaming. (b) pentagon-shaped solid mounted resonator (SMR) of different areas . (c) Structure of SMR. The scale bar is 100 μm.

Results and discussion

In order to separate the two types of particles clearly, the power effect of SMR was investigated. As the power of applied to SMR decreased, the capture capacity of 300 nm particles (green) declined in Figure 2a. When the was power reduced to 50mW, the 300 nm particles (green) were nearly unaffected by the acoustic

streaming and flowed forward. While, at the same power, the SMR can capture the 10 μm particles (red) stably (Figure 2b). 50mW was then chosen as the critical power to separate the two size particles. The capture of smaller particles require stronger acoustic streaming, thus we chose the SMR of larger area which is of better performance to trap 300 nm particles (Figure 1b).

The sample mixture of particles flowed through the microchannel at a stable velocity (0.5 μL/min). When the SMR was actuated, the 10 μm particles (red) were concentrated to the first SMR ($f = 2.45$GHz, power = 50 mW) due to the acoustic vortices, while the 300 nm particles (green) passed free through the first SMR. When the 300 nm particles (green) reaches the second SMR ($f = 2.45$GHz, power = 200 mW), they were trapped in the second acoustic vortices. Figure 2c shows the concentrated particles at specific locations inside the microchannel after washing by deionized water. It is clearly shown that two sized particles were separated and enriched in the desire position. Besides, as the acoustic streaming status can be controlled by the external power, the particles can be released in a controllable way.
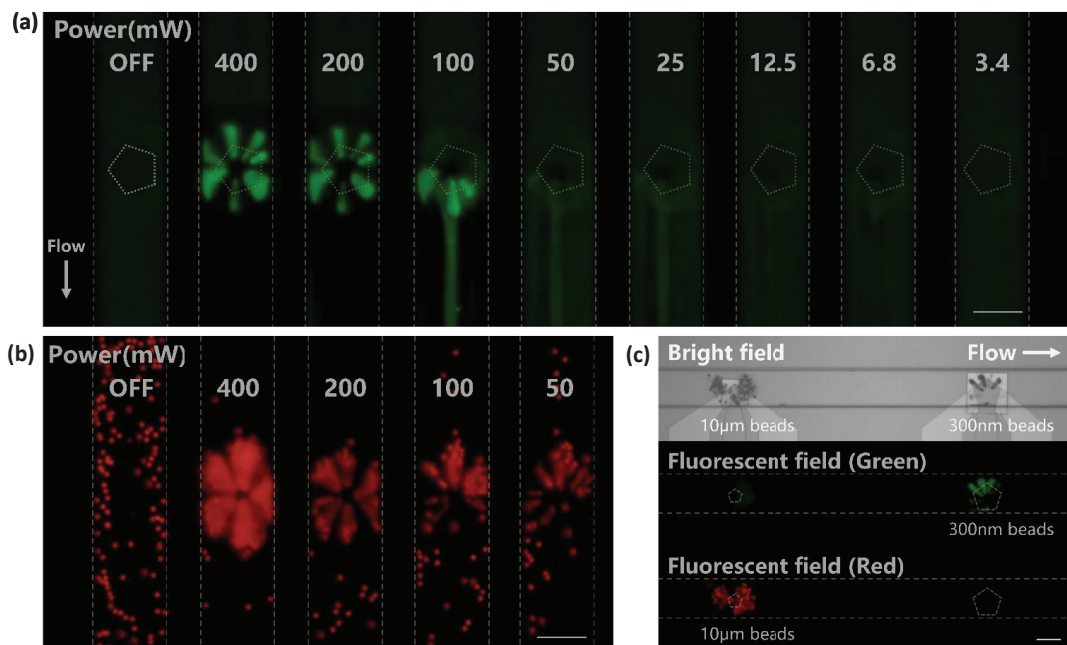

Figure 2: (a) The capture of 300 nm particles (green) at different power of SMR. (b) The capture of 10 μm particles (red) at different power of SMR. (c) Top view of microchannel as the particles were finally trapped at the specific location. The scale bar is 100 μm.

Conclusion

We developed an acoustofluidic approach for selectively trapping, concentrating and separating particles of different size inside a straight microchannel. The platform could work as a powerful tool for many bioanalytical applications, e.g. for multiplexed immuno assay.

References

[1] Sajeesh P, Sen A K. Microfluidics & Nanofluidics, 2014, 17(1):1-52.
[2] Mahnoush Tayebi, Dahou Yang, David J. Collins, and Ye Ai. Nano Letters 2021 21 (16), 6835-6842
[3] Yupan Wu, Rajarshi Chattaraj, Yukun Ren, Hongyuan Jiang, and Daeyeon Lee. Analytical Chemistry 2021 93 (21), 7635-764
[4] Qu, B.-Y.; Wu, Z.-Y.; Fang, F.; Bai, Z.-M.; Yang, D.-Z.; Xu, S.-K. Anal. Bioanal. Chem. 2008, 392 (7), 1317.
[5] Ding, X.; Li, P.; Lin, S.-C. S.; Stratton, Z. S.; Nama, N.; Guo, F.;Slotcavage, D.; Mao, X.; Shi, J.; Costanzo, F.; Huang, T. J. Lab Chip 2013, 13 (18), 3626−3649.
[6] Wu H , Tang Z , You R , et al. Nanotechnology and Precision Engineering, 2022, 5(2):11.
[7] Smith, A. J.; O'Rorke, R. D.; Kale, A.; Rimsa, R.; Tomlinson, M.J.; Kirkham, J.; Davies, A. G.; Wälti, C.; Wood, C. D. Sci. Rep. 2017, 7 (1), 41872.
[8] Shafiee, H.; Sano, M. B.; Henslee, E. A.; Caldwell, J. L. Lab Chip 2010, 10 (4), 438−445.

Acoustic streaming flow induced in-droplet chemical concentration control of picoliter scale droplet

Woohyuk Kim[1], Jinsoo Park[1]

[1]Department of Mechanical Engineering, Chonnam National University, Gwangju, Republic of Korea
E-mail: kwh1129@jnu.ac.kr

Introduction

Microfluidics with droplets composed of two immiscible fluids have been widely utilized for high-throughput screening [1], single-cell analysis [2], and microbiology [3]. Especially, cells and microbes are able to obtain their biological responses such as chemotaxis, inflammation, and proliferation by retaining an interaction with a varying chemical concentration of microenvironment [4,5]. In this respect, chemical concentration control within microscale range becomes essential. The precise and continuous generation of a chemical concentration within batches of microfluidic chips is available as microfluidic could utilize tiny chips. Due to these advantages, techniques to control the chemical concentration within a similar length scale of cells and microbes based on a microfluidic platform have been developed. This development of chemical concentration control method enables a continuous generation of droplets with precisely controlled chemical concentration and also in-droplet chemical concentration. Despite numerous methods to control a chemical concentration are exist, in-droplet chemical concentration control for picoliter scale droplets with high throughput is still limited. Here, we propose an acoustofluidic chemical concentration control method based on acoustic streaming flow.

Experimental

Acoustofluidic chemical concentration control is available by generating surface acoustic wave via interdigital transducer [6]. We utilized a slanted finger interdigital transducer to generate a surface acoustic wave within narrow region. This slanted finger interdigital transducer was placed beneath of microchannel where parallel laminar flows are downstream as shown in Figure 1 (a). This acoustofluidic chip was fabricated through the following process. First, photolithography was conducted to fabricate PR mold with appropriate geometries and soft lithography was continued with 10:1 ratio of base and curing agent of polydimethylsiloxane (PDMS) mixture. This process enables a fabrication of PDMS microchannel chip and we additionally fabricated a thin PDMS membrane and attached with PDMS microfluidic chip to ensure a fabrication of disposable microfluidic chip. The parallel laminar flows are consisted with sheath fluid and sample fluid which are pure DI water and erioglaucine disodium salt solution with 16.11 mM as shown in Figure 1 (b). An acoustic streaming flow is generated within the parallel laminar flow by dissipation of surface acoustic waves induced by slanted finger interdigital transducer. A part of agitated parallel laminar flows fed into a T-junction as a dispersed phase and face with continuous phase with fluorocarbon oil and finally turn into several droplets as shown in Figure 1 (c). A precise control of the droplet chemical concentration control is available by easily fine-tuning an amplitude of electrical signals that actuated on slanted finger interdigital transducer.

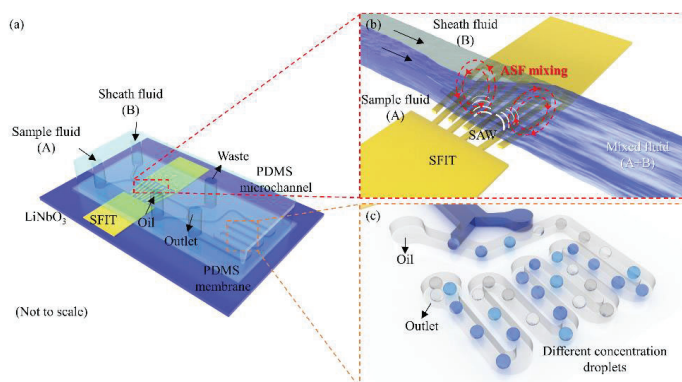**Figure 1:** Schematic diagram of the acoustofluidic chemical concentration control device for in-droplet chemical concentration control. (a) Perspective view of the acoustofluidic device. (b) Agitation of the parallel laminar flow based on acoustic streaming flow induced by surface acoustic waves generated from SFIT. (c) Droplet generation with varying chemical compounds inside of individual droplets.

Results and discussion

Varying amplitude of electrical signals enables a generation of the acoustic streaming flow with varying magnitude. This acoustic streaming flow with varying magnitude could generate a microscale vortex with varying vorticities and this microscale vortex could differently agitate the parallel laminar flow as shown in Figure 2 (a). As a part of the parallel laminar flow was utilized as a dispersed phase at the T-junction, varying magnitude of the electrical signals could determine the chemical concentration of droplet as shown in Figure 2 (b). An investigation of chemical concentration, volume, and throughput was conducted with Image J program with varying conditions of amplitude. As a result, upregulated electrical signal could agitate parallel laminar flow with high intensity so that the chemical concentration of droplets could be increased. Further, generation of multiple droplets with varying chemical concentration was available by easily controlling a sequence of an electrical signals. This fine-tuned modulation of the electrical signals could allow a generation of the controlled flow mixing based on microscale vortical flows where in-droplet chemical concentration control could be ensured.
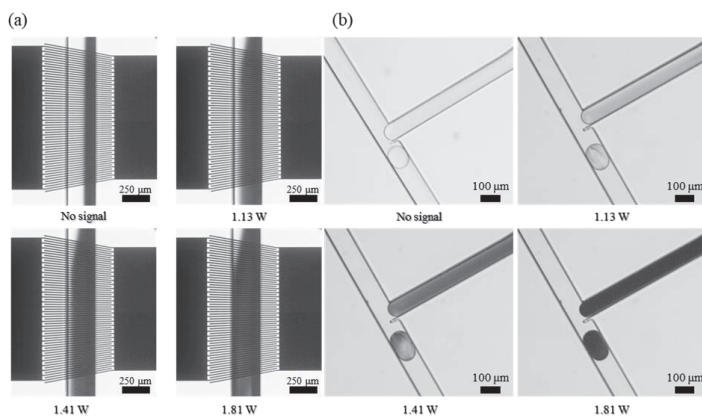

Figure 2: Experimental images of varying chemical concentration (a) Acoustic streaming flow induced flow agitation of parallel laminar flow. (b) Generation of droplets with varying chemical concentration.

Conclusion

We have developed an effective acoustofluidic chemical concentration control method for the on-demand dynamic control of the chemical compounds within the encapsulated droplets.

Acknowledgements

References

[1] D.J. Collins, A. Neilds, A. DeMello, A.-Q, Liu and Y. Ai. Lab on a chip 15, 3439-3459 (2015)
[2] S. Marre and K. F. Jensen Chemical society reviews 58, 145 (2014)
[3] T. S. Kaminski, O. Scheler and P. Garstecki Lab on a chip 16, 2168-2187 (2016)
[4] T. M Keenan and A. Folch Lab on a chip 8, 34-57 (2008)
[5] A. Karbalaei and H. J. Cho. Micromachines 9, 149 (2018)
[6] J. Park, J. H. Jung, K. Park, G. Destgeer, H. Ahmed, R. Ahmad and H. J. Sung. Lab on a chip 18, 422-432 (2018)

Rapid droplet mixing using stereo acoustofluidic vortices

Xiaotian Shen[1], Tiechuan Li[1], and Xuexin Duan[1]

[1]State Key Laboratory of Precision Measuring Technology & Instruments and College of Precision Instrument and Opto-electronics Engineering, Tianjin University, Tianjin, China
E-mail: xduan@tju.edu.cn, URL: http://www.tjumbios.com/

Introduction
High-throughput droplet microfluidics has demonstrated significant advantages for performing bioassays and chemical synthesis. However, due to low Reynolds numbers, the mixing of droplets is hindered by laminar flow conditions[1]. Even though there is an internal circulation flow in droplets, the flow is slow and only within half of their respective ranges. Free diffusion at the solution interface is inefficient and time-consuming. Therefore, a method is needed to promote heat and mass transfer inside the droplets. In this work, we developed a new approach for rapid droplet mixing using stereo micro-vortices induced by GHz bulk acoustic waves[2]. Efficient mixing (Mixing Index, MI>0.9) within milliseconds (<6ms) at high throughput (~7000/min) was achieved.

References
[1] Xia, Y.et al. In Situ Microreaction Platform Based on Acoustic Droplet Manipulation for Ultra-High-Precision Multiplex Bioassay. *Anal. Chem*. 94, 6347–6354 (2022).
[2] Yang, Y. et al. Self-adaptive virtual microchannel for continuous enrichment and separation of nanoparticles. *Sci. Adv.* 8440, (2022).

The analytical study of cell counting device based of Focused Surface Acoustic Wave

Yingqi Jiang[1], Weipeng Xuan[1,*]

[1]Ministry of Education Key Lab. of RF Circuits and Systems, College of Electronics & Information, Hangzhou Dianzi University, Hangzhou310018, China
*Corresponding author, E-mail: xuanweipeng@hdu.edu.cn

Introduction

Surface acoustic sensors have been widely used in biosensing because of their reliability and high sensitivity [1,2]. Biosensing applications typically require the detection and measurement of biomarkers in fluid media. The fully coupled 3D model structure of complex IDT, such as F-IDT (Focused-IDT) is helpful to study of particles sensing in the microfluidic channel, while minimizing the impact of flow force on the sensing layer, thus improving the sensitivity.

In this work, a 3D model was established to study and analyze F-SAW devices' particle sensing performance, which can be used for cell counting. The effects of the focused surface acoustic wave device on the particles sensing were analyzed by using the 3D fluid-structure interaction model. Time domain analysis was used to study the signal amplitude change dependent on the particle size.

The device design

The fluid-structure coupling model of piezoelectric device and fluid contact requires the combination of piezoelectric constitutive equation and fluid dynamics equation. A system of four coupled wave equations for the electric potential and the three components of displacement in piezoelectric materials are solved for the piezoelectric substrate [3]

$$-\rho \frac{\partial^2 u_i}{\partial t^2} + c_{ijkl}^E \frac{\partial^2 u_k}{\partial x_j \partial x_l} + e_{kij} \frac{\partial^2 \phi}{\partial x_k \partial x_j} = 0, \tag{1}$$

$$e_{ikl} \frac{\partial^2 u_k}{\partial x_i \partial x_l} - \varepsilon_{ik}^s \frac{\partial^2 \phi}{\partial x_i \partial x_k} = 0, \tag{2}$$

c, e and ε represent structural elasticity matrix at constant electric field, piezoelectric stress matrix, and dielectric matrix at constant mechanical strain, respectively, and denotes the electric potential. The fluid domain is modeled as followed:

$$\rho(\frac{\partial v_f}{\partial t}) + v_f \cdot \nabla v_f + \nabla P - 2\eta \nabla \cdot D = 0, \tag{3}$$

where v_f, P, ρ and η denote the fluid velocity, pressure, density, viscosity, respectively. D is the rate of deformation tensor.

Results and discussion

We conducted structural simulations of various F-IDT configurations with varying degrees of arc (D), focal length (F), and wavelength (A) to determine the optimal F-IDT configuration to enhance the acoustic wave intensity [4]. The displacement amplitude of the device is analyzed, and it is found that the device with period/wavelength of 40 um, focal length of 60 um and arc degree (D) of 120°is the best design.

Rayleigh wave was stimulated by LiNbO3 substrate and the wave energy distribution was shown in Figure 1, the wave decays as the distance of the input IDT increases. This mode shift eventually creates a pressure gradient in the direction in which waves travel through the fluid, resulting in an acoustic flow. Compared with traditional surface acoustic wave (SAW) devices, the acoustic wave energy of F-SAW devices enhances the acoustic flow, making F-SAW devices more suitable for microfluidic applications. In the current configuration, due to the focusing of acoustic energy in the F-SAW device, the displacement in the central of the device generated in the substrate is the highest as shown in Figure 2, which is preferable for particle sensing.
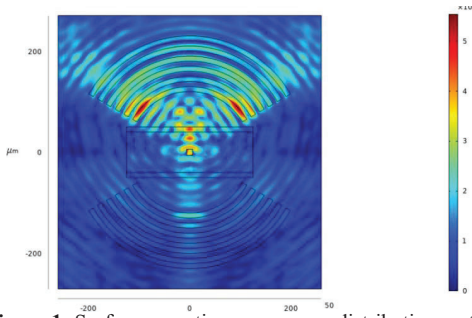
Figure 1: Surface acoustic wave energy distribution on the surface of the designed device.

Figure 2: Wave direction displacement of device surface.

Based on the above model, As shown in Figure 3, the output signal received by the output end of the IDT is obtained by setting 8-micron particles into the channel (amplified by 103). Figure 4 is the energy diagram of the interface under the same situation of the cross section, from which it can be observed that the energy is focused on the center of the device. Then, the output of different micro particles was compared to obtain the change of output signal voltage at the output end as shown in Figure 5. It can be seen that the influence received also increases with the increase of particles.
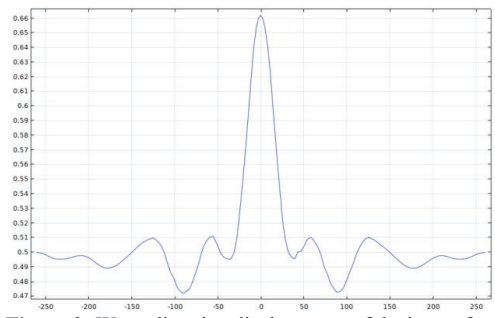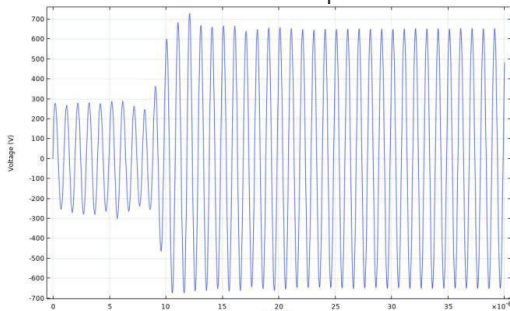

Figure 3: The voltage output signal received by the particle at the receiving end through the micro channel.
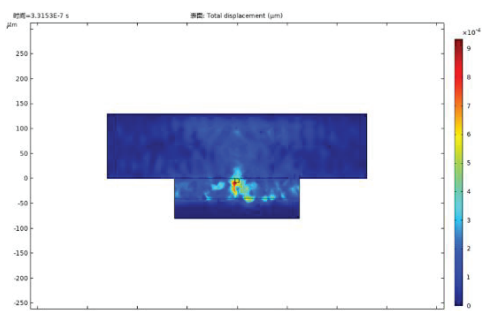
Figure 4: The energy of the cross section is concentrated at the center.
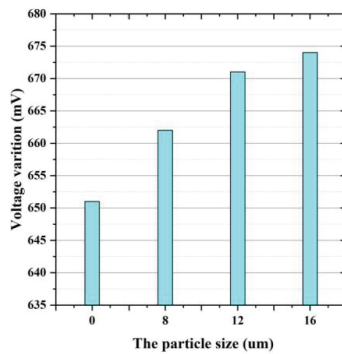
Figure 5: Contrast diagram of voltage output for different particle sizes.

Conclusion

We have built a 3D model for F-SAW devices to study the acoustic flow field. F-SAW devices have strong effects and different characteristics in the field of acoustic flow-induced particles. The results of this study have a great significance for other microfluidic actuation applications of SAW devices.

References

[1] F. Josse, F. Bender, and R. W. Cernosek, Anal. Chem. 73, 5937 (2001).
[2] Z. Li, Y. Jones, J. Hossenlopp, R. Cernosek, and F. Josse, Anal. Chem. 77,4595 (2005).
[3] D. S. Ballantine, S. J. Martin, A. J. Ricco, G. C. Frye, R. M.White,and E.T. Zellers, Acoustic Wave Sensors: Theory, Design, and Physico-Chemical Applications(Academic, San Diego, 1997).
[4] J. Donea, S. Giuliani, and J. P. Halleux, Comput. Methods Appl. Mech.Eng. 33, 689(1982).

Study of the acoustothermal heating inside a liquid droplet using IR thermography

Etien Martinez Roman[1], Diego Sánchez Saldaña[1], Maria Fernandino[1] and Carlos A. Dorao[1]

[1]Department of Energy and Process Engineering, Norwegian University of Science and Technology, Trondheim, Norway
E-mail: etien.martinez@ntnu.no,

Introduction

Surface acoustic waves (SAWs) based devices for particle manipulation have attracted vast research due to its dual advantage of acting on both the liquid and the particles in the liquid. The surface acoustic waves can be generated using a piezoelectric material which converts an external electric potential to mechanical deformation and vice versa. By switching the polarity of the applied electric potential, the piezoelectric material can be expanded and contracted along one axis with amplitudes in the order of the nanometers and with frequencies ranging from a few Hz to GHz which in turn generates acoustic waves. When the plane surface wave meets a bulk liquid in contact with the substrate, the wave will refract into the liquid inducing a longitudinal wave that generates fluctuations in density, pressure and velocity fields. Due to non-linearities, there is a non-zero time-averaged force at second order applied at the interface between two media with different acoustic properties, called acoustic radiation force or ARF. This force enables the manipulation of particles with sound intensities of less than 10Wcm^{-2} on the target agents which makes it safe for sensitive label-free handling of biological organisms such as embryos and cells. In parallel, the attenuation of an acoustic wave leads to the transfer of pseudo-momentum from the wave to the fluid inducing a flow called acoustic streaming. This flow streaming enables the manipulation of the flow and therefore indirect manipulation of particles. An important drawback for temperature sensitive samples is that the dissipation of the acoustic energy can leads to a significant increase of the temperature of the substrate, local structures like the wall of the microchannels and the liquid [1]. At the same time, the control of the rapid induced heating can be of value for diverse micro-fluidics-based applications such as nucleic acid amplification and cell lysis where localized heating is needed.

Assuming the case of a droplet placed on the wave path of a traveling SAW generated by an interdigitated transducer (IDTs) deposited on a piezoelectric substrate, three dominant heat transfer processes can be observed. First, the IDT can be considered a Joule heater when an alternating current flows through the metal of the IDT. The induced surface wave results into alternating voltage that polarizes the piezoelectric substrate and thus inducing a displacement current. Then, the polarization relaxation leads to dissipated heat. Then, the longitudinal waves inside the liquid attenuate rapidly in a short distance leading to another heat source in this case inside the droplet. The interplay of the velocity and temperature fields have attracted substantial research particularly using numerical and analytical methods. However, experimental studies have been rather limited due to the challenges related to the small spatial and temporal scales involved. For instance, in [2] is presented a study of the temperature field of a droplet by using a SAW-based microfluidic heater. The experimental study consisted in visualizing the temperature of the substrate around the droplet and on temperature of surface of the droplet when observed from the bottom of the droplet using an IR thermography. In this work, the temperature field at the base of the droplet deposited on the piezoelectric substrate is studied using infrared thermography by observing the droplet from below. The heating process induced by the SAW is investigated on two types of interdigital transducer namely a straight and spiral interdigitated transducer. These two different IDT designs impose different thermal boundary conditions to the droplet while inducing a different internal flow motion inside the droplet.

Material and Methods

Two SAW devices have been designed and fabricated for the study namely a straight and spiral IDTs operating in a frequency range between 20 MHz and 160 MHz and in a power range between 300 and 900 mW. The transducers were fabricated using a piezoelectric substrate (128 YX LiNbO3) via maskless aligner MLA lithography and e-beam metal evaporation. The device is driven by BELEKTRONIG SAW generator BSG. The experiments consist in depositing a DI-water droplet of about 2 microliters on substrate near the IDT and then observed the heating process when the SAW is turned on using an IR FLIR X6803sc camera with a 4x microscope lens for a spatial resolution of 3.7micron/pixel and acquiring the images at 200fps. The IR camera

was operated using the software FLIR ResearchIR Max Version 4.40.11.35. The position of the droplet in the substrate was determined by an additional camara mounted on the top of the droplet. The images from both cameras were combined using a mapping algorithm using the Matlab Image Processing toolkit.

Results and discussion

Figure 1 shows two examples of the study depicting the visualization of the temperature field at the bottom of the droplet during the heating process induced by the SAW corresponding to the straight and spiral IDT design. The case corresponds to a power applied of 130 mW and operating at a frequency of 120 MHz for the straight IDT and 449 mW and 30 MHz for the spiral one. After the SAW is turned appears a fast transient process which is before the final steady state is reached. Finally, a steady state condition of the temperature field was achieved which remained almost unchanged during the evaporation phase of the droplet. We find the same qualitative patterns, in each type of IDT, for most of the values of frequency and power analyzed as well as for different positions of the droplet. For the spiral IDT we observed that the heat source is located around the center of the droplet but mainly shifted in opposite direction of the IDT terminals. Once the steady state dominates, the heat source is always located in a region close to these terminals where there is an asymmetry in the design of the finger's distribution. For the straight IDT, the transient state shows a heterogenous temperature field surrounding the droplet, where the heat source is located around its center, being more intense in the region closer to the IDT. In the steady state, the heat source is mainly focalized in this region, being the heat transmission more non-uniform than for the same configuration in the spiral IDT. Adittionaly, we placed the droplet directly on the fingers with no detectable contribution to the heat diffusion pattern already described.
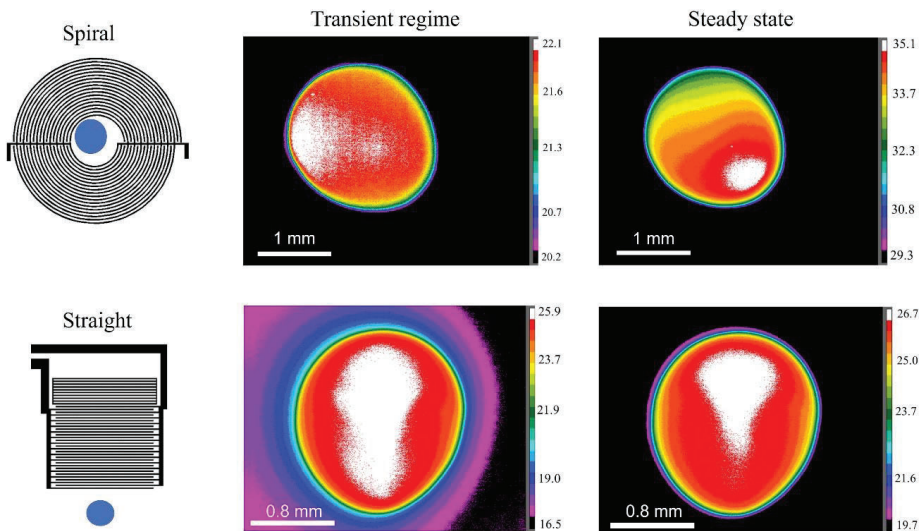
Figure 1: Temporal evolution for the temperature field in a droplet under the action of a SAW generated by two types of IDTs. A sketch of these devices is presented in the left column, where a blue circle indicates a characteristic droplet. In the middle and right columns appears color map indicating the temperature field in ^{0}C for the initial (transient) and intermediate and final (steady) stages of the droplet lifetime before evaporates. The frequencies and powers in these cases are 130 mW and 120MHz for the straight IDT and 449 mW and 30MHz for the spiral configuration.

References
[1] Luong, T. D., Phan, V. N., and Nguyen, N. T. *Microfluidics and nanofluidics*, *10*(3), 619-625 (2011)
[2] Li, L., Wu, E., Jia, K., and Yang, K. *Lab on a Chip*, *21*(16), 3184-3194 (2021)

Nonlinear large deformation of a spherical red blood cell induced by ultrasonic standing wave

Fengxian Xin[1,2], and Yifan Liu[1,2]

[1]State Key Laboratory for Strength and Vibration of Mechanical Structures, Xi'an Jiaotong University, Xi'an 710049, P.R. China
[2]MOE Key Laboratory for Multifunctional Materials and Structures, Xi'an Jiaotong University, Xi'an 710049, P.R. China
E-mail: fxxin@mail.xjtu.edu.cn

ABSTRACT

A computational model is developed to investigate the nonlinear static deformation of a spherical (osmotically swollen) red blood cell (RBC) induced by ultrasonic standing wave. The ultrasonic standing wave can generate steady acoustic radiation stress to deform the cell, and in turn the deformed cell reshapes the acoustic field. This is a real-time coupling problem between the acoustic field and the mechanical field. In the computational model, the acoustic radiation stress acting on the RBC membrane is modeled by adopting the nonviscous momentum flux theory. The RBC membrane is modeled as a hyperelastic shell considering the in-plane elasticity, bending elasticity and surface tension of the membrane. The volume conservation constraint of the membrane sealing fluid is applied to ensure the osmotic balance of the membrane. To address this real-time coupling problem, the computational model is implemented by a finite element method (FEM) algorithm. The numerical results are compared with the existing theoretical model and experimental data, and the strain hardening trend of the experimental data is successfully predicted, which verifies the accuracy and effectiveness of the computational model. The computational model can accurately extract the mechanical properties of cells from acoustic deformation experiments, which is helpful for the diagnosis of some human diseases.

Keywords: Nonlinear acoustic deformation, red blood cell, ultrasonic standing wave, acoustic radiation stress, microfluidics

Abstracts - Poster Session II

Micromixer Based on GHz Bulk Acoustic Wave for Controllable Liposome Synthesis

Huihui Xu[1], Chen Wu[1], Zhaoxun Wang[1] and Xuexin Duan[1]

[1]State Key Laboratory of Precision Measurement Technology and Instruments, School of Precision Instruments and Opto-Electronics Engineering, Tianjin University, NO.92 Weijin Road, Tianjin 300072, China
E-mail: xduan@tju.edu.cn, URL: http://www.tjumbios.com/

Introduction

Liposome is essentially a small artificial cell, which has been largely applied for bioimaging,[1] biochemical analyzing[2] and drug delivery carrier[3] due to their attractive physicochemical properties. However, there are still some challenges of conventional bulk synthesis methods to reach the requirements of clinic translation because the products usually undesirable quality due to the lacks of precise control of reaction process and low automation of operation.[4] Acoustofluidics have been reported for liposome synthesis and modification due to their mechanical induced mixing and manipulations [5][6]. In this study, we propose a novel micromixer that can directly drive the fluid flow to form acoustic streaming and generate controlled convection in microchannel without any assistant of most of microbubbles or microstructures. The mechanism is based on the short dissipation distance of the ultra-high frequency bulk acoustic waves at liquid-solid interface.[7] For the proof of this platform, the feasibility of controllable synthesis of liposome was implemented. It is worth noting that the proposed platform can control the size distribution of the products only by adjusting the drive power while keeping the flow velocity of the multiphase solutions constant, which is rarely achieved by existing nanoparticle synthesis platforms.

References

[1] Dong, S.,Teo, J. D. W.,Chan, L. Y.,Lee, C.-L. K. and Sou, K. ACS Applied Nano Materials **1**, 1009–1013 (2018).
[2] Zhao, Y.,Du, D. and Lin, Y. Biosensors and Bioelectronics **72**, 348–354 (2015).
[3] Li, Y. *et al.* Nanomedicine: Nanotechnology, Biology and Medicine **13**, 371–381 (2017).
[4] Ma, J.,Lee, S. M.-Y.,Yi, C. and Li, C.-W. Lab on a Chip **17**, 209–226 (2017).
[5] Huang, P. *et al.* Advanced Science **6**, 1900913 (2019).
[6] Rasouli, M. R. and Tabrizian, M. Lab on a Chip **19**, 3316–3325 (2019).
[7] Lu, Y. *et al.* Angewandte Chemie - International Edition **58**, 159–163 (2019).

A manipulation system for phase-controllable acoustofluidic manipulations of microparticles

Hayato Yamaki, Natsumi Hirata and Takeshi Hayakawa

Department of Precision engineering, Chuo University, Tokyo, Japan
hayaka-t@mech.chuo-u.ac.jp

Introduction

Analysis of microparticles is strongly demanded for early detection of diseases and regenerative medicine. In order to analyze microparticles, manipulation techniques are highly required to manipulate micro- and nanoparticles such as CTCs or red blood cells in a high throughput and non-contact manner [1]. Acoustofluidics has been promising tool because of its biocompatibility, simple system and high throughput characteristics. However, acoustic field in a microchannel can be disturbed due to the scattering of acoustic waves and variation of environments such as temperature of a microchannel [2]. These disturbances of acoustic vibration can decrease efficiency and stability of acoustofluidic manipulations and make practical or clinical uses difficult. In this study, we propose a method for stable and phase-controllable acoustofluidic manipulations. We designed a device by considering a propagation efficiency of acoustic waves to stabilize the acoustic vibration. As a result, we succeeded in switching the uniaxial and circular patten of acoustic streaming by adjusting the phase difference of the acoustic vibrations.

Method

Figure 1 (a) shows an experimental setup for stable and phase-controllable manipulation of microparticles. Two piezoelectric transducers (PZT) are attached to a glass-silicon microfluidic chip with orthogonal direction to each other. Acoustic streaming around the micropillar is generated by propagating acoustic waves into the microchannel [3]. In addition, we can switch the flow pattens by adjusting the phase difference between the vibrations of PZTs. when the phase difference of acoustic waves: $\varphi = 0°$, uniaxial flow tilted $45°$ is generated, as shown in Fig. 1 (b-1). On the other hand, circular flow pattern is generated at $\varphi = 90°$, as shown in Fig. 1 (b-2). Thus, we can switch the manipulations such as concentration and trapping in a microfluidic chip by changing the phase difference of acoustic vibrations.

To increase stability and propagation efficiency of acoustic waves, a wedge-shaped metal jig is inserted between the transducer to the microfluidic chip. Acoustic vibrations of the transducer can directly propagate into the microchannel by considering an incident angle of acoustic waves and speed of sound in materials [4]. In addition, to uniformly propagate acoustic waves into the microfluidic chip, it is important to increase the transmittance and reduce the reflectance of acoustic waves in the materials. The transmittance of acoustic
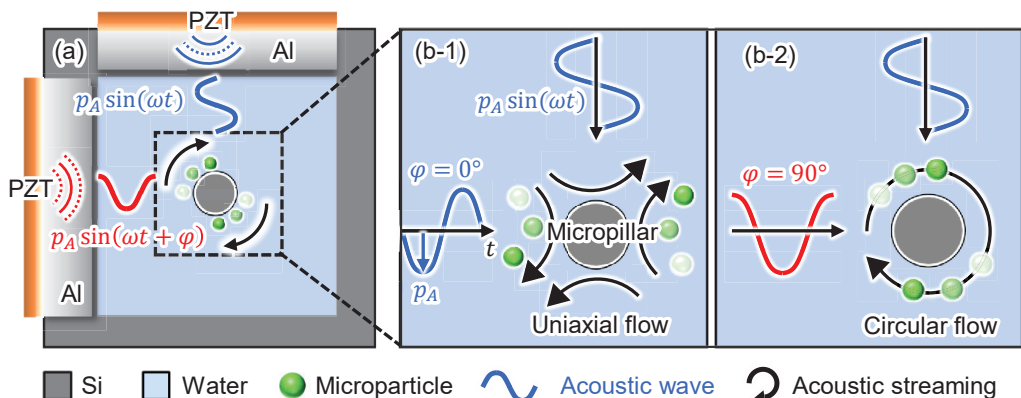

Figure 1: A microfluidic device which has two piezoelectric transducers (PZT) to switch manipulations.
(a) Concept of switching manipulations by applying acoustic waves in water.
(b-1) Uniaxial flow, (b-2) Circular flow

waves become higher as acoustic impedances of each other materials, in this case glass and wedge-shaped metal jig, are closer. Thus, we chose aluminum as the material of the jig because it has an acoustic impedance close to PZT and glass. Moreover, the center length of jig in vibration direction is designed to correspond to the integral multiple of half wavelength of acoustic waves.

Experiment

In this study, we observed acoustic streaming around the micropillar. A glass-silicon-glass chip was fabricated by using anodic bonding and deep-RIE technique. First, we bonded a silicon chip to a glass substrate. Then, microchannels were fabricated on the silicon chip by using deep-RIE. After that, a glass cover with inlet/outlet holes was bonded to the glass-silicon chip by using anodic bonding. Wedge-shaped aluminum jigs were machined by using a CNC milling machine. Moreover, the length of microchamber is determined by the speed of sound in water and a driving frequency. Therefore, the width of microchamber is designed to 507 μm which corresponds to one wavelength of the acoustic waves of 3.0 MHz.

Two wedge-shaped jigs glued with PZTs were glued to the glass-silicon-glass chip with orthogonal directions, as shown in Fig. 2 (a). We used microparticles with a diameter of 1 μm and microscopy to visualize an acoustic streaming around the micropillar in the microchamber.

Results

Figures 2 (b) show the streamline of the acoustic streaming when various acoustic vibrations were applied to the chip. Figure 2 (b-1) shows x-axis vibration, Fig. 2 (b-2) shows y-axis vibration, Fig. 2 (b-3) shows xy axis vibration at $\varphi = 0°$, and Fig. 2 (b-4) shows xy axis at $\varphi = 90°$, respectively. Similarly, Figs. 2 (c) show vector fields acquired by performing PIV analysis for results of Figs. 2 (b). The applied frequency was 3.446 MHz and voltage was 15 V. Rectilinear vibrations were generated when x or y vibration was applied, as shown in Fig.2 (b-1), (b-2), (c-1) and (c-2). However, directions of these flows are opposite as shown in Fig. 2 (c-1) and (c-2). When x and y vibrations at $\varphi = 0°$ are applied (Fig. 2 (b-3)), flow pattern became also uniaxial but the direction is tilted $45°$ compared to the uniaxial vibrations. This result indicates two vibrations were superimposed each other. Similarly, we succeeded in generating circular flow around the micropillar at by applying x and y vibrations at $\varphi = 90°$, as shown in Fig. 2 (b-4) and (c-4).
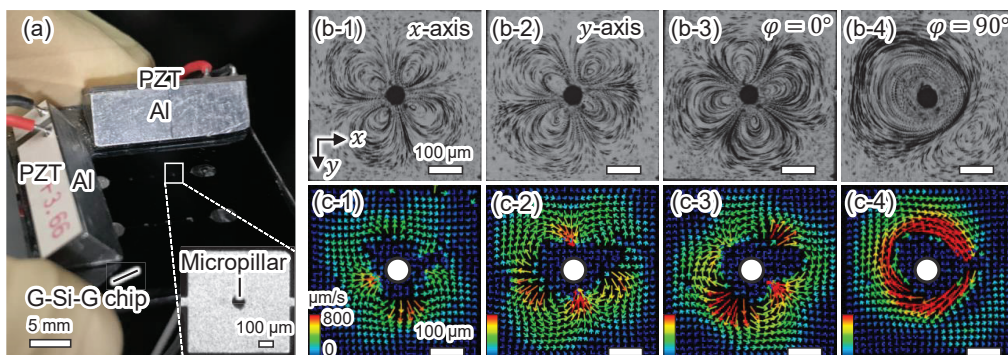

Figure 2: Experimental device and results. (a) Glass-silicon-glass chip with two wedge-shaped jigs.
(b) Results of streamlines of acoustic streaming around micropillar.
(c) Results of the flow velocities analyzed by using PIV.

Conclusions

We constructed the micromanipulation system for phase-controllable acoustofluidic system. We succeeded in generating circular flow and switching the flow patterns of acoustic streaming by adjusting the phase difference of the acoustic vibrations. In the future works, we investigate a repeatability and accuracy of the switching manipulations. Furthermore, we evaluate a relationship between acoustic streaming and an acoustic field in a microchamber by using an observation system which is combined microscopy with schlieren method.

Acknowledgement

References

[1] Thomas Laurell *et al.*, *Chem. Soc. Rev.*, 2007, **36**, 492– 506.
[2] Per Augustsson, Rune Barnkob, Steven T. Wereley, Henrik Bruus and Thomas Laurell, Lab Chip, 2011, **11**, 4152-4164.
[3] S. S. Sadhal, Lab Chip, 2012, **12**, 2292-2300
[4] Iranmanesh *et al.*, 2013 J. Micromech. Microeng. **23** 105002.
[5] M. Greenspan, and C. E. Tschiegg, Journal of Rese arch of the National Bureau of Standards **59** (4), (1957)

Piezoelectric micromachined ultrasound transducers (PMUTs) for acoustic positioning of suspended microtissues

<u>Emilie Vuille-dit-Bille</u>[1,2], Dara Zaman Bayat[1], Marc-Alexandre Dubois[1], Thomas Overstolz[1], Sarah Heub[1], Michel Despont[1], Mahmut Selman Sakar[2] and Gilles Weder[1]

[1] CSEM SA, Neuchâtel, Switzerland
 e-mail: emilie.vuille-dit-bille@csem.ch
[2] Institute of Mechanical Engineering, EPFL, Lausanne, Switzerland.

Introduction

Three-dimensional (3D) microscale *in vitro* culture models (microtissues) have become conventional drug development and regenerative medicine platforms. The physical manipulation of microtissues is instrumental throughout the whole microtissue use cycle. Existing techniques for handling are based on manual pipetting, which has limited precision and is time consuming. To unlock the full potential of microtissue technology, there is a pressing need to develop effective tools for controlled manipulation and positioning of such large and heterogenous biological entities, which we aim to address using acoustic manipulation. In this study, sound pressure fields generated by elastic membranes, which are actuated by piezoelectric thin-film transducers, are studied numerically. Strong trapping regions are formed 500 μm above the membranes and are shown to trap 200 μm microtissues. High trapping strength is achieved by mechanical decoupling between the membranes and the substrate.

Acoustic manipulation of microtissues

Acoustophoresis has been recently proposed as a label-free and biocompatible technique to manipulate and position microtissues. [1-2] Acoustophoresis uses non-contact forces arising from sound pressure fields to control the motion and the position of objects suspended in a fluid. In most techniques, acoustic standing waves are produced, creating pressure nodes toward which biological samples are pulled and trapped. Typically, acoustic waves are generated by bulk transducers made of lead zirconate titanate or interdigital transducers made of lithium niobate. In this study, we propose an innovative acoustic platform that leverages the power of piezoelectric micromachined ultrasound transducers (PMUT) to position suspended microtissues in 3D space. PMUTs are widely used in acoustic imaging and sensing, but only a few studies used them in acoustofluidic [3].
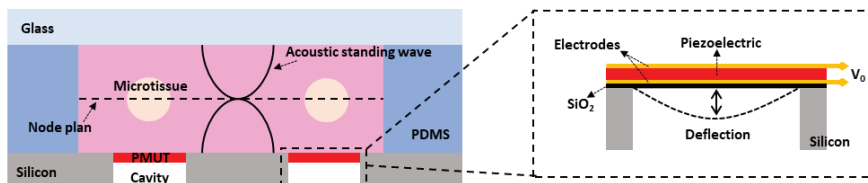

Figure 1: Schematic view showing the acoustofluidic positioning device.

PMUT-based acoustofluidic platform

A PMUT is a membrane composed of a passive elastic layer, usually silicon, and a piezoelectric layer such as aluminum nitride. PMUTs allow the miniaturization of high-resolution ultrasonic transducer arrays while offering good acoustic matching. The flexural vibrations of the membrane, which are caused by lateral strains generated from the piezoelectric effect, produce the acoustic waves. The resonance frequency of PMUTs depends on several parameters, including the density, flexural rigidity, and geometry of the membrane, therefore offering a large design space.

We envision a platform composed of a silicon chip containing an array of PMUTs with on top an acoustofluidic chamber with PDMS walls and a glass lid. A schematic of the platform is depicted in Fig. 1. The glass lid reflects the acoustic waves generated by the transducers and creates vertical standing waves in the chamber. PDMS has a very high transmission factor; therefore, the acoustic waves are expected to travel outside the chamber. This way, we can reduce the interference pattern's complexity and produce standing waves uniquely along the thickness direction. The height of the chamber was designed considering the resonance frequency of

the PMUTs to generate acoustic nodes in the middle of the chamber. This configuration would levitate the microtissues into the same plane and arrange them in an array defined by the sound pressure profile generated by a specific PMUT array design.

Numerical study

The platform's performance was numerically studied using a commercial FEM software (COMSOL Multiphysics). The chamber walls were set as perfect matching layers and the lid was considered a hard wall boundary to capture the behavior of PDMS and glass, respectively. The 1 mm diameter PMUTs consist of an elastic silicon membrane (80 μm thickness) and a piezoelectric actuator in aluminum nitride (1 μm thickness). Fig. 4A shows Gor'kov minima that form 500 μm above the PMUTs. These regions serve as strong acoustic traps for microtissues. The pitch between the PMUTs was found to strongly influence the intensity and the location of the potential minima. For example, by increasing the pitch from 1250 μm to 1500 μm, we could double the number of minima from two to four. The potential gradient along the vertical direction also increased, strengthening the trap. Figure 4A also shows that the transducers on the edges are less efficient in generating potential minima; thereby, particles might not be captured in this area. This effect is hypothesized to arise from the asymmetric environment of the edge transducers, which have only one neighbor, influencing the interference pattern. The impact of the edge effect can be minimized by optimizing the platform's design to generate a high potential gradient (e.g., with a 1500 μm pitch). These results show that the interference pattern of the acoustic waves is highly sensitive to small variations in the platform's design. Consequently, optimizing the design using FEM software is an important and cost-effective step in developing the platform. Current simulations indicate that the most promising layout possesses a pitch of 1500 μm.

Additionally, the simulations have shown that acoustic forces required for the levitation of 200 μm diameter microtissues could be generated by making trenches around the PMUTs. The trenches mechanically decouple the edges of the PMUTs from the silicon substrate, resulting in larger deflection than clamped membranes (Fig. 4B). Acoustic pressure is proportional to the deflection. Thus, the mechanical decoupling of the membranes also increases the strength of the acoustic traps. In the simulation, the trenches' effect was modeled by anchoring the membrane (fixed constraint condition) from a ring at its bottom, while the anchorage is made from the sides for a clamped membrane. The acoustic force was calculated based on the Gor'kov theory. For microtissues of 200 μm diameter, the z component of the maximal acoustic force, $F_{ac,z}$=35 nN, is about 9x larger than the sum of gravitation and Archimedes force, F_g=4 nN, showing the potential of the platform to levitate big particles in acoustic traps.
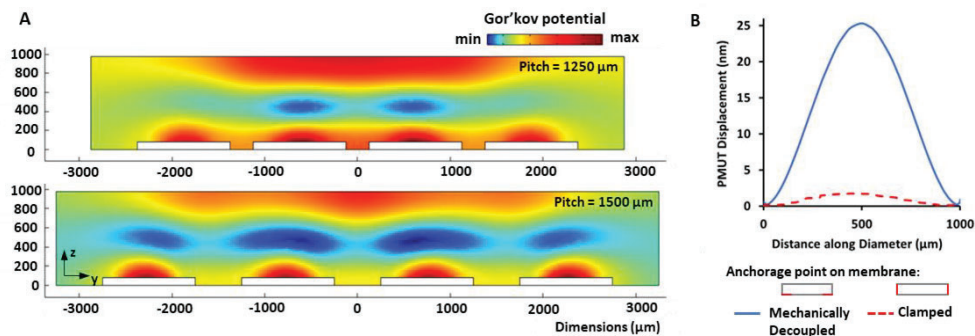

Figure 2: A) Gor'kov potential generated by 4 PMUTs at f_{res}= 777 kHz and V = 50 V with two different pitches. Color indicates the intensity of the potential. **B)** Deformation along the diameter of the membrane for clamped and mechanically decoupled PMUTs excited in the fundamental vibrational mode. A schematic of the anchorage is depicted for a clamped and mechanically decoupled membrane.

Conclusion

The numerical assessment of the platform showed that sufficient acoustic power is generated to levitate 200 μm diameter microtissues. The generation of high acoustic power in a minimally invasive fashion makes this technology a promising candidate for controlled positioning and manipulation of microtissues. Particularly, the technique would find applications in end-point analysis such as micro-histology, in which positioning several microtissues on the same plane is critical. Transducers are currently in fabrication and will be characterized. Additionally, the platform's accuracy and speed of positioning will be tested with microtissues of different sizes.

References

[1] H. Cai, Z. Wu, Z. Ao, A. Nunez, B. Chen, L. Jiang, M. Bondesson and F. Guo, Biofabrication **12**, 035025, (2020).
[2] P. Chen, S. Güven, O. B. Usta, M. L. Yarmush and U. Demirci, Adv. Healthc. Mater. **4**, 1937–1943, (2015).
[3] C. Y. Cheng, A. Dangi, L. Ren, S. Tiwari, R. R. Benoit, Y. Qiu, H. S. Lay, S. Agrawal, R. Pratap, S.-R. Kothapalli T. E. Mallouk, S. Cochran and S. Trolier-Mckinstry, IEEE Trans. Ultrason. Ferroelectr. Freq. Control **66**, 1606–1615, (2019).

Added Mass Controls: the Separation, Alignment and Intensity of Nodes in Acoustofluidic Capillary Bridges

Jeremy J Hawkes[1], Sadaf Maramizonouz[2,3], Mohammad Rahmati[2], Yong-Qing Fu[2], Stephen J. Wilkinson[4]

[1]Acoustic machines Ltd., Liverpool, L25 4TQ, UK. E-mail: JeremyJHawkes@AcousticMachines.co.uk
[2] Faculty of Engineering and Environment, Northumbria University, Newcastle upon Tyne NE1 8ST, UK
[3] School of Engineering, Newcastle University, Newcastle upon Tyne, NE1 7RU
[4] Chemical engineering Department, University of Chester, Thornton Science Park, Pool Ln, Chester CH2 4NU

Introduction When a channel width is less than the node-to-node separation only a single node will form in the channel.

In the 1990's the first single-node-channels were produced using only symmetric (compression) wave modes in the structural (solid) elements of the channel. These channels had, ½ an acoustic wavelength (λ) in the liquid with pressure anti-nodes at the walls and a pressure node along the centre[1-2]. Sound travelled on a linear path from the PZT passing through, transmission/coupling layers, the liquid and reflector to an outer air interface. The resonance spanned all the layers. ½ λ was used for transmission layers and ¼ λ for reflectors[3] or for more precision a one dimensional model was employed to increase the force on the particles by optimizing the channels for maximum resonance quality [4]. Particle focusing was efficient however when miniaturized these channels were difficult to use because particles had to be observed in the flow downstream from the sound field.

In most channels today antisymmetric (plate or SAW) wave modes propagate in a solid drive-plate structure. The system is popular because particles are observed directly in the sound field and some operate over a broad range of frequencies, however since sound is generally not transferred along a linear path there are no analytical methods for increasing the force on the particles. It has been reported on many occasions that the liquid is not a ½ λ wide[5-7]. None-the-less the term half-wavelength-channel is sometimes still used for single-node-channels.

Figure 1: Demonstrating that waves in the water radiate from antinodes in σ_y. Simulations of the X and Y components of acceleration in the water (a and b) show the pattern of radiation. However these single component plots cannot show the curved radiation pattern. In (c and d) the red and blue arrows in the water show the expected acceleration (at one instant) the nodes produced by these acceleration patterns are shown as dotted lines. These nodes are in the same position as the simulation (a and b). This indicates that sound in the water radiates from antinodes of σ_y on the glass surface.
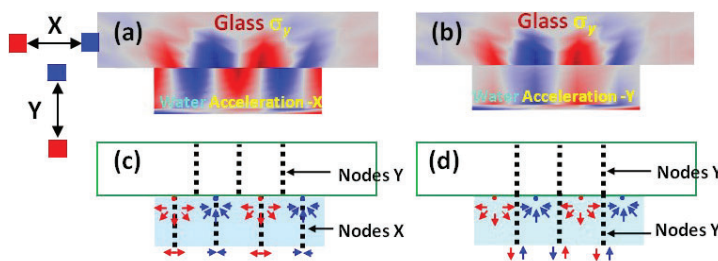
Nodes formation formed by non-resonant interference This year some of the authors reported a new capillary-bridge-channel[8] and found that node separation decreases with increasing liquid depth. The observation was explained with a node theory model NTM-1. In this model there is no resonance in the liquid and no reflections at the sidewalls. Pressure nodes are formed in the liquid from interference of pressure waves which emerge and radiate from antinodes of the stress tensor normal to the drive-plate, σ_y. Fig. 1 shows acceleration of the water which further confirms that waves in the water emerge from stress antinodes on the glass surface.

The capillary bridge channel is formed beneath a glass microscope slide. The slide has minimal supports to allow it to vibrate freely and it is driven from the side with 1 MHz sound see Fig. 2a.

The model NTM-1 consists of 6 steps the first 3 are due to the effects of added mass
Added mass (also known as mass loading). Liquids in contact with the glass add mass to the glass which decreases λ in the glass (NTM-1 steps 1 and 2). The effect contrasts with increasing the thickness of the glass where the mass and stress of the additional glass affect the whole system and λ in the glass increases.

The combination of node to node separation of stress σ_y in the substrate governed by added mass from the liquid together with pressure nodes in the liquid form at σ_y nodes introduces some new concepts for node control. At a fixed drive frequency, node to node separation is decreased with: Liquid depth or Substrate density, and node to node separation is increased with substrate: Thickness, elastic modulus or Poisons ratio.

The step change in added mass along the channel edge produces a step change in the glass wavelength. (NTM-1 step 3). Fig. 2 shows that this secondary effect of the added mass controls node alignment, stress σ_y and waveguiding. A small step enhances alignment across the whole slide whereas a large step is disruptive except in the channel region. Higher stress and waveguide is produced in the glass near the contact with the water because of an evanescent effect which traps the y component of sound.
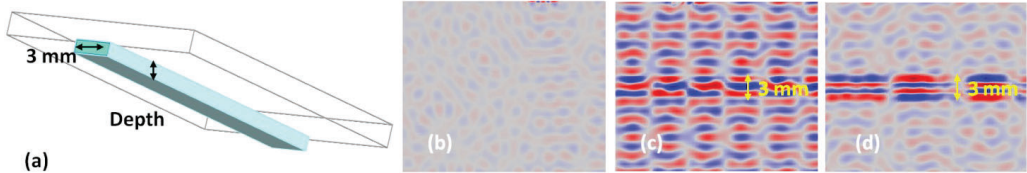
	(b)	**(c)**	**(d)**
Water depth (mm)	0	0.2	0.75
Nodes along channel	N/A	2	3
Node spacing, with added mass.	N/A	< rest of glass	< (c)
Node alignment across the whole glass surface	Poor	Good	Weak
Increased σ_y due to added mass (wave guiding)	N/A	Weak	Strong

Figure 2: (a) System simulated in (b-d): A water channel (a capillary bridge) below a microscope slide. The slide is driven at near 1 MHz with a PZT pressed against one side. (b-d) σ_y on the microscope slide lower surface. Images show a central 30 mm section of the slide.

Filter developments. To obtain quantitative measurements of focusing of particles in the capillary bridge channel the system is being developed as a filter. Our simulations show the acoustic efficiency and patterns, the filter will also be influenced by other effects mainly acoustic streaming allowing us to observe both effects. Novel technologies being developed for this filter include: 1) A battery operated drive for the PZT. 2) A gravity based multi-channel microfluidic siphon with floating reservoirs for constant flow. 3) Flowing liquid acoustic coupling for constant temperature and time invariant acoustic power. 4) Capillary bridges structures to increase node linearity.

References
[1] Z.I. Mandralis, D.L. Feke, R.J.Alder, Transient Response of fine particle suspensions to mild planar ultrasonic fields, Fluid/Particle separation Journal, 3 (1990) 115-121.
[2] K. Yasuda, S.-i. Umemura, K. Takeda, Concentration and fractionation of small particles in liquid by ultrasound, Japaneese Journal of Applied Physics, 34 (1995) 2715-2720.
[3] J. Blitz, Fundamentals of Ultrasound, in, Butterworth, London, 1967, pp. 27.
[4] J.J. Hawkes, W.T. Coakley, M. Gröschl, E. Benes, S. Armstrong, P.J. Tasker, H. Nowotny, Single half-wavelength ultrasonic particle filter: Predictions of the transfer matrix multi-layer resonator model and experimental filtration results, J. Acoust. Soc. Am., 111 (2002) 1259-1266.
[5] C. Devendran, D.J. Collins, Y. Ai, A. Neild, Huygens-Fresnel Acoustic Interference and the Development of Robust Time-Averaged Patterns from Traveling Surface Acoustic Waves, Physical review letters, 118 (2017) 6.
[6] L. Johansson, J. Enlund, S. Johansson, I. Katardjiev, V. Yantchev, Surface acoustic wave induced particle manipulation in a PDMS channel—principle concepts for continuous flow applications, Biomedical Microdevises, 14 (2012) 279-289.
[7] A. Aghakhan, H. Cetin, P. Erkoc, G.I. Tombak, M. Sitti, Flexural wave-based soft attractor walls for trapping microparticles and cells, Lab on a chip, 21 (2021) 582 —596.
[8] J.J. Hawkes, S. Maramizonouz, C. Jia, M. Rahmati, T. Zheng, M.B. McDonnell, Y.-Q. Fu, Node formation mechanisms in acoustofluidic capillary bridges, Ultrasonics, 121 (2022) 106690.

An acoustofluidic micromanipulation system with an open microfluidic chip

Natsumi HIRATA[1], and Takeshi HAYAKAWA[2]

[1]Department of Precision Engineering, Chuo University, Tokyo, Japan
E-mail: hirata_natsumi@mnrobo.mech.chuo-u.ac.jp
[2]Department of Precision Engineering, Chuo University, Tokyo, Japan
E-mail: hayaka-t@mech.chuo-u.ac.jp, URL: https://www.mech.chuo-u.ac.jp/~hayakawalab/

Introduction

In recent years, analyses of micro/ nano-particles is attracting large attentions in fields of medicine or biology. In order to analyze micro/ nano-particles, it is necessary to concentrate them and separate them from primary samples. As a conventional method for a concentration and a separation of micro/ nano-particles, ultracentrifugation is a major method [1]. This method can handle large number of particles at one time, but it takes a long time and requires a large amount of samples. To solve this problem, microfluidic devices for concentration and separation of micro/ nano-particles have been proposed because of its controllability of environments, high throughput and low-cost characteristics [2]. However, they have practical problems that it is difficult to remove debris or bubbles trapped in a microchannel because most of conventional microfluidic chips have closed structures. In this study, we constructed an acoustofluidic micromanipulation system with an open microfluidic chip, as shown in Fig. 1. As a result, we succeeded in constructing a system to focus microparticles by using an open chip system with an acoustic radiation force.

Methods

To realize an acoustofluidic micromanipulation system with an open microfluidic chip, we made mechanical jigs that were used to hold a chip, as shown in Fig. 1. A cover glass and a piezoelectric transducer (PZT) are also placed on the jig. Acoustic vibration is applied to the chip by driving the PZT which is pressed to a glass-silicon chip by using a rubber sheet. Four corners of the jigs are locked by bolts and nuts. A glass-silicon chip having microchannels is fabricated by using deep-RIE and anodic bonding techniques. By using this system, a glass-silicon chip can be easily set and removed from the jigs and problems of debris or bubbles can be prevented.
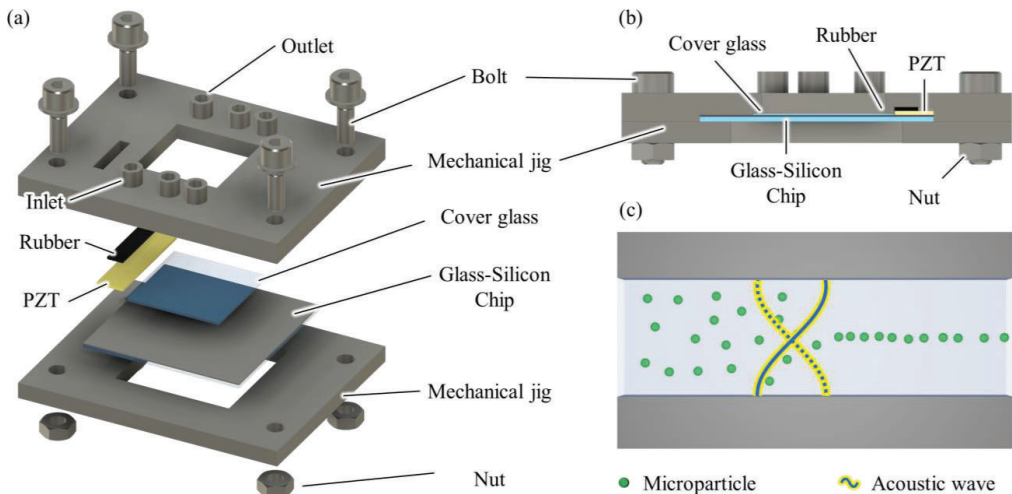

Figure 1: An acoustofluidic micromanipulation system with an open microfluidic chip
(a) Schematic figure of an open microfluidic chip and mechanical jigs
(b) Side view of the acoustofluidic micromanipulation system
(c) Top view of the microchannel which is applied an acoustic vibration

The materials of the experimental device were determined by considering values of their acoustic impedances that affects the transmittance of acoustic waves. According to the theory of wave propagation, when acoustic wave propagates a boundary surface of different materials, transmittance of acoustic waves become higher when the acoustic impedances of the two materials are closer. Therefore, the device was fabricated by using silicon and glass, whose acoustic impedances are close to that of the PZT. Moreover, a design value of the width of the microchannel was determined from the integer multiple of half wavelength of the acoustic wave. The wavelength is also determined from the speed of sound in water and the frequency. Therefore, the width of the microchannel is set to 400 μm, which is half wavelength of the acoustic wave.

Experiments

In this study, we observe acoustic radiation force in the microchannel of the chip. Constructed mechanical jigs and the chip are shown in Fig. 2 (a). We use microparticles with diameter of 15 μm and microscopy to observe manipulations of microparticles with acoustic radiation force. We observe manipulations with an acoustic radiation force applied to microparticles in the straight microchannel.

By tracking movements of microparticles, we calculate position-independent acoustic energy density E_{ac} from Eq. (1).

$$E_{ac} = \frac{9\eta}{4\Phi(k_y a)^2 t} \ln\left[\frac{tan[k_y y(t)]}{tan[k_y y(0)]}\right] \tag{1}$$

In this equation, t is time, η is viscosity of the quiescent liquid, Φ is acoustophoretic coefficient, k_y is wave number, a is radius of microparticles and y is transverse position in a microchannel.

Results

Figure 2 (b) shows results of observation of acoustic radiation force in the straight microchannel at frequency of 2.44 MHz and voltage of 40 V. Fig. 2 (b-1) and (b-2) are microscopic images before and after applying the acoustic wave and Fig. 2 (c) shows overlap image of movement of particles, respectively. From this result, microparticles were arranged at the center of the microchannel by applying the acoustic wave. Then, by calculating the acoustic energy density form Eq. (1), we obtained $0.174 \, J/m^3$. This result shows the acoustic energy density is not very far from that of conventional method obtained with closed chip, that value is 6.69 J/m^3 [3].
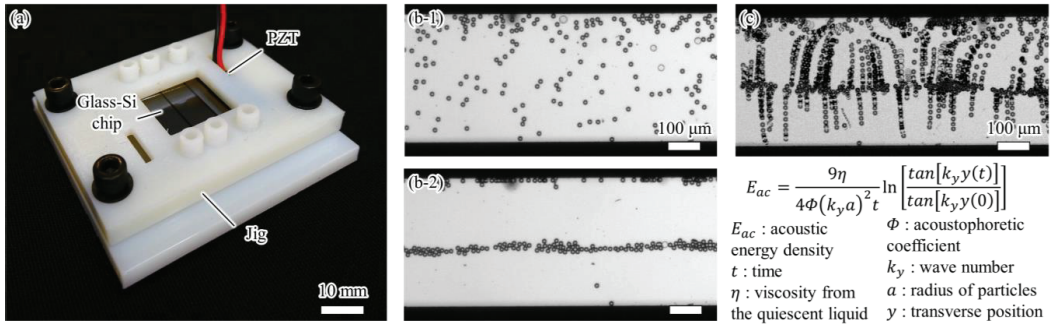

Figure 2: An experimental system and the results. (a) An image of the experimental system,
(b) Result of acoustic radiation force applied to microparticles in the straight microchannel,
(b-1) Before applying the acoustic wave, (b-2) After applying the acoustic wave,
(c) Tracking of movements of the microparticles [4].

Conclusion

In conclusion, we succeeded in observing acoustic radiation force applied for microparticles by using the open chip system and calculating the acoustic energy density. The value of energy density of the acoustic wave in our system was $0.174 \, J/m^3$ and we will try to improve this value by improving design of the mechanical jigs. In the future, we will perform concentration of micro/ nano-particles and separate them from primary samples.

References

[1] H. Zhu, and G. C. Fan, American journal of cardiovascular disease **1** (2), 138 (2011)
[2] T. Salafi, K. K. Zeming, and Y. Zhang, Lab Chip **17** (1), 11–33 (2017)
[3] R. Barnkob, P. Augustsson, T. Laurell, and H. Bruus, Lab on a Chip **10** (5), 563-570 (2010)
[4] M.D. Abramoff, P.J. Magalhaes, and S.J. Ram, Biophotonics, International **11** (7), 36-42 (2004)

Coupling acoustophoresis and thermophoresis for enriching nanoparticles

Jing Dong [1], Dongfang Liang [1], and Xin Yang[2]

[1]1 Department of Engineering, University of Cambridge, Cambridge CB2 1PZ, UK
E-mail: jd704@cam.uk
[2] Department of Electrical and Electronic Engineering, Cardiff University, Cardiff CF24 3AA, UK

Introduction

Low-cost, easy-to-operate and fast diagnostic tests are in high demand for early detection of cancer based on circulating biomarkers. Recently, thermophoresis has been proposed as an efficient method to manipulate nanoparticle species [1]. However, the convection caused by local heating can increase the enrichment time of nanoparticles. This shortcoming can be mitigated by incorporating Standing Surface Acoustic Waves (SSAW). The streaming eddies induced by SSAW can be controlled to counterbalance the convection and thus minimise the convection impact on thermophoresis, which lead to reducing the time of enrichment. This paper reports on a finite element (FE) model to study the effectiveness of the SSAW incorporation on the efficiency and suitability of the enrichment systems.

Model setup

Figure 1(a) gives a 3D view of the thermophoretic enrichment system for accumulating nanoparticles. The whole system is made of three parts, a glass top slide, a $1000 \times 1000 \times 240$ μm microchamber in the middle, and a sapphire bottom slide. The liquid and nanoparticle mixture is locally heated with a 1,480-nm laser, with a power of 194 mW, focusing on the microchamber bottom. The purpose of such local heating setup is to generate thermal gradients [1]. To simplify the problem, a cross-sectional 2D model is established to represent the whole domain. As shown in Figures 1(b) and 1(c), this simulation include two steps, one with only temperature gradients generated by laser heating referred to as case (a) and the other with both temperature gradients and SSAW acting on the microchamber bottom as case (b). The acoustic wavelength is $\lambda = 666$ μm, and the frequency is $f = 5.99$ MHz [2]. The coupled solutions of the acoustic field, flow field, heat transfer and particle movement are achieved with the Finite Element Method (FEM). We use polystyrene particles each with a radius of 50 nm to represent nanovesicles, in consistency with the previous experiments. As illustrated in Figure 1(d), to facilitate analyses, a target box with 100 μm width and 10 μm height is centred around the final positions of nanoparticles. The time taken for nanoparticles to reach their final destinations is t_d.
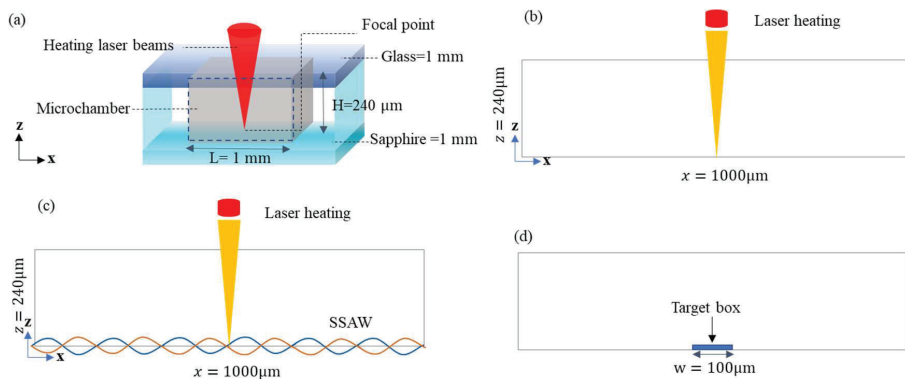

Figure 1: (a) Schematic of the model setup. (b) The simplified cross-sectional 2D model with only temperature gradient. (c) The simplified cross-sectional 2D model with both temperature gradient and SSAW (d) Schematic of the target box

Results and discussion

To validate the model, simulations are compared with the results reported in the literature. The temperature field, the velocity field and the particle distributions show good agreements with both the numerical and experimental results in Liu et al. [1].

The verified thermophoresis model is then used to study the influence of SSAW. Figure 2(a) shows the temperature field in case (a) with a maximum temperature difference of 32°C. Figure 2(b) illustrates the convection velocity field of case (a) with the magnitude ranging from 0 to 60 μm/s. Figure 2(c) shows the distribution of acoustic pressure field ranging from -11KPa to 11 KPa. Figure 2(d) shows that the temperature field in case (b) is the same as that in case (a). Figure 2(e) illustrates that in the velocity field of case (b), the maximum convection velocity is reduced to 43 μm/s. Figure 2(f-h) are the distributions of 100 nm particles at different stages. Figure 2(f) presents the initial positions of 20000 particles. Figure 2(g) demonstrates the positions of 100nm particles in case (a) after exposing to the thermal gradients for 5s. In Figure 2(h), particles finally move into the target box and reach the final position. In case(b), nanoparticles are also set up in the same way as in case (a), and then they move towards the centre of the microchamber bottom with a higher speed. The reason is that SSAW reduces the convection's adverse impact on thermophoresis, and thus effectively reduces the time for particles to reach their destinations. Then, we repeated the simulations with the maximum temperature ranging from 32°C to 41°C, and calculated t_d as plotted in Figure 2(i). It indicates that, by incorporating SSAW, the enrichment time can be reduced by about 40% on average.
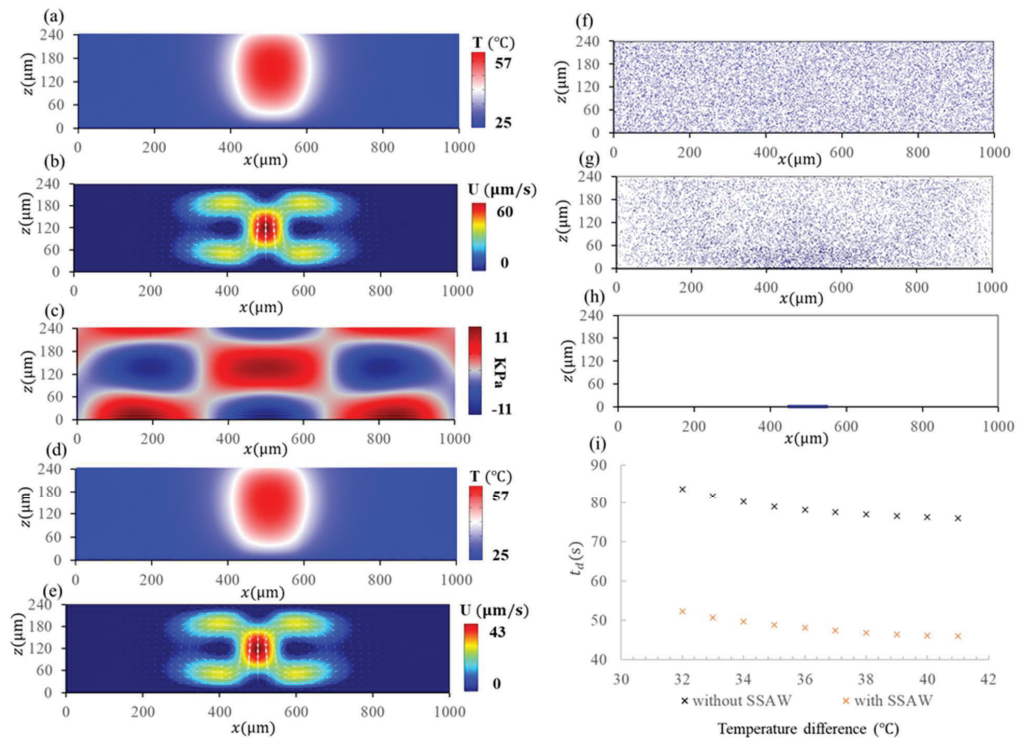

Figure 2: (a) The temperature field in case (a). (b) The velocity field in case (a). (c) The acoustic pressure field in case (b). (d) The temperature field in case (b). (e)The velocity field in case (b). (f) The initial state of particles in case (a). (g) Particle positions in case (a) at 5s. (h) Particles reaching final positions of case (a). (i) The times to the destinations of the 100nm particles under the different temperature gradients with or without SSAW

Conclusion
The paper used a FEM model to examine the thermophoretic enrichment system under the influence of SSAW, which was validated against previous studies. The results showed that SSAW could enhance the nanoparticle accumulation efficiency. With the current geometry and target box size, the study suggested that, by integrating the SSAW with proper frequencies and amplitudes, the accumulation time of nanoparticles could be shortened by 40%.

References
[1] C. Liu, J. Zhao, F. Tian, L. Cai, W. Zhang, Q. Feng, J. Chang, F. Wan, Y. Yang, B. Dai, Y. Cong, B. Ding, J. Sun, W. Tan. "Low-cost thermophoretic profiling of extracellular-vesicle surface proteins for the early detection and classification of cancers", *Nature Biomedical Engineering*, 3, 183-193(2019).
[2] Dong J, Liang D, Yang X, Sun C. "Influences of microparticle radius and microchannel height on SSAW-based acoustophoretic aggregation", *Ultrasonics*, (2021).

Droplet Acoustofluidics and Pico-injection for Long-term Cell Culture

Sagar Narhari Agnihotri[1], Zhenhua Liu[1], Laurent Barbe[1], Anna Fornell[2] and Maria Tenje[1] *

[1] Department of Materials Science and Engineering, Science for Life Laboratory, Uppsala University, Uppsala, Sweden

[2] MAX IV Laboratory, Lund University, Lund, Sweden

*Corresponding author email: maria.tenje@angstrom.uu.se

Introduction

Droplet microfluidics is proving to be an important tool for a biological application like single-cell analysis[1]. However, the concentration of nutrients in nano- to picoliter-sized droplets decreases, and catabolic byproducts increases over time, making long-term cell culture difficult. Here, we developed a droplet acoustofluidic chip capable of cell medium exchange with the help of pico-injection that allows for extended cell cultures.

Theory

Our group has previously demonstrated that acoustophoresis can be used for the manipulation of particles inside droplets[2]. In this work, the encapsulated cells are focused in a bulk acoustic half wavelength standing wavefield. In this case, there is a pressure node along the center-line of the channel and pressure antinodes along the channel sidewalls. The primary acoustic radiation force (F^{rad}) can focus particles on the pressure node or the pressure antinodes.

Device design and operation

Standard T-junction (schematically shown in figure 1a) was used to generate droplets (cell medium) encapsulating yeast cells. Light mineral oil with 3% PGPR (Polyglycerol polyricinoleate) surfactant and an aqueous phase with yeast cells were used as a continuous and dispersed phase respectively. A silicon chip was used to exchange the cell medium of droplets (schematically shown in figure 1b). The silicon chip consists of droplet reinjection, pico-injection[3], and droplet splitter with acoustophoresis.
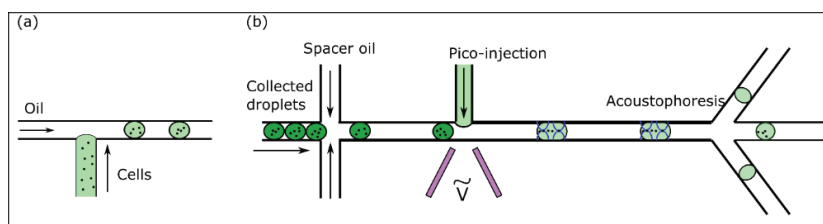

Figure 1. (a) A PDMS chip is used for cell encapsulation in droplets. (b) A silicon chip is used to exchange cell medium in droplets by the combination of the pico-injection and droplet split with acoustophoresis.

The channel width of the silicon chip was 150 µm which matches the acoustic frequency of 4.5 MHz to form a λ/2 standing wavefield. A piezoelectric element (Pz 26, Meggitt) with the fundamental resonance frequency of 5 MHz was glued to the silicon chip to couple the acoustic wave into the chip. For quantification of cell growth in droplets, the droplets with encapsulated cells were loaded on a glass chip with an array of 3D printed pillars.

On-chip cell culture

Droplets with yeast cells were incubated for 6 hours and 8 hours. These incubated droplets were introduced into a microfluidic system for pico-injection. In the first step, fresh media was introduced in droplets, in the

second step, acoustophoresis was used to move yeast cells along the center-line of the droplet and finally, we used passive droplet splitting to bring the droplet back to its original volume.

In the first case, we observed yeast cell growth in a droplet without using pico-injection. We can observe that after 8 hours there is no cell growth (figure 2a). In absence of fresh cell media, yeast cells do not grow after a certain time due to a lack of nutrients. We injected fresh cell media into the droplet after 6 hours of incubation using pico-injection in the second case. Contrary to the first case, yeast cells in a droplet with refreshed media continue to grow up to 16 to 18 hours (figure 2b). In the third case, we injected fresh cell media into the droplet after 8 hours. Similar to the second case, we observe continued growth of yeast cells up to 20 hours (figure 2c). In figure 2d, we plotted the average per hour of yeast cell growth of collected droplets against time for all three cases. We observe from the plot, that without the pico-injection, the rate of yeast cell growth increases for the first 4-5 hours, and the rate of yeast cell growth decreases for the next 2-3 hours and becomes minimum after that. Hence, we can say that without pico-injection yeast cells grow for only the first 8 hours and stop growing afterward. Contrary to this, when fresh media was injected into the droplets after 6 and 8 hours, yeast cells continue to grow up to 12-15 hours.
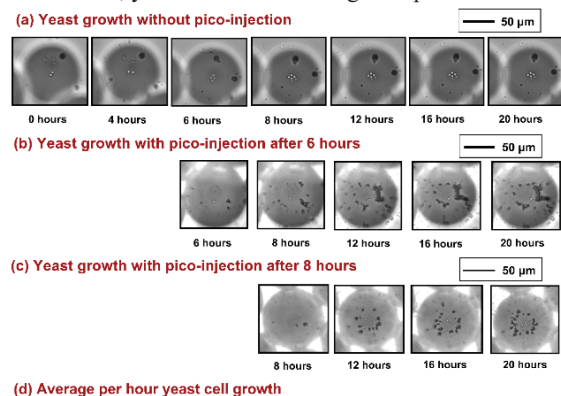

Figure 2: (a) Image sequence showing yeast cell growth without pico-injection. With an initial yeast cell number of 2, grows to become 6 after 8 hours. After 8 hours there is no yeast cell growth. (b-c) Image sequence showing yeast cell growth with pico-injection after 6 and 8 hours. Initially, there is only a single cell in the droplet, which grows till the time 20 hours. (d) Average per hour yeast cell growth plotted against time for 100 cells for all three cases.
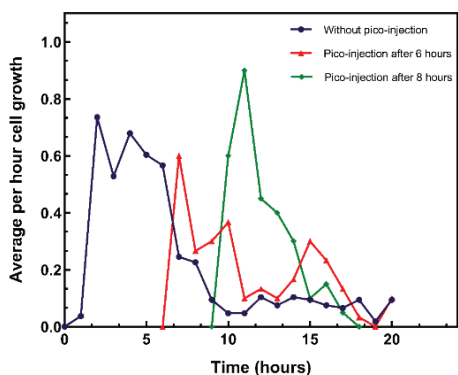
Conclusion

We demonstrate the combination of pico-injection, acoustic waves, and passive droplet splitting for exchanging the nutrient-depleted cell media with nutrient-rich cell media for yeast cell growth for a longer time. The microfluidic chip shows the capability to allow the yeast cell to grow for a longer period of time.

References

1   K. Matuła, F. Rivello and W. T. S. Huck, *Advanced Biosystems*, 2020, 4.
2   A. Fornell, J. Nilsson, L. Jonsson, P. K. Periyannan Rajeswari, H. N. Joensson and M. Tenje, *Analytical Chemistry*, 2015, **87**, 10521–10526.
3   Z. Liu, A. Fornell, L. Barbe, K. Hjort and M. Tenje, *Biomicrofluidics*,, DOI:10.1063/1.5129256.

Manipulation of micro-size particle induced by focused helical progressive waves

Diego Sánchez Saldaña[1], Etien Martinez Roman[1], Maria Fernandino[1] and Carlos A. Dorao[1]

[1]Department of Energy and Process Engineering, Norwegian University of Science and Technology, Trondheim, Norway
E-mail: diego.s.sanchez@ntnu.no

Introduction

Non-contact manipulation methods of micro- and nano-size particles play a major role in microsystem technologies due to their relevance in diverse biomedical applications such as tissue engineering and clinical diagnostics. The main approach to achieve non-contact manipulation is based on harvesting energy from indirect physical forces (optical, magnetic, plasmonics, acoustics) to enable remote actuation. The trade-offs for achieving a non-contact, safe, low-power and precise handling of sensitive micro-agents while being biocompatible and requiring a minimum hardware has placed the attention on the contactless actuation using acoustics. The acoustic waves can be generated by an interdigital transducer, IDT, deposited on a piezoelectric material which converts an external electric potential to mechanical deformation by switching the polarity of the applied electric potential. A common approach has been the use of parallel fingers IDT which leads to a plane wave. When this plane wave interacts with a liquid droplet containing particles deposited on the substrate, the induced flow streaming can lead to the formation of a complex 3D flow structure inside the droplet. First studies have suggested that the concentration of particles inside the droplet is led by a balance between the acoustic streaming trying to disperse the particles and a shear induce migration [1] trying to transport the particle to the center of the droplet [2]. Then at low power it is possible to achieve the accumulation of particle in the center of the droplet, while at higher power the acoustic streaming will dominate dispersing the particles. A 3D-study of the flow inside the droplet [3] suggests that in the bulk of the droplet the fluid motion is like a forced vortex or rigid body with an azimuthal velocity that scales linearly with the radius and decays to zero at the vortex center. The suspended particles are transported to the bottom of the droplet by a helical spiral-like trajectory. Then when the particles are close to the substrate, an inward radial velocity transport the particle to a stagnation point provided that the flow streaming is not sufficient to redisperse them. As in the case of the parallel fingers IDT the SAW interacts with a fraction of the contact line of the droplet. To overcome this problem, an omnidirectional spiral design was proposed for inducing a rotational symmetric SAW around the droplet [4]. The design of the IDT induces a tangent SAW along the droplet periphery, so the net effect can be considered equivalent to an array of parallel fingers IDT located around the droplet. This concept increases the average angular velocity inside the droplet compared to the common parallel fingers IDT located in one side of the droplet. Furthermore, the concept was able to separate and accumulate large particles in the center of the droplet while smaller at the periphery of the droplet. However, spiral IDTs can also be designed for inducing acoustical vortices [5]. For example, Baudoin [6] proposed a spiral IDT concept as acoustic tweezers by synthesizing a spherically focused acoustical vortex. In this case, the IDT consists of intertwined spiraling electrodes of inverse polarity. This spiral IDT leads to the formation of focused helical progressive waves that spin around a central axis wherein the pressure amplitude vanishes surrounded by a ring of high-pressure intensity, which pushes particles toward the central node. Recently, Zhou [7] proposed the use of spiral IDT for inducing an acoustic screw dislocation for studying the hydrodynamic helicity of the flow inside a sessile droplet. It was found that helicity can be generated by acoustic streaming by forcing flow recirculation or using a helical force field. This helical progressive wave generated by spiral IDTs provide an alternative for controlling the characteristics of the flow inside the droplet that can be used for separation and accumulation of particles in the fluid. In this work we show an experimental investigation of (i) different dynamics inside the sessile drop depending on the design of the IDT a configuration and that (ii) micro sized particle aggregation is allowed when using the spiral IDT.

Material and Methods

Two SAW devices have been designed and fabricated for the study namely a straight and spiral IDTs. The transducers were fabricated using a piezoelectric substrate (128 YX LiNbO3) via maskless aligner MLA lithography and e-beam metal evaporation. The devices can operate in a frequency range between 20 MHz and 160 MHz and in a power range between 300 and 900 mW. The device is driven by BELEKTRONIG SAW generator BSG. The experiments consist in depositing a DI-water droplet of about 2 microliters on substrate near the IDT using a Micro-Volume Kit micropipette. The study is conducted using a Nikon Eclipse Ti2

fluorescence inverted microscope with a Photron Fastcam Mini UX100 type 800K high speed camera. For the visualization 7 µm particles form Bangs Laboratory were dissolved in the water with concentration 0.17% w/v. For the study of the flow structure inside the droplet the images were acquired at 250fps, while for studying the aggregation process 50fps were used. The images were postprocessed using the Matlab Image Processing Toolkit and the PIVLab in Matlab [8].

Results and discussion

Figure 1 illustrates the flow field induced by two different IDTs designs and the resulting aggregation pattern of the initially dispersed particles in the liquid phase. The experiment corresponds to the case of the device operating at 300 mW and at a frequency of 20 MHz and 160 MHz, and after 1 minute after the SAW was turned on. It is clearly observed that the velocity field depends strongly on the design of the IDT. It is observed that the spiral IDT, Figure 1(b) can induce a strong vorticity inside the droplet almost double in magnitude compared to the case of the droplet located in off-center of the IDT, Figure 1 (a). The two cases corresponding to the IDT operating at 20MHz shows the formation of a single vortex. It is observed that even when the vorticity in the spiral IDT is almost a factor two compared to the case of the straight IDT, the aggregation of the particles was not possible for the spiral IDT. In fact, the droplet placed off-center shows a better aggregation on the surface of the substrate even at lower values of the vorticity. On the other hand, when compared IDTs operating at 160MHz, it is observed the formation of 2 vortices for the two cases. Again, the spiral IDT can induce a larger vorticity compared to the case of the straight IDTs. In this case, the spiral IDT can aggregate the particles efficiently in two regions corresponding to the centers of each vortex. The formation of the two vortices for the case of the spiral IDT can be attributed to the asymmetry of the propagation of the substrate used. The improved aggregation of the particles in the case of the spiral IDT can be attributed to the helical progressive wave which helps to focus the particles towards the top part and thus to facilitate the aggregation of the particles contrary to the straight IDT.
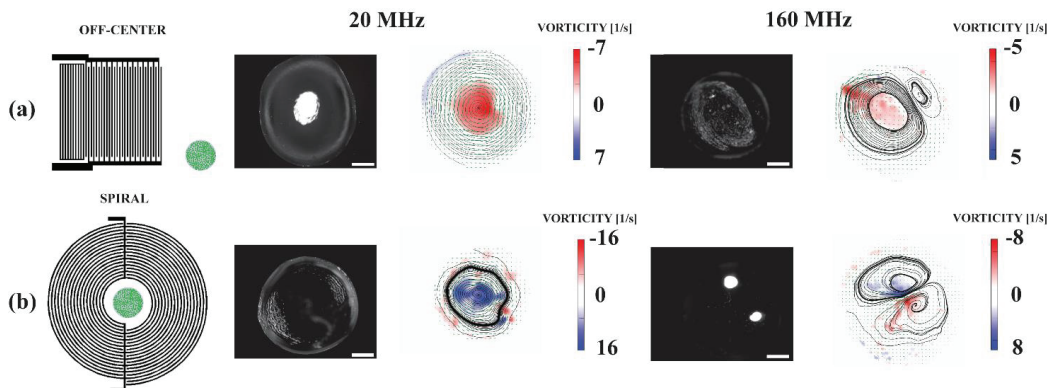

Figure 1:
First column of the panel shows the configuration of the experiment. Second column illustrates the final stage of the aggregation of the particles and the corresponding velocity field and vorticity field at 20MHz. The third column shows the case for 160MHz. Scale bar is 500 µm. Images shows the state after 1 minute after the SAW was applied.

References
[1] Eckstein, E. C. et al. Journal of Fluid Mechanics, 79(1), 191-208 (1977).
[2] Li, H. et al. Biomed Microdevices 9, 647–656 (2007).
[3] Raghavan, R. V. et al. Microfluidics and Nanofluidics, 8(1), 73-84 (2010).
[4] Zhang, N. et al. Lab on a Chip, 21(5), 904-915 (2021).
[5] Hefner, B. T. et al. The Journal of the Acoustical Society of America, 106(6), 3313-3316 (1999).
[6] Baudoin, M. et al. Nature communications, 11(1), 1-10 (2020).
[7] Zhou, J. et al. Physics of Fluids, 34(6), 064101 (2022).
[8] Thielicke, William et al. Journal of Open Research Software, vol. 9 (2021).

Trap Stability Under Acoustic Levitation - A Numerical and Machine Learning Approach

Shirsendu Mitra, and Ruchi Gupta*

School of Chemistry, University of Birmingham, United Kingdom
*Email of Corresponding Author: R.Gupta.3@bham.ac.uk

Abstract:

Introduction:

Spatiotemporal manipulation of particles and droplets in free-space using acoustic forces has gained significant research interests with applications in contact less object manipulation, enhanced chemical catalysis, drying and crystallization, disease diagnosis, and industrial biotechnology[1, 2]. Acoustic levitators have been designed using arrays of commercially available transducers[3]. On demand spatial distribution of acoustic pressure for the creation of holograms and spatial manipulation of particles has been achieved by varying the relative phases of acoustic waves generated either by a continuous source or arrays of transducers[4, 5]. However, there has been a limited understanding of the stability of acoustic traps and their accurate relations with pressure distributions. To address this gap, we develop a numerical model employing finite element based COMSOL Multiphysics software to solve for trap stability of multiple particles under a desired acoustic force field created numerically to mimic the real pressure field that can be generated by an array of commercially available transducers in a portable acoustic levitator.

Modelling and Methodology:

Figure 1a shows the acoustic levitator setup that has array of acoustic transducers at the top and bottom planes which create an acoustic radiation field in the free space between these two planes. The pressure field generated by individual commercial transducer was obtained using the analytical expression provided in Figure 1 and then taking algebraic summation for all the transducers present in the portable levitator. Further, this acoustic pressure field data was integrated with the particle tracing module of COMSOL Multiphysics via numerical interpolation functions. This approach reduced the computational burden and increased convergence in COMSOL Multiphysics. We employed pseudo-three-dimensional (3D) approach where we simulated pressure and particle distribution in individual planes (refer to Figure 1) and then took a cumulative effect to obtain a three-dimensional picture. Currently, simulations have been performed using 500 number of particles.

Gist of the Results:

The simulations revealed that despite the presence of numerous acoustic nodes, particles were trapped only at the pressure nodes that nullified all surrounding forces. Simulations were performed to investigate the pattern of acoustically trapped particles as a function of numbers of transducers, acoustic pressure, initial phases, particle sizes and their initial positions. Figure 2a shows acoustic pressure field at a xz cut plane (y = 2.2 cm) for a 3×3 array of transducer set up present at both top and bottom planes. The stable acoustic trap positions generated by the created pressure field is shown in Figure 2c. In further parametric studies we work with higher number of transducer arrays to understand the trap stability under complex pressure fields. In addition to that we explored the effect of relative phase changes on acoustic pressure field and thereby on the position of stable traps. The images generated by COMSOL simulations formed the training dataset for a Convolutional Neural Network based Machine Learning model for predicting selected particle traps for a definite pressure fields. The initial findings pave the pathway to utilize the developed model for predicting pressure fields required to pattern even larger number of particles.

Conclusions:

Conclusively, the present work explored finite features of multi-particle acoustic traps and locations of equilibrium nodes. The CNN based machine learning approach gives a newer insight to the acoustic trap stability and also helps in identifying stable trap positions for an unknown pressure field obtained for an arbitrary set of transducer phases. The present study also facilitates further research scopes wherein externally controlled patterning of large number of particles is targeted.
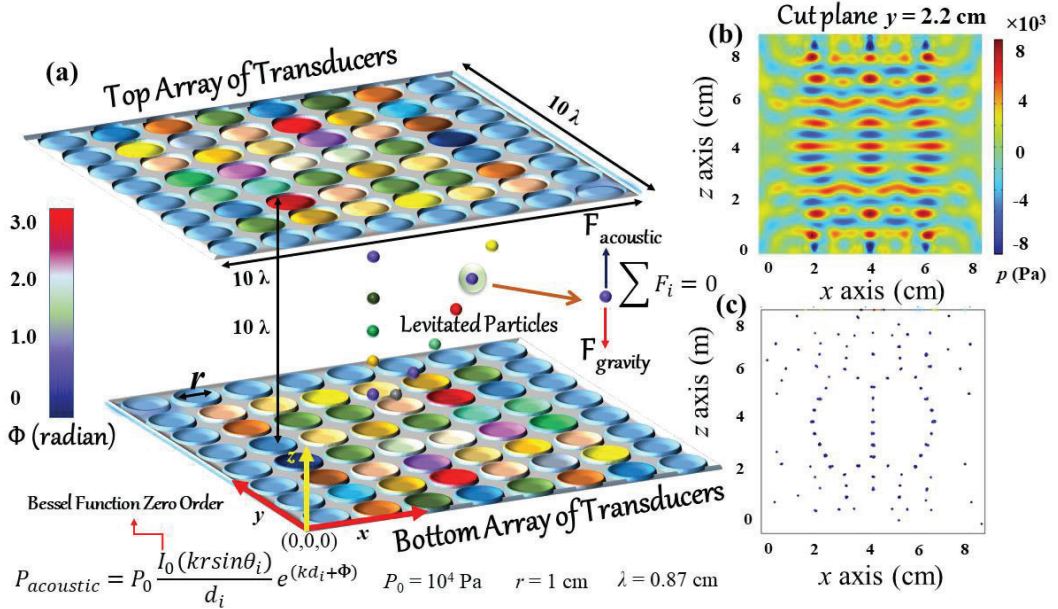

$$P_{acoustic} = P_0 \frac{I_0(krsin\theta_i)}{d_i} e^{(kd_i+\Phi)} \quad P_0 = 10^4 \text{ Pa} \quad r = 1 \text{ cm} \quad \lambda = 0.87 \text{ cm}$$

Figure 1: (a) Schematic of an acoustic levitator with top and bottom arrays of transducers (Φ is the phase of acoustic wave produced by each transducer), (b) Pressure distribution at a xz plane, $y = 2.2$ cm for 3×3 arrays of transducers, and (c) distribution of levitated particles for the acoustic pressure shown in (b). The frequency of acoustic wave was 40 kHz, and the simulation was done for a square plane with dimension 10×wavelength (i.e., 8.7 cm). Particle diameter and density were 0.1×wavelength and 1000 kg/m³, respectively.

References:

[1] M. A. Andrade, N. Pérez, J. C. Adamowski, *Brazilian Journal of Physics* **48**(2), 190-213 (2018).
[2] M. Shi, K. Feng, J. Hu, J. Zhu, H. Cui, *International Journal of Extreme Manufacturing* **1**(3), 032002 (2019).
[3] A. Marzo, A. Barnes, B. W. Drinkwater, *Review of Scientific Instruments* **88**(8), 085105 (2017).
[4] K. Melde, A. G. Mark, T. Qiu, P. Fischer, *Nature* **537**(7621), 518-522 (2016).
[5] A. Marzo, S. A. Seah, B. W. Drinkwater, D. R. Sahoo, B. Long, S. Subramanian, *Nature communications*. **6**(1) 1-7 (2015).

"An Acoustically-Activated Sub-Nanoliter Droplet Generation Device as Interface Prototype to Mass Spectrometer for Protein Detection"

G. Marinaro[1,2,*], A. Tojo[1], M. Bengtsson[1], T. Kitamori[2], T. Laurell[1], J. Nilsson[1]

[1] Department of Biomedical Engineering, Lund University, Lund, Sweden
[2] School of Engineering, Department of Mechanical Engineering, The University of Tokio, Japan
*E-mail: giovanni.marinaro@bme.lth.se

Introduction: Droplet generation is important for inkjet systems [1] and, in the last decades, also attracted interest for a wide range of applications from single molecule detection to conventional microfluidic systems [2],[3]. Droplet size and frequency are fundamental parameters when engineering droplet generator devices. A microchip enabling the formation of pL droplet at low flow rates was designed by Kazoe et al. [2] and shown in **fig .1**. The ejection process relies on a combination of capillary and drag forces acting on the droplet with ejected volumes in the range of few pL at kHz frequencies. The droplet generator is intended to be the end part of a nanofluidic system for protein analysis, where cells are subject to in-chip lysis and proteolytic digestion of the intracellular components, followed by in-chip nano-Liquid Chromatography (LC) separation. Finally, the outlet of the LC will be integrated with the droplet generator, positioned directly at the injection port of a mass spectrometer. Our paper presents the first steps of a suggested improvement of this approach by the introduction of a piezoelectric actuator based at the kHz vibrations to control the Rayleigh instability for droplet generation. The operation is verified by controlling the droplet generation of a fluid jet from a similar glass chip, at this point without the gas flow supported feature.
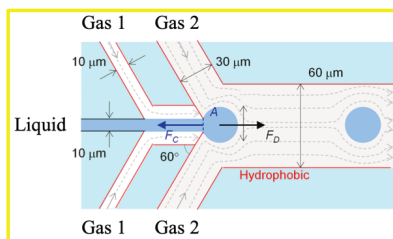

Figure 1. The microfluidic droplet ejector shears the main channel flow to a thin fluid stream by the high speed gas flow (Gas 1), still with channel wall contact at the top and bottom. A second gas flow (Gas 2) supports the droplet formation from the thin fluid stream.

Materials and Methods: A glass microfluidic device is fabricated in clean room according nanotechnology methods which include photolithography and glass etching. An illustration of the device is shown in **fig.2**. A 3x3x2 mm multilayer Lead Zirconate Titanate (PZT) piezo actuator providing 6.4 N/V is placed between a glass microchip and a Polyether Ether Ketone (PEEK) holder (for simplicity of visualization, the holder is omitted in **fig. 2**). Glycerol was used as coupling layer between the transducer and the chip. A microchannel inside the glass chip located close to the piezo actuator. When a fluid stream is exposed to vibrations of a wavelength of at least π times the cross-section of the stream, the vibrations match the Rayleigh instability of the stream, **fig. 2**. Laser Doppler Vibrometer measurements of the piezo mounted in contact with the PEEK holder and the glass chip were taken. The laser was focused on the piezo and a meander scan, 20x20 positions, was executed on the entire 3x3 mm surface area with a step size of 150 μm. The piezo actuation was set to 16V peak to peak at 10 KHz. A stroboscope setup was built to monitor the droplet formation and compute the velocity of the droplets.
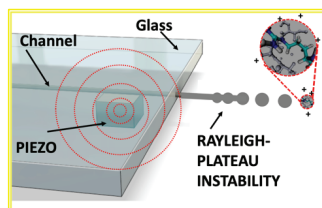

Figure 2. Sketch of the glass chip and the piezo underneath. The illustration also shows the Rayleigh-Plateau instability of a liquid stream containing dissolved peptides. In the final version droplets are supposed to be electrically charged in order to deflect the molecules in a magnetic field in the mass spectrometer once the fluid is evaporated

Results: Butterworth-Van Dyke model of a 3x3x2 mm PZT piezo actuator (CTS Corporation) was implemented in LTSpice. The circuit is illustrated in **fig. 3A**. The values of the electrical components are: L_1=1.1 μH, R_1=59.1 mΩ, C_1=104.4 nF, C_0=295.6nF. Impedance analysis (HP4195A) suggests that the model and the measurements match (**fig. 3B**) as the resonances at 320 KHz and 560 KHz result the same. We attribute the other resonances to the contact with the glass and PEEK holder. All resonances are far away from the intended operation range around 10 kHz and will not interfere. Laser Doppler Vibrometer analysis suggests that the piezo in contact with PEEK and actuated at 10 KHz, shows oscillations between 150 and 200 nm on the glass chip top surface (**fig. 3C**).
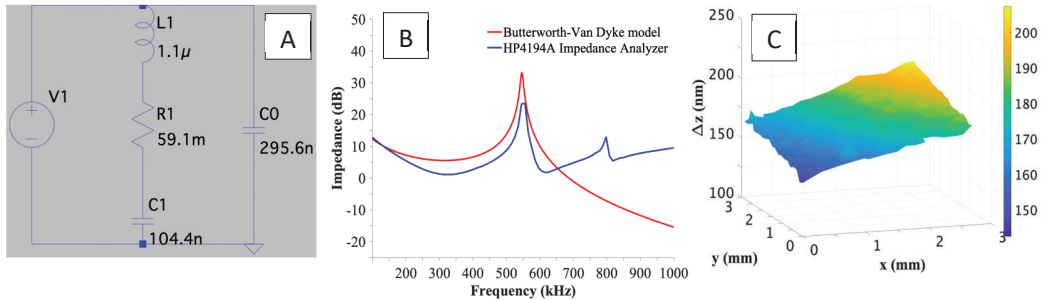

Figure 3A. Electrical model of the PZT piezo-actuator . **B.** Simulated Impedance of the actuator (red) and measured with an HP4194A Impedance Analyzer. **C.** Map of vibrations of the PZT at 10 KHz.

A water jet at the outlet of the chip was formed at a flow rate of about 170 μl/s (**fig. 4A**). With the actuation off, only a thin stream was observed (**fig. 4B**). When the PZT was actuated around 10 kHz a stable droplet formation was observed (**fig. 4C**) via stroboscopic imaging. The stroboscope setup includes a stereomicroscope, a green LED powered with periodic pulses of 100 ns, synchronized with the PZT actuation. The camera was set at about 2 frames per second (fps) with an exposure time of 400 ms. The optimal frequency found to stabilize the droplets on the frame view was 8.8 KHz (**fig. 4C**) suggesting a velocity of the droplets of about 4.4 m/s according to *(1)*:

$$v = f \cdot \lambda \tag{1}$$

where f is the actuation frequency and λ is the distance center to center between consecutives droplets. The droplets were visualized at a distance of few mm from the outlet. For smaller volumes and including the gas support, a new version of the droplet ejector design will be soon available as illustrated in **fig. 4D**.
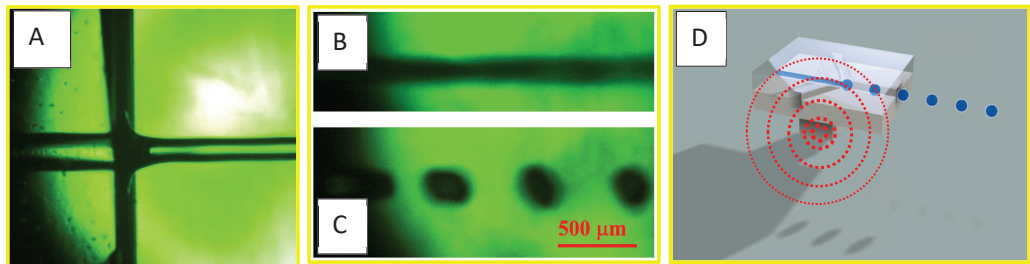

Figure 4A. Water jet near the outlet of the chip. **B.** Liquid stream when the actuation is turned off. **C.** Image of a droplet series acquired with the stroboscope showing the Rayleigh-Plateau instability induced by the piezo. **D.** Illustration of a device performing femtoliter droplet ejection with the integration a of piezo-acoustic actuator

Conclusions: The current chip/PZT set-up enables acoustically stabilized droplet formation in the 10 kHz range. On-going development will adapt this droplet stabilization configuration to the femtoliter droplet generation system developed in **[2]**, with a similar operation of droplet frequencies in the 10 kHz range (**fig. 4D**).

Bibliography:
[1] T. Laurell, *et al.*, *J. of Micromechanics and Microengineering*, vol. 9, no. 4, pp. 369–376, Nov. 1999.
[2] Y. Kazoe *et al.*, *Sensors and Actuators B: Chemical*, vol. 340, p. 129957, 2021.
[3] G. Marinaro *et al.*, *Optics and Lasers in Engineering*, vol. 76, pp. 57–63, Sep. 2014.

Influences of aspect ratio of microchannel on SSAW-based acoustophoresis

Yiming Li[1], Dongfang Liang[1]

[1]Department of Engineering, University of Cambridge, Cambridge CB2 1PZ, UK
E-mail: yl842@cam.ac.uk

Introduction

The acoustofluidic technique has been increasingly applied to the precise and contact-free manipulation of microparticles and cells in recent years. We present a numerical study of the acoustophoretic particle motions induced by standing surface acoustic waves (SSAW) in a Polydimethylsiloxane (PDMS) microchannel. The study aims to provide a guidance on the design of acoustofluidic devices by exploring the optimum heights of the microchannel. The model configuration is based on the work of Nama *et al* [1]. The perturbation method is utilized to solve the nonlinear governing equations of the fluid motion by approximating the overall solutions with the first-order and second-order flow components. The motions of particles of different radii are analyzed, and the critical particle size, which indicates the transition from the drag force dominant regime to the radiation force dominant regime, is determined for different channel heights. We carry out extensive parametric studies that involve a series of channel aspect ratios. The optimum height of the channel is found that corresponds to the high accuracy and small time scale of the particle manipulation. The results from this study provide useful guidelines on the design of the SSAW-based devices.

Model Setup

The numerical model setup is presented in **Figure** 1. **Figure** 1(a) demonstrates a 3D view of the SSAW-based device consisting of a pair of interdigital transducers (IDTs) bonded on the piezoelectric substrate and a rectangular PDMS microchannel (width $W = 600$ μm and height $h = 125$ μm) filled with water inside. **Figure** 1(b) shows a 2D cross-sectional view of the device, a standing surface acoustic wave (SSAW) is generated at the surface of the substrate by triggering the IDTs with harmonic signals, whose frequency is of 6.65MHz and wavelength is of 600 μm. In **Figure** 1(c), a 2D reduced computation domain Ω is presented with the velocity boundary condition at the bottom boundary Γ_v to model the acoustic actuation and the impedance boundary condition at impedance boundaries Γ_i to represent the PDMS material. As shown in **Figure** 1(d), three target boxes with 5 μm width and 125 μm height are set at pressure nodes (PNs) where the final position of the particles located at. The model is verified through comparing the simulation results with both numerical and experimental results in Mikhaylov *et al* [3]. Our results show good agreements with results in Mikhaylov.

In terms of the mathematical model, the Navier-Stokes equation and the continuity equation, as the governing equation of the fluid motion, is solved by the perturbation method [2] and the Finite Element Method (FEM).
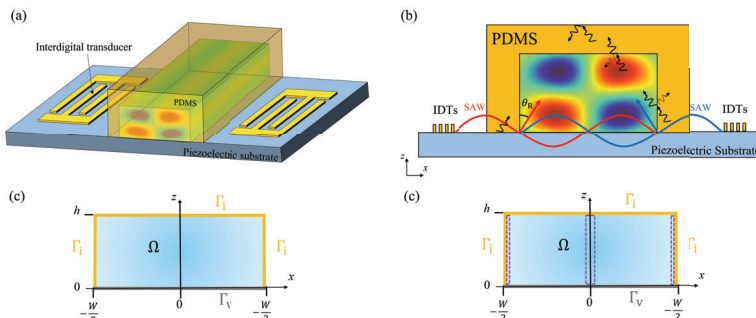

Figure 1: (a) Three-dimensional Sketch of the Model setup. (b) Physical picture of the SSAW-based device in cross-sectional view. (c) 2D reduced cross sectional sketch of computational domain Ω. (d) Schematic of the target boxes.

Parametric study for the channel height

The motion of the particles in the SSAW-based devices are mainly governed by the radiation force and the Stokes drag force, while the gravity force and buoyance are almost canceled out. The radiation force is

proportional to the particle radius cubed, while the Stokes drag force is linearly proportional to the particle radius. Particle acoustophoresis is induced by the radiation force, under whose influence particles will aggregate to pressure nodes (PNs) where the minimal pressure located at. For this to take place, the particle radius is required to be larger than a critical radius r_{crit}, as shown in **Figure** 2(a). Furthermore, the critical particle radii are determined for various channel heights in **Figure** 2(b). The critical particle radius decreases about 55% with the increase of the channel height from 100 μm to 900 μm.

In addition, **Figure** 2(c) captures the accuracy and the time scale of the particle separation within four times the wavelength. The accuracy is defined as the ratio of the particles collected at the target boxes at the final phase over the total number of the particles in the channel. To the knowledge of the authors, it is the first time that the optimum heights are determined for the devices with heights ranging from less than a wavelength to four times the wavelength. In accordance with the high separation accuracy over 95% and separation time below 50 s, we determine the optimum heights and find the existence of fluid wavelength λ_f dependence on optimum heights. The optimum heights are within the range of $0.6{\sim}0.8\lambda_f$, $1.1{\sim}1.3\lambda_f$, $1.6{\sim}1.8\lambda_f$, $2.2{\sim}2.4\lambda_f$, $2.8{\sim}3\lambda_f$, $3.3{\sim}3.5\lambda_f$, $3.9{\sim}4\lambda_f$. Normally, for the field with certain pressure distribution, the particles near the upper and lower boundaries move diagonally towards PNs resulting in being stuck at these two boundaries causing low separation accuracy, as shown in **Figure** 2(d)-(e). Instead of being stuck at the lower boundary, the particles near the lower boundary move diagonally upwards in **Figure** 2(f)-(g), which potentially prevent them from being stuck. In addition, it is worth mentioning that the vertical distances between two adjacent maximal first-order absolute pressure are not all exactly equal to half the fluid wavelength λ_f due to the slight difference of the pressure distribution with the increase of the channel height. Therefore, the optimum heights range for over three times λ_f has a small shift towards higher heights.
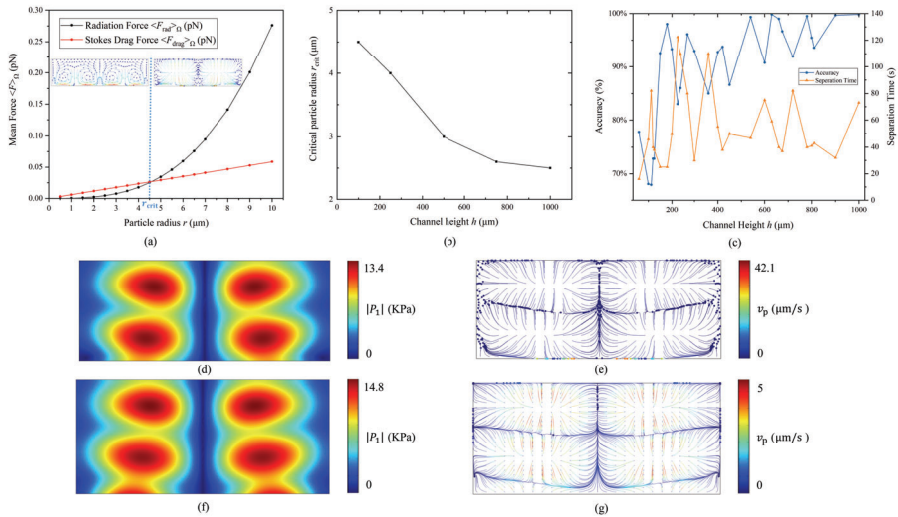

Figure 2: (a)Mean radiation force and Stokes drag force over the channel cross-section Ω at different particle radii for channel height $h = 125$ μm. (b) The critical particle radii at different channel height. (c) Particle separation accuracy and separation time at different channel heights. (d)-(g) First-order absolute pressure distribution and particle trajectories for channel height $h = 240$ μm (d)-(g) and $h = 270$ μm (f)-(g), respectively.

Conclusion

We have reported the results of our parametric studies concerning the channel heights. The critical particle size, the particle separation accuracy and the separation efficiency are used as criteria to determine optimum channel heights. The model is validated against previous studies with good agreement. The results shows that the critical particle size decreases about 55% with the increment of the channel heights from 100 μm to 900 μm. Furthermore, the optimum channel heights, which have a fluid wavelength dependent, are determined for the channel heights from less than one fluid wavelength to four times the fluid wavelength.

References

[1] Nama, N. et al. Numerical study of acoustophoretic motion of particles in a PDMS microchannel driven by surface acoustic waves. Lab. Chip 15, 2700–2709 (2015).
[2] H. Bruus, 'Acoustofluidics 2: Perturbation theory and ultrasound resonance modes', Lab Chip, vol. 12, no. 1, pp. 20–28, 2012, doi: 10.1039/C1LC20770A.
[3] Mikhaylov, R., et al., Development and characterisation of acoustofluidic devices using detachable electrodes made from PCB. Lab Chip, 2020. 20(10): p. 1807-1814.

Characterising low frequency bulk-driven acoustic streaming in air

Christopher Stone[1], Bruce W Drinkwater[1], Anthony Croxford[1] and Mahdi Azarpeyvand[1]

[1]Department of Mechanical Engineering, University of Bristol, Bristol, United Kingdom
E-mail: c.stone@bristol.ac.uk, URL: http://www.bristol.ac.uk/engineering/research/ndt/

Introduction

The majority of applications of acoustic streaming thus far have been limited to high-frequency (MHz) microfluidics, where boundary effects dominate. However, due to recent developments in areas of research in ultrasonics such as haptics [1], bulk-driven 'Eckart' streaming is becoming increasingly relevant. While the radiation force is predominantly utilised in haptic configurations, acoustic streaming flows can introduce cooling sensations on the skin and can potentially be sensed by hairs [2], hence it is important to be able to accurately characterise the streaming field. This research focusses on the numerical modelling and experimental measurements of airborne acoustic streaming induced by high amplitude, low frequency ultrasound produced by two types of transducers: Langevin horns and focussed arrays of parking sensors. Studies investigating how parameters such as frequency, beam divergence, attenuation, air temperature and humidity affected the streaming field were conducted.

Modelling approach

A two-step method was used in COMSOL Multiphysics to model the streaming velocity field induced by a high intensity acoustic pressure field. In the first step, the first order acoustic fields are calculated in the frequency domain, with the excitation modelled by a simple velocity condition (the magnitude of which was scaled to match experimental measurements). A second steady state step is then used to compute the fluid dynamics, where the streaming force vector, $\mathbf{F}_s$, is imparted on a unit volume dv using the acoustic intensity vector, $\mathbf{I}$, from the previous step:

$$\mathbf{F}_s = \frac{2\beta\mathbf{I}}{c}dv \tag{1}$$

where β is the attenuation coefficient (in Nepers per metre) and c is the speed of sound. An example of the predicted acoustic pressure field for a 26 kHz Langevin horn is displayed in Figure 1a, with the resulting streaming velocity field shown in Figure 1b. Here the transducer is modelled as a piston source with a velocity condition on a boundary representing the transducer face.
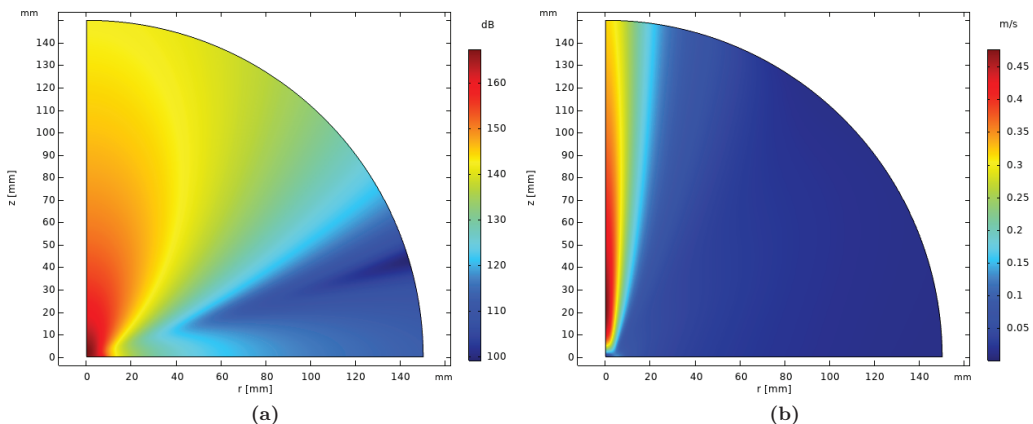

Figure 1: Axi-symmetric plots of COMSOL predictions for **(a)** the acoustic field from a 26 kHz Langevin horn and **(b)** the resulting streaming velocity field using a k-ϵ turbulent fluid dynamics model.

Experimental measurements

Two different experimental examples were explored: a Langevin horn with a resonant frequency of approximately 26 kHz, and a 36-element focussed array of 40 kHz parking sensor transducers. The array was designed to have an equivalent acoustic pressure at the focal point to the maximum acoustic pressure of the Langevin horn (≈ 170 dB), so the streaming velocity results could be compared. Naturally, the acoustic field of the focussed array is very different to that of a Langevin horn (which can be assumed to act as a dipole source); beyond the focal point the acoustic beam diverges due to the layout of the individual transducers. However, a circular aperture can be introduced to alter the acoustic field beyond the focal point, so that it is similar to that of a Langevin horn. Again, this allows experimental results to be more comparable. Acoustic pressure measurements were made using a Brüel & Kjær Type 4138 1/8" Pressure-Field Microphone, while streaming velocity fields were acquired using hot-wire anemometry with a Dantec 55P51 single-wire probe operated by a Dantec StreamWare Pro frame with CTA91C10 modules. Both the microphone and hot-wire probe were mounted to an x-y-z scanning system, allowing the 3D field to be characterised. These experimental measurements were used to validate and improve the accuracy of the numerical model.

Parametric studies

Various fluid mechanics interfaces were implemented for the streaming velocity field model: Figure 2 shows the axial streaming velocity predictions of a laminar versus a turbulent k-ϵ model [3]. The velocity in the turbulent model decays much faster than the laminar model predicts, due to the streaming jet spreading wider as the distance from the source increases (see Figure 1b). Considering the Reynolds number (Re ≈ 430 in this case, taking the wavelength as the characteristic dimension at 26 kHz) some turbulent effects are to be expected, and it follows that the turbulent model yielded a streaming field that was closer in agreement with experimental measurements than the laminar flow model.

Various studies were performed to identify what parameters were the most influential on the streaming field. It is well known that higher acoustic frequencies lead to higher streaming velocities due to the increased attenuation, however

Figure 2: An example of predicted axial streaming velocities with turbulent and laminar fluid mechanics models.

the capabilities of generating Eckart streaming with real transducers has thus far not been explored. The shape of the acoustic field affects the acoustic intensity and hence the streaming field, and is inherently coupled to the frequency. By using different apertures and frequencies the shape of the acoustic field can be modified and thus the streaming field can be customised to suit any scenario. Furthermore, the effects of humidity and temperature are quantified, highlighting the importance of the environmental conditions on the streaming field that can be achieved.
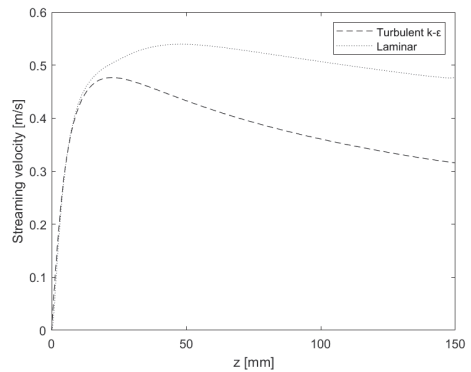
Conclusion

An experimentally validated finite-element model of low-frequency 'Eckart' streaming has been created, exploring the effects of various transducer properties as well as environmental conditions on the streaming field. The work presented here provides greater understanding of the mechanisms behind bulk-driven acoustic streaming, which allows haptics users to optimise their set-ups to either maximise or minimise acoustic streaming.

References

[1] A. Marzo, T. Corkett, and B. Drinkwater. *IEEE Transactions on Ultrasonics, Ferroelectrics, and Frequency Control* **65(1)**, 102-111 (2018).

[2] M. Nakajima, K. Hasegawa, Y Makino and H. Shinoda. *IEEE Transactions on Haptics* **14(4)**, 874-884 (2021).

[3] COMSOL Multiphysics® v. 5.5. *The Fluid Flow Interface User's Guide* 887-916 (2021).

Thermoacoustic streaming in a linear temperature gradient for perpendicular and parallel ultrasound fields

Enrico Corato[1], Jonas Helboe Joergensen[2], Ola Jakobsson[1], Wei Qiu[1], Henrik Bruus[2], and Per Augustsson[1]

[1]Department of Biomedical Engineering, Lund University, Lund, Sweden
e-mail: enrico.corato@bme.lth.se
[2]Department of Physics, Technical University of Denmark, Kongens Lyngby, Denmark

Introduction

Thermal gradients inside acoustic resonators have been previously shown to drive a fast thermoacoustic streaming flow [1]. In this work, we investigate how a stationary linear temperature gradient affects acoustic streaming. The fluid flow is observed in experiments with an acoustic field either perpendicular or parallel to the thermal gradient, comparing the streaming with numerical simulation.

Theory and background

In an acoustic resonator, physical properties variations in the propagation medium result in an acoustic body force [2], which is dependent on density and compressibility gradients. Temperature affects the properties of the media, and this can be exploited to induce a sustained acoustic body force. We previously investigated how a liquid heated by light absorption can induce a non-dissipative body force [1]. A thermal gradient of only few degrees decisively distorts and enhances acoustic streaming, which transitions from boundary- to bulk-driven by the thermally induced acoustic body force. Furthermore, this phenomenon can arise due to heating by viscous friction at the resonator boundaries, significant especially if the cavity is not confined by materials with similar thermal properties [3]. Here, we studied how linear temperature gradients established by heat conduction can affect acoustic streaming.

Experimental procedure

Both outer side walls of a glass-silicon-glass chip were put in thermal contact with two aluminium plates, whose temperature were independently controlled by peltier elements. A channel ($W = 375$ µm, $H = 150$ µm) was etched through the silicon and, due to its high thermal conductivity, the inner side walls were assumed to have the same temperature as the aluminium plates, leading to a steep linear temperature drop across the width of the water-filled channel. The temperature was mapped employing Rhodamine B as thermosensitive fluorophore.

Once the temperature gradient was confirmed, an acoustic standing wave was introduced into the system by piezoelectric actuation. The steaming was characterised via general defocusing particle tracking (GDPT) [4], employing 1 µm polystyrene beads as tracer particles. Thermoacoustic streaming induced by a sound field resonating either along the height or the width of the channel was investigated.

Results and Discussion

With a standing wave in the channel height, the boundary-driven acoustic streaming was barely noticeable (Figure 1a). However, as seen in Figure 1b, once a thermal field across the width is introduced, fast thermoacoustic streaming arises due to the considerable role of the acoustic body force. One peculiar result to consider in this experiment is the asymmetric shape of the resulting flow. If compared with 2D simulation using an ideal sound field (Figure 1c), the resulting thermoacoustic streaming would comprise two symmetric rolls along the channel height. This is because the body force pushes the liquid towards the hot wall at the pressure antinodes, due to the higher magnitude of the compressbility term compared to the density term. The flow would then close the circulation in the centre. However, if the sound field is deformed (with a curved pressure node), a result as in Figure 1d is to be expected. Here, the lower roll would expand in most of the channel, choking the top roll and confining it in the top corners. This is in good agreement with the experimental result shown in Figure 1b. The deformed sound field was indeed confirmed by GDPT of 5 µm polystyrene particles levitation, whose final position is shown in grey in Figure 1b bottom left black box.
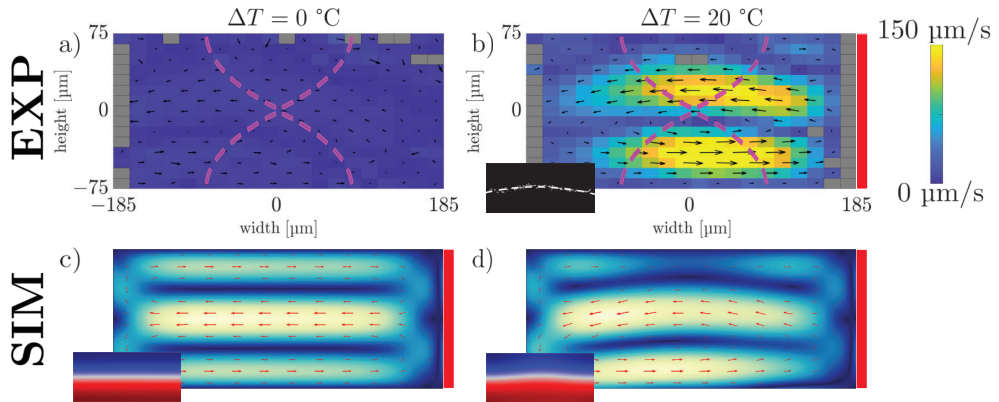
Figure 1: a-b) GDPT results showing the cross-sectional streaming in the channel with sound actuated at 4.96 MHz. The colour represents the velocity magnitude, while the black arrows its direction. Areas with no data are in grey. The ideal standing wave is represented in magenta. The cold wall was at 20 °C, and the hot one at 40 °C (shown as a red rectangle). a) Without any T difference, acoustic streaming is barely detectable. b) Once the thermal gradient is introduced, the thermoacoustic streaming becomes immediately very fast. The final positions of levitated 5 µm polystyrene beads are shown in grey in the black box in b), with a parabolic fitting shown by the dotted white line. c-d) 2D simulation of thermoacoustic streaming with perpendicular sound and thermal fields (blue- low speed, yellow-high speed), with red arrows giving the direction. Parameters were different from the experiments. The corresponding pressure field is shown in the bottom left of each figure, with the nodal line in white. The hot wall is depicted in red. c) Perfect acoustic field leads to symmetric thermoacoustic rolls. d) Even a slightly curved pressure field results in disruption of the streaming symmetry.

With a standing wave in the channel width, the classic Rayleigh streaming is present (Figure 2a). When the temperature difference is introduced, this latter is heavily deformed until it reaches an "eight" shape (Figure 2b). The flow is faster (roughly double the speed), but its main feature is its strong three-dimensionality. In the ideal case, with perfect sound and thermal fields, the liquid should not move: the acoustic body force would always be pointing towards the hot wall with constant magnitude in the xz plane. In real systems, however, even small variation in the acoustic or thermal field will break this equilibrium. Where the sound field is relatively strong, the body force pushes the liquid to the hot wall, and it then recirculates where the sound pressure is low.
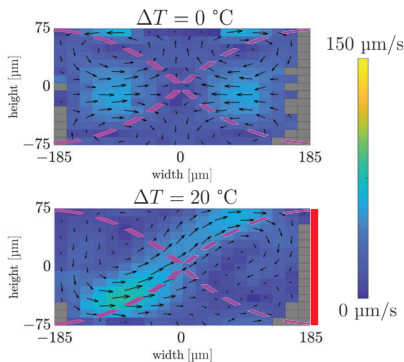

Figure 2: GDPT results showing the cross-sectional streaming in the channel with sound actuated at 1.97 MHz. The colour represents the velocity magnitude, while the black arrows its direction. Areas with no data are in grey. The ideal standing wave is represented in magenta. The cold wall was set at 20 °C, and the hot one at 40 °C (shown as a red rectangle). a) With a standing wave along the channel width, the classic Rayleigh streaming can be observed. b) Once the thermal field is introduced, the body force drives the fluid at more than double the speed, which deforms the streaming rolls.

Conclusion

The interaction of standing sound waves with a linear thermal field was investigated. On the one hand, when the two fields were parallel, a highly complex flow pattern was observed, strongly three-dimensional and dependent on the sound pressure inhomogeneities. On the other hand, with a standing wave perpendicular to the thermal field, the flow was more ordered (i.e, mainly 2D) and the velocity increase was dramatic: the acoustic streaming went from barely noticeable to exceeding 150 µm/s, which is fast enough to deform the thermal field.

In conclusion, further investigation is needed to fully understand the complex interaction between sound and temperature differences in fluids. Nevertheless, the results here presented give a good indication of what can be achieved, with applications ranging from fast mixing, enhanced heat transfer, and overall device optimisation. All considered, this type of sound-temperature interaction is very dependent on system-specific inhomogeneities, which make the modelling and understanding of the phenomena inherently difficult.

References
[1] Qiu, W. *et al.*, Phys. Rev. Lett. **127**, 064501 (2021).
[2] Karlsen, J.T. *et al.*, Phys. Rev. Lett. **117**, 114504 (2016).
[3] Joergensen, J.H. *et al.*, https://arxiv.org/abs/2112.11410 (2021).
[4] Barnkob, R. and Rossi, M., Fluids **61**, 110 (2020).

Simulation of SAW-Biological cell interaction for extract shear stress on osteoblastic SaOs-2 bone cells

D.S.Bidouba Sanvany[1], F.Kosior[1], D.Beyssen[1], A.Gigodot[1], E.Gaudoin[1] and F.Sarry[1]

[1] Université de Lorraine, CNRS, IJL, F-54000 Nancy, France
E-mail: doll-spencerh.bidouba-sanvany@univ-lorraine.fr

I. Introduction

Surface acoustic waves (SAW) are currently being used to study their interaction with biological particles to perform studies on cell proliferation, growth, death, and migration. The effect of shear stress on cells has been shown to play a major role in cell modification, providing more details about their function and potential changes.

Stamp et al.[1] present an ultrasound approach to dynamic stimulation and tissue healing in osteoblast-like SaOs-2 cells using surface acoustic waves (SAW) on a chip. Her studies are performed without undesirable side effects such as increased substrate temperature or nutrient flux associated with SAW. Her results show that dynamic mechanical and electrical stimulation induced by surface waves directly promotes cell growth and thus rapid tissue regeneration.

S. Brugger[2] presents studies on wound healing and cell growth in vitro under the influence of radiofrequency (rf) cell stimuli. These stimuli are generated either by piezo-active surface acoustic waves (SAW) or by electric fields generated by microelectrodes, both at frequencies of about 100 MHz. Using live cell imaging, he studied the healing of artificial wounds on a piezoelectric chip as a function of time and power for different cell lines. His results show that vibration stimulation of cells based on surface acoustic waves can be an alternative to conventional ultrasound treatment.

The shear stresses acting on the cells are responsible for the different changes observed after acoustic wave stimulation. Their physiological value is between 5 and 12 dyn/cm^2[3]. However, it is not possible to determine the shear stress values experimentally with surface acoustic wave devices, so a simulation model must be developed. In this abstract, we present the simulation developed to extract stresses from osteoblastic SaOs-2 bone cells for well stimulation for a 40 MHz probe and optimize fluid height for better stimulation.

II. Theorical simulation approach

Based on the theory of perturbation [4] and taking into account the mass law conservation and the angular moment conservation, we are able to rewrite the sound equation (first order):

$$\frac{\partial \rho_1}{\partial t} + \rho_0 (\nabla . u_1) = 0 \tag{1.a}$$

$$\rho_0 \frac{\partial u_1}{\partial t} = -\nabla p_1 + \left[\mu_B + \frac{\mu}{3}\right] \nabla(\nabla . u_1) - \mu \nabla^2 u_1 \tag{1.b}$$

and also the streaming equation (second order):

$$\rho_0 \nabla . \langle u_2 \rangle = -\nabla . \langle \rho_1 u_1 \rangle \tag{2.a}$$

$$-\langle \nabla p_2 \rangle + \left[\mu_B + \frac{\mu}{3}\right] \langle \nabla(\nabla . u_2) \rangle - \langle \mu \nabla^2 u_2 \rangle = \langle \rho_1 \frac{\partial u_1}{\partial t} \rangle + \rho_0 \langle (u_1 . \nabla) u_1 \rangle \tag{2.b}$$

where μ is the dynamic viscosity, μ_B is the volumic viscosity, u_1 is the first order velocity of the fluid particle ρ_1 is the first order density and ρ_0 is the fluid density at equilibrium. $\langle A \rangle$ is the time average of A. From this theorical approach we prosed a simulation model with Comsol Multiphysics.

III. Results and Discussion

We performed our simulations on Comsol 5.6 and divided our resolution method into 4 parts. The first step is the generation of the acoustic wave. A 3 cm long 128 Y-X lithium niobate substrate with piezoelectric coupling is used as a probe. Thermoacoustic physics is used to generate the acoustic field with impedance boundary conditions to account for the interaction between the wave and the fluid. Laminar physics is used to generate the flow, considering the non-slip condition. Particles are considered by particle tracking.

The simulations were performed in 2D due to the complexity of building a 3D model. The first important point is the generation of the wave. Figure 1.a) shows the comparison of the evolution of the amplitude of SAW between the experiment and the simulation. We observe a perfect agreement between the profile of the curves and a maximum difference of 4.5% at 19 dBm. Figure 1.b) shows the evolution of the maximum particle velocity as a function of the power applied to the electrodes for a 40 MHz probe. We generally observe a relative error of less than 10%, except at 19 dBm (79 mW) where we have a relative error of 33.9%. Thus, only a few points are available for estimating the velocities, which can significantly increase the error between simulation and experiment at certain powers. Figure 1.c) shows the evolution of adherent cells for different liquid height, with the same evolution for all applied powers. For a fixed liquid height, it can be observed that the shear stress increases with increasing power. The maximum shear stress is reached at a liquid height of 5 mm.
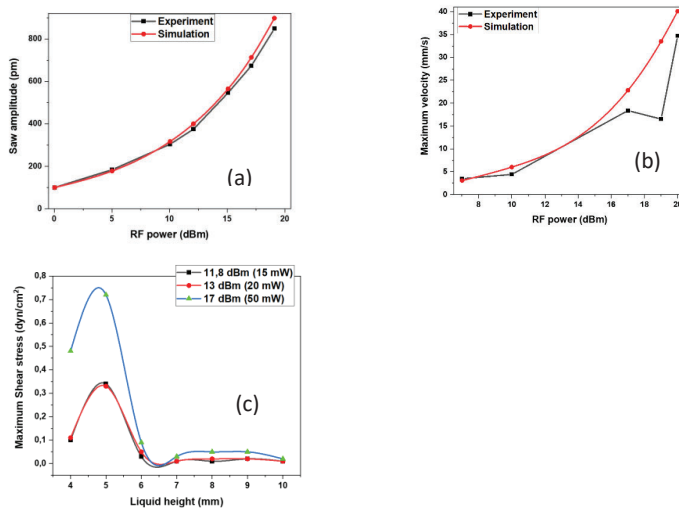

Figure1 : Comparison between simulation and experiment and simulation result for shear stress, (a) saw amplitude, the experimental results are extracted from Greco for a 50 MHz probe ; (b) particle velocity at 40 MHz; (c) simulation results of shear stress for adherent cells with a 40 MHz probe.

IV. Conclusion

Numerical simulation was performed on a two dimensional model. Comparison with experiment to validate our simulation model showed good agreement in the electrical and mechanical properties of the SAW, in the velocity of the particles, and even in the shape of the stream and the direction of rotation of the particles. Using our model, we found that the optimal liquid height for the stimulation of the osteoblastic SaOs-2 bone cells is 5 mm.

References
[1] M. E. M. Stamp *et al.*, « Exploring the Limits of Cell Adhesion under Shear Stress within Physiological Conditions and beyond on a Chip », *Diagnostics*, vol. 6, nº 4, Art. nº 4, déc. 2016, doi: 10.3390/diagnostics6040038.
[2] M. E. M. Stamp, M. S. Brugger, A. Wixforth, et C. Westerhausen, « Acoustotaxis – in vitro stimulation in a wound healing assay employing surface acoustic waves », *Biomaterials Science*, vol. 4, nº 7, p. 1092-1099, 2016, doi: 10.1039/C6BM00125D.
[3] X. Xu *et al.*, « Low shear stress regulates vascular endothelial cell pyroptosis through miR-181b-5p/STAT-3 axis », *Journal of Cellular Physiology*, vol. 236, nº 1, p. 318-327, 2021, doi: 10.1002/jcp.29844.
[4] N. Wesley Le Mars, « Acoustic Streaming », 1965.

Ultrasound-enhanced 3D cell cultures in a multi-chambered microwell chip for anticancer cytotoxicity studies

<u>Martin Wiklund</u>[1], Niklas Sandström[1], Valentina Carannante[2], Karl Olofsson[1], Patrick A. Sandoz[1], Hanna Van Ooijen[1], Quentin Verron[1], Thomas Frisk[1] and Björn Önfelt[1,2]

[1] Dept. of Applied Physics, SciLifeLab, KTH Royal Institute of Technology, Stockholm, Sweden
[2] Dept. of Microbiology, Tumor and Cell Biology, SciLifeLab, Karolinska Institutet, Stockholm, Sweden
E-mail: martin@biox.kth.se, URL: http://www.kth.se/profile/bmw

Introduction

Here, we present a set of miniaturized cytotoxicity assays for multiplexed high-content screening of drug and immune sensitivity for personalized medicine, enabled by a novel ultrasound-actuated multi-chambered microwell chip. In contrast to conventional systems [1] and our previous work [2], this methodology [3] offers the unique and flexible combination of rapid and multiplexed high-resolution cytotoxicity screening in 2D or 3D cell cultures in a single experiment.

Method

The multichambered microwell device consists of a Si-glass microwell chip and a bonded multichambered polymer frame, forming liquid chambers above each microwell array (figure 1). In the bottom of the chip, an ultrasound transducer is placed, creating half-wavelength resonances in each of the microwells in parallel. Target cells are cultured in monolayers (in 2D – without ultrasound) or as spheroids (in 3D – with ultrasound). Cell culture media, cells, drugs, and reagents are pipetted into each chamber and live cell imaging using an inverted fluorescence microscope is performed in the microwells over several days.
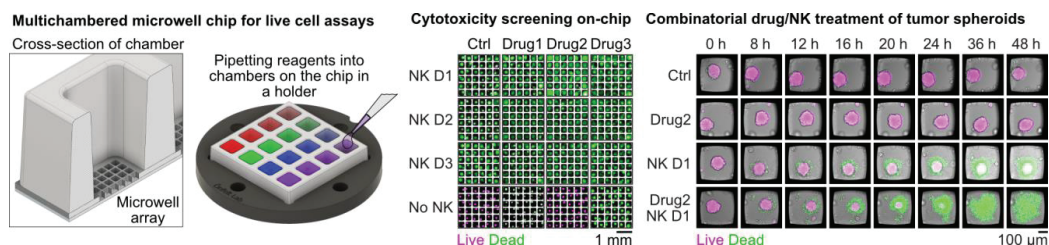

Figure 1: Miniaturized live cell assays for cytotoxicity screening in a multichambered microwell chip.

Results

Four different screening assays for drug and immune cell cytotoxicity are reported. We demonstrate the concentration response of ovarian cancer cells treated with the drug Paclitaxel, long-term multiplexed drug cytotoxicity screening using tumor spheroids of ovarian or non-small lung cancer cells, long-term cytotoxicity screening of primary immune cells against renal carcinoma spheroids and combinatorial treatments of ovarian cancer spheroids. Additionally, we also provide detailed analyses of single cells or intracellular proteins in each assay.

Conclusion

With this work, we demonstrate a novel methodology based on the miniaturization of cell culture substrates and live cell assays aiming for applications in drug development and precision medicine.

References

[1] K. V. Kitaeva *et al.*, "*Cell Culture Based in vitro Test Systems for Anticancer Drug Screening*", Frontiers Bioeng. Biotechnol. **8**, 322 (2020).
[2] K. Olofsson *et al.*, "*Acoustic formation of multicellular tumor spheroids enabling on-chip functional and structural imaging*", Lab Chip **18**, 2466 (2018).
[3] N. Sandström *et al.*, "*Miniaturized and multiplexed high-content screening of drug and immune sensitivity in a multichambered microwell chip*", Cell Report Meth. **2**, 100256 (2022).

Abstracts Only Presentations

A Flexible Printed Circuit Board Based SAW Device for Effective Concentration of Micro-particles

Povilas Dumčius[1], Roman Mikhaylov[1], Xiaoyan Zhang[1], Mercedes Stringer Martin[1], Aled Clayton[2], Chao Sun[3] and Xin Yang[1]

[1] Department of Electrical and Electronic Engineering, School of Engineering, Cardiff University, Cardiff CF24 3AA, UK
[2] Tissue Micro-Environment Group, Division of Cancer & Genetics, School of Medicine, Cardiff University, Cardiff CF14 4XN, UK
[3] School of Life Sciences, Northwestern Polytechnical University, 710072, P.R. China

E-mail: yangX26@cardiff.ac.uk

Introduction Microparticle concentration is critical in various fields, such as micro-assembly [1], microfabrication [2], and tissue engineering [3]. Besides improving the sensitivity of analytes detection, it is a valuable diagnostic tool in the purification of blood plasma from its cellular components. Ultracentrifugation is one of the most widely used methods for performing such tasks, however time and labour costs, as well as costly equipment, prevent most labs from utilizing it. Alternative methods [4] exist, including optical, dielectrophoretic, magnetic, hydrodynamic, and acoustic. Several factors have contributed to the popularity of acoustic methods, such as their biocompatibility, ease of use, low contamination rate, speed, simple operation, and low cost. To construct a surface acoustic wave (SAW) device, a cleanroom facility is required to pattern an interdigital transducer (IDT) using photolithography. The process permanently patterns IDTs on a piezoelectric wafer, any damage or modification to the IDT requires another run of photolithography process. It is desired to have a fast-prototyping technique to fabricate IDTs on demand, which will be able to reduce the requirement of cleanroom fabrication for fabricating the device for efficient cell concentration.

Device A thorough assembly and design methods are described in our previous work where we show particle patterning using standing surface acoustic waves (SSAW) [5], [6]. Here we focus on expanding the device applications by using the Flexible Printed Circuit Board (FPCB) capability of performing particle concentration. Figure 1 shows an FPCB IDT pressed on the surface of a 128º Y-Cut Lithium Niobate. A 20MHz signal is then applied, sending travelling SAW along the surface. The wave then couples into a sample held together by a ring of polydimethylsiloxane (PDMS). To avoid a clean room for PDMS mould manufacturing a 3D printed jig was used to make the boundary rings. As the travelling SAW passes through the sample a rotation is induced, causing the dispersed particles to concentrate due to centrifugal forces.
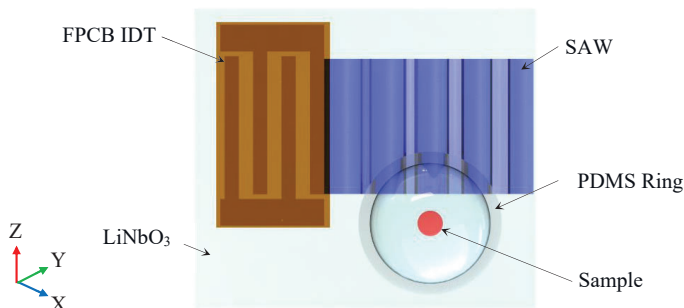

Figure 1. Flexible Printed Circuit Board (PCB) interdigital transducer (IDT) setup on a 128 Y-Cut Lithium Niobate for particle concentration. A 20MHz signal is applied to cause the SAW to induce a centrifugal force on the suspended particles for concentration.

Results and Discussion To demonstrate the capabilities of the concentration Figure 2 shows 8 µm and 1 µm suspended in 15 µL of phosphate-buffered saline (PBS). Initially, the particles randomly disperse in the fluid, once the SAW is turned on, a small aggregate form in the middle and continue to grow over time, ultimately demonstrating a quick concentration effect in under 15 s for both 8 µm and 1 µm particles. The device features a major advantage of reconfigurability. If the manufactured IDT is desired no more, another one can be replaced without having to replace the LiNbO₃. Our method compares with cleanroom fabricated IDTs

where a similar device [7] was able to concentrate 10 μm particles in approximately 20 s. Other studies [8], [9] have also shown similar time of concentration for 5 μm. Alternative methods [10] utilizing ultrasonic waves were shown to concentrate particles in 10-15 s. Since FPCB IDTs can perform equipollently to that of cleanroom manufactured and other existing acoustic methods, it could be regarded as a viable candidate in the SAW generation as an alternative method.
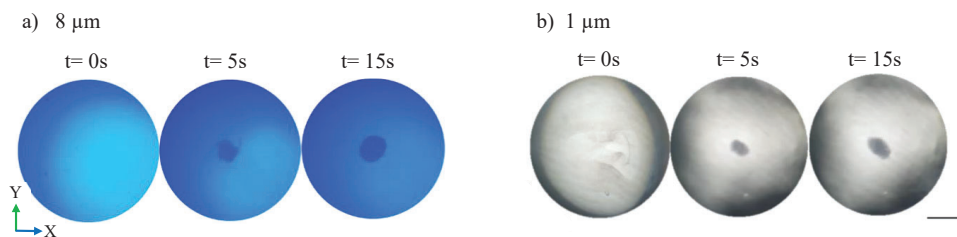

Figure 2. Flexible PCB IDT centrifuge demonstrating a) 8μm and b) 1μm concentration over time. Scale bars 2mm.

Conclusions Our group explores alternative methods of making acoustofluidic devices, to allow the technology to reach a wider audience of laboratories and researchers. By utilizing FPCB and a 3D printer, a SAW can be generated without the need of using a cleanroom facility. We demonstrate that it is possible to create a travelling SAW for concentrating different-sized particles, ultimately proving itself as a viable candidate for the use of future acoustofluidic applications where costs, time, reconfigurability, and ease of use are essential.

References
[1]   H. Kim, T. Kim, D. Kim, and W. Shim, "Wave-Tunable Lattice Equivalents toward Micro- and Nanomanipulation," *Nano Lett.*, vol. 16, no. 10, pp. 6472–6479, Oct. 2016, doi: 10.1021/acs.nanolett.6b02973.
[2]   M. K. Nichols *et al.*, "Fabrication of Micropatterned Dipeptide Hydrogels by Acoustic Trapping of Stimulus-Responsive Coacervate Droplets," *Small*, vol. 14, no. 26, p. 1800739, Jun. 2018, doi: 10.1002/smll.201800739.
[3]   "Engineering multi-layered tissue constructs using acoustic levitation," p. 11.
[4]   S. Gurunathan, M.-H. Kang, M. Jeyaraj, M. Qasim, and J.-H. Kim, "Review of the Isolation, Characterization, Biological Function, and Multifarious Therapeutic Approaches of Exosomes," *Cells*, vol. 8, no. 4, p. 307, Apr. 2019, doi: 10.3390/cells8040307.
[5]   R. Mikhaylov *et al.*, "A reconfigurable and portable acoustofluidic system based on flexible printed circuit board for the manipulation of microspheres," *J. Micromech. Microeng.*, vol. 31, no. 7, p. 074003, Jul. 2021, doi: 10.1088/1361-6439/ac0515.
[6]   R. Mikhaylov *et al.*, "Development and characterisation of acoustofluidic devices using detachable electrodes made from PCB," *Lab Chip*, vol. 20, no. 10, pp. 1807–1814, 2020, doi: 10.1039/C9LC01192G.
[7]   G. Destgeer, H. Cho, B. H. Ha, J. H. Jung, J. Park, and H. J. Sung, "Acoustofluidic particle manipulation inside a sessile droplet: four distinct regimes of particle concentration," *Lab Chip*, vol. 16, no. 4, pp. 660–667, 2016, doi: 10.1039/C5LC01104C.
[8]   A. Sudeepthi, A. K. Sen, and L. Yeo, "Aggregation of a dense suspension of particles in a microwell using surface acoustic wave microcentrifugation," *Microfluid Nanofluid*, vol. 23, no. 5, p. 76, May 2019, doi: 10.1007/s10404-019-2243-9.
[9]   H. Nam, H. J. Sung, J. Park, and J. S. Jeon, "Manipulation of cancer cells in a sessile droplet *via* travelling surface acoustic waves," *Lab Chip*, vol. 22, no. 1, pp. 47–56, 2022, doi: 10.1039/D1LC00801C.
[10]   Y. Kurashina, K. Takemura, and J. Friend, "Cell agglomeration in the wells of a 24-well plate using acoustic streaming," *Lab Chip*, vol. 17, no. 5, pp. 876–886, 2017, doi: 10.1039/C6LC01310D.

Acoustofluidic-assisted colorimetric analysis for point-of-care testing

Liying Zhang[1], Panpan Chen[1], and Shuhu Du[1]

[1] School of Pharmacy, Nanjing Medical University, Nanjing, Jiangsu 211166, China
E-mail: zly@njmu.edu.cn

Introduction

It is well known that point-of-care (POC) testing has the potential to revolutionize global healthcare, especially in resource constrained or non-centralized settings, owing to the fact that prompt analysis reduces delays caused by clinical sample collection and storage, transport to a central laboratory for analysis, and enables earlier disease diagnosis [1]. Numerous POC diagnostic systems that allow for the assaying of analytes in complex samples have been developed.

Acoustofluidics, which integrates acoustic manipulation with microfluidic devices, has revealed enormous capability in bioanalytical chemistry [2]. The acoustofluidic-based devices are miniaturized with reduced sample volume requirements and an overall reduction in device footprint. With these advantages, acoustofluidic technologies are emerging as promising tools especially for POC applications [3]. However, to become practical POC tools, acoustofluidics-based diagnostic devices still face one practical challenge. Acoustofluidic platforms mainly provide for sample preparation or manipulation of micro/nano-scale objects, meaning that they cannot be implemented in POC settings by themselves. The additional downstream analytical techniques, based on expensive or bulky instrumentation, will still be required for quantitative characterization, signal readout, or medical testing. To addresses the limitations of acoustofluidics techniques as analytical tool, we have developed a cellphone-based acoustofluidic platform (Figure 1A) that can achieve POC analysis by integrating colorimetric detection and cellphone camera-based imaging with acoustofluidic nanoparticle concentration. Through synthesizing a series of nanoprobes, the platform can be used for rapid and sensitive analysis of different targets, such as hemoglobin (Hb) and dipicolinic acid (DPA). With the specific advantages of low cost, small sample volume and short detection time, we believe that acoustofluidics-assisted visual platform will be a prospective candidate for POC testing applications.

Mechanism of acoustofluidic assisted colorimetric analysis

For visual detection, as the fluorescence intensity emitted by a group of probes is proportional to their concentration in the medium, high-concentrations of the probes are usually needed to provide emission light that is strong enough to be easily observed by naked eyes. However, for the single-responsive probe, especially the "off-on" mode, the increased usage of probe also causes a decrease in the sensitivity of detection because more target sample is needed to cause the fluorescence change. To improve the sensitivity of visual detection, acoustofluidic nanoparticle concentration device was fabricated and integrated with traditional fluorescent-probe-based testing (Figure 1A). With the activation of acoustic signal, particles will be enriched by acoustic radiation force producing from the scattering of the acoustic waves, and the localized particle concentration is increased. The acoustofluidics-assisted enrichment of fluorescent probes will enhance visual sensitivity of colorimetric assay using as few probes as possible (Figure 1B and C).
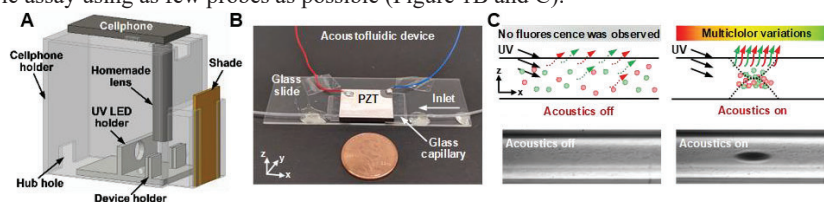

Figure 1: (A) 3D diagram of the portable cell-phone-based acoustofluidic platform. (B) Photo of the acoustofluidic nanoparticle-concentration device. (C) Illustration of visual testing using the acoustofluidic-based nanoparticle-concentration device. The figures are from Ref. 4

Dual-emitting fluorescent probes-based acoustofluidic platform for Hb colorimetric detection

For colorimetric testing, red and green quantum dots-embedded silica nanoparticles ($SiO_2@R$ and $G@SiO_2$) were synthesized and mixed with samples to function as target identifiers and interior labels, respectively. Acoustofluidic-based nanoparticle concentration was utilized to aggregate the quantum dot-embedded nanoparticles in the viewing area and to enhance the intensity of the signals emitted from the quantum dots (QDs). This concentration step ensured that the relatively weak signal could be amplified and imaged using a low-cost and portable cellphone camera, removing the reliance on bulky and expensive optical equipment.

Using this system, various colors in the red-green spectrum can be detected depending on the ratio of red and green probes. The color at the concentrated spot of nanoparticles observed by a cellphone camera is proportional to the concentration of Hb because of the quenching of red fluorescence, while the green fluorescence remains unchanged regardless of the levels of Hb.
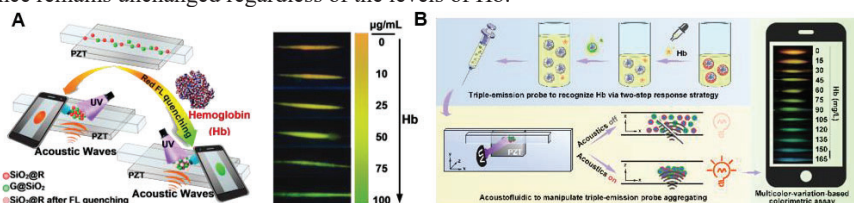

Figure 2: Illustration of Hb visual detection using (A) dual-emitting and (B) triple-emitting fluorescent probes-based acoustofluidic platform. The figures are from Ref. 4 and Ref. 5.

Triple-emitting fluorescent probe-based acoustofluidic platform for Hb quantitative assay with multicolor-variation

To overcome the problem of narrow color evolution window of dual-emitting probe, triple-emitting fluorescent probe-based acoustofluidic platform was developed (Figure 2B). Two ratiometric fluorescent probes (blue-organosilane-polymerized carbon dots@SiO$_2$@red-CdTe/CdS quantum dots (b@SiO$_2$@r) and blue-organosilane-polymerized carbon dots@SiO$_2$@green-CdTe/CdS quantum dots (b@SiO$_2$@g)) was synthesized. As signal reporters of the triple-emission probe, outer modified "r" and "g" will be quenched in sequence by target via two-step response strategy while the inner "b" as internal standard remains constant. When acoustic field is applied, the effect of acoustofluidics-based nanoparticles concentration makes triple-emission probe aggregate completely, accompanying fluorescence color signal being enhanced, sensitivity of colorimetric assay being improved and multicolor-variation (from orange to dark-goldenrod to dark-olive-green to sea-green to dark-cyan to final steel-blue) with the increase of analyte amount. For Hb detection, the limit of detection was 1.99 mg/L.

Integrated ratiometric fluorescence probe-based acoustofluidic platform for visual detection of anthrax biomarker

For acoustofluidic platform based dual- and triple-emitting fluorescent probes, despite the sensitivity of fluorescence colorimetry has been improved, the repeatability of the method needs to be further enhanced due to color inhomogeneity of formed fluorescent aggregates. It may be caused by simply mixing two kinds of fluorescence probes NPs, which cannot be completely identical in physicochemical properties (e.g., size and surface potential). So, a more robust ratiometric probe system in which internal reference and sensing moiety are present in the same carrier was developed (Figure 3). Herein, Eu^{3+}-EDTA complex as a signal report unit was grafted onto the surface of organosilane functionalized carbon dots (SiCDs)-doped SiO$_2$ nanoparticles, resulting in an integrated ratiometric fluorescence probe (INT-probe) for sensitive and visual DPA via smartphone-based acoustofluidic sensing platform. As for detection, Eu^{3+} from the INT-probe were sensitized by DPA to exhibit red fluorescence "off-on" response, while the blue fluorescence of entrapped SiCDs as an internal reference still maintain unchanged. With the increase of DPA concentration, obvious color variations of INT-probe/DPA aggregates from blue to pink could be observed, and the color information of the fluorescent aggregates was converted to red, green and blue values for quantitative analysis, whose lowest detectable concentration reached 100 nM that is about 2~3 orders of magnitude lower than the infectious dosage of Bacillus anthracis spores (60 μM).
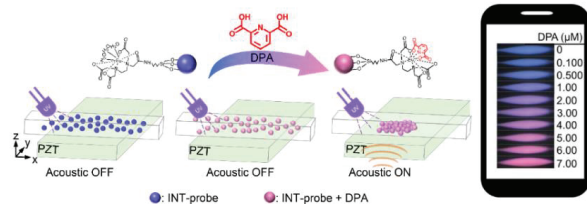

Figure 3: Illustration of DPA visual detection using Integrated ratiometric fluorescence probe-based acoustofluidic platform. The figures are from Ref. 6

Conclusion

We have found some amazing results, which we are looking forward to presenting for the international acoustofluidics community at the *Acoustofluidics 2022 in person Conference* on 19 - 21 October 2022.

References

[1] S. Sharma, J. Zapatero-Rodríguez, P. Estrela, and R. O'Kennedy. Biosensors **5**, 577-601 (2015).

[2] P. Li, and T. J. Huang. Analytical Chemistry **91**, 757-767 (2019).

[3] H. Bachman, P. H. Huang, S. Zhao, S. Yang, P. Zhang, H. Fu, and T. J. Huang. Lab Chip **18**, 433- 441 (2018).

[4] L. Zhang, Z. Tian, H. Bachman, P. Zhang, and T. J. Huang. ACS Nano **14**, 3159-3169 (2020).

[5] P. Chen, J. Wu, H. Fei, H. He, S. Cao, L. Zuo, Y. Jin, L. Zhang, and S. Du. Chemical Engineering Journal **441**, 135976 (2022)

[6] J. Wu, P. Chen, J. Chen, X. Ye, S. Cao, C. Sun, Y. Jin, L. Zhang, and S. Hu. Biosensors and Bioelectronics **214**, 114538 (2022).

Dynamic ultrasound manipulations in air with a perforated reflector

Xiaolong Lu[1,2], Jens Twiefel[3], Zhichao Ma[2] and Peer Fischer[2]

[1] State Key Laboratory of Mechanics and Control of Mechanical Structures, Nanjing University of Aeronautics and Astronautics, Nanjing, Jiangsu 210016, China
E-mail: long_8446110@nuaa.edu.cn
[2] Max Planck Institute for Intelligent Systems, Heisenbergstr. 3, 70569 Stuttgart, Germany
[3] Institute of Dynamics and Vibration Research, Leibniz Universität Hannover, An der Universität 1, 30823 Garbsen, Germany

Introduction

Acoustic levitation is an attractive contactless manipulation strategy to handle matter across a wide range of sizes [1] with diverse applications ranging from biomedicine, analytical chemistry, nanotechnology, and advanced manufacturing.[2] While the phased array of ultrasonic transducers (PAT) platform shows great flexibility in controlling the trajectory of levitated objects, it is also rather complex and requires the use of several transducers that need to be individually powered and addressed.[3] Here, we present a manipulation mechanism that can transform the well-known single-axis levitator into a dynamic acoustic levitator via controlling one perforated reflector with subwavelength apertures. Its main advantages are its simplicity and the ability to achieve dynamic levitation with a single, high-power transducer. Subwavelength apertures are mechanically manipulated to give rise to dynamic trapping fields. The motion of the trapped object inside the levitator can give rise to feedback that causes oscillations and rotations in the trapping potential without external intervention. A number of objects are successfully manipulated inside this setup and indicate its potential for practical applications.

Fundamental working principles

The working principle is shown in Figure 1a. The reflector contains several openings (apertures). It is placed at a distance of one wavelength above the surface of an ultrasound transducer, which acts as the emitter. Blocking an aperture deforms the otherwise flat nodal (ND) plane, and introduces a new stable trapping point below the blocked aperture. Based on this principle, we have constructed one reflector with a circular pattern of 12 apertures. The apertures, A1 to A12, are positioned at exactly one wavelength away from the center aperture A0. All apertures have the identical diameter of 1/4 wavelength of the acoustic wave. The bottom ND plane is selected for levitation and the location for the levitated particles is controlled by blocking and unblocking apertures.
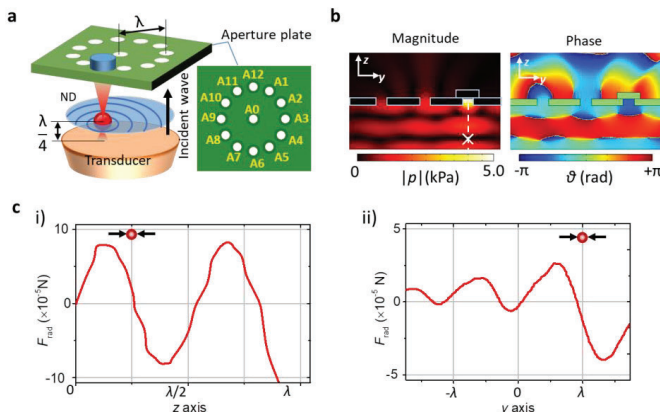

Figure 1: Working mechanism of the dynamic levitator. (a) Schematic of working principle. Selected trapping and manipulation of a levitated particle (red) in the nodal plane (ND, light blue) which lies between the transducer (orange) and the aperture plate (green). (b) Acoustic pressure and phase distribution, respectively, with a blocked aperture A3. The white cross denotes the corresponding locations in the two planes. (c) The radiation force calculated along the dashed line in the yz-plane (i) and the xy-plane (ii). Black arrows indicate the direction of radiation force.

Numerical simulations (conducted with COMSOL Multiphysics 5.3) were used to calculate the corresponding acoustic field distributions. The aperture (open or blocked) is assumed to be perfectly absorbing. The spatial distribution of the acoustic field, including the pressure magnitude and phase angle at different opening conditions, has been calculated and the results are shown in Figure 1b. When one aperture

(e.g. A3) is blocked, an acoustic pressure gradient is formed underneath the aperture A3. The acoustic radiation force on a 3 mm Expanded Polystyrene Sphere (EPS) particle, is calculated for a blocked aperture (Figure 1c). The blocked aperture A3 in Figure 1c results in a lateral force pointing to the position $(0, \lambda, \lambda/4)$.

Experimental results

The experimental setup to demonstrate the dynamic levitation is displayed in Figure 2a. In particular, the solid flat aperture plate (100 mm×100 mm×1.6 mm) is a standard printed circuit board (PCB). The metal-epoxy-metal stacked multilayer of the PCB offers good insulation for acoustic waves and is sufficiently stiff to maintain its shape during operation. There is large acoustic impedance mismatch between air ($\sim 4 \times 10^2$ kg m-2 s^{-1}) and PCB ($\sim 6.7 \times 10^6$ kg m^{-2} s^{-1}), thus we assume perfect reflection at the boundary.

Dynamically closing and opening apertures can be used to manipulate the levitated EPS particles within the setup. As shown in Figure 2b, we manipulated the apertures of the setup in such a way that the EPS particle was moved along the predefined manipulation paths represented by three letters M, P and I. The distance between two neighboring apertures is a critical factor that affects the motion of the trapped object (both in continuity and accuracy). We found that a smooth movement with a high motion accuracy is achieved, if two adjacent apertures have a distance of $\lambda/2$ (6 mm). We found experimentally for the levitated objects of this proposal, that the blocks should be moved at a rate not exceeding 10 mm/s.
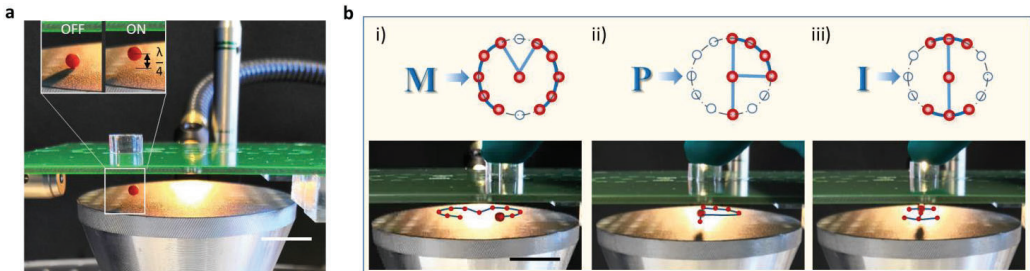

Figure 2: EPS particle levitation and positioning by blocking apertures at different locations. (a) Levitation of an EPS particle by switching the applied ultrasound ON/OFF. (b) Dynamic transport for a levitated particle enabled by moving the block to trace the letters M (i), P (ii) and I (iii). Scale bar: 20 mm.

The apertures of the setup can also be manipulated in such a way that the levitated particles move laterally over larger distances. A trapped particle below aperture A9 can be released by removing block b1. Due to the planar radiation force shown in Figure 1 the particle jumps along the y axis, until it reaches the target position below the blocked aperture A3. Balanced by the net radiation force due to block b2, the particle will eventually settle at this new equilibrium point. Superimposed images in Figure 3a illustrate the fast linear locomotion for an EPS particle. Within a short time of 100 ms, the particle is driven to move linearly from A9 towards A3 at a comparatively high speed of 240 mm/s. The movement can be repeated by periodically moving b1 and b2 (see Figure 3b).
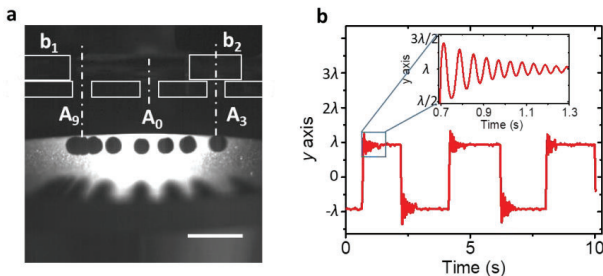

Figure 3: Dynamic response of levitated particles. (a) Superimposed images illustrating the linear motion from the site underneath A9 to A3 via A0. Time lapse: 15 ms. Scale bar: 12 mm. (b) Repeated translation by periodically moving/holding blocks b1 and b2. The inset shows the transient response of overshooting and attenuation when the particle reaches the target location.

Conclusion

In summary, we have demonstrated an acoustic levitator that contains subwavelength apertures in its reflector to permit the dynamic mechanical manipulation of levitated objects [4]. The proposed strategy enables the conventional single-axis acoustic levitator system to achieve on-demand contactless transport in a facile manner. The blocking of subwavelength apertures can give rise to a time-varying Gor'kov potential that can be used to realize long distance translation, without the need for any time-varying input fields.

References

[1] A. Ozcelik, J. Rufo, F. Guo, Y. Y. Gu, P. Li, J. Lata, T. J. Huang, Nat. Methods **15**, 1021 (2018).
[2] M. A. B. Andrade, A. Marzo, J. C. Adamowski, Appl. Phys. Lett. **116**, 250501 (2020).
[3] A. Marzo, S. A. Seah, B. W. Drinkwater, D. R. Sahoo, B. Long, S. Subramanian, Nat. Commun. **6**, 8661 (2015).
[4] X. Lu, J. Twiefel, Z. Ma, T. Yu, J. Wallaschek, P. Fischer, Adv. Sci. **8**, 2100888 (2021).

Efficient acoustofluidics and active surface cleaning using ZnO/glass thin film acoustic waves

Hui Ling Ong, Jikai Zhang, Prashant Agrawal, Hamdi Torun, Kunyapat Thummavichai, Qiang Wu, and Yong-Qing (Richard) Fu

[1]Faculty of Engineering and Environment, Northumbria University, Newcastle upon Tyne, NE1 8ST, UK
E-mail: huiling.ong@northumbria.ac.uk/ h.l.ong@northumbria.ac.uk

Introduction

Photovoltaics (PV) panels are prone to surface contamination caused by dirt, dust, or ice accretion, and contamination of PV panels poses great issue of degraded efficiency. To solve this issue, there have been various methods used [1,2], which can be classified into passive and active methods. An example of passive methods is using micro/nanostructured surfaces, which however often have poor durability [1]. There have been studies which looks into active or self-cleaning methods such as surface acoustic waves (SAWs), which allow the control in the motion of the droplets [3,4].

Figure 1(a) illustrates the SAW interaction with water droplets, which causes streaming and facilitating droplet movement. When the SAWs are in contact with the droplet, part of the SAWs are refracted into the liquid as a longitudinal wave following Rayleigh angle [3], $\theta_R = sin^{-1}V_L/V_s$, where V_L is the speed of sound in water (1480 m/s), and V_s is the wave propagation velocities in solid. The forces on a particle exposed by the acoustic waves are those due to direct irradiation by the acoustic field and indirect irradiation from scattering of the acoustic field from other objects. Particles in fluid experience both acoustic radiation force (F_{ARF}) and acoustic streaming induced Stokes drag force F_{drag}. The SAW induced streaming force for this work, is mostly governed by the acoustic streaming induced Stokes drag force, $\boldsymbol{F}^{drag} = 6\pi\eta r v$. When the SAWs interact with the contaminants, they are quickly mixed into water droplet and driven away as shown in Figure 1(a), causing significant streaming inside the water droplet as it moves along the SAW propagating path, which perform the active surface cleaning process.
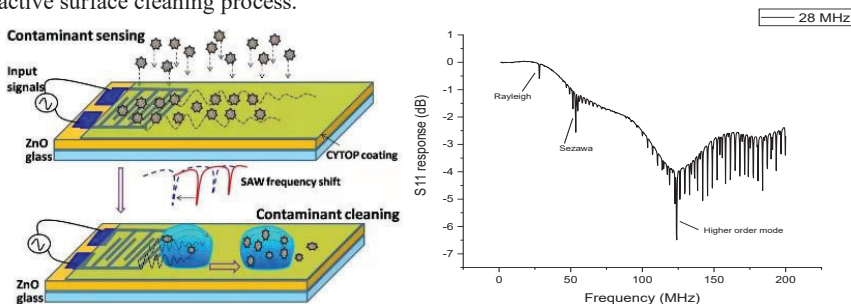

Figure 1: (a) SAW interaction with water droplets and contaminants [4]; (b) S11 spectrum of ZnO/glass SAW device

SAW acoustofluidics platform

In this work, ZnO thin film was deposited onto glass, and then SAW devices were fabricated using lithography methods. Figure 1(b) shows the S11 Spectrum of the SAW devices where it shows different waves modes. The wavelength of the SAW device is 100 μm, and the resonant frequency of the Rayleigh wave mode was determined to be 28.12 MHz. For effective facilitation of water droplet during operation with SAW agitations, the SAW devices were treated with CYTOP, a hydrophobic fluoropolymer. This hydrophobic layer allows the water droplet to experience pumping at a suitable RF power range along the SAW propagating paths upon operation, fulfilling the cleaning process.

The ZnO/glass SAW devices were explored for active surface cleaning based on the evaluation on its acoustofluidics performance which includes transportation, jetting, and nebulization. Active surface cleaning of the contaminants (ash particles, starch solutions, and powder mixture in gel were used as model contaminants) were demonstrated based on the transportation of water droplets, and varied SAW powers were applied and induced strong interactions between water droplet and contaminants.
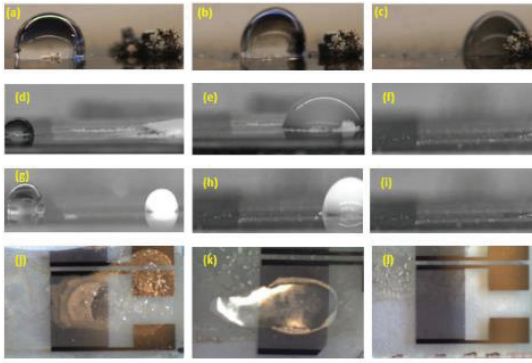
Figure 2: Different active cleaning scenarios with 2 µL droplet: (a)-(c) loose ash particles; (d)-(f) solid particles; (g)-(i) starch mixture; (j)-(l) contaminant layer

Demonstration on active surface cleaning at different scenarios

Active cleaning demonstrations were conducted using various particles being placed onto the SAW propagating paths. Figures 2(a)-(c) show examples of the cleaning stages of ash particles on the surface of the ZnO/glass SAW device. When the droplet encounters the ash particles during the pumping process, the ash particles quickly mixed into water droplet and driven away [5].

Figures 2(d)-(f) shows the cleaning stages of dried solid starch powders. As the SAW power is applied, the starch is observed to rapidly mixed with the water droplet, leading to significant streaming within the water droplet. During this process, more water droplets were continuously dispensed to facilitate mixing and driving of dried solid starch particles. The acoustic heating effects occurs simultaneously which provides an effective role to dislodge particles from the surface by overcoming the adhesion forces of the liquid starch solution [2]. Figures 2(g)-(i) shows the cleaning stages of liquid starch solution to simulate birds' excrement. Similarly, under significant internal streaming and acoustic heating effects, the liquid starch solution is observed to be fully driven away.

Figures 2(j)-(l) shows the cleaning stages of the contaminated layer. Upon SAW agitations, the water droplet is mixed and blended with the contaminated layer upon interaction, which ultimately cause streaming effect and dilution effect. As the water droplets are continuously dispensed, streaming continues to occur, and the acoustic heating experienced during this process further cause the contaminated layer to detach from the surface. This in turns overcome the adhesion forces of the contaminated layer from the surface of the SAW device, demonstrating the active surface cleaning mechanisms.
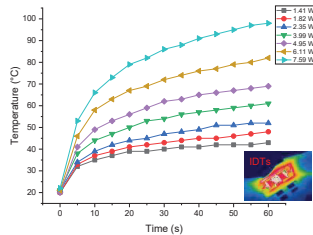

Figure 3: Surface temperature of ZnO/glass SAW device as a function of time using different RF powers with an inset showing the snapshot of infrared imaging of the thermal distribution on the surface

Acousto-thermal effects on ZnO/glass SAW devices

Figure 3 shows the acousto-thermal effects on the surface of the ZnO/glass SAW devices at different RF powers. The surface temperature was observed to be increasing instantly for 30 seconds during the heating process. Subsequently, a slow increase of temperature can be observed from 30s to 60s. Acousto-thermal effect experienced during active cleaning posed as an important factor. As the temperature increases, the SAW devices will heat up and this can trigger the water droplet to interact with the surface contaminants and be driven away more effectively during liquid transportation. It can also be implied that with localized surface heating, it allows the surface contaminants to be easily dislodged by overcoming the adhesion forces from the surface during active cleaning process. Additionally, based on the results of acoustic heating from Figure 3, the temperature of ZnO/glass SAW devices need to be monitored, and should ensure that it is operated in the suitable range of the applied power. This is to prevent overheating of the SAW device and damaging the SAW electrodes (IDTs).

Conclusion

In this work, the acoustofluidics performance of ZnO/glass SAW devices were evaluated where both pumping and jetting phenomenon were observed when the SAW device was treated with CYTOP. The transparent glass structures with integrated SAW devices are implemented as an active surface cleaning platform with the ability of contamination detection. Elimination of surface contaminants were illustrated in this work, where particles which were used as model contaminants was demonstrated at different RF powers to evaluate the cleaning efficiency and acousto-thermal effect on ZnO/glass SAW device. This active sensing and surface cleaning work can serve as a platform for autonomous cleaning in future work by implementing a closed loop feedback.

References

[1] J. Farrokhi Derakhshandeh et al., Sustain. Energy Technol. Assessments **47**, 101518 (2021)
[2] D. Sun and K. F. Böhringer, Microsystems Nanoeng **6**, pp. 1-12 (2020)
[3] H. Song, D. Jang, J. Lee, K. Yong Lee, and S. Kug Chung, J. Micromechanics Microengineering **31**, 125007 (2021)
[4] H. Ong et al., Mater. Chem. Phys. **287**, 126290 (2022)
[5] S. Alagoz and Y. Apak, J. Clean. Prod. **253**, 119992 (2020)
[6] J. Li et al., J. Phys. D. Appl. Phys **53**(35), 355402 (2020)
[7] G. Potter, N. Tokranova, A. Rastegar, J. Castracane, Microelectronic Engineering **162**, 100-104 (2016)

Localised mechanical characterisation of small organisms enabled through microbubble-based manipulation

<u>Nino F. Läubli</u>[1,2], Jan T. Burri[1], Gabriele S. Kaminski Schierle[2], Daniel Ahmed[1], and Bradley J. Nelson[1]

[1]Department of Mechanical and Process Engineering, ETH Zurich, Zurich, Switzerland
[2]Department of Chemical Engineering and Biotechnology, University of Cambridge, Cambridge, UK
E-mail: nl431@cam.ac.uk, URL: https://www.ceb-mng.org/

Introduction

While of relevance for a variety of research fields including biology and biomedicine, the investigation of small organisms is often severely limited by a lack of appropriate handling tools. In recent years, acoustofluidic rotational manipulation [1, 2], including its application *via* microbubbles [3 - 5], has been presented as an accessible method to allow for the controlled yet non-invasive handling and rotation of various small objects and their corresponding optical evaluation. However, despite its simplicity and flexibility in design, the integration of acoustic manipulation systems into further technologies remains challenging. In this experimental study [6], we introduce the 3D mechanical characterisation of single plant cells and *C. elegans* nematodes by combining bubble-based manipulations with microindentations to quantify the specimens' local variations in stiffness – a task crucial to further our understanding of these small organisms.

Experimental Setup

The acoustofluidic manipulation system (see Fig. 1a) consists of an array of elongated microcavities with a width, height, and separation of 80 μm, 150 μm, and 100 μm, respectively, and is fabricated using standard soft lithography. The produced channels are cut perpendicularly to great microcavities that subsequently allow for direct access to the manipulated samples while maintaining the stiff substrate required for the force measurements. The air bubbles trapped within the PDMS cavities are excited *via* a piezoelectric transducer at an excitation frequency of 24 kHz which leads to the formation of strong out-of-plane vortices and enables controllable rotational manipulations, as shown in Fig. 1b and 1c. The acoustofluidic component is integrated into a custom force microscopy setup (see Fig. 1d) consisting of a MEMS-based capacitive force sensor mounted to a 3D positioner on a fast, high-resolution z-stage and fixed to an inverted microscope. To ensure locally confined mechanical characterisations, a tungsten probe with a tip diameter of <2 μm is attached to the force sensor.
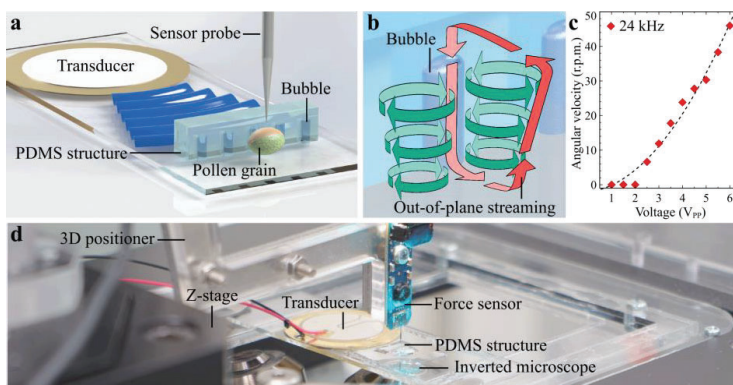
Figure 1: Experimental setup and acoustofluidic manipulation. (a) A schematic showing the PDMS structure with the accessible microbubbles and the nearby transducer. (b) Illustration of vortices generated at the air-liquid interface. (c) The angular velocity of an out-of-plane rotating specimen in dependence of the excitation voltage (V_{PP}). (d) A photograph of the experimental setup including the force sensor (attached to the 3D positioner), the z-stage used for the indentations, the acoustofluidic component used for the manipulations, as well as the inverted microscope.

3D Mechanical Characterisation of Plant Cells

Pollen play a crucial role in sexual plant reproduction as they have to protect the sperm cells during transportation while, subsequently, deliver them to the ovules by locally weakening the cell wall. To accomplish these tasks, pollen grains possess two layers of cell wall, which allow them to undergo

morphological changes depending on their hydration state. However, as the inner cell wall (intine, see Fig. 2a) is usually only accessible at specific regions of the pollen grain, controlled manipulations are required to enable the quantification of both layers on individual samples. Using our acoustofluidic component, *Lilium longiflorum* pollen grains suspended in water are trapped near the bubbles' surfaces *via* radiation forces and rotated using the acoustic streaming. By that, we are able to make multiple regions of individual samples accessible to the sensor probe to perform controlled microindentations (Fig. 2b). The subsequently derived stiffness ratios allows for the reduction of noise produced by biological variations (see Fig. 2c) by quantifying different surface areas of individual specimens, rather than of multiple samples, and enables the detection of localised cell wall changes based on environmental parameters such as the Ca^{2+} concentration in the surrounding liquid.

3D Mechanical Characterisation of Animal Models

C. elegans nematodes are a prominent animal model organisms and of major interest for biomedical research due to their fully sequenced genome. Similar to the characterisation of pollen grains, paralysed nematodes are submerged in liquid before being attracted to the microbubbles by radiation forces. In contrast to the smaller pollen grains, multiple parallel bubbles are used for the controlled out-of-plane rotation of *C. elegans* (Fig. 2d). Individual indentations are performed in sequence (red dots in Fig. 2d) along the specimen before rotating it *via* the generated acoustic streaming to access previously obstructed regions (Fig. 2e). The obtained results expose significant variations in stiffness (p = 3.14e-10, Fig. 2f) on individual *C. elegans* depending on the indented region. The observed differences are likely caused by variations in the underlying tissue, such as the body wall muscles indicated in green in Fig. 2f, and possibly further enhanced through the use of paralysing drugs. Nevertheless, our results highlight the relevance of 3D mechanical quantifications to prevent possible misinterpretations based on randomly performed single measurements.
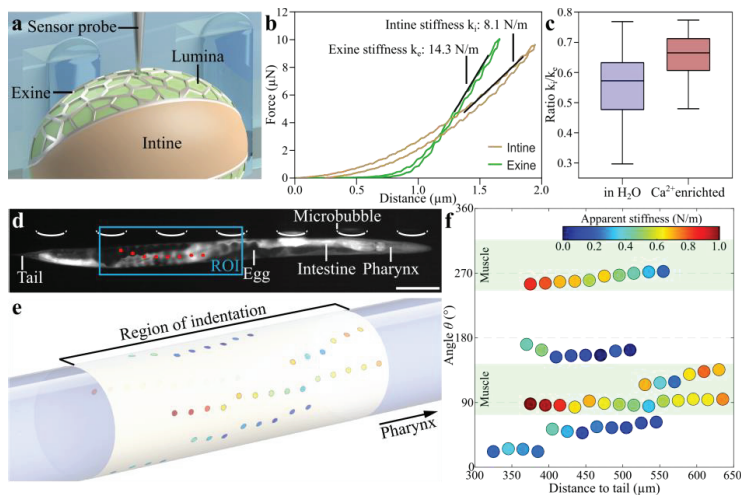

Figure 2: 3D characterisation of pollen grains and *C. elegans*. (a) A schematic of a pollen grain with the two cell wall layers intine and exine. (b) Indentation curves obtained for the different cell wall layers on a single specimen. (c) The ratios between intine and exine stiffness of pollen grains for varying environments. (d) A paralysed nematode trapped near the microbubble array. The measurements (red spots) are performed in the region of indentation (ROI). (e) Dots representing the distribution of the different indentations within the ROI around a single *C. elegans*. (f) The varying apparent stiffnesses detected on a single nematode with the location of the underlying tissue, *i.e.*, the muscles, indicated in green. Scale bar = 100 μm.

Conclusion

In this experimental work, we integrate microbubble-based acoustofluidic manipulation into a custom force microscopy setup to enable the full 3D mechanical quantification of individual small organisms, *i.e.*, pollen grains and C. elegans. By making previously obstructed regions accessible through the controlled rotational manipulation of the specimen, we are able to significantly reduce the influence of noise produced by biological variations while further highlighting the relevance of controlled localised characterisations as a tool to prevent subsequent misinterpretations.

References

[1] F. Guo, *et al.*. PNAS **113**, 1522-1527 (2016).
[2] A. Ozcelik, *et al.*. Small **12**, 5120-5125 (2016).
[3] D. Ahmed *et al.*. Nature Communications **7**, 11085 (2016).
[4] N.F. Läubli et al., Analytical Chemistry **93**, 9760–9770 (2021).
[5] Y. Li, X. Liu, Q. Huang, T., and T. Arai. Applied Physics Letters **118**, 063701 (2021).
[6] N.F. Läubli *et al.*. Nature Communications **12**, 2583 (2021).